

Electronic Thesis and Dissertation Repository

11-6-2019 3:00 PM

Extrusion-based 3D Printing of Macro/Microstructures for Advanced Lithium/Sodium Batteries

Jiwei Wang

The University of Western Ontario

Supervisor

Tsun-Kong Sham

The University of Western Ontario Co-Supervisor

Xueliang Sun

The University of Western Ontario

Graduate Program in Chemistry

A thesis submitted in partial fulfillment of the requirements for the degree in Doctor of
Philosophy

© Jiwei Wang 2019

Follow this and additional works at: <https://ir.lib.uwo.ca/etd>

Recommended Citation

Wang, Jiwei, "Extrusion-based 3D Printing of Macro/Microstructures for Advanced Lithium/Sodium Batteries" (2019). *Electronic Thesis and Dissertation Repository*. 6775.

<https://ir.lib.uwo.ca/etd/6775>

This Dissertation/Thesis is brought to you for free and open access by Scholarship@Western. It has been accepted for inclusion in Electronic Thesis and Dissertation Repository by an authorized administrator of Scholarship@Western. For more information, please contact wlsadmin@uwo.ca.

Abstract

With the development of electronics and electric vehicles, high-performance batteries with high energy density, high safety, and aesthetic diversity are greatly needed as dominating power sources. However, the electrodes and electrolytes fabricated with traditional techniques have limited form factors, mechanical flexibility, and poor performance. Extrusion-type 3D printing techniques have thus been applied to fabricate 3D batteries with high performance since 3D printing techniques have great advantages in the fabrication of complex 3D structures and geometric shapes from various materials. The research in this thesis aims at fabricating high-performance Li/Na batteries via 3D printing of advanced electrodes and solid electrolytes.

Firstly, an extrusion-type 3D printing method was applied for fabricating 3D-patterned ultrathick LiFePO_4 electrodes. The designed unique 3D architectures could greatly improve the electron/ion transport even within the thick electrodes. We also demonstrated the 3D printing of patterned silicon (Si) anodes with vertically aligned and multi-scaled porous structures for achieving high-areal capacity LIBs by using a low-cost aqueous-based ink.

Besides fabricating electrodes, we also fabricated LAGP ($\text{Li}_{1.5}\text{Al}_{0.5}\text{Ge}_{1.5}\text{P}_3\text{O}_{12}$) thin solid electrolytes through an extrusion-type 3D printing approach. The printed thin solid electrolyte with short Li^+ transport path can increase the energy density and power density of a solid battery.

An extrusion-based 3D printing approach was also developed to construct a high-performance sodium metal battery (SMB) consisting of a printed Na@rGO/CNT anode and a printed $\text{O}_3\text{-NaCu}_{1/9}\text{Ni}_{2/9}\text{Fe}_{3/9}\text{Mn}_{3/9}\text{O}_2$ (denoted as NCFM) cathode. The 3D-printed Na@rGO/CNT anode possesses multiple porosities, which could provide abundant active reaction sites and enable fast Na^+ transport. Moreover, the resultant 3D structured Na@rGO/CNT can effectively suppress the Na dendrite growth by decreasing the local current density and releasing the huge volume change of Na during cycling. On the other hand, the 3D-printed micro-structured NCFM cathode composed of interconnected CNTs and porous polymer framework can enable fast electron and ion transport as well as facilitated electrolyte penetration within the whole electrode.

To further increase the energy density of a sodium-ion battery, we developed high-voltage layered $P2\text{-Na}_{2/3}\text{Ni}_{1/3}\text{Mn}_{2/3}\text{O}_2$ (NMO) cathodes. By applying ALD AlPO_4 coating layer on the NMO particles, the reduction of Mn was suppressed upon cycling, which could improve the structural stability of the cathode. This high-voltage cathode can be used as materials for 3D printing of high energy density sodium-ion battery in the future.

In summary, this thesis has successfully developed various printable inks and designed unique 3D architectures via an advanced extrusion-type 3D printing technique for achieving high-performance Li/Na batteries.

Keywords

High energy density, Extrusion-type 3D printing, 3D batteries, Solid electrolyte, 3D-patterned LiFePO_4 , Patterned silicon, LAGP thin electrolyte, Short Li^+ transport path, Sodium metal battery (SMB), Sodium dendrite growth, High-voltage layered cathodes, Atomic layer deposition (ALD), Aluminum Phosphate (AlPO_4)

Lay Summary

Extrusion-type 3D printing is a technique that extrudes a paste-like ink with shear-thinning behavior through a nozzle to build 3D architectures in a layer-by-layer way. After extrusion, the 3D architectures usually become solidification through the evaporation of solvents, chemical changes (cross-linking) or freeze-drying.

Rechargeable batteries have attracted significant attention due to their high energy density and power density as well as pollution-free operation. However, traditional manufacturing methods are hard to fabricate thick electrodes with fast electron/ion transport due to the planar structure limitations. Moreover, electrodes and electrolytes fabricated by traditional techniques have limited form factors and mechanical flexibility. Extrusion-type 3D printing techniques thus have been applied to design various 3D architectures for achieving high-performance Li/Na batteries.

Co-Authorship Statement

Chapter 3

Title: Toward High Areal Energy and Power Density Electrode for Li-Ion Batteries via Optimized 3D Printing Approach

The final version of this manuscript has been published in **ACS Appl. Mater. Interfaces**, 2018, 10, 39794-39801

X. Sun, T.K. Sham, and X. Sun directed the project. J. Wang conceived the idea, designed the experiments and wrote the manuscript. Q. Sun gave some suggestions for the experiments and manuscript. X. Gao helped with the freeze-drying. W. Li and C. Wang helped with SEM characterization. F. Holness and A. Price gave some suggestions on the 3D printing technique. M. Zheng gave some suggestions for the writing. R. Li helped with purchasing chemicals and characterizations. All authors discussed the results and commented on the manuscript.

Chapter 4

Title: 3D Printing of Vertically Aligned and Patternable Silicon Anodes for High Areal Capacity Li-Ion Batteries

The final version of this manuscript is to be submitted for publishing

X. Sun, T.K. Sham, and X. Sun directed the project. J. Wang conceived the idea, designed the experiments and wrote the manuscript. Q. Sun gave some suggestions for the experiments and manuscript. X. Gao helped with the freeze-drying. W. Li and Y. Sun helped with SEM characterization. X. Lin and J. Liang helped with the Raman measurements. M. Zheng gave some suggestions for the writing. R. Li helped with purchasing chemicals and characterizations. All authors discussed the results and commented on the manuscript.

Chapter 5

Title: 3D Printing of Shape-Versatile and Thin Solid Electrolyte for High-Performance Solid-State Li-Metal Batteries

The final version of this manuscript is to be submitted for publishing

X. Sun, T.K. Sham, and X. Sun directed the project. J. Wang conceived the idea, designed the experiments and wrote the manuscript. Q. Sun gave some suggestions for the experiments and manuscript. C. Zhao prepared the gel polymer electrolyte. J. Luo provided the cathode electrodes. J. Liang helped with the XRD measurements. C. Wang and Y. Sun helped on the ionic conductivity testing. M. Zheng gave some suggestions on the manuscript writing. R. Li helped with purchasing chemicals and characterizations. All authors discussed the results and commented on the manuscript.

Chapter 6

Title: 3D Printing of High-Performance Na-Metal Batteries

The final version of this manuscript is to be submitted for publishing

X. Sun, T.K. Sham, and X. Sun directed the project. J. Wang conceived the idea and designed the experiments and wrote the manuscript. Q. Sun and C. Wang gave some suggestions for the experiments and manuscript. W. Li and X. Lin helped with the SEM measurements. X. Gao helped with the freeze-drying. J. Luo gave some suggestions on the manuscript writing. R. Li helped with purchasing chemicals and characterizations. All authors discussed the results and commented on the manuscript.

Chapter 7

Title: Nanoscale Surface Modification of High-Voltage Layered Sodium Cathode via Atomic Layer Deposition of Aluminum Phosphate with Enhanced Cycle Performance

The final version of this manuscript is to be submitted for publishing

X. Sun, T.K. Sham, and X. Sun directed the project. J. Wang conceived the idea and designed the experiments and wrote the manuscript. Q. Sun gave some suggestions for the experiments and manuscript. C. Wang and X. Gao helped with the SEM measurements. B. Wang helped with the ALD coating experiments. X. Lin and C. Wang helped with the XRD measurements. Y. Sun gave some suggestions on the manuscript writing. R. Li helped with purchasing chemicals and characterizations. All authors discussed the results and commented on the manuscript.

Acknowledgements

First of all, I would like to express my sincerest appreciation to my supervisors, Prof. Tsun-Kong Sham, and Prof. Xueliang (Andy) Sun. It is my great honor for me to have a valuable opportunity working with such two great researchers. Prof. Sun's dedication to work, his passions to science, and his patience have greatly inspired me. Prof. Sham's profound knowledge, creative ideas, and kindness have impressed me a lot throughout my graduate study. Without their unconditional support and guidance, I would not have been completed my Ph.D. study.

Second, I would like to thank Mrs. Ruying Li, who is the wife of Dr. Sun and a research engineer in Dr. Sun's lab. She has dedicated many efforts on the lab management. I am truly grateful for her help in training me the experimental techniques and her care on my research and life.

I would also like to thank my past and present group members that I have worked with during the past four years. I would especially like to thank Dr. Qian Sun who is always patient and ready to answer any questions and provide helpful instructions on my research. I would also like to express my appreciations to Mr. Changhong Wang and Mr. Yipeng Sun for helping me a lot in both my research and daily life. I would also like to thank other group members: Dr. Yun-Mui You, Dr. Zhiqiang Wang, Dr. Xiao Xuan Guo, Dr. Lijia Liu, Dr. Jun Li, Dr. Mohammad Norouzi Banis, Dr. Madalena Sophia Kozachuk, Dr. Weihan Li, Dr. Xia Li, Dr. Lei Zhang, Dr. Jianwen Liang, Dr. Xiaona Li, Dr. Changtai Zhao, Dr. Xulei Sui, Dr. Yang Zhao, Dr. Biqiong Wang, Dr. Biwei Xiao, Dr. Wei Xiao, Dr. Niancai Cheng, Dr. Yulong Liu, Dr. Karthikeyan Kaliyappan, Dr. Andrew Lushington, Dr. Dawei Wang, Dr. Zhongxin Song, Mr. Jiatang Chen, Ms. Fei Sun, Mr. Heng Xiang, Ms. Xiaoting Lin, Mr. Jianneng Liang, Mr. Junjie Li, Mr. Feipeng Zhao, Ms. Xuejie Gao, Ms. Jing Luo, Ms. Minsi Li, Mr. Keegan Adair, Mr. Sixu Deng, Ms. Shumin Zhang, Mr. Xuchun Wang, and Ms. Lu Yao. It has been a great pleasure working with you.

I would also like to thank the funding support from the Natural Science and Engineering Research Council of Canada (NSERC), the Canada Research Chair Program (CRC), the Canada Foundation for Innovation (CFI), Jiangsu Key Laboratory for Carbon-Based Functional Materials and Devices and Collaborative Innovation Center of Suzhou Nano Science & Technology, Canadian Light Source (CLS) at the University of Saskatchewan, the Canadian Institute of Health Research (CIHR), and the University of Western Ontario (UWO). I acknowledge the support of a travel grant by CLS.

I would also like to thank my collaborators. Dr. Aaron David Price, Mr. Frederick Benjamin Holness at UWO, Dr. Xuhui Sun and Mr. Kun Feng at Soochow University.

Lastly, I have to thank my mother and my older sisters in China for all of their support and love throughout my graduate study. It was not easy to start a new life and graduate study here in Canada. I would not do it without your encouragement and love.

Table of Contents

Abstract.....	II
Co-Authorship Statement.....	IV
Acknowledgements.....	VII
Table of Contents.....	IX
List of Figures.....	XIV
List of Abbreviations.....	XXIII
Chapter 1.....	1
1.1 General introduction.....	1
1.2 3D printing of electrodes for energy storage.....	6
1.2.1 3D-printed electrodes for Li-ion batteries.....	6
1.2.2 3D-printed electrodes for Li-S battery.....	8
1.2.3 3D-printed electrodes for Li-O ₂ /CO ₂ batteries.....	10
1.2.4 3D-printed electrodes for Na-ion batteries.....	12
1.2.5 3D-printed electrodes for supercapacitors.....	15
1.3 3D printing of electrolytes and separator membranes for energy storage.....	17
1.3.1 3D printing of polymer separator for Li-metal batteries.....	17
1.3.2 3D printing of Solid-State Electrolyte.....	18
1.3.3 3D printing of Hybrid Solid-State Electrolyte.....	19
1.4 All 3D-Printed Energy Storage Devices.....	21
1.4.1 All 3D-printed LIBs/LMBs.....	21
1.4.2 All 3D-Printed Supercapacitors.....	24
1.4.3 All 3D-printed Zn-based Batteries.....	25
1.5 Thesis objectives.....	27
1.6 Thesis outline.....	28

1.7 References.....	30
Chapter 2.....	54
2 Experimental Methods and Characterization Techniques	54
2.1 Experimental methods	54
2.1.1 3D printing of free-standing patterned LiFePO ₄ (LFP) thick electrodes.....	54
2.1.2 3D Printing of Patternable Silicon Electrodes	56
2.1.3 3D Printing of Thin Solid-State Electrolyte LAGP (Li _{1.5} Al _{0.5} Ge _{1.5} P ₃ O ₁₂)	57
2.1.4 3D Printing of GO/CNT skeleton	58
2.1.5 Fabrication of 3D Na@rGO/CNT composite electrode	58
2.1.6 Synthesis of O3-NaCu _{1/9} Ni _{2/9} Fe _{3/9} Mn _{3/9} O ₂ by Solid-State Reaction Method	58
2.1.7 3D Printing of O3-NCNFM skeleton.....	59
2.1.8 Synthesis of P2-Na _{2/3} Ni _{1/3} Mn _{2/3} O ₂ (NMO)by Solid-State Reaction Method.....	60
2.1.9 Atomic layer deposition coating of AlPO ₄ on P2-Na _{2/3} Ni _{1/3} Mn _{2/3} O ₂ Cathode	60
2.2 Characterization Techniques.....	61
2.2.1 Physical Characterization methods	61
2.2.2 Electrochemical measurements.....	65
Chapter 3.....	68
3 Toward High Areal Energy and Power Density Electrode for Li-Ion Batteries via Optimized 3D Printing Approach.....	68
3.1 Introduction.....	69
3.2 Experiment Section.....	71
3.2.1 Preparation of LFP ink.....	71
3.2.2 3D printing process	71
3.2.3 Materials characterizations	71
3.2.4 Electrochemical measurements.....	71
3.3 Results and Discussion	72

3.3.1 Morphology and Structural Characterization.....	72
3.3.2 Electrochemical Characterization	75
3.4 Conclusion	80
Acknowledgements.....	81
3.5 References.....	81
Chapter 4.....	91
4 3D Printing of Vertically Aligned and Patternable Silicon Anodes for High Areal Capacity Li-Ion Batteries	91
4.1 Introduction.....	92
4.2 Experimental Section	93
4.2.1 Si-SA Ink Preparation	93
4.2.2 3D Printing Process.....	94
4.2.3 Materials characterizations	94
4.2.4 Electrochemical Measurements	94
4.3 Results and Discussion	94
4.3.1 Morphology and Structure Characterization.....	94
4.3.2 Electrochemical Characterization	97
4.3.3 Post-cycled Electrode Morphology Characterization	100
4.4 Conclusion	102
Acknowledgements.....	102
4.5 References.....	103
Chapter 5.....	114
5 3D Printing of Shape-Versatile and Thin Solid Electrolyte for High-Performance Solid- State Li-Metal Batteries	114
5.1 Introduction.....	115
5.2 Experimental Section	116

5.2.1 Ink Preparation.....	116
5.2.2 3D printing process	117
5.2.3 Materials Characterizations	117
5.2.4 Electrochemical Measurements	117
5.3 Results and Discussion	118
5.3.1 Morphology and Structure Characterization.....	118
5.3.2 Electrochemical Characterization	121
5.4 Conclusion	124
Acknowledgements.....	124
5.5 References.....	124
Chapter 6.....	134
6 3D Printing of High-Performance Sodium Metal Batteries.....	134
6.1 Introduction.....	135
6.2 Experimental Section	137
6.2.1 Material synthesis	137
6.2.2 Preparation of GO/CNT ink.....	137
6.2.3 Preparation of NCNFM ink	137
6.2.4 3D printing process	138
6.2.5 Fabrication of Na@rGO/CNT composite electrodes.....	138
6.2.6 Materials Characterizations:	138
6.2.7 Electrochemical Measurements:	138
6.3 Results and Discussions.....	139
6.3.1 Morphology and Structure Characterization.....	139
6.3.2 Electrochemical Characterization	143
6.4 Conclusions.....	146

Acknowledgements.....	146
6.5 References.....	147
Chapter 7.....	154
7 Nanoscale Surface Modification of High-Voltage Layered Sodium Cathode via Atomic Layer Deposition of Aluminum Phosphate with Enhanced Cycle Performance	154
7.1 Introduction.....	155
7.2 Experimental Section	157
7.2.1 Preparation of P2-Na _{2/3} Ni _{1/3} Mn _{2/3} O ₂	157
7.2.2 Atomic layer deposition of AlPO ₄ on P2-Na _{2/3} Ni _{1/3} Mn _{2/3} O ₂	157
7.2.3 Materials characterization.....	157
7.2.4 Electrochemical performance measurements	158
7.3 Results and Discussions	158
7.3.1 Morphology and Structure Characterization.....	158
7.3.2 Electrochemical Characterization	162
7.3.3 Post-cycling Characterization	167
7.4 Conclusions.....	168
Acknowledgements.....	168
7.5 References.....	169
Chapter 8.....	179
8 Summary and Future Work.....	179
8.1 Conclusions.....	179
8.2 Future Work	181
Appendices.....	184
Curriculum Vitae	185

List of Figures

Figure 1.1.1 Schematic of the FDM printing system.....	2
Figure 1.1.2 Schematic of the SLA printing system.....	3
Figure 1.1.3 Schematic of the SLS printing system.....	4
Figure 1.1.4 Schematic of the extrusion-type DIW printing system.....	5
Figure 1.2.1 (a) Schematic illustration of 3D printing of LMFP cathode and battery package process based on 3D-printed LMFP electrode; (b) Rate capability comparison between the conventional electrode and 3D-printed LMFP electrode at various rates; (c) Long cycling performance comparison between the traditional electrode and 3D-printed electrode at 10C and 20C; (d) SEM images of the 3D-printed Ag microlattice structures using the Aerosol Jet 3D printing method; (e) Areal capacity comparison of the microlattice and block structures with different thickness; (f) Schematic of the 3D printing of SnO ₂ QDs/G architectures; (g) Digital image of the continuously 3D-printed filament; (h) Digital images of various 3D-printed patterns; (i) Cross-sectional SEM image of the printed SnO ₂ QDs/G architectures; (j) Rate capabilities comparison among the 3DP-SnO ₂ QDs/G, SnO ₂ QDs/G and SnO ₂ QDs; (k) Areal capacities of 2-layer, 4-layer, and 6-layer 3DP-SnO ₂ QDs/G architectures.....	8
Figure 1.2.2 (a) Schematic illustration of 3D printing sulfur copolymer-graphene (3DP-pSG) architectures; (b) Top-view SEM image of the 3D architecture, showing periodic macropores; (c) Cross-sectional SEM image of the 3D architecture; (d) Cycle performances of 3DP-pSG and 3DP-SG at 50 mA g ⁻¹ ; (e) Schematic demonstration of the 3D printing of S/BP 2000 thick cathodes; (f-h) SEM images of the 3D electrode at different magnifications from top view; (i) Cycling performance of the 3DP-FDE electrodes with a sulfur loading of 5.5 mg cm ⁻² at various rates.....	10
Figure 1.2.3 (a) Digital image showing the process of printing complex 3D architectures line-by-line; (b) Digital image of the printed hGO mesh after freeze-drying; (c) Optical image of the printed freeze-dried hGO mesh. Scale bar is 500 μm. (d) Cross-sectional SEM image of the porous 3D printed hGO mesh structure. Scale bar is 50 μm. (e) Deep discharge performance of the printed r-	

hGO mesh; (f) and (h) Optical images, (g) and (i) SEM image of 3DP-Co-MOF and 3DP-NC-Co, respectively; (j) First discharge curves of the marked cathodes; (k) Rate capability of 3DP-NC-Co with different current densities; (l) Schematic of the synthesis of Ni-rGO framework; (m) Digital images of the GO and Ni-rGO frameworks; (n) and (o) SEM images of the Ni-rGO; (p) Cycling performance (q) Discharge/charge curves of the Ni-rGO at various current densities with a limit capacity.....12

Figure 1.2.4 Printed SIBs electrodes via 3D and inkjet printing. (a) Schematic illustration of 3D-printing GO-NVP hierarchical porous frameworks; (b, c) SEM images of 3D-printed GO-NVP architectures at different magnifications; (d) Cycle performance at 2C, and (e) rate capability of the 3D-printed rGO-NVP electrodes; Schematic of (f) the inkjet printing setup, and (g, h) the printing process of the ATM-GO droplets in a raster fashion, ice template formation (i) during printing, and the resulting ATM-GO aerogel after freeze-drying (j); (k) An example macrostructure of the 3D printed ATM-GO aerogel after freeze-drying and the resulting MoS₂-rGO aerogel after thermal reduction; (l) High-magnification SEM image of the MoS₂-rGO printed on a Ni foam; (m) Rate performance of the MoS₂-rGO aerogel at various current densities.....14

Figure 1.2.5 (a) Schematic illustration of 3D printing graphene aerogel micro-lattice. (b) Gravimetric capacitance and capacitive retention calculated as a function of current density. Inset: schematic demonstration of the 3S-GCA SSC. (c) Cycling performance measured at a scan rate of 200 mV/s for 10 000 cycles. Inset shows the first and last cyclic voltammograms collected during the cycling stability test. (d) Comparison of the 3D-GCA SSC with reported values in terms of gravimetric energy densities and power densities. (e) Schematic of 3D printing r-GO micro-lattice based on GO-CaCl₂ ink. (f) Optical image of the printed GO micro-lattice. (g) SEM image of the printed GO micro-lattice. (h-j) Electrochemical performance of the 3D printed r-GO micro-lattice. (k) Schematic of fabrication of a 3D printed graphene aerogel/MnO₂ electrode. (l) SEM image of the 3D printed graphene aerogel/MnO₂ electrode. (m) Gravimetric capacitances and volumetric capacitances of the 3D G/MnO₂ electrodes with different mass loading of MnO₂. (n) Areal capacitances of 3D G/MnO₂ and non-3D printed G/MnO₂ electrodes at different current densities.....16

Figure 1.3.1 (a) Schematic illustration of the 3D printing machine and BN in PVDF-HFP separator; (b) Optical images of the 3D-printed BN/PVDF-HFP separator at different stages during the printing process; (c-e) SEM images of the 3D-BN/PVDF-HFP separator; (f-i) Cycling performance of the Li-Li symmetric cells at a current density of 1 mA cm^{-2}18

Figure 1.3.2 (a) Schematic illustration of the process of 3D printing LLZO structures and electrode infiltration into the 3D LLZO structures; (b) Schematic of Li melted into the pores of the 3D-printed LLZO grids on an LLZO substrate; (c) Cross-sectional SEM of 3D-printed LLZO/Li metal interface; (d) Voltage profile of the Li/3D-Printed LLZO/Li metal symmetric cell at various current densities.....19

Figure 1.3.3 (a) Schematic of the fabrication process of 3D-printed hybrid electrolytes. Corresponding SEM images of each synthesis stage of the 3D LAGP-epoxy hybrid electrolytes are listed below each schematic; (b) Galvanostatic cycling of Li-Li cells with LAGP pellet and gyroid LAGP-epoxy electrolytes cycled at a current density of 0.7 mA cm^{-2} ; (c) Schematic of the elevated-temperature direct ink writing system and solid-electrolyte ink fabrication process; (d-g) Electrochemical impedance spectroscopy (EIS) of the hybrid solid-state electrolyte.....21

Figure 1.4.1 3D-printed interdigitated Li micro-batteries. (a) Schematic illustration of 3D-printed interdigitated micro-battery architectures on the gold current collector with printed $\text{Li}_4\text{Ti}_5\text{O}_{12}$ (LTO) and LiFePO_4 (LFP) as the anode and cathode, followed by packaging. (b) SEM images of printed and annealed 16-layer interdigitated LTO-LFP electrode architectures, respectively. (c) Optical image of 3D-printed micro-battery composed of LTO-LFP electrodes after packaging. (d) Schematic of the 3D-printed interdigitated electrodes with LTO/GO and LFP/GO as the ink for anode and cathode electrodes, respectively. The gel polymer composite ink is injected in the channel between the annealed electrodes. (e) Digital image of the interdigitated electrodes. (f) Cycling stability of the 3D-printed full cell. (g) Charge/discharge profiles of the 3D-printed full cell. (h, i) Digital images of a miniaturized version of the 3D-printed electrodes. (j) Digital image of the 3D-printed electrodes arrays. (k) Schematic illustration of the CNF ink derived from trees and 3D-printed LMBs fabricated by printing c-CNF/LFP cathode and c-CNF/Li anode. (i-n) Photographs of a CNF scaffold after freeze-drying and before carbonization, c-CNF scaffold after carbonization, and c-CNF/Li electrode with designed 3D structure. (o) Cycling performance

comparison of c-CNF/Li and Li foil in a symmetric cell at a current density of 5 mA cm^{-2} with areal capacity fixed at 2.5 mAh cm^{-2}23

Figure 1.4.2 (a) Schematic illustration of 3D printing of an interdigitated asymmetric MSC on the gold current collector. The gel-like electrolyte was injected into the channels between the anode and cathode. (b) SEM image of 3D-printed 4-layer electrodes. (c) Areal and volumetric capacitances of the 3D printed asymmetric MSC. (d) Comparison of the 3D printed MSC and other reported asymmetric interdigitated MSCs. (e) Schematic of 3D printing of the FASC device. (f) Digital image of the wet fiber during the printing process. (g, h) SEM images of the printed fiber electrode and assembled FASC device. (i) Schematic of the assembled FASCs device. (j) CV of the assembled device measured at different voltage window. (k) Capacitance retention of the FASC devices after repeated bending.....25

Figure 1.4.3 (a) Schematic illustration of the fabrication process of the Ag-Zn cell through the screen printing method and the prototype of the Ag-Zn cell on temporary transfer tattoo support. (b) Flow diagram showing the fabrication steps for the mesh-embedded printed MnO_2 cathode and Zn anode with a printed silver current collector, and the optical image of a flexible Zn- MnO_2 battery laminated inside a polyethylene pouch. (c) Schematic of screen printing of a Zn- Ag_2O battery on a stretchable textile and corresponding digital photos of sealed battery with different stretched stages. (d) Schematic illustration of fabrication process of the printed Zn- Ag_2O battery and 1mm printed Zn anode compared to a commercially packaged device and an unpackaged chip.....27

Figure 2.1 ARM 310 Thinky Mixer for ink preparation.....54

Figure 2.2 Fused filament fabrication (FFF) DeltaMaker 3D printer55

Figure 2.3 Freeze-Drier for drying the printed structures.....56

Figure 2.4 Thermal furnace for heating the O3-NCNFM precursor pellet.....59

Figure 2.5 Ball-milling machine used for preparing $\text{P2-Na}_{2/3}\text{Ni}_{1/3}\text{Mn}_{2/3}\text{O}_2$ precursor.....60

Figure 2.6 Savannah 100 ALD system (Cambridge Nanotech, USA).....	61
Figure 2.7 High-Resolution Field-Emission SEM (Hitachi 4800).....	62
Figure 2.8 X-ray Diffraction System (Bruker D8 Advance).....	63
Figure 2.9 Raman Spectroscopy System (HORIBA Scientific LabRAM HR).....	63
Figure 2.10 High-Resolution Field-Emission TEM (FEI Quanta FRG 200F).....	64
Figure 2.11 Nicolet 6700 FTIR spectrometer.....	64
Figure 2.12 Schematic of beamlines at Canadian Light Source.....	65
Figure 2.13 Argon-filled glove box for coin-cell assembly.....	66
Figure 2.14 Digital photo of the LAND battery testing system.....	67
Figure 2.15 Photo of the Bio-Logic multichannel potentiostat 3/Z (VMP3).....	67
Figure 3.1 a) Schematic illustration of 3D-printed self-supported LFP electrodes, and b) Optical images of 3D-printed LFP structure with various patterns.....	72
Figure 3.2 Schematic and SEM images of three types of 3D-printed LFP electrodes. a) Schematic illustration and b, c, and d) SEM images of 3D-printed circle-grid pattern LFP electrode. e) Schematic illustration and f, g, and h) SEM images of 3D-printed circle-ring pattern LFP electrode. i) Schematic illustration and j, k, and l) SEM images of 3D-printed circle-line pattern LFP electrode.....	74
Figure 3.3 Electrochemical performance of the three types of 3D-printed LFP electrodes. a) Comparison of rate performance of the three types of LFP electrodes. Charge-discharge voltage curves of b) 3D-printed grid pattern, c) 3D-printed ring pattern and d) 3D-printed line pattern LFP electrodes at various rates. e) Cycling performance of the three types of LFP electrodes at 1C with the first six cycles activated at 0.1 C.	77

Figure 3.4 a) Practical and theoretical thickness of the 3D-printed electrodes as a function of the printing layer number (inset: optical images of 3D-printed electrodes with different printing layers). b) Comparison of the areal capacity of the LFP electrodes with different layer numbers. c) Charge/discharge profiles of the LFP electrodes with different layer numbers. d) Comparison of power density and energy density of this work with previously reported values.....79

Figure 3.5 Schematic illustration of the comparison between ultra-thick a) traditional electrodes and b) 3D electrodes.....80

Figure 4.1. Fabrication process and material characterization of the 3D-VLMP Si electrode. (a) Schematic illustration of 3D printing of vertically aligned silicon electrodes with multiple levels of porosities. (b to e) SEM images of the 3D-VLMP Si electrodes under different magnifications; (f and g) SEM image and corresponding EDX mappings of the 3D-VLMP Si electrode.....95

Figure 4.2 Electrochemical performances comparison of the Si electrodes with different structures. (a) Areal capacity vs. cycle number at a current of 1 Ag^{-1} for 60 cycles; (b and c) Charge-discharge profiles of the various Si electrodes at their 60th cycle; (d) Rate capability of the 3D-VLMP and Flat-NVLMP Si electrodes at various current densities from 0.5 to 5 mA cm^{-2} ; (e and f) Charge-discharge profiles of the 3D-VLMP and Flat-NVLMP Si electrodes at various current densities from 0.5 to 5 mA cm^{-2} ; (g) The capacity retentions of the 3D-VLMP and Flat-NVLMP Si electrodes at a current density of 2 Ag^{-1} , along with the Coulombic efficiency of the 3D-VLMP Si electrode over 300 cycles.....97

Figure 4.3 Performance metrics for 3D-VLMP Si electrodes with high areal mass loading. (a) Schematic illustration of the 3D-printed VLMP Si electrodes with different thickness and mass loadings; (b) Comparison of the electrochemical impedance of the 3D-VLMP Si electrodes with different mass loadings; (c) Various areal mass loading tests (up to 3.81 mg cm^{-2}) of the printed 3D-VLMP Si electrodes. All electrodes were cycled at 0.3 mA cm^{-2} for the initial cycle up to 1.0 mA cm^{-2} for the later cycles. (d) Areal capacity of the 3D-VLMP Si electrodes with different mass loading at the 1st, 20th, and 40th cycle, respectively; (e) Comparison of areal performance between the 3D VLMP Si electrodes with Si anodes as reported in other works, as noted.....99

Figure 4.4 (a) Schematic illustration of cyclic pulverization of the Flat-NVLMP Si electrode; (b) Schematic illustration of the volume expansion mitigation of the 3D-VLMP Si electrode cycling (c-e) SEM images of the 3D-VLMP Si electrode after 30 cycles.....101

Figure 5.1 (a) Schematic illustration of 3D printing of LAGP solid electrolytes. (b) Schematic illustration of the procedure for the synthesis of the thick LAGP pellet with a conventional method. Optical images of 3D-printed LAGP with (c) unique letter shapes and (d) microlattice structures in different sizes. (e) Top-view SEM image of the microlattice structured LAGP.....118

Figure 5.2. Digital photos of (a) the Con-LAGP thick pellet and (d) the 3DP-LAGP thin film. (b-c) Cross-sectional SEM images of (b-c) the Con-LAGP and (e-f) the 3DP-LAGP at different magnifications, respectively. (g) XRD patterns of 3DP-LAGP before and after thermal annealing. (h) EIS plots of the 3DP-LAGP at different temperatures of 25-75°C. (i) Conductivity vs. 1000/T of 3DP-LAGP electrolyte.....119

Figure 5.3 Electrochemical performance characterization of the printed LAGP thin film. (a) EIS of the LiFePO₄/Li batteries with 3DP-LAGP and Con-LAGP as the electrolytes, respectively (b) Rate capabilities of 3DP-LAGP based solid Li-battery and Con-LAGP based solid Li-battery at a current density range of 0.1C to 5C. Typical charge/discharge voltage profiles of (c) Con-LAGP based solid Li-battery and (d) 3DP-LAGP based solid Li-battery at various current densities. (e) Long-term cycling performance of 3DP-LAGP based solid Li-battery at a current density of 0.5 C.....122

Figure 5.4 Schematic illustration of Li⁺ transport kinetics in solid-state Li batteries with (a) 3D-printed thin LAGP and (b) conventional thick LAGP as solid electrolytes.....123

Figure 6.1 Fabrication of the 3D micro-structured Na@rGO/CNT anodes. (a) Schematic process of a typical 3D-printed Na@rGO/CNT electrode. (b-d) Optical images of the GO/CNT skeletons with different 3D-printing patterns. (e-f) Corresponding optical images of 3D-printed Na@rGO/CNT electrodes after Na infusion into the different 3D-printed skeletons.....139

Figure 6.2 Morphological characterizations of the 3D-printed architectures. Top-view SEM images of the 3D-printed GO/CNT skeleton (a and b) and the 3D-printed Na@rGO/CNT

composite electrode (d and e). Cross-sectional SEM images of (c) 3D-printed GO/CNT and (f) Na@rGO/CNT.140

Figure 6.3 Morphology characterizations of the 3D-printed sodium cathode architectures. a) Optical image of the 3D-printed interdigital patterned cathode. b) Cross-sectional SEM image of the cathode electrode. c) High-magnification cross-sectional SEM image of the electrode, indicating an internal porous structure. (d-f) Top-view SEM images of the cathode electrode. (g-k) Elemental mappings of the Cu, Ni, Fe, and Mn distributed in the cathode electrode.142

Figure 6.4 Cycling performance of symmetric cells with the 3D-printed Na@rGO/CNT and Na foil electrodes at current densities of (a) 1mA cm^{-2} and (b) 3mA cm^{-2} with an areal capacity of 1mAh cm^{-2} . c) Symmetric cell cycling performance at a current density of 3mA cm^{-2} with a high areal capacity of 3mAh cm^{-2}143

Figure 6.5 Electrochemical performance of the sodium metal full cell (a) Schematic illustrating the assembled cell structure with printed Na@rGO/CNT anode and printed NCNFM cathode. (b and c) The 1st, 20th, 40th, and 60th charge/discharge profiles of the full cell with Na@rGO/CNT anode and NCNFM cathode. (d) Cycling performance of the full cell with Na@rGO/CNT anode and NCNFM cathode. at 0.2C over 60 cycles. (e) Comparison of current sodium metal full cell with those reported in literature.145

Figure 7.1 f) XRD patterns of pristine NMO and AlPO_4 -coated NMO samples; Typical SEM images of b) bare NMO, c) NMO-2AP, d) NMO-5AP, e) NMO-10AP, and f) NMO-20AP.158

Figure 7.2 a) Low-resolution TEM image, b) and c) HRTEM images; (d-i) elemental mapping of Na, Ni, Mn, O, Al, and P of the NMO-20AP, respectively.160

Figure 7.3 a) XAS spectra of Mn $L_{3,2}$ -edges and Ni $L_{3,2}$ edges of bare NMO, NMO-10AP, and standard MnO_2 ; b) XAS spectra of Ni $L_{3,2}$ -edges of NMO, NMO-10AP, and standard NiO collected in TEY mode; c) and d) O K-edges of bare NMO and NMO-10AP collected in FY and TEY modes, respectively.162

Figure 7.4 Cyclic voltammetry of a) bare NMO, b) NMO-2AP, c) NMO-5AP, d) NMO-10AP, and (e) NMO-20AP.162

Figure 7.5 Electrochemical performance comparison of a) the initial galvanostatic charge/discharge profiles of bare NMO and various AlPO_4 -coated NMO samples within the voltage range of 2.0-4.3V at 0.5 C; b) cyclic performance of bare NMO and AlPO_4 -coated NMO samples at 0.5 C; c) rate capabilities of bare NMO and AlPO_4 -coated NMO samples at various current densities; d) A comparison of the rate performance between this work and the work previously reported in the literature; e) The long-term cyclic performance of bare NMO and AlPO_4 -coated NMO samples over 200 cycles at a rate of 2C.....164

Figure 7.6 Cyclic voltammogram curves of (a) NMO-2AP and (c) bare NMO electrodes at various scanning rates (0.1, 0.2, 0.4, 0.6, 0.8, 1.0, 1.2, and 1.4 mVs^{-1}); (b) and (d) are the corresponding linear relationship between the peak current and the square root of the scan rates; (e) and (f) are EIS curves after 10 cycles and 50 cycles.....166

Figure 7.7 XANES Mn $L_{3,2}$ -edges of bare NMO and NMO-10 AP electrodes after (a) 1 cycle and (b) 50 cycles compared with standard MnO , MnO_2 , and Mn_2O_3168

List of Abbreviations

2D	Two-dimensional
3D	Three-dimensional
3DP-FDE	Three-dimensional printed freeze-dried electrode
3DFP	Three-dimensional freeze-printing

A

AJ	Aerosol jet
AB	Acetylene black
ALD	Atomic layer deposition
AM	Additive manufacturing

B

BN	Boron nitride
----	---------------

C

CPEs	Ceramic-polymer electrolytes
CNF	Cellulose nanofiber
CEI	Cathode-electrolyte interface
CV	Cyclic voltammetry
CLS	Canadian Light Source
CFI	Canada Foundation for Innovation
CRC	Canada Research Chair Program
CIHR	Canadian Institute of Health Research

D

DIW	Direct ink writing
DIB	Diisopropenylbenzene
DEC	Diethyl carbonate
DMC	Dimethyl carbonate
DGM	Diglyme

E

EES	Electrochemical energy storage
EC	Ethylene carbonate
EVs	Electric vehicles
EDX	Energy-dispersive X-ray spectroscopy
EIS	Electrochemical impedance spectra

F

FDM	Fused deposition modeling
FASCs	Fiber-shaped asymmetric supercapacitors
FTSs	Fiber-shaped temperature sensors
FFF	Fused filament fabrication
FY	Fluorescence yield

G

GO	Graphene oxide
G	Graphene
GNP	Graphene nanoplate
GAMs	Graphene aerogels micro-lattices
GF	Glass fiber

H

hGO	Holey graphene oxide
HRTEM	High-resolution transmission electron microscopy

I

IoT	Internet of Things
-----	--------------------

K

KOH	Potassium hydroxide
-----	---------------------

L

LIBs	Lithium-ion batteries
Li-S	Lithium-sulfur
LMFP	Lithium manganese iron phosphate
LTO	Lithium titanium oxide
LFP	Lithium iron phosphate
LLZO	Lithium lanthanum zirconium oxide
LAGP	Lithium aluminium germanium phosphate
LMBs	Lithium metal batteries

M

MWCNTs	Multiwall carbon nanotubes
MOF	Metal-organic framework
MSCs	Micro-supercapacitors
MNC	Sodium manganese nickel cobalt oxide

N

NVP	Sodium vanadium phosphate
-----	---------------------------

NMP	N-methyl-2-pyrrolidone
NMO	Sodium nickel manganese oxide
NVLMP	Non-vertically aligned without micro-pore structures
NCNFM	Sodium copper nickel iron manganese oxide
NSERC	Natural Science and Engineering Research Council of Canada
NSFC	Natural Science Foundation of China
NRC	National Research Council of Canada

P

PVDF-HFP	Polyvinylidene fluoride-hexafluoro propylene
PVA	Polyvinyl alcohol
PDMS	Polydimethylsiloxane
PC	Propylene carbonate
PVDF	Polyvinylidene fluoride
PAPD	Priority Academic Program Development

Q

QDs	Quantum dots
-----	--------------

R

RGO	Reduced graphene oxide
-----	------------------------

S

SLA	Stereolithography
SLS	Selective laser sintering
SEM	Scanning electron microscopy
SIBs	Sodium-ion batteries

SIS Polystyrene-block-polyisoprene-block-polystyrene

SSR Solid-state-reaction

SEI Solid electrolyte interface

SMBs Sodium metal batteries

SA Sodium alginate

SGM Spherical Grating Monochromator

T

TEM Transmission electron microscopy

TEY Total electron yield

TMA Trimethylaluminum

TMPO Trimethyl phosphate

U

UWO University of Western Ontario

V

VLMP Vertically aligned structure with multi-scaled porosities

X

XRD X-ray diffraction

XAS X-ray absorption spectroscopy

XANES X-ray absorption near edge spectroscopy

XPS X-ray photoelectron spectroscopy

Chapter 1

1.1 General introduction

The issues of global warming and depletion of fossil fuels have stimulated the search for clean and renewable energy sources, such as solar, wind, hydro and tidal energies. Accordingly, reliable and cost-effective energy storage system are in great need to ensure the full utilization of these renewable energy sources.¹ In the past few decades, various electrochemical energy storage (EES) devices have been investigated. Among them, rechargeable batteries and electrochemical supercapacitors have attracted significant attention due to the high energy density and power density as well as pollution-free operation.²⁻⁴ In general, a rechargeable battery or electrochemical capacitor is composed of two electrodes, current collectors, and liquid electrolyte together with separators or solid electrolytes.⁵ Electrode fabrication, current collector engineering, separator modification, electrolyte development, and device assembly are all important factors that could determine the electrochemical performance and practical application of energy storage devices.⁶⁻⁸

Conventionally, an EES device is fabricated by winding or stacking cell components (anodes, cathodes, and separator membranes) and then packaging these components into metallic canisters or pouch films, followed by liquid-electrolyte injection.¹ Although this manufacturing method is mature and successful, the energy storage devices fabricated by conventional techniques have limited form factors and mechanical flexibility.⁹ However, with the rapid development of the Internet of Things (IoT), the future energy storage devices are required to be flexible, wearable, shape versatile, and on-chip integration into other electronics.¹⁰⁻¹¹ In other words, future EES devices need to be customizable. Therefore, it is believed that advanced state-of-the-art manufacturing techniques are needed to meet the requirements for future EES devices. 3D printing thus has been expected to be applied and regarded as a promising technique for electrochemical energy storage devices.¹²⁻²⁰

3D printing, also known as additive manufacturing (AM), is a representative of advanced manufacturing technologies for constructing complex 3D architectures. Comparing with traditional methods, 3D printing is a process of constructing a three-dimensional product by stacking layer-upon-layer of materials starting from a digital computer model designed by a 3D

software (CAD). The 3D printing technique is considered as an ideal manufacturing method since it can significantly reduce the manufacturing cost by preventing the loss of valuable materials while simplifying the design for manufacturing and reducing the number of fabrication steps. To date, there are tremendous types of printing techniques being developed, and the most popular 3D printing technologies can be classified into the following four types:

(1) Fused deposition modeling (FDM): FDM technique was first developed and patented by S. Scott Crump in 1989. It creates 3D objects layer-by-layer from filament shaped molten plastic materials extruded through a nozzle (**Figure 1.1.1**).²¹ The plastic filament is wound on a coil and unreeled to supply material to the extrusion nozzle, while the nozzle or the object is moved along three axes, which is controlled by a computer. The plastic material solidifies after extruded from the nozzle. The main advantages of this technique are low-cost, high speed and large size capabilities. However, an intrinsically limited accuracy and surface finishing and a limited number of feedstock materials available still limit its wide applicability in many areas.²²

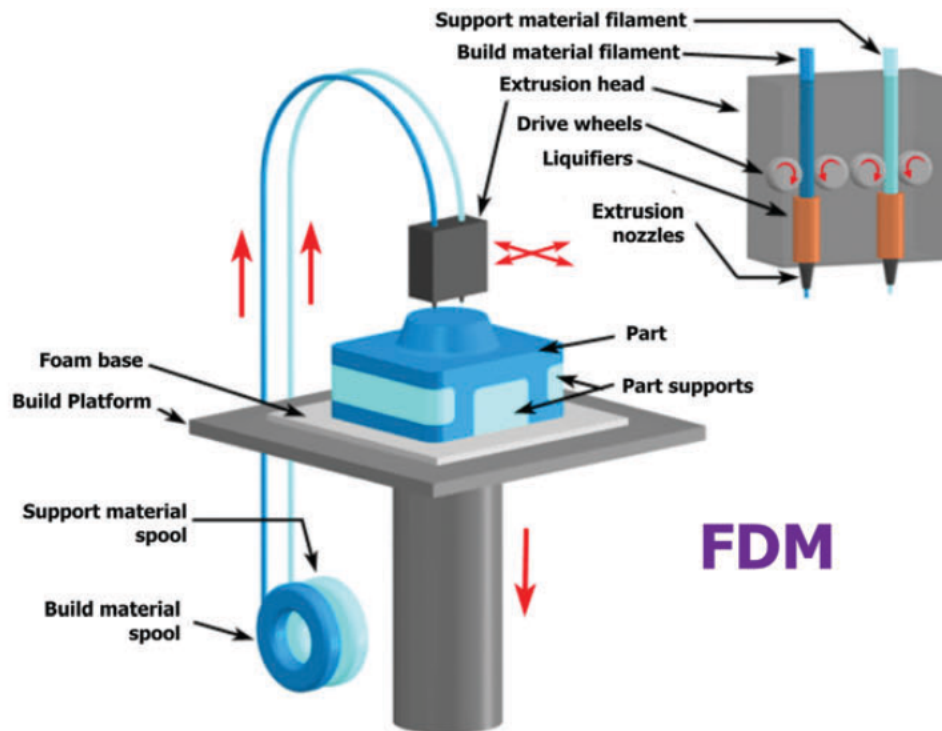


Figure 1.1.1 Schematic of the FDM printing system.¹⁴

(2) Stereolithography (SLA): SLA is a 3D printing technique that creates 3D objects through curing the photosensitive resins lay-by-layer using light. In detail, SLA utilizes a fine laser spot through a focused beam or lamp to scan over the photocurable resins, which induces a photopolymerization and subsequent solidification process (**Figure 1.1.2**). SLA can be applied to multiple materials, including ceramics and composites.²³ It has proved to be an excellent method for constructing dense structural ceramic with high resolution and excellent surface finish.²⁴ However, SLA has a limitation in the multi-material deposition that greatly limits its applicability in multi-component devices.²⁵

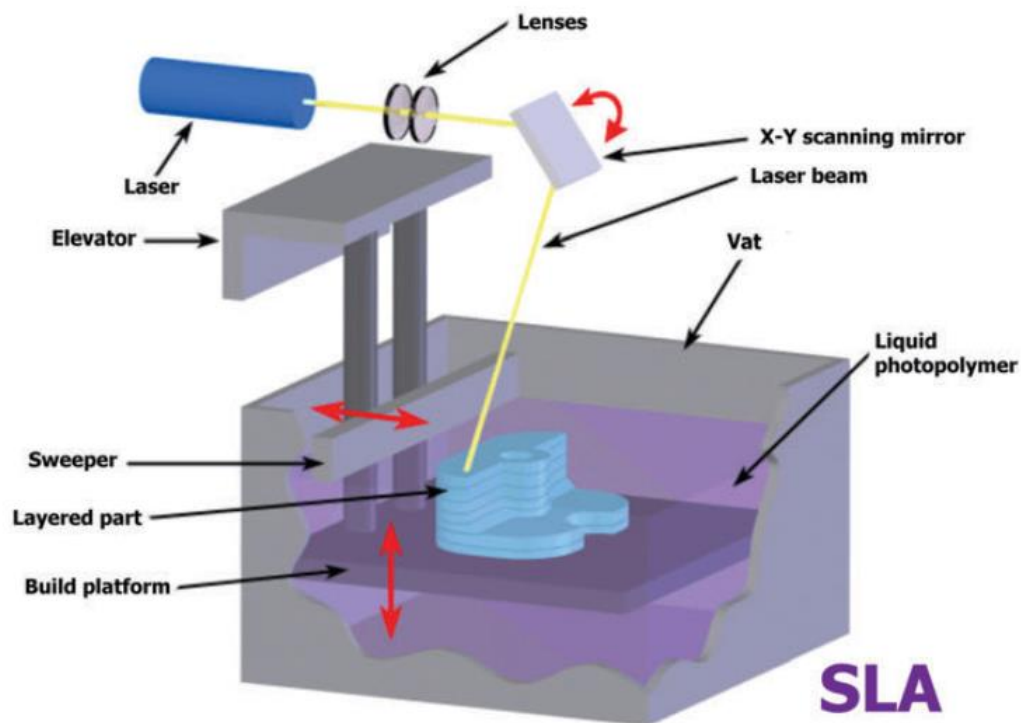


Figure 1.1.2 Schematic of the SLA printing system.¹⁴

(3) Selective laser sintering (SLS): SLS is a powder-based 3D printing technique that is capable of constructing durable and functional 3D objects through selectively fusing successive layers of solid material by a high-power laser beam.²⁶ The un-sintered materials in a printing process can be reused for another printing job, resulting in a reduction of materials wastage.²⁷⁻²⁸ However, the

strong limitation appears when applied to metals and oxides with high-temperature melting points.²⁹

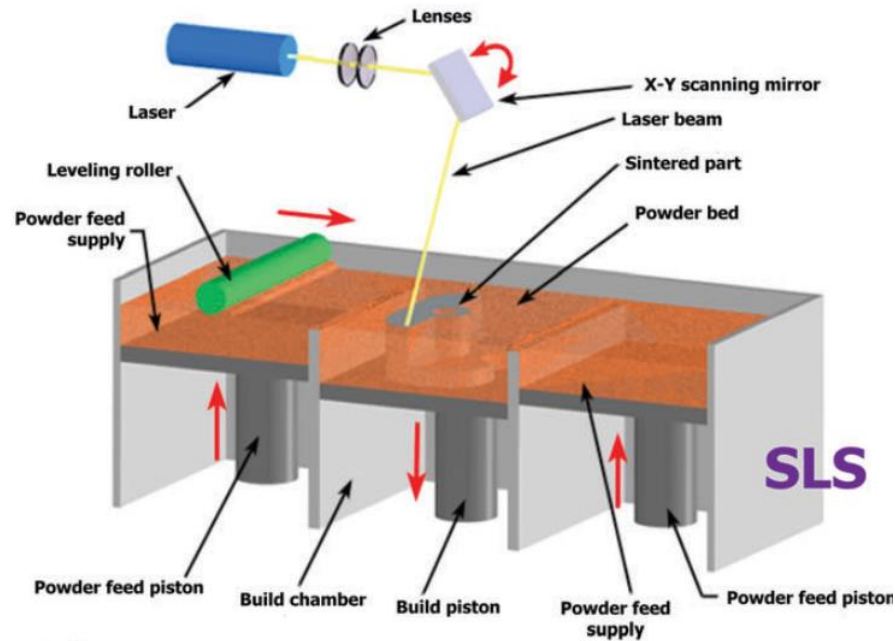


Figure 1.1.3 Schematic of the SLS printing system.¹⁴

(4) Extrusion-type direct ink writing (DIW): Extrusion-type DIW is a 3D printing technique that extrudes a paste-like ink with shear-thinning behavior through a nozzle to build 3D architectures in a layer-by-layer way. After extrusion, the 3D architectures usually become solidification through the evaporation of solvents, chemical changes (cross-linking) or freeze-drying. DIW printing technique can be applied to a broad range of materials including polymers, ceramics, metal oxides, metal alloys, and electronically functional materials.³⁰⁻³² This feature has broadened its applicability in a wide range of areas.^{16-17, 33-35}

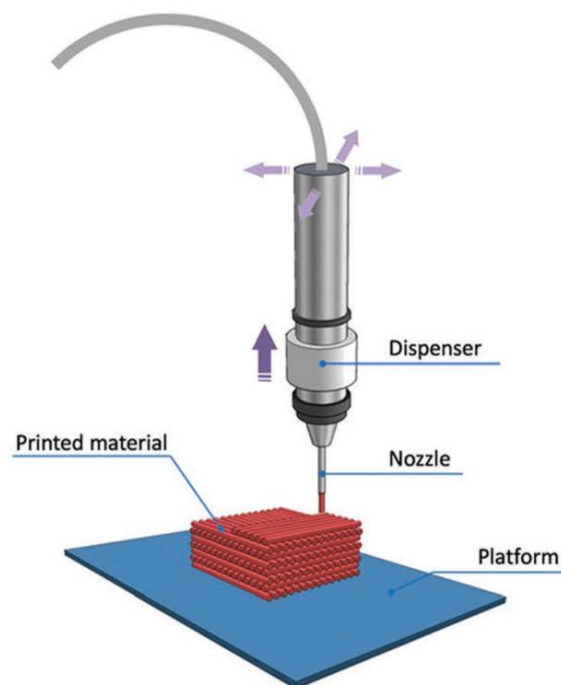


Figure 1.1.4 Schematic of the extrusion-type DIW printing system.³⁶

Compared with conventional manufacturing methods, the 3D printing technique possesses several advantages for fabricating EES devices:

(1) The thickness of electrodes can be well controlled by 3D printing because of the layer-by-layer additive manufacturing nature. Thin-film devices can be fabricated by just depositing materials over a few layers, which could be applicable for flexible and wearable energy storage devices. On the other hand, ultra-thick electrodes can also be obtained by 3D printing, realizing high areal energy density EES devices. Therefore, the accurate layer-by-layer building feature of 3D printing allows the electrode thickness to be well controlled.

(2) 3D printing can realize facile and accurate construction of electrodes and other components with controlled shapes, and interconnected porosity.^{19, 37-39} The designed 3D architectures with periodic or aligned pores enable fast ion/electron transport which is beneficial for achieving high power density and energy density.

(3) 3D printing technique can fabricate micro-structured EES devices with high-aspect-ratio within a small areal footprint, which is hardly realized by conventional manufacturing methods.⁴⁰

Meanwhile, the printed EES devices can be easily on-chip integrated with other shape complexed electronics through directly depositing the electrodes/electrolytes onto the electronics.⁴¹⁻⁴²

(4) 3D printing is a low-cost, efficient, and environment-friendly technology. This can be attributed to the simplified one-step fabrication process. 3D printing adopts the additive manufacturing strategy, suggesting that the material is deposited on demand. This feature maximally eliminates the materials wastage, making it much more energy-conservation and environment-friendly than conventional manufacturing methods.

Among lots of developed printing techniques, extrusion-type direct ink writing is the most popular and widely used in many areas. In recent years, numerous researches have employed this technique to design novel structures for energy storage devices.

1.2 3D printing of electrodes for energy storage

1.2.1 3D-printed electrodes for Li-ion batteries

Li-ion batteries have been commercialized for decades and been widely used in various areas including portable electronics and electric vehicles.⁴³⁻⁴⁷ As one of the most important components in the LIBs system, electrodes play a vital role in determining the capacity and energy density. To meet the increasing energy density demand, many efforts have been devoted to optimizing the electrode structures for improving the electron/ion kinetics. In recent years, many researchers have employed 3D printing technique to fabricate advanced LIB electrodes with high performance. For instance, Pan et al. reported the 3D printing of $\text{LiMn}_{1-x}\text{Fe}_x\text{PO}_4$ nanocrystal cathodes and assembled the LIBs based on the printed electrodes.⁴⁸ **Figure 1.2.1a** is the schematic illustration of 3D printing of LMFP cathode and the packaging process based on the printed LMFP electrode. The synthesis process for the LMFP nanocrystals involves precursor calcination and carbon coating. The LMFP slurry was extruded out through a metal nozzle and directly printed onto an Al foil. The electrode morphology can be adjusted by changing the dispenser pressure, printing speed, and the diameter of the nozzle. The electrochemical performance testing in **Figure 1.2.1b and c** shows that the 3D-printed LMFP cathodes exhibited much higher capacity at various rates than that of the traditional electrodes. More recently, 3D printing technique was used to fabricate high-performance Li-ion battery anodes. Rahul et al. developed a novel approach for fabricating 3D microlattice Ag electrodes with hierarchical porosity through Aerosol Jet (AJ) 3D printing method (**Figure 1.2.1d**).⁴⁹ The microlattice Ag electrode delivered a great improvement in areal capacity

and high electrode volume utilization when compared to a solid Ag bulk electrode. The superior electrochemical performances indicate that the 3D microlattice architectures can effectively facilitate the electrolyte penetration into the electrode and enhance the electrochemical reaction sites due to the numerous open pores within the 3D electrode. Yang et al. successfully employed 3D printing to fabricate SnO₂ QDs/graphene architectures which exhibit impressive electrochemical performance.⁵⁰ As illustrated in **Figure 1.2.1f**, the ultra-small and mono-disperse SnO₂ QDs were first synthesized through a controllable sol-gel approach, and they can be mixed with graphene oxide in water to form a GO-based ink with high viscosity and shear-thinning properties for continuous printing without clogging. **Figure 1.2.1g** shows a continuously 3D printed filament with a length of 5 meters. Moreover, various sophisticated architectures can be printed out (**Figure 1.2.1h**), suggesting the excellent rheological properties of the hybrid ink. The cross-sectional SEM image (**Figure 1.2.1i**) shows the filaments are stacked closely, and numerous macropores originated from the freeze-drying treatment occurred in the filaments. The electrochemical performance testing shows that the 3D-printed SnO₂ QDs/graphene electrode displays highest rate performance for lithium storage compared with the SnO₂ QDs/G and pure SnO₂ QDs (**Figure 1.2.1j**). The superior electrochemical performance can be ascribed to the favorable kinetics for both electrons and ions in the 3D printed architectures.

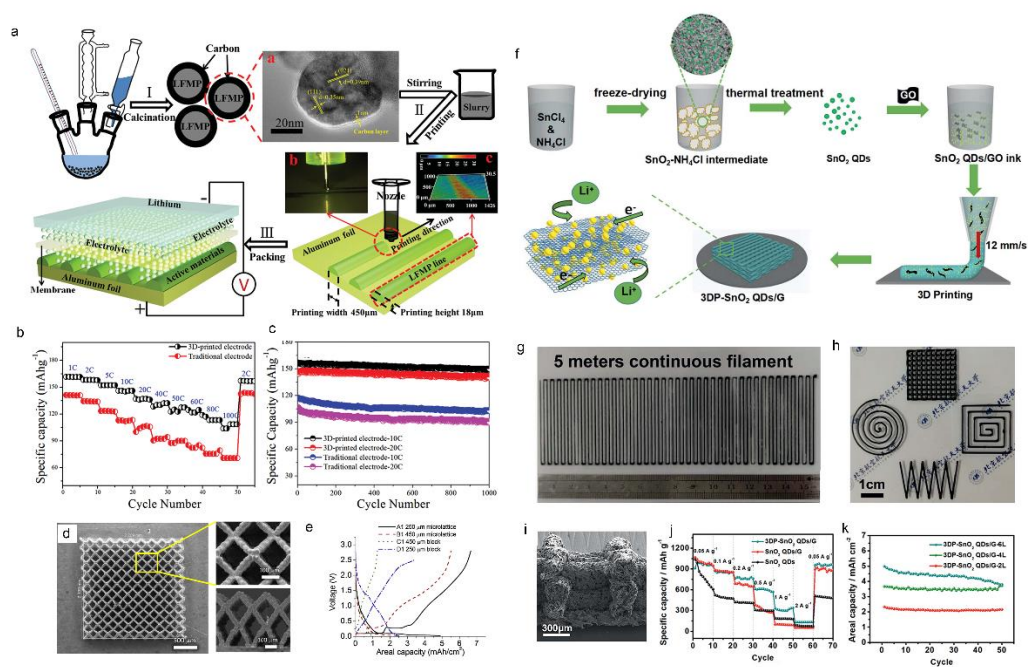


Figure 1.2.1 (a) Schematic illustration of 3D printing of LMFP cathode and battery package process based on 3D-printed LMFP electrode; (b) Rate capability comparison between the conventional electrode and 3D-printed LMFP electrode at various rates; (c) Long cycling performance comparison between the traditional electrode and 3D-printed electrode at 10C and 20C;⁴⁸ (d) SEM images of the 3D-printed Ag microlattice structures using the Aerosol Jet 3D printing method; (e) Areal capacity comparison of the microlattice and block structures with different thickness;⁴⁹ (f) Schematic of the 3D printing of SnO₂ QDs/G architectures; (g) Digital image of the continuously 3D-printed filament; (h) Digital images of various 3D-printed patterns; (i) Cross-sectional SEM image of the printed SnO₂ QDs/G architectures; (j) Rate capabilities comparison among the 3DP-SnO₂ QDs/G, SnO₂ QDs/G and SnO₂ QDs; (k) Areal capacities of 2-layer, 4-layer, and 6-layer 3DP-SnO₂ QDs/G architectures.⁵⁰

1.2.2 3D-printed electrodes for Li-S battery

Lithium-sulfur (Li-S) batteries have emerged as a promising substitute to LIBs due to the high theoretical capacity of 1675 mAh g⁻¹ and an energy density of 2600 Wh g⁻¹.⁵¹⁻⁵³ However, developing high loading sulfur-based cathodes with high-performance is still facing great challenges: (1) Both sulfur and lithium sulfides have a low electron conductivity, making charge transfer difficult in the cathode; (2) A large volumetric expansion (80%) happens during the lithiation process, leading to exfoliation of the cathode and rapid capacity decay.⁵⁴⁻⁵⁶

For solving these problems, fabricating of a 3D architecture with interconnected electron and ion channels within the electrode is quite promising for improving the sulfur utilization for high-loading sulfur cathodes.⁵⁷⁻⁵⁸ In this regard, the 3D printing technique has been employed to construct high-loading sulfur cathodes since 3D printing technique has great advantages in fabricating complex 3D architectures and easily controlling the sulfur loadings by controlling the printing layers. For instance, Craig et al. reported the Li-S battery cathodes fabricated by the direct ink writing method based on a printable multiwall carbon nanotubes (MWCNTs) ink.⁵⁹ The printed MWCNTs-based sulfur electrodes are highly conductive and multi-scaled porous, which can facilitate the electrolyte access into the electrodes and enhance the electron/ion diffusion. As a result, the printed micro-electrodes can achieve a high areal capacity of around 7 mAh cm⁻² at a

current density of 11.5 mA cm^{-2} with 50% active material loading. More recently, Yang et al. employed an extrusion-based 3D printing approach to developing 3D sulfur copolymer-graphene architectures (3DP-pSG) with well-designed periodic microlattices.⁶⁰ **Figure 1.2.2a** demonstrates the fabrication procedure of 3D printing sulfur copolymer-graphene architectures. The printing ink is based on highly concentrated graphene oxide (GO) suspensions composed of S particles and 1,3-diisopropenylbenzene (DIB). The sulfur copolymer is formed onto the surface of reduced graphene oxide (RGO) after a sample thermal treatment of the 3D printed architectures. The resultant structures can partially suppress poly-sulfides dissolution into electrolyte due to the strong S-C bonds and enhance the electron conductivity because of the formed graphene network. Moreover, the well-designed macropores in the 3D architectures as shown in **Figure 1.2.2b** can promote the access of electrolyte to the electrodes. The 3DP-pSG electrode thus delivers a higher reversible capacity of 812.8 mAh g^{-1} with a high thickness of around $600 \text{ }\mu\text{m}$. Although the 3D-printed sulfur copolymer-graphene architecture could improve the capacity of thick electrodes, the initial capacity is still too low due to the low electronic conductivity of the sulfur copolymer.

In this regard, our group developed a 3D-printed freeze-dried S/C composite electrode (3DP-FDE) via a facile 3D printing technique for achieving high-energy-density and high-power-density Li-S batteries.⁶¹ As illustrated in **Figure 1.2.2e**, the printing ink is composed of the S/C active materials, acetylene black (AB) and commercial carbon nanotubes (CNTs) as the conductive additives, and polyvinylidene fluoride-hexafluoro propylene (PVDF-HFP) as the binder. The high loading amount of sulfur cathodes can be easily obtained via the layer-by-layer manufacturing process. The printed sulfur cathodes possess multiple levels of porosity: macroscale (several hundred micrometers from 3D printing design), and microscale (tens of micrometers induced by phase-inversion and freeze-drying process), which can effectively facilitate the electron/ion transport within the whole electrodes (**Figure 1.2.2f-h**). Benefiting from the hierarchical porous architectures, the 3DP-FDE exhibits superior electrochemical performance, even with a sulfur loading of 5.5 mg cm^{-2} , it can display high initial discharge capacities of 1009 mAh g^{-1} and 912 mAh g^{-1} at 1C and 2C (corresponding to areal current densities of 9.2 mA cm^{-2} and 18.4 mA cm^{-2}), respectively. Moreover, the capacity retentions are as high as 87% and 85% after 200 cycles at 1C and 2C (**Figure 1.2.2i**).

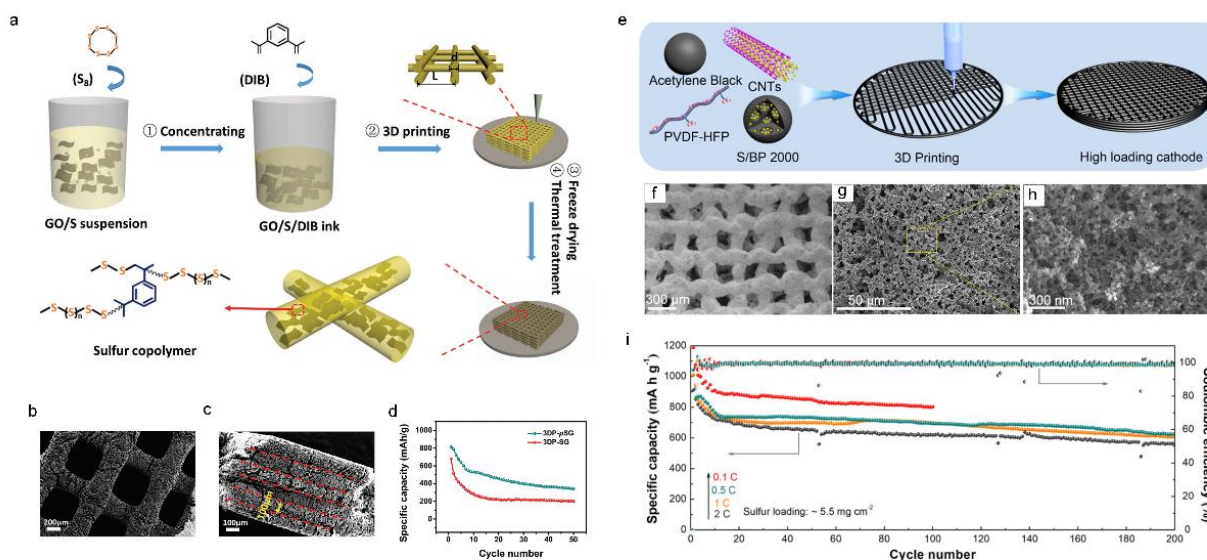


Figure 1.2.2 (a) Schematic illustration of 3D printing sulfur copolymer-graphene (3DP-pSG) architectures; (b) Top-view SEM image of the 3D architecture, showing periodic macropores; (c) Cross-sectional SEM image of the 3D architecture; (d) Cycle performances of 3DP-pSG and 3DP-SG at 50 mA g^{-1} ;⁶⁰ (e) Schematic demonstration of the 3D printing of S/BP 2000 thick cathodes; (f-h) SEM images of the 3D electrode at different magnifications from top view; (i) Cycling performance of the 3DP-FDE electrodes with a sulfur loading of 5.5 mg cm^{-2} at various rates.⁶¹

1.2.3 3D-printed electrodes for Li-O₂/CO₂ batteries

Li-O₂ batteries with Li metal as the anode and O₂ cathode possess extremely high theoretical specific capacity energy (3505 Wh kg^{-1}), which has attracted great attention in the past few years.⁶²⁻⁶⁶ However, the insulating Li₂O₂ formed during the discharging process greatly restricts the practical specific energy. By using a porous conducting matrix to support and confine the accumulated insulating Li₂O₂ within the pores, the electrode capacity and the practical specific energy density can be considerably enhanced. Thus, it is vital to develop a conducting catalyst material with a proper porous framework.

Extrusion-based 3D printing has been proven to be a powerful tool for constructing complex 3D architecture. Recently, Hu et al. employed extrusion-based 3D printing to construct hierarchical porous frameworks and demonstrated the first 3D-printed Li-O₂ cathodes.⁶⁷ In their work, the

printable ink was prepared by directly adding holey graphene oxide (hGO) to H₂O at high concentrations (~100mg/ml). The aqueous hGO ink with proper viscoelastic behavior can be dispensed fine lines in a layer-by-layer arrangement (**Figure 1.2.3a**) and be stacked together to construct complex 3D printed mesh structures (**Figure 1.2.3b**). The freestanding 3D printed hGO cathodes possess multi-scaled porosity (from macroscale to nanoscale) as displayed in **Figure 1.2.3c and d**, which facilitate the mass/ionic transport and improve active-site utilization, leading to a dramatical enhancement in overall Li-O₂ battery performance. The reduced 3D printed h-GO mesh shows a remarkable areal capacity of 13.3 mAh cm⁻² (corresponding to 3879 mAh g⁻¹) when tested at 0.1 mA cm⁻² (**Figure 1.2.3 e**), which is much higher than that of the vacuum filtrated hGO film. The result confirms that the macro- and microscale porosity induced by 3D printing play a critical role in improving the overall air cathode capacity.

Later on, Wang et al. reported a novel and freestanding hierarchically porous framework constructed by 3D printing of Co-based metal-organic framework (Co-MOF), followed by thermal annealing. The 3D printed Co-MOF (**Figure 1.2.3f and g**) exhibits a mesh-like architecture with macro-sized pores (~200 μm). The 3D printed mesh-like architecture can be well maintained after annealing in N₂ gas (**Figure 1.2.3h and i**), resulting in the conducting catalyst consisted of Co nanoparticles assembled in nitrogen-doped mesoporous carbon flakes (3DP-NC-Co). The 3DP-NC-Co cathode could deliver a high discharge capacity of 1124 mAh g⁻¹ based on the total mass of the electrode (**Figure 1.2.3j**). Moreover, the 3DP-NC-Co cathode also exhibits a superior rate capability, reaching a high discharge capacity of 525 mAh g⁻¹ at a high current density of 0.8 mA cm⁻² (**Figure 1.2.3k**). The superb Li-O₂ battery performance can be attributed to the unique 3DP architectures consisting of abundant micrometer-sized pores formed between Co-MOF derived carbon flakes and meso- and micropores formed with the flakes, which benefit the efficient deposition of Li₂O₂ and facilitate their decomposition due to the confinement of insulating Li₂O₂ within the pores and presence of Co electrocatalysts.

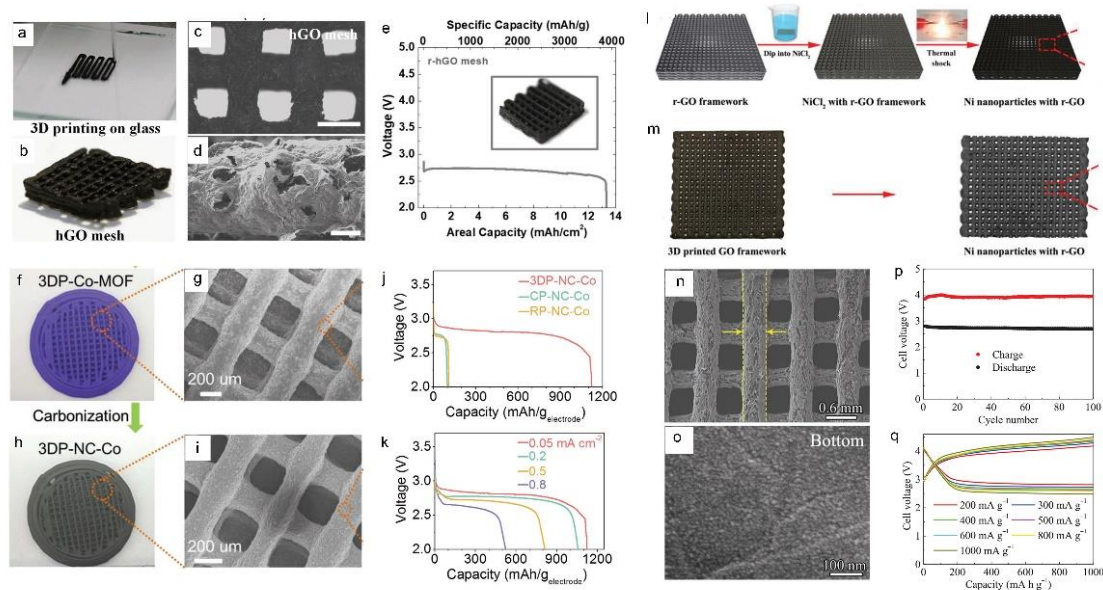


Figure 1.2.3 (a) Digital image showing the process of printing complex 3D architectures line-by-line; (b) Digital image of the printed hGO mesh after freeze-drying; (c) Optical image of the printed freeze-dried hGO mesh. Scale bar is 500 μm . (d) Cross-sectional SEM image of the porous 3D printed hGO mesh structure. Scale bar is 50 μm . (e) Deep discharge performance of the printed r-hGO mesh;⁶⁷ (f) and (h) Optical images, (g) and (i) SEM image of 3DP-Co-MOF and 3DP-NC-Co, respectively; (j) First discharge curves of the marked cathodes; (k) Rate capability of 3DP-NC-Co with different current densities;⁶⁸ (l) Schematic of the synthesis of Ni-rGO framework; (m) Digital images of the GO and Ni-rGO frameworks; (n) and (o) SEM images of the Ni-rGO; (p) Cycling performance (q) Discharge/charge curves of the Ni-rGO at various current densities with a limit capacity.⁶⁹

1.2.4 3D-printed electrodes for Na-ion batteries

Sodium-ion batteries (SIBs) are attracting tremendous interest recently due to the abundance and low cost of Na.⁷⁰⁻⁷⁵ However, it is more difficult to achieve high reversible capacities and good rate capabilities due to the bigger size of Na^+ (0.102 nm) than that of Li^+ (0.076 nm). 3D printing has shown great potential in designing unique 3D architectures for optimizing Li-based electrodes for achieving high-performance LIBs. Similar to LIBs, extrusion-based 3D printing technique has also been employed in sodium storage.

For example, Yang et al. first demonstrated a facile 3D printing approach to fabricate hierarchically porous GO/Na₃V₂(PO₄)₃ (GO/NVP) frameworks for sodium storage.⁷⁶ **Figure 1.2.4a** illustrates the process of 3D printing GO/NVP mesh structures, the printable ink was prepared by adding the NVP nanoparticles into the GO solution. The concentrated GO/NVP inks with suitable rheological properties can be dispensed into 3D mesh structures. The as-printed frameworks possess continuous conducting filaments with numerous hierarchical pores (**Figure 1.2.4b and c**), which are able to facilitate the fast transportation of both sodium ion and electron. The 3D printed porous frameworks thus show high capacity and excellent rate performance (**Figure 1.2.4d and e**). Following this work, Brown et al. employed a 3D freeze-printing (3DFP) method to fabricate highly porous MoS₂/graphene hybrid aerogels as the anode for SIBs.⁷⁷ The key innovation in this work is that a cold substrate plate (-30°C) is employed to rapidly freeze the aqueous ink droplets to the ice during the printing (**Figure 1.2.4f to j**). After thermal reduction, the printed hybrid aerogels form a continuous conductive rGO framework with MoS₂ sheets attached to the graphene surface as the Na⁺ intercalation host (**Figure 1.2.4k and l**). The 3D printed rGO/MoS₂ porous framework thus delivers high specific capacity at various current densities (**Figure 1.2.4m**).

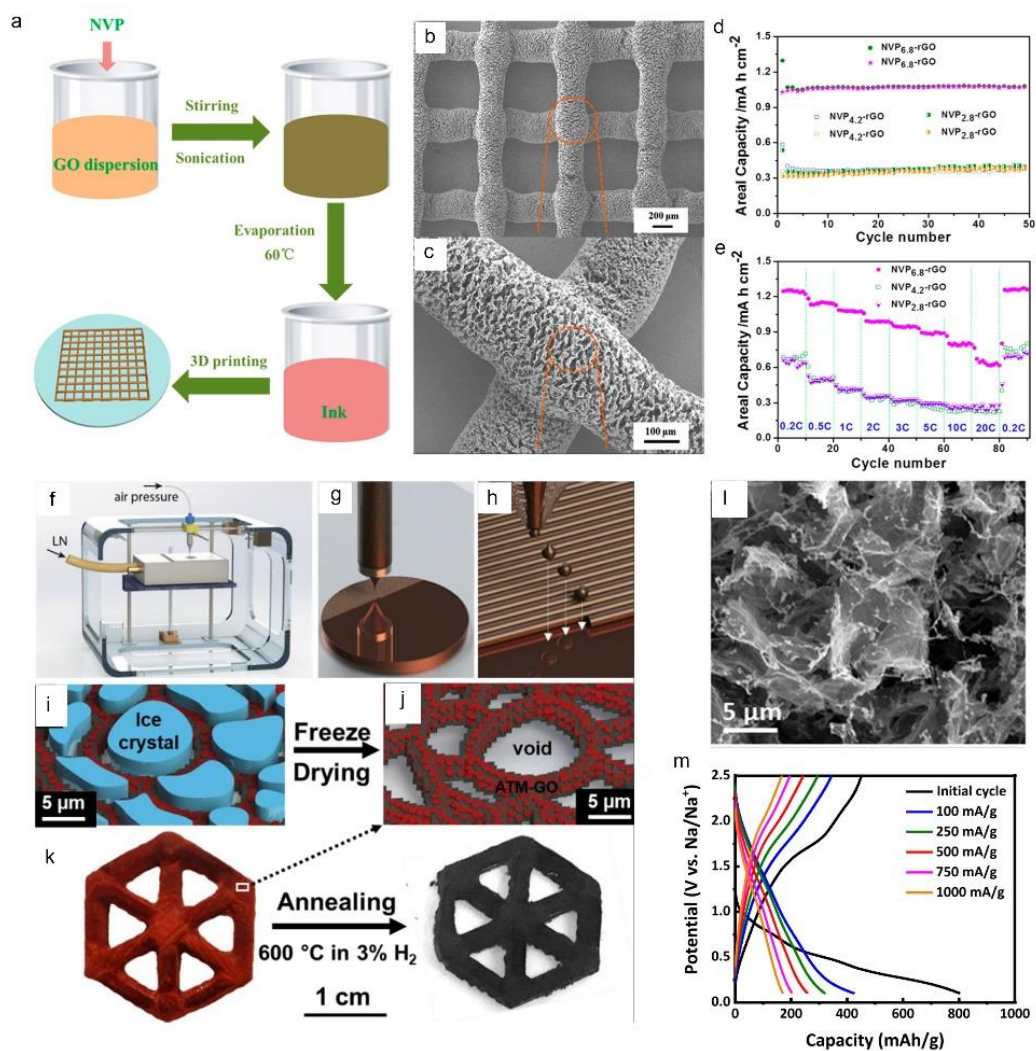
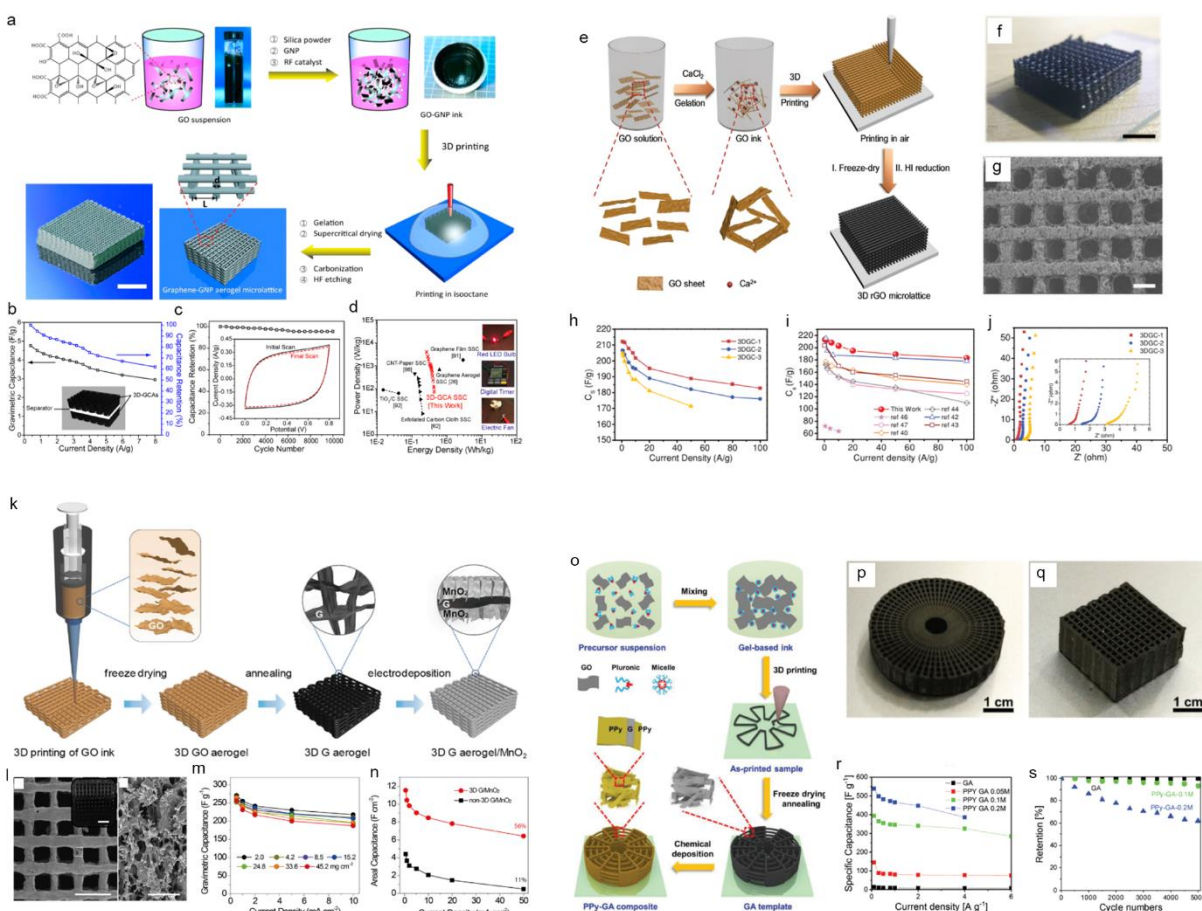


Figure 1.2.4 Printed SIBs electrodes via 3D and inkjet printing. (a) Schematic illustration of 3D-printing GO-NVP hierarchical porous frameworks; (b, c) SEM images of 3D-printed GO-NVP architectures at different magnifications; (d) Cycle performance at 2C, and (e) rate capability of the 3D-printed rGO-NVP electrodes;⁷⁶ Schematic of (f) the inkjet printing setup, and (g, h) the printing process of the ATM-GO droplets in a raster fashion, ice template formation (i) during printing, and the resulting ATM-GO aerogel after freeze-drying (j); (k) An example macrostructure of the 3D printed ATM-GO aerogel after freeze-drying and the resulting MoS₂-rGO aerogel after thermal reduction; (l) High-magnification SEM image of the MoS₂-rGO printed on a Ni foam; (m) Rate performance of the MoS₂-rGO aerogel at various current densities.⁷⁷

1.2.5 3D-printed electrodes for supercapacitors

Supercapacitors are a promising class of energy storage devices that could balance the high energy density and high-power density.⁷⁸⁻⁸² However, there are still lots of challenges for achieving high-performance supercapacitors due to the sluggish of electron/ion transport within thick electrodes. Recently, 3D printing technology has provided some new possibilities to address the existing challenges in supercapacitors.⁸³⁻⁸⁴

3D-printed GO aerogels based-electrodes have shown great potential in high-performance supercapacitors. For example, Li et al. reported the fabrication of 3D graphene composite aerogel microlattices via a DIW 3D printing technique for supercapacitor.⁸⁵ As illustrated in **Figure 1.2.5a**, the printable inks consist of GO, graphene nanoplate (GNP), and silica fillers. The 3D-printed graphene composite aerogel (3D-GCA) electrodes with engineered periodic macroporosity can facilitate mass transport, resulting in excellent electrochemical properties. Gao et al. developed a facile ion-induced gelation method to fabricate graphene aerogels microlattices (GAMs) from GO-based ink.⁸⁶ By adding trace of Ca^{2+} , the aqueous GO can be converted into printable ink with suitable rheological properties (**Figure 1.2.5e**). The well-designed hierarchical pores and excellent compressibility and electrical conductivity of the GAMs ensure admirable supercapacitor performances. The 3D-printed GAMs thus display extraordinary capacitive rate and cycle performance. Following their previous work, Li et al. recently reported a 3D printed graphene aerogel scaffold, followed by electrodepositing MnO_2 on the printed scaffold.⁸⁷ The 3D printed aerogels are macroporous with 5-50 μm pores within the 3D printed filaments as shown in **Figure 1.2.5**. The 3D architectures facilitate uniform deposition of MnO_2 throughout the entire graphene aerogel and efficient ion diffusion during charging/discharging even at an ultrahigh mass loading of 182.2 mg cm^{-2} , achieving a record-high areal capacitance of 44.13 F cm^{-2} . More importantly, the liner increasing of areal capacitance with the thickness of 3D printed monolithic electrodes suggests great potential for practical application and could innovate the conventional layer-by-layer stacking fabrication process of commercial supercapacitors.



1.3 3D printing of electrolytes and separator membranes for energy storage

Electrolytes / separator membranes are one of the important components in a battery system. However, the conventional liquid electrolytes have serious limitations in 3D cell assembly and safety problems, which limits the form factors, design of flexible batteries, and realization of high-energy-density Li-metal batteries. In this case, it is vital to develop advanced electrolytes to replace the liquid electrolytes. Moreover, advanced preparation methods are required to design flexible and even 3D structured electrolyte and separator membranes for meeting alien shaped batteries. Extrusion-based 3D printing technique has shown great potential in fabricating flexible separator membranes and 3D structured solid electrolytes.

1.3.1 3D printing of polymer separator for Li-metal batteries

Li-metal anodes have received great attention for advanced Li-metal based batteries in recent years, such as Li-O₂ and Li-S batteries, because of its high theoretical capacity (3860 mAh g⁻¹) and low redox potential (-3.04 V vs standard hydrogen electrode).⁸⁸⁻⁹⁷ However, several intrinsic problems, like the growth of Li dendrites, infinite volume change, and high chemical reactivity, have greatly hindered its widespread utilization in consumer markets.⁹⁸⁻⁹⁹ Many efforts have been devoted to solving these challenges. Designing a functional separator membrane can be a facile and effective approach to suppress the Li dendrite growth for improving the cycling performance of Li metal batteries¹⁰⁰⁻¹⁰⁴.

Recently, 3D printing technique has been used to fabricate functional separators for Li metal batteries as 3D printing is a facile and sophisticated strategy for multi-materials design and fabrication. Hu et al. first reported the fabrication of a novel and safe boron nitride (BN)/PVDF-HFP composite separator via an extrusion-based 3D printing method¹⁰⁵. The printed BN-based separator owes good flexibility with good mechanical strength (**Figure 1.3.1b**). The exiting of BN nanosheets in the separator could ensure a uniform thermal distribution at the interface, resulting in homogeneous Li nucleation. The symmetric cells with printed BN/PVDF-HFP separator thus displayed enhanced cycling stability with a lower overpotential over 500h (**Figure 1.3.1f-i**).

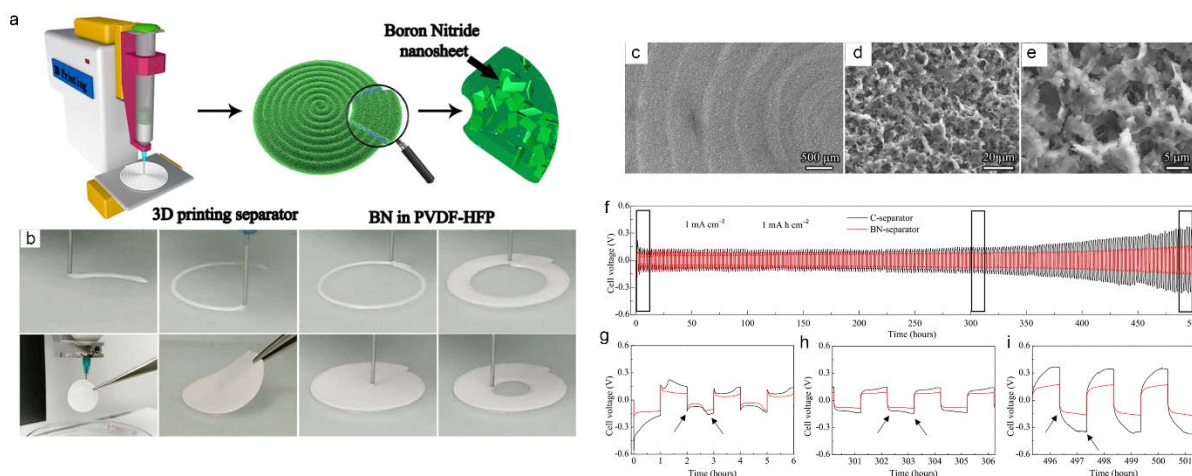


Figure 1.3.1 (a) Schematic illustration of the 3D printing machine and BN in PVDF-HFP separator; (b) Optical images of the 3D-printed BN/PVDF-HFP separator at different stages during the printing process;¹⁰⁵ (c-e) SEM images of the 3D-BN/PVDF-HFP separator; (f-i) Cycling performance of the Li-Li symmetric cells at a current density of 1 mA cm^{-2}

1.3.2 3D printing of Solid-State Electrolyte

For achieving high-energy-density Li-metal batteries, solid-state electrolyte should be applied to replace the traditional unsafe liquid electrolytes. However, the conventional solid-state electrolyte with a flat and planar geometry usually shows a high interfacial impedance due to the limited contact area between the electrolyte and electrodes.¹⁰⁶⁻¹¹⁰ Furthermore, the conventional manufacturing method is hard to obtain a thin solid electrolyte (less than $150 \mu\text{m}$), leading to a decreased energy density due to the high weight of the solid electrolytes.¹¹¹⁻¹¹²

Accordingly, 3D printing, as advanced manufacturing technology, can be employed to design solid-state electrolytes with unique microstructures to solve the aforementioned challenges. Hu et al. for the first time developed multiple solid electrolyte inks using garnet-type $\text{Li}_7\text{La}_3\text{Zr}_2\text{O}_{12}$ (LLZO) as a model material and successfully fabricated various micro-structured LLZO solid electrolyte via an advanced extrusion 3D printing approach¹¹³. **Figure 1.3.2a** illustrated the cell fabrication process using the 3D printed LLZO solid electrolyte. Micro-structured and porous LLZO based on the “self-supporting” ink was printed on both sides of an LLZO tape substrate and sintered revealing thin and 3D architectures composed only of LLZO solid electrolyte. Electrodes can be infiltrated into the printed microporous LLZO to complete battery assembly. A symmetric

cell was made from the 3D printed LLZO with Li infusion into both sides (**Figure 1.3.3b and c**) and displayed lower overpotential at various current densities, indicating the high conductivity of the 3D printed LLZO.

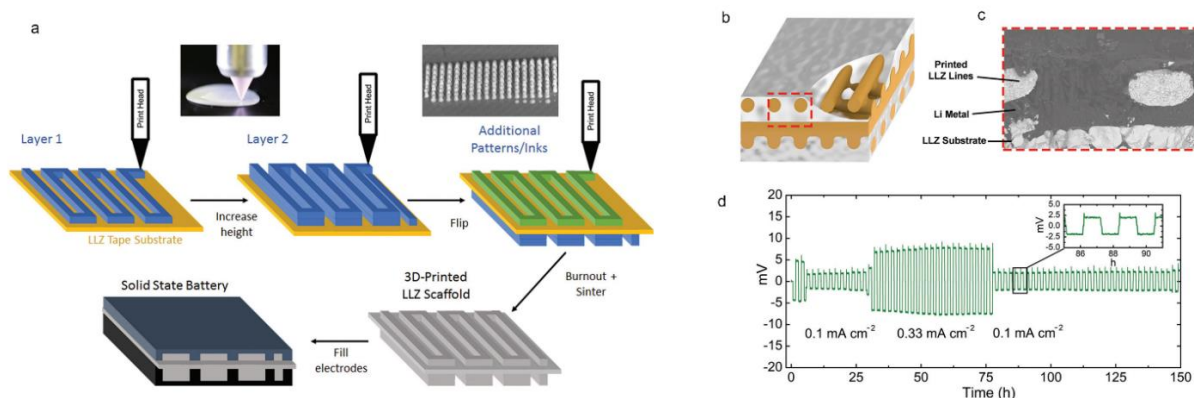


Figure 1.3.2 (a) Schematic illustration of the process of 3D printing LLZO structures and electrode infiltration into the 3D LLZO structures; (b) Schematic of Li melted into the pores of the 3D-printed LLZO grids on an LLZO substrate; (c) Cross-sectional SEM of 3D-printed LLZO/Li metal interface; (d) Voltage profile of the Li/3D-Printed LLZO/Li metal symmetric cell at various current densities.¹¹³

1.3.3 3D printing of Hybrid Solid-State Electrolyte

Although ceramic solid-state electrolytes exhibit great advantages in conductivities, which is even comparable to the liquid electrolytes, ceramic solid electrolytes usually show poor mechanical properties and bad contact with electrodes.¹¹⁴⁻¹¹⁸ Flexible polymer electrolytes have good mechanical properties while show lower conductivity at room temperature and poor stability at high temperatures.^{90, 119-122} The combination of ceramic and polymer electrolytes thus could provide a new possibility to fabricate ideal electrolytes with suitable ionic conductivity and desirable mechanical strength.¹²³⁻¹²⁸

3D printing technique has also been used in this area for developing unique and customized hybrid electrolytes. For example, Blake et al. reported the fabrication of high-performance and printable ceramic-polymer electrolytes (CPEs) by the DIW printing method¹²⁹. The printable ink was composed of PVDF in a mixture of NMP and glycerol solution with nanosized Al₂O₃ filler. The

printed hybrid electrolyte was highly flexible and porous induced from the phase-inversion process. It can also be printed directly over an electrode layer for achieving high electrochemical performance, which provides a new avenue toward integration of flexible power on other device surfaces via the facile DIW printing approach. Furthermore, Bruce et al. developed a 3D ordered bicontinuous ceramic and polymer hybrid solid electrolyte by 3D printing.¹³⁰ As illustrated in **Figure 1.3.3a**, a 3D micro-architected polymer template was constructed by stereolithography 3D printing technique, followed by filling LAGP powder into the empty channels of the 3D template and sintering the template in the air for obtaining the 3D LAGP scaffold. Symmetric lithium cells of printed 3D gyroid LAGP-epoxy electrolytes performed better cycling stability with lower overpotential than that of the LAGP pellet (**Figure 1.3.3b**), which is due to the improved mechanical properties and high conductivity of the 3D ordered and bicontinuous hybrid electrolytes. More recently, Shahbazian-Yassar et al. developed a novel approach to fabricate hybrid solid electrolytes by using an elevated-temperature DIW 3D printing technique (**Figure 1.3.3c**).¹³¹ The hybrid solid electrolyte ink was composed of PVDF-HFP matrices and Li⁺-conducting ionic-liquid electrolyte. Nanosized TiO₂ was added into the polymer inks to modify the viscosity for achieving desired rheological properties. The electrolytes can be directly printed onto the electrode surfaces without any surface treatment. The integration of electrode and electrolytes was found to greatly reduce the interfacial resistance (**Figure 1.3.3d to g**), which ensured an improved capacity and rate performance than the batteries fabricated with traditional solution-casting prepared electrolyte.

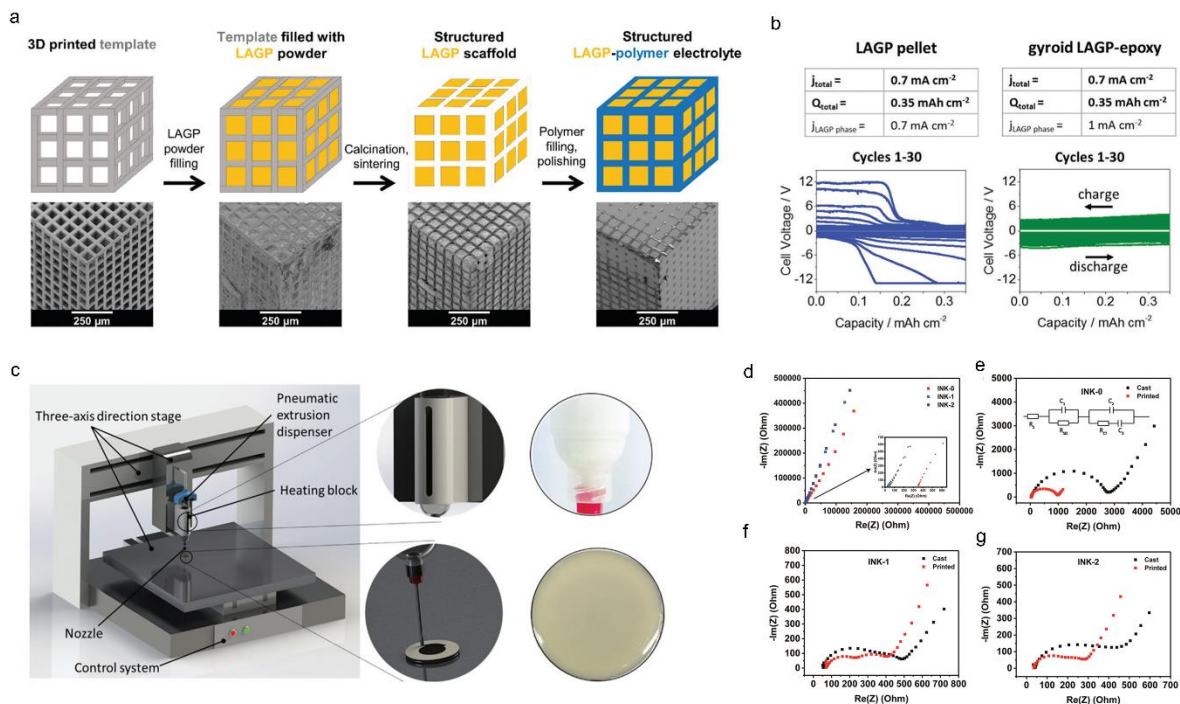


Figure 1.3.3 (a) Schematic of the fabrication process of 3D-printed hybrid electrolytes. Corresponding SEM images of each synthesis stage of the 3D LAGP-epoxy hybrid electrolytes are listed below each schematic; (b) Galvanostatic cycling of Li-Li cells with LAGP pellet and gyroid LAGP-epoxy electrolytes cycled at a current density of 0.7 mA cm^{-2} ,¹³⁰ (c) Schematic of the elevated-temperature direct ink writing system and solid-electrolyte ink fabrication process; (d-g) Electrochemical impedance spectroscopy (EIS) of the hybrid solid-state electrolyte.¹³¹

1.4 All 3D-Printed Energy Storage Devices

1.4.1 All 3D-printed LIBs/LMBs

With the development of microscale technologies, future electronic devices are becoming smaller and miniaturized. In this case, a micro lithium-ion battery would be in great need to power these miniaturized devices, such as microscale sensors,¹³²⁻¹³³ microscale actuators,¹³⁴⁻¹³⁶ and portable and implantable medical devices.¹³⁷⁻¹³⁸ Although 2D thin-film micro-batteries have been greatly developed and could deliver a high-power density, it is a big challenge for thin-film micro-batteries to achieve a high energy density due to the low active materials loading.¹³⁹⁻¹⁴⁰ 3D micro-batteries could be a promising strategy for powering the miniaturizing electronic devices.¹⁴¹⁻¹⁴² Traditional

methods including electrodeposition and vapor deposition technique have been demonstrated to fabricate 3D electrodes with high-aspect-ratio micropillar structures.¹⁴³⁻¹⁴⁵ However, these methods are inefficient and expensive, which are not suitable for large-scale applications. In contrast, 3D printing has been proven to be a promising technique to construct various 3D architectures.

In 2013, the Lewis group first fabricated an interdigitated 3D micro-battery composed of 3D printed high-aspect-ratio LTO anode and LFO cathode micro-arrays that are directly printed on a gold current collector (**Figure 1.4.1a and b**).¹⁴⁶ The printed fully packaged 3D micro-battery (**Figure 1.4.1c**) exhibited a high areal energy density of 9.7 J cm^{-2} at a power density of 2.7 mW cm^{-2} . Later on, Hu and coworkers successfully fabricated an interdigitated Li-ion micro-battery via a 3D printing technique based on graphene oxide (GO) composite inks consisting of highly concentrated GO suspensions with the cathode (LFP) and anode (LTO) active materials added (**Figure 1.4.1d and e**).¹⁴⁷ The printed full cell displayed a relatively stable discharge capacity of 91 mA h g^{-1} (Figure 1.4.1 f and g), corresponding to a high areal capacity of $1.64 \text{ mA h cm}^{-2}$ based on the high electrode mass loading of around 18 mg cm^{-2} . Very recently, 3D printing technique has been employed to fabricate high-performance Li metal batteries (LMBs) with a 3D-printed Li anode and a 3D-printed LFP cathode by using cellulose nanofiber (CNF)-based inks (**Figure 1.4.1k**),¹⁴⁸ which significantly improved the energy density due to the utilization of the printed Li metal anode. The main novelty of this work is the utilization of printed c-CNF structures to host the Li metal forming a 3D c-CNF/Li anode (**Figure 1.4.1i-n**), which could greatly improve the cyclic stability of Li metal anode (**Figure 1.4.1o**).

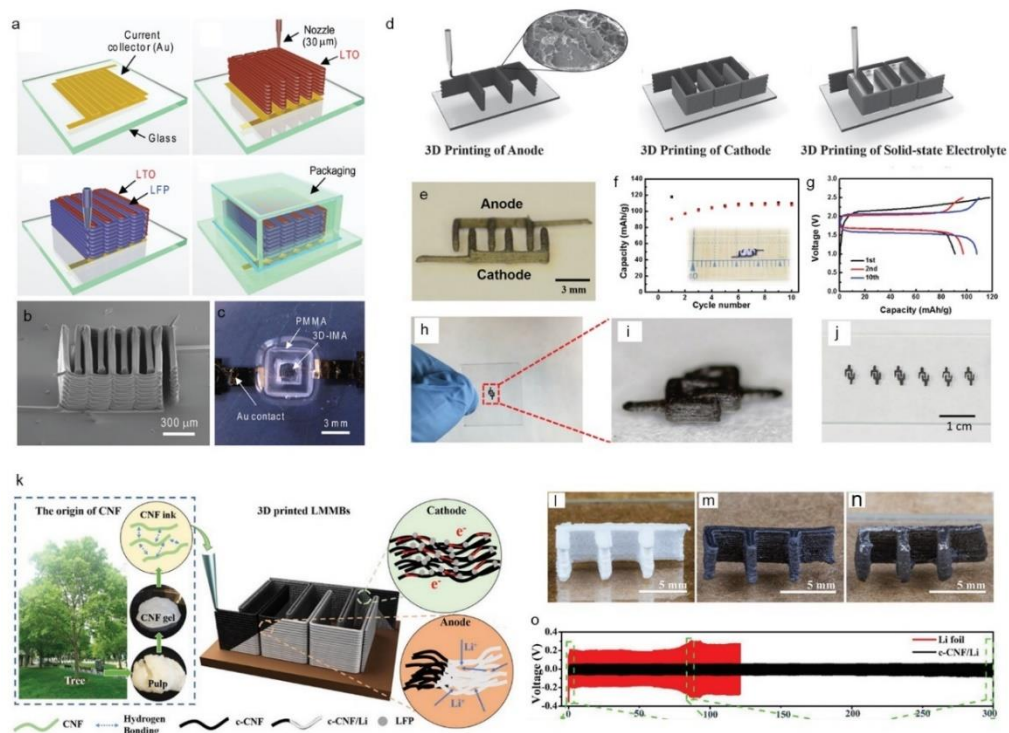


Figure 1.4.1 3D-printed interdigitated Li micro-batteries. (a) Schematic illustration of 3D-printed interdigitated micro-battery architectures on the gold current collector with printed $\text{Li}_4\text{Ti}_5\text{O}_{12}$ (LTO) and LiFePO_4 (LFP) as the anode and cathode, followed by packaging. (b) SEM images of printed and annealed 16-layer interdigitated LTO-LFP electrode architectures, respectively. (c) Optical image of 3D-printed micro-battery composed of LTO-LFP electrodes after packaging.¹⁴⁶ (d) Schematic of the 3D-printed interdigitated electrodes with LTO/GO and LFP/GO as the ink for anode and cathode electrodes, respectively. The gel polymer composite ink is injected in the channel between the annealed electrodes. (e) Digital image of the interdigitated electrodes. (f) Cycling stability of the 3D-printed full cell. (g) Charge/discharge profiles of the 3D-printed full cell. (h, i) Digital images of a miniaturized version of the 3D-printed electrodes. (j) Digital image of the 3D-printed electrodes arrays.¹⁴⁹ (k) Schematic illustration of the CNF ink derived from trees and 3D-printed LMBs fabricated by printing c-CNF/LFP cathode and c-CNF/Li anode. (i-n) Photographs of a CNF scaffold after freeze-drying and before carbonization, c-CNF scaffold after carbonization, and c-CNF/Li electrode with designed 3D structure. (o) Cycling performance comparison of c-CNF/Li and Li foil in a symmetric cell at a current density of 5 mA cm^{-2} with areal capacity fixed at 2.5 mAh cm^{-2} .¹⁴⁸

1.4.2 All 3D-Printed Supercapacitors

Micro-supercapacitors (MSCs) have been considered as one of the most promising power sources for various portable electronics since they can exhibit fast charge/discharge, relatively high capacity, and excellent cycling stability.¹⁵⁰⁻¹⁵⁶ However, most of the reported micro-supercapacitors show lower areal energy densities, which limited their further development in many areas.¹⁵⁷⁻¹⁵⁹

3D printing has been explored to fabricate various 3D micro-structured supercapacitor electrodes and even 3D Li-ion micro-batteries with high areal capacity. Based on previous studies, Yang et al. first reported the fabrication of quasi-solid-state asymmetric micro-supercapacitors (MSC) via an extrusion-based 3D printing approach for realizing high areal energy density ($74 \mu\text{Wh cm}^{-2}$).¹⁶⁰ The fabrication process included the printing of interdigitated electrodes and gel-like electrolyte on the substrate (**Figure 1.4.2a**). A thick electrode ($412 \mu\text{m}$) with an areal mass loading of 3 mg cm^{-2} was fabricated with the printing method (**Figure 1.4.2b**). The 3D printed micro-supercapacitor thus delivered an ultrahigh areal capacitance of 208 mF cm^{-2} , which outperforms most of the reported interdigitated micro-supercapacitors (**Figure 1.4.2c and d**).

Apart from designing 3D micro-supercapacitors, 3D printing has also been employed to fabricate fiber-shaped asymmetric supercapacitors (FASCs). Although fiber-shaped supercapacitors have been widely studied, most of the fabrication methods used in the reported studies have limitations in fabrication cost, efficiency, and scalability that hinder their wide application in wearable devices.¹⁶¹⁻¹⁷² In this case, as illustrated in **Figure 1.4.2e**, a facile and low-cost extrusion-based 3D printing approach was developed to fabricate an all-fiber integrated electronic device via combining printed fiber-shaped temperature sensors (FTSs) with printed FASCs.¹⁷³ It should be noted that the PVA/KOH gel electrolyte was also printed on the as-printed positive and negative fibers (**Figure 1.4.2 g**). The assembled all printed fiber device showed high flexibility and excellent cycling stability under repeated bending (**Figure 1.4.2h-k**).

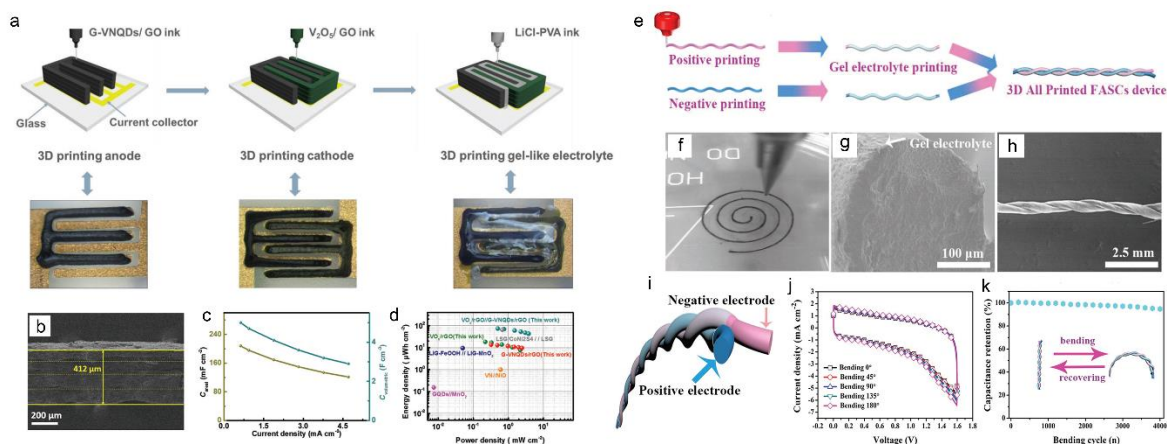


Figure 1.4.2 (a) Schematic illustration of 3D printing of an interdigitated asymmetric MSC on the gold current collector. The gel-like electrolyte was injected into the channels between the anode and cathode. (b) SEM image of 3D-printed 4-layer electrodes. (c) Areal and volumetric capacitances of the 3D printed asymmetric MSC. (d) Comparison of the 3D printed MSC and other reported asymmetric interdigitated MSCs.¹⁶⁰ (e) Schematic of 3D printing of the FASC device. (f) Digital image of the wet fiber during the printing process. (g, h) SEM images of the printed fiber electrode and assembled FASC device. (i) Schematic of the assembled FASCs device. (j) CV of the assembled device measured at different voltage window. (k) Capacitance retention of the FASC devices after repeated bending.¹⁷³

1.4.3 All 3D-printed Zn-based Batteries

In addition to Li/Na batteries, Zn-based battery is another new type energy storage system, which has attracted much attention due to the low cost of zinc metal and high safety of using aqueous electrolytes.¹⁷⁴⁻¹⁸⁴ Printing techniques are efficient and low-cost additive manufacturing method. Thus, the employment of printing technique in Zn-based batteries can further reduce the total fabrication cost and improve the efficiency, thereby boosting the development of Zn-based batteries as promising energy storage system, especially wearable power source systems.¹⁸⁵⁻¹⁸⁷

For example, Wang et al. first reported the fabrication of a rechargeable, skin-worn Ag-Zn tattoo battery consisting of screen-printed electrodes, temporary tattoo paper, alkaline gel electrolytes and a PDMS cover for sealing the battery (**Figure 1.4.3a**).¹⁸⁸ The designed Ag-Zn tattoo battery exhibited a high capacity in the range of 1.3-2.1 mAh cm⁻² and can be easily worn by a person for

powering a red LED. Steingart et al. reported highly flexible, printed Zn-MnO₂ batteries based on mesh-embedded electrodes by using the stencil printing method.¹⁸⁹ As illustrated in **Figure 1.4.3b**, a nylon mesh was applied as a support for the electroactive inks. The Zn and MnO₂ inks were then stencil printed on the nylon-mesh substrates. Silver ink was stencil printed onto the mesh as the current collector. Finally, the battery was assembled by stacking the mesh-embedded electrodes and a PAA gel polymer electrolyte. The flexible Zn-MnO₂ battery displayed a high discharge capacity of 5.6 mAh cm⁻² at a current of 0.5 mA. Moreover, the discharge capacity remained well without any decrease even after repeated bending. Wang et al. reported for the first time an all-printed, stretchable Zn-Ag₂O rechargeable battery by using low-cost screen printing of highly elastic, conductive inks.¹⁹⁰ The novelty of this study hinged on the using of polystyrene-block-polyisoprene-block-polystyrene (SIS) as an elastic binder for stretchable batteries. The printed Zn-Ag₂O battery can be stretched into various shapes and exhibited a reversible capacity of around 2.5 mAh cm⁻² even after multiple iterations of 100% stretching. Despite the great progress in printed Zn-based batteries, the capacity densities are still not desirable. More recently, Subramanian et al. developed a packaged, fully printed Zn-Ag₂O battery with a vertical cell geometry by using the stencil printing approach (**Figure 1.4.3d**).¹⁹¹ The printed battery was constructed by a zinc anode and a monovalent silver oxide cathode with an aqueous potassium hydroxide (KOH) electrolyte. The fully printed cell with vertical geometry and electrodes as small as 1 mm² was achieved, demonstrating a high areal capacity of 11 mAh cm⁻² with 250 μm thick electrodes.

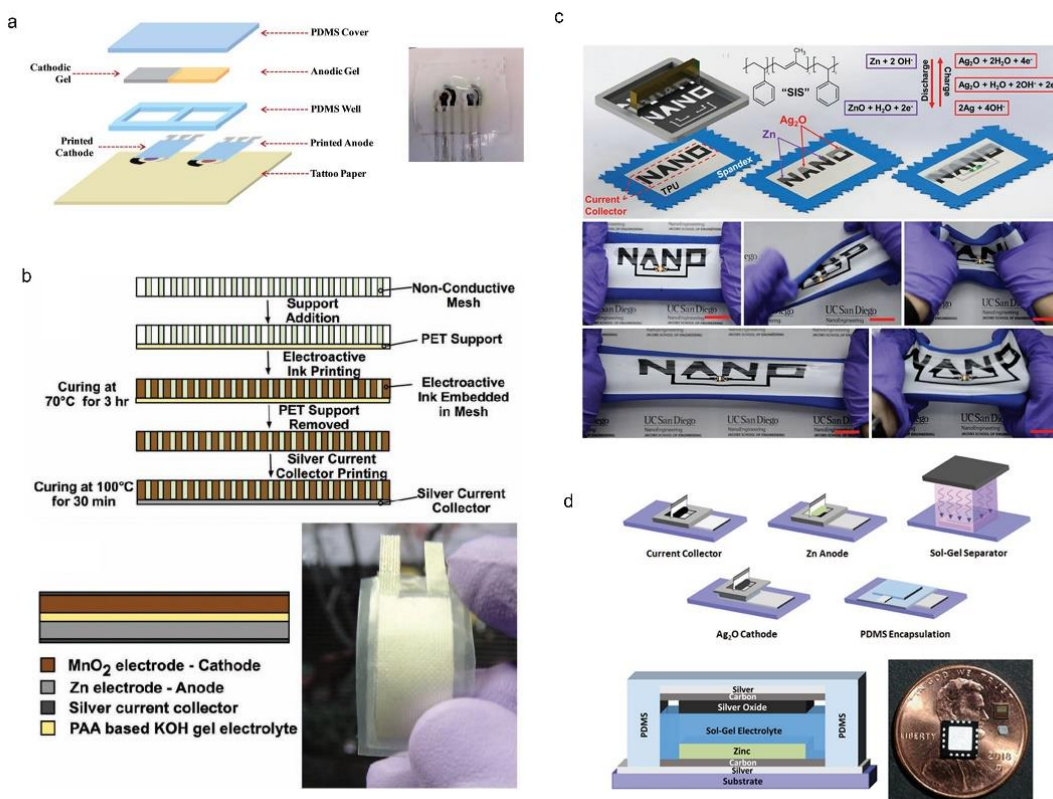


Figure 1.4.3 (a) Schematic illustration of the fabrication process of the Ag-Zn cell through the screen printing method and the prototype of the Ag-Zn cell on temporary transfer tattoo support.¹⁸⁸ (b) Flow diagram showing the fabrication steps for the mesh-embedded, printed MnO₂ cathode and Zn anode with a printed silver current collector, and the optical image of a flexible Zn-MnO₂ battery laminated inside a polyethylene pouch.¹⁸⁹ (c) Schematic of screen printing of a Zn-Ag₂O battery on a stretchable textile and corresponding digital photos of sealed battery with different stretched stages.¹⁹⁰ (d) Schematic illustration of fabrication process of the printed Zn-Ag₂O battery and 1mm printed Zn anode compared to a commercially packaged device and an unpackaged chip.¹⁹¹

1.5 Thesis objectives

As has been thoroughly reviewed, the extrusion-based 3D printing technique has been widely used in energy storage fields due to its great advantages in fabricating 3D macro/microstructures with controllable shape and thickness. The application of 3D printing in batteries are mainly divided

into three categories: 1) 3D printing of advanced anodes or cathodes, 2) 3D printing of solid-state electrolytes, and 3) fabrication of all 3D-printed high-energy-density micro-structured batteries.

Based on this, the thesis objectives are divided into five topics.

(1) To fabricate 3D macro/micro-structured Li-ion battery cathodes (LiFePO_4) via the 3D printing method. The designed 3D structures can facilitate the electron/ion transport within thick electrodes, which can realize high energy and power density LIBs.

(2) To construct hierarchically porous Si electrodes via a low-cost and efficient 3D printing approach. The 3D-printed hierarchically porous structures can effectively address the huge volume change of Si anodes. Meanwhile, the unique structures can allow fast electron/ion transport.

(3) To fabricate thin solid-state electrolytes via a low-cost and scalable 3D printing approach. Solid-state batteries are promising due to high safety and high energy density. However, it is of great challenge to fabricate a thin solid electrolyte via a low-cost and facile approach. Thus, 3D printing offers a promising strategy to fabricate shape-versatile and thin solid electrolytes, which can reduce the total weight of a cell and shorten the Li^+ transport path, thereby increasing the energy density and power density of a solid battery.

(4) To construct high-performance sodium metal batteries via the 3D printing method. 3D-printed Na@rGO/CNT composites were fabricated for suppressing the Na dendrite problem during cycling. Meanwhile, a sodium layered cathode was printed for achieving a high energy density sodium metal battery.

(5) To develop high-voltage layered oxides cathodes for SIBs. In order to further improve the energy density of 3D-printed sodium batteries, P2- $\text{Na}_{2/3}\text{Ni}_{1/3}\text{Mn}_{2/3}\text{O}_2$ high-voltage cathodes were synthesized. Atomic layer deposition (ALD) of AlPO_4 was applied to the cathode for improving the cycling performance.

1.6 Thesis outline

The outline of this thesis is listed as follows:

Chapter 1 presents a general introduction of various 3D printing techniques, particularly the extrusion-type 3D printing technology, and an overview of current research states of extrusion-type 3D printing applied in fabricating various 3D architectures for energy storages devices.

Chapter 2 describes the experimental methods and characterization apparatus used in the work of this thesis.

Chapter 3 describes the employing of extrusion-type 3D printing method for constructing 3D-patterned ultrathick LiFePO_4 electrodes for high-areal-energy and high-power-density LIBs. The excellent electrochemical performances are attributed to the unique 3D architectures which could greatly improve the ion and electron transport within the whole electrode.

Chapter 4 demonstrates the realization of patterned silicon electrodes with vertically aligned and multi-scaled porous structures for achieving high-areal capacity LIBs through a facile and low-cost 3D printing approach. Compared to conventional flat 2D Si electrodes, the 3D-printed Si electrodes possess vertically aligned mass/ionic transport pathways and macro/micro-scaled porosities, which can facilitate the electron/ion transport and effectively mitigate the huge volume expansion during the cycling process by providing extra free space.

Chapter 5 presents the fabrication of shape-versatile and thin LAGP solid electrolytes for high-performance solid-state Li-metal batteries via a low-cost and efficient extrusion-based 3D printing approach. Compared with the conventional pressed thick solid-state electrolyte pellets, the 3D-printed LAGP thin electrolytes can increase the energy density and power density of a cell. In addition, various patterned LAGP architectures are easily fabricated, which broadens the diversity of solid batteries with various size and shapes.

Chapter 6 describes the constructing of a high-performance SMB consisting of a printed Na@rGO/CNT anode and a printed $\text{O}_3\text{-NaCu}_{1/9}\text{Ni}_{2/9}\text{Fe}_{3/9}\text{Mn}_{3/9}\text{O}_2$ (denoted as NCFM) cathode. The 3D-printed Na@rGO/CNT can effectively suppress the Na dendrite growth by decreasing the local current density and releasing the huge volume change of Na during cycling. On the other hand, the 3D-printed micro-structured NCFM cathode composed of interconnected CNTs and porous polymer framework can enable fast electron and ion transport as well as facilitated electrolyte penetration within the whole electrode.

Chapter 7 describes the study of using an electrochemically stable nanoscale surface coating of AlPO_4 to stabilize the P2- $\text{Na}_{2/3}\text{Ni}_{1/3}\text{Mn}_{2/3}\text{O}_2$ with controllable thickness via atomic layer deposition (ALD). The right amount of AlPO_4 coating layer can suppress the reduction of Mn upon cycling, thus improving the structural stability of the cathode material.

Chapter 8 presents a summary of the work in this thesis and describes future work.

1.7 References

1. Tarascon, J. M.; Armand, M., Issues and challenges facing rechargeable lithium batteries. *Nature* **2001**, *414*, 359.
2. Chu, S.; Majumdar, A., Opportunities and challenges for a sustainable energy future. *Nature* **2012**, *488* (7411), 294-303.
3. Winter, M.; Brodd, R. J., What Are Batteries, Fuel Cells, and Supercapacitors? *Chem. Rev.* **2004**, *104* (10), 4245-4270.
4. Chen, K.; Xue, D., Materials chemistry toward electrochemical energy storage. *J. Mater. Chem. A* **2016**, *4* (20), 7522-7537.
5. Stoller, M. D.; Ruoff, R. S., Best practice methods for determining an electrode material's performance for ultracapacitors. *Energy Environ. Sci.* **2010**, *3* (9), 1294-1301.
6. Aricò, A. S.; Bruce, P.; Scrosati, B.; Tarascon, J.-M.; van Schalkwijk, W., Nanostructured materials for advanced energy conversion and storage devices. *Nat. Mater.* **2005**, *4* (5), 366-377.
7. Aurbach, D., Review of selected electrode-solution interactions which determine the performance of Li and Li ion batteries. *J. Power Sources* **2000**, *89*, 206-218.

8. Salanne, M.; Rotenberg, B.; Naoi, K.; Kaneko, K.; Taberna, P. L.; Grey, C. P.; Dunn, B.; Simon, P., Efficient storage mechanisms for building better supercapacitors. *Nat. Energy* **2016**, *1*, 16070.
9. Abhinav M. Gaikwad; Ana Claudia Arias; Steingart, D. A., Recent Progress on Printed Flexible Batteries: Mechanical Challenges, Printing Technologies, and Future Prospects. *Energy Tech.* **2014**, *3*, 305-328.
10. Choi, K.-H.; Yoo, J.; Lee, C. K.; Lee, S.-Y., All-inkjet-printed, solid-state flexible supercapacitors on paper. *Energy Environ. Sci.* **2016**, *9* (9), 2812-2821.
11. Yang, P.; Mai, W., Flexible solid-state electrochemical supercapacitors. *Nano Energy* **2014**, *8*, 274-290.
12. Calvert, P., Inkjet Printing for Materials and Devices. *Chem. Mater.* **2001**, *13* (10), 3299-3305.
13. Symes, M. D.; Kitson, P. J.; Yan, J.; Richmond, C. J.; Cooper, G. J. T.; Bowman, R. W.; Vilbrandt, T.; Cronin, L., Integrated 3D-printed reactionware for chemical synthesis and analysis. *Nat. Chem.* **2012**, *4*, 349.
14. Ruiz-Morales, J. C.; Tarancón, A.; Canales-Vázquez, J.; Méndez-Ramos, J.; Hernández-Afonso, L.; Acosta-Mora, P.; Marín Rueda, J. R.; Fernández-González, R., Three dimensional printing of components and functional devices for energy and environmental applications. *Energy Environ. Sci.* **2017**.
15. Ambrosi, A.; Pumera, M., 3D-printing technologies for electrochemical applications. *Chem. Soc. Rev.* **2016**, *45* (10), 2740-2755.

16. Tang, X.; Zhu, C.; Cheng, D.; Zhou, H.; Liu, X.; Xie, P.; Zhao, Q.; Zhang, D.; Fan, T., Architected Leaf-Inspired Ni_{0.33}Co_{0.66}S₂/Graphene Aerogels via 3D Printing for High-Performance Energy Storage. *Adv. Funct. Mater.* **2018**, 28 (51), 1805057.
17. Díaz-Marta, A. S.; Tubío, C. R.; Carbajales, C.; Fernández, C.; Escalante, L.; Sotelo, E.; Guitián, F.; Barrio, V. L.; Gil, A.; Coelho, A., Three-Dimensional Printing in Catalysis: Combining 3D Heterogeneous Copper and Palladium Catalysts for Multicatalytic Multicomponent Reactions. *ACS Catal.* **2017**, 8 (1), 392-404.
18. Gao, T.; Zhou, Z.; Yu, J.; Zhao, J.; Wang, G.; Cao, D.; Ding, B.; Li, Y., 3D Printing of Tunable Energy Storage Devices with Both High Areal and Volumetric Energy Densities. *Adv. Energy Mater.* **2019**, 9 (8), 1802578.
19. Chen, L.; Tang, X.; Xie, P.; Xu, J.; Chen, Z.; Cai, Z.; He, P.; Zhou, H.; Zhang, D.; Fan, T., 3D Printing of Artificial Leaf With Tunable Hierarchical Porosity for CO₂ Photoreduction. *Chem. Mater.* **2018**, 30, 799-806.
20. Manzano, J. S.; Weinstein, Z. B.; Sadow, A. D.; Slowing, I. I., Direct 3D Printing of Catalytically Active Structures. *ACS Catalysis* **2017**, 7567-7577.
21. Dudek, P., FDM 3D Printing Technology in Manufacturing Composite Elements. *Arch. Metall. Mater.* **2013**, 58 (4), 1415-1418.
22. Weng, Z.; Wang, J.; Senthil, T.; Wu, L., Mechanical and thermal properties of ABS/montmorillonite nanocomposites for fused deposition modeling 3D printing. *Mater. Design* **2016**, 102, 276-283.
23. Nguyen, D. T.; Meyers, C.; Yee, T. D.; Dudukovic, N. A.; Destino, J. F.; Zhu, C.; Duoss, E. B.; Baumann, T. F.; Suratwala, T.; Smay, J. E.; Dylla-Spears, R., 3D-Printed Transparent Glass. *Adv. Mater.* **2017**, 29 (26), 1701181-n/a.

24. Zarek, M.; Layani, M.; Cooperstein, I.; Sachyani, E.; Cohn, D.; Magdassi, S., 3D Printing of Shape Memory Polymers for Flexible Electronic Devices. *Adv. Mater.* **2016**, *28* (22), 4449-4454.
25. Layani, M.; Wang, X.; Magdassi, S., Novel Materials for 3D Printing by Photopolymerization. *Adv. Mater.* **2018**, *30* (41), e1706344.
26. Shirazi, S. F.; Gharehkhani, S.; Mehrali, M.; Yarmand, H.; Metselaar, H. S.; Adib Kadri, N.; Osman, N. A., A review on powder-based additive manufacturing for tissue engineering: selective laser sintering and inkjet 3D printing. *Sci. Tech. Adv. Mater.* **2015**, *16* (3), 033502.
27. Mazhar, H.; Osswald, T.; Negrut, D., On the use of computational multi-body dynamics analysis in SLS-based 3D printing. *Addit. Manuf.* **2016**, *12*, 291-295.
28. Tan, W. S.; Chua, C. K.; Chong, T. H.; Fane, A. G.; Jia, A., 3D printing by selective laser sintering of polypropylene feed channel spacers for spiral wound membrane modules for the water industry. *Virtual and Physical Prototyping* **2016**, *11* (3), 151-158.
29. J-P. Kruth, P. M., J. Van Vaerenbergh, L. Froyen, M. Rombouts, Binding Mechanisms in Selective Laser Sintering and Selective Laser Melting. *Rapid Prototyping Journal* **2005**, *11*, 26-36.
30. Yan, P.; Brown, E.; Su, Q.; Li, J.; Wang, J.; Xu, C.; Zhou, C.; Lin, D., 3D Printing Hierarchical Silver Nanowire Aerogel with Highly Compressive Resilience and Tensile Elongation through Tunable Poisson's Ratio. *Small* **2017**, 1701756-n/a.
31. Gao, F.; Xu, Z.; Liang, Q.; Liu, B.; Li, H.; Wu, Y.; Zhang, Y.; Lin, Z.; Wu, M.; Ruan, C.; Liu, W., Direct 3D Printing of High Strength Biohybrid Gradient Hydrogel Scaffolds for Efficient Repair of Osteochondral Defect. *Adv. Funct. Mater.* **2018**, 1706644-n/a.

32. Elsayed, H.; Colombo, P.; Bernardo, E., Direct ink writing of wollastonite-diopside glass-ceramic scaffolds from a silicone resin and engineered fillers. *Journal of the European Ceramic Society* **2017**, *37* (13), 4187-4195.
33. Qian, F.; Zhu, C.; Knipe, J. M.; Ruelas, S.; Stolaroff, J. K.; DeOtte, J. R.; Duoss, E. B.; Spadaccini, C. M.; Henard, C. A.; Guarnieri, M. T.; Baker, S. E., Direct Writing of Tunable Living Inks for Bioprocess Intensification. *Nano Lett.* **2019**.
34. Zhu, C.; Liu, T.; Qian, F.; Chen, W.; Chandrasekaran, S.; Yao, B.; Song, Y.; Duoss, E. B.; Kuntz, J. D.; Spadaccini, C. M.; Worsley, M. A.; Li, Y., 3D printed functional nanomaterials for electrochemical energy storage. *Nano Today* **2017**, *15* (Supplement C), 107-120.
35. Wang, X.; Li, T.; Ma, H.; Zhai, D.; Jiang, C.; Chang, J.; Wang, J.; Wu, C., A 3D-printed scaffold with MoS₂ nanosheets for tumor therapy and tissue regeneration. *Npg Asia Mater.* **2017**, *9*, e376.
36. Tian, X.; Jin, J.; Yuan, S.; Chua, C. K.; Tor, S. B.; Zhou, K., Emerging 3D-Printed Electrochemical Energy Storage Devices: A Critical Review. *Adv. Energy Mater.* **2017**, *7* (17), 1700127.
37. Fu, K.; Yao, Y.; Dai, J.; Hu, L., Progress in 3D Printing of Carbon Materials for Energy-Related Applications. *Adv. Mater.* **2017**, *29* (9).
38. Zhang, Q.; Zhang, F.; Xu, X.; Zhou, C.; Lin, D., Three-Dimensional Printing Hollow Polymer Template-Mediated Graphene Lattices with Tailorable Architectures and Multifunctional Properties. *ACS Nano* **2018**.
39. Choi, K.-H.; Ahn, D. B.; Lee, S.-Y., Current Status and Challenges in Printed Batteries: Toward Form Factor-Free, Monolithic Integrated Power Sources. *ACS Energy Lett.* **2017**, *3*, 220-236.

40. Liu, L.; Weng, Q.; Lu, X.; Sun, X.; Zhang, L.; Schmidt, O. G., Advances on Microsized On-Chip Lithium-Ion Batteries. *Small* **2017**, *13* (45).
41. Kim, F.; Kwon, B.; Eom, Y.; Lee, J. E.; Park, S.; Jo, S.; Park, S. H.; Kim, B.-S.; Im, H. J.; Lee, M. H.; Min, T. S.; Kim, K. T.; Chae, H. G.; King, W. P.; Son, J. S., 3D printing of shape-conformable thermoelectric materials using all-inorganic Bi₂Te₃-based inks. *Nat. Energy* **2018**.
42. Kim, S.-H.; Choi, K.-H.; Cho, S.-J.; Yoo, J.; Lee, S.-S.; Lee, S.-Y., Flexible/Shape-Versatile, Bipolar All-Solid-State Lithium-Ion Batteries Prepared by Multistage Printing. *Energy Environ. Sci.* **2017**.
43. Etacheri, V.; Marom, R.; Elazari, R.; Salitra, G.; Aurbach, D., Challenges in the development of advanced Li-ion batteries: a review. *Energy Environ. Sci.* **2011**, *4* (9), 3243.
44. Lu, L.; Han, X.; Li, J.; Hua, J.; Ouyang, M., A review on the key issues for lithium-ion battery management in electric vehicles. *J. Power Sources* **2013**, *226*, 272-288.
45. Nitta, N.; Wu, F.; Lee, J. T.; Yushin, G., Li-ion battery materials: present and future. *Mater. Today* **2015**, *18* (5), 252-264.
46. Feng, X.; Ouyang, M.; Liu, X.; Lu, L.; Xia, Y.; He, X., Thermal runaway mechanism of lithium ion battery for electric vehicles: A review. *Energy Storage Mater.* **2018**, *10*, 246-267.
47. Blomgren, G. E., The Development and Future of Lithium Ion Batteries. *J. Electrochem. Soc.* **2016**, *164* (1), A5019-A5025.
48. Hu, J.; Jiang, Y.; Cui, S.; Duan, Y.; Liu, T.; Guo, H.; Lin, L.; Lin, Y.; Zheng, J.; Amine, K.; Pan, F., 3D-Printed Cathodes of LiMn_{1-x}Fe_xPO₄ Nanocrystals Achieve Both Ultrahigh Rate and High Capacity for Advanced Lithium-Ion Battery. *Adv. Energy Mater.* **2016**, *6*, 1600856.

49. Saleh, M. S.; Li, J.; Park, J.; Panat, R., 3D printed hierarchically-porous microlattice electrode materials for exceptionally high specific capacity and areal capacity lithium ion batteries. *Addit. Manuf.* **2018**, *23*, 70-78.
50. Zhang, C.; Shen, K.; Li, B.; Li, S.; Yang, S., Continuously 3D printed quantum dot-based electrodes for lithium storage with ultrahigh capacities. *J. Mater. Chem. A* **2018**, *6* (41), 19960-19966.
51. Nazar, S. E. a. L. F., New Approaches for High Energy Density Lithium-Sulfur Battery Cathodes. *Acc. Chem. Res.* **2013**, *46* (5), 1135-1143.
52. Yin, Y. X.; Xin, S.; Guo, Y. G.; Wan, L. J., Lithium-sulfur batteries: electrochemistry, materials, and prospects. *Angew. Chem. Int. Ed. Engl.* **2013**, *52* (50), 13186-200.
53. Liu, X.; Huang, J. Q.; Zhang, Q.; Mai, L., Nanostructured Metal Oxides and Sulfides for Lithium-Sulfur Batteries. *Adv. Mater.* **2017**, *29* (20).
54. Peng, H.-J.; Huang, J.-Q.; Cheng, X.-B.; Zhang, Q., Review on High-Loading and High-Energy Lithium-Sulfur Batteries. *Adv. Energy Mater.* **2017**, *7* (24), 1700260.
55. Peng, H.-J.; Xu, W.-T.; Zhu, L.; Wang, D.-W.; Huang, J.-Q.; Cheng, X.-B.; Yuan, Z.; Wei, F.; Zhang, Q., 3D Carbonaceous Current Collectors: The Origin of Enhanced Cycling Stability for High-Sulfur-Loading Lithium-Sulfur Batteries. *Adv. Funct. Mater.* **2016**, *26* (35), 6351-6358.
56. Qie, L.; Zu, C.; Manthiram, A., A High Energy Lithium-Sulfur Battery with Ultrahigh-Loading Lithium Polysulfide Cathode and its Failure Mechanism. *Adv. Energy Mater.* **2016**, *6* (7), 1502459.
57. Zhang, J.; Li, J.-Y.; Wang, W.-P.; Zhang, X.-H.; Tan, X.-H.; Chu, W.-G.; Guo, Y.-G., Microemulsion Assisted Assembly of 3D Porous S/Graphene@g-C₃N₄ Hybrid Sponge as Free-

Standing Cathodes for High Energy Density Li-S Batteries. *Adv. Energy Mater.* **2018**, 8 (14), 1702839.

58. Zhang, J.; Huang, H.; Bae, J.; Chung, S.-H.; Zhang, W.; Manthiram, A.; Yu, G., Nanostructured Host Materials for Trapping Sulfur in Rechargeable Li-S Batteries: Structure Design and Interfacial Chemistry. *Small Methods* **2018**, 2 (1), 1700279.

59. Milroy, C.; Manthiram, A., Printed Microelectrodes for Scalable, High-Areal-Capacity Lithium–Sulfur Batteries. *Chem. Commun.* **2016**, 52 (23), 4282-4285.

60. Shen, K.; Mei, H.; Li, B.; Ding, J.; Yang, S., 3D Printing Sulfur Copolymer-Graphene Architectures for Li-S Batteries. *Adv. Energy Mater.* **2018**, 8 (4), 1701527.

61. Gao, X.; Sun, Q.; Yang, X.; Liang, J.; Koo, A.; Li, W.; Liang, J.; Wang, J.; Li, R.; Holness, F. B.; Price, A. D.; Yang, S.; Sham, T.-K.; Sun, X., Toward a Remarkable Li-S battery via 3D Printing. *Nano Energy* **2019**, 56, 595-603.

62. Peng, Z.; Freunberger, S. A.; Chen, Y.; Bruce, P. G., A reversible and higher-rate Li-O₂ battery. *Science* **2012**, 337 (6094), 563-566.

63. Lau, S.; Archer, L. A., Nucleation and Growth of Lithium Peroxide in the Li-O₂ Battery. *Nano Lett.* **2015**, 15 (9), 5995-6002.

64. Feng, N.; He, P.; Zhou, H., Critical Challenges in Rechargeable Aprotic Li-O₂Batteries. *Adv. Energy Mater.* **2016**, 6 (9), 1502303.

65. Chang, Z.; Xu, J.; Zhang, X., Recent Progress in Electrocatalyst for Li-O₂ Batteries. *Adv. Energy Mater.* **2017**, 7 (23), 1700875.

66. Kwak, W.-J.; Kim, H.; Jung, H.-G.; Aurbach, D.; Sun, Y.-K., Review—A Comparative Evaluation of Redox Mediators for Li-O₂Batteries: A Critical Review. *J. Electrochem. Soc.* **2018**, *165* (10), A2274-A2293.
67. Lacey, S. D.; Kirsch, D. J.; Li, Y.; Morgenstern, J. T.; Zarket, B. C.; Yao, Y.; Dai, J.; Garcia, L. Q.; Liu, B.; Gao, T.; Xu, S.; Raghavan, S. R.; Connell, J. W.; Lin, Y.; Hu, L., Extrusion-Based 3D Printing of Hierarchically Porous Advanced Battery Electrodes. *Adv. Mater.* **2016**, 1705651-n/a.
68. Lyu, Z.; Lim, G. J. H.; Guo, R.; Kou, Z.; Wang, T.; Guan, C.; Ding, J.; Chen, W.; Wang, J., 3D-Printed MOF-Derived Hierarchically Porous Frameworks for Practical High-Energy Density Li-O₂ Batteries. *Adv. Funct. Mater.* **2019**, *29* (1), 1806658.
69. Qiao, Y.; Liu, Y.; Chen, C.; Xie, H.; Yao, Y.; He, S.; Ping, W.; Liu, B.; Hu, L., 3D-Printed Graphene Oxide Framework with Thermal Shock Synthesized Nanoparticles for Li-CO₂ Batteries. *Adv. Funct. Mater.* **2018**, *28* (51), 1805899.
70. Pan, H.; Hu, Y.-S.; Chen, L., Room-temperature stationary sodium-ion batteries for large-scale electric energy storage. *Energy Environ. Sci.* **2013**, *6* (8), 2338-2360.
71. Han, M. H.; Gonzalo, E.; Singh, G.; Rojo, T., A comprehensive review of sodium layered oxides: powerful cathodes for Na-ion batteries. *Energy Environ. Sci.* **2015**, *8* (1), 81-102.
72. Kim, H.; Kim, H.; Ding, Z.; Lee, M. H.; Lim, K.; Yoon, G.; Kang, K., Recent Progress in Electrode Materials for Sodium-Ion Batteries. *Adv. Energy Mater.* **2016**, *6* (19), 1600943-n/a.
73. Hwang, J.-Y.; Myung, S.-T.; Sun, Y.-K., Sodium-ion batteries: present and future. *Chem. Soc. Rev.* **2017**, *46* (12), 3529-3614.

74. Ni, Q.; Bai, Y.; Wu, F.; Wu, C., Polyanion-Type Electrode Materials for Sodium-Ion Batteries. *Adv. Sci.* **2017**, *4* (3), 1600275-n/a.
75. Ortiz Vitoriano, N.; Drewett, N.; Gonzalo, E.; Rojo, T., High Performance Manganese-based Layered Oxide Cathodes: Overcoming the Challenges of Sodium Ion Batteries. *Energy Environ. Sci.* **2017**.
76. Ding, J.; Shen, K.; Du, Z.; Li, B.; Yang, S., 3D-Printed Hierarchical Porous Frameworks for Sodium Storage. *ACS Appl. Mater. Interfaces* **2017**, *9* (48), 41871-41877.
77. Brown, E.; Yan, P.; Tekik, H.; Elangovan, A.; Wang, J.; Lin, D.; Li, J., 3D printing of hybrid MoS₂-graphene aerogels as highly porous electrode materials for sodium ion battery anodes. *Mater. Design* **2019**, *170*, 107689.
78. Gogotsi, P. S. a. Y., Materials for electrochemical capacitors. *Nat. Mater.* **2008**, *7*, 845-854.
79. Augustyn, V.; Simon, P.; Dunn, B., Pseudocapacitive oxide materials for high-rate electrochemical energy storage. *Energy Environ. Sci.* **2014**, *7* (5), 1597-1614.
80. Augustyn, V.; Come, J.; Lowe, M. A.; Kim, J. W.; Taberna, P.-L.; Tolbert, S. H.; Abruña, H. D.; Simon, P.; Dunn, B., High-rate electrochemical energy storage through Li⁺ intercalation pseudocapacitance. *Nat. Mater.* **2013**, *12*, 518.
81. Lukatskaya, M. R.; Mashtalir, O.; Ren, C. E.; Dall'Agnese, Y.; Rozier, P.; Taberna, P. L.; Naguib, M.; Simon, P.; Barsoum, M. W.; Gogotsi, Y., Cation Intercalation and High Volumetric Capacitance of Two-Dimensional Titanium Carbide. *Science* **2013**, *341* (6153), 1502-1505.
82. Ghidui, M.; Lukatskaya, M. R.; Zhao, M.-Q.; Gogotsi, Y.; Barsoum, M. W., Conductive two-dimensional titanium carbide 'clay' with high volumetric capacitance. *Nature* **2014**, *516*, 78.

83. Wang, Z.; Zhang, Q. E.; Long, S.; Luo, Y.; Yu, P.; Tan, Z.; Bai, J.; Qu, B.; Yang, Y.; Shi, J.; Zhou, H.; Xiao, Z. Y.; Hong, W.; Bai, H., Three-Dimensional Printing of Polyaniline/Reduced Graphene Oxide Composite for High-Performance Planar Supercapacitor. *ACS Appl. Mater. Interfaces* **2018**, *10* (12), 10437-10444.
84. Zhang, F.; Wei, M.; Viswanathan, V. V.; Swart, B.; Shao, Y.; Wu, G.; Zhou, C., 3D printing technologies for electrochemical energy storage. *Nano Energy* **2017**, *40*, 418-431.
85. Zhu, C.; Liu, T.; Qian, F.; Han, T. Y.; Duoss, E. B.; Kuntz, J. D.; Spadaccini, C. M.; Worsley, M. A.; Li, Y., Supercapacitors Based on Three-Dimensional Hierarchical Graphene Aerogels with Periodic Macropores. *Nano Lett.* **2016**, *16* (6), 3448-56.
86. Jiang, Y.; Xu, Z.; Huang, T.; Liu, Y.; Guo, F.; Xi, J.; Gao, W.; Gao, C., Direct 3D Printing of Ultralight Graphene Oxide Aerogel Microlattices. *Adv. Funct. Mater.* **2018**, *28* (16), 1707024.
87. Yao, B.; Chandrasekaran, S.; Zhang, J.; Xiao, W.; Qian, F.; Zhu, C.; Duoss, E. B.; Spadaccini, C. M.; Worsley, M. A.; Li, Y., Efficient 3D Printed Pseudocapacitive Electrodes with Ultrahigh MnO₂ Loading. *Joule* **2019**, *3* (2), 459-470.
88. Lin, D.; Liu, Y.; Cui, Y., Reviving the lithium metal anode for high-energy batteries. *Nat. Nanotech.* **2017**, *12* (3), 194-206.
89. Zhang, R.; Chen, X.-R.; Chen, X.; Cheng, X.-B.; Zhang, X.-Q.; Yan, C.; Zhang, Q., Lithiophilic Sites in Doped Graphene Guide Uniform Lithium Nucleation for Dendrite-Free Lithium Metal Anodes. *Angew. Chem. Int. Ed. Engl.* **2017**, *56* (27), 7764-7768.
90. Zhang, X.; Wang, S.; Xue, C.; Xin, C.; Lin, Y.; Shen, Y.; Li, L.; Nan, C.-W., Self-Suppression of Lithium Dendrite in All-Solid-State Lithium Metal Batteries with Poly(vinylidene difluoride)-Based Solid Electrolytes. *Adv. Mater.* **2019**, *31* (11), 1806082.

91. Lu, Z.; Liang, Q.; Wang, B.; Tao, Y.; Zhao, Y.; Lv, W.; Liu, D.; Zhang, C.; Weng, Z.; Liang, J.; Li, H.; Yang, Q.-H., Graphitic Carbon Nitride Induced Micro-Electric Field for Dendrite-Free Lithium Metal Anodes. *Adv. Energy Mater.* **2019**, *9* (7), 1803186.
92. Zeng, X.-X.; Yin, Y.-X.; Shi, Y.; Zhang, X.-D.; Yao, H.-R.; Wen, R.; Wu, X.-W.; Guo, Y.-G., Lithiation-Derived Repellent toward Lithium Anode Safeguard in Quasi-solid Batteries. *Chem* **2018**.
93. Xu, Y.; Menon, A. S.; Harks, P. P. R. M. L.; Hermes, D. C.; Haverkate, L. A.; Unnikrishnan, S.; Mulder, F. M., Honeycomb-like porous 3D nickel electrodeposition for stable Li and Na metal anodes. *Energy Storage Mater.* **2018**, *12*, 69-78.
94. Xu, R.; Zhang, X.-Q.; Cheng, X.-B.; Peng, H.-J.; Zhao, C.-Z.; Yan, C.; Huang, J.-Q., Artificial Soft-Rigid Protective Layer for Dendrite-Free Lithium Metal Anode. *Adv. Funct. Mater.* **2018**, 1705838-n/a.
95. Guo, F.; Wang, Y.; Kang, T.; Liu, C.; Shen, Y.; Lu, W.; Wu, X.; Chen, L., A Li-dual carbon composite as stable anode material for Li batteries. *Energy Storage Mater.* **2018**, *15*, 116-123.
96. Zhu, B.; Jin, Y.; Hu, X.; Zheng, Q.; Zhang, S.; Wang, Q.; Zhu, J., Poly(dimethylsiloxane) Thin Film as a Stable Interfacial Layer for High-Performance Lithium-Metal Battery Anodes. *Adv. Mater.* **2017**, *29* (2), 1603755-n/a.
97. Raji, A.-R. O.; Villegas Salvatierra, R.; Kim, N. D.; Fan, X.; Li, Y.; Silva, G. A. L.; Sha, J.; Tour, J. M., Lithium Batteries with Nearly Maximum Metal Storage. *ACS Nano* **2017**.
98. Ye, H.; Xin, S.; Yin, Y.-X.; Guo, Y.-G., Advanced Porous Carbon Materials for High-Efficient Lithium Metal Anodes. *Adv. Energy Mater.* **2017**, 1700530-n/a.

99. Liu, Y.; Liu, Q.; Xin, L.; Liu, Y.; Yang, F.; Stach, E. A.; Xie, J., Making Li-metal electrodes rechargeable by controlling the dendrite growth direction. *Nat. Energy* **2017**, *2*, 17083.
100. Luo, W.; Zhou, L.; Fu, K.; Yang, Z.; Wan, J.; Manno, M.; Yao, Y.; Zhu, H.; Yang, B.; Hu, L., A Thermally Conductive Separator for Stable Li Metal Anodes. *Nano Lett.* **2015**, *15* (9), 6149-6154.
101. Pan, R.; Xu, X.; Sun, R.; Wang, Z.; Lindh, J.; Edström, K.; Strømme, M.; Nyholm, L., Nanocellulose Modified Polyethylene Separators for Lithium Metal Batteries. *Small* **2018**, *14* (21), 1704371.
102. Liu, Y.; Xiong, S.; Wang, J.; Jiao, X.; Li, S.; Zhang, C.; Song, Z.; Song, J., Dendrite-free lithium metal anode enabled by separator engineering via uniform loading of lithiophilic nucleation sites. *Energy Storage Mater.* **2019**, *19*, 24-30.
103. Li, Y.; Wang, W.; Liu, X.; Mao, E.; Wang, M.; Li, G.; Fu, L.; Li, Z.; Eng, A. Y. S.; Seh, Z. W.; Sun, Y., Engineering stable electrode-separator interfaces with ultrathin conductive polymer layer for high-energy-density Li-S batteries. *Energy Storage Mater.* **2019**.
104. Li, C.; Liu, S.; Shi, C.; Liang, G.; Lu, Z.; Fu, R.; Wu, D., Two-dimensional molecular brush-functionalized porous bilayer composite separators toward ultrastable high-current density lithium metal anodes. *Nat. Commun.* **2019**, *10* (1), 1363.
105. Liu, Y.; Qiao, Y.; Zhang, Y.; Yang, Z.; Gao, T.; Kirsch, D.; Liu, B.; Song, J.; Yang, B.; Hu, L., 3D printed separator for the thermal management of high-performance Li metal anodes. *Energy Storage Mater.* **2018**, *12*, 197-203.
106. Kotobuki, M.; Munakata, H.; Kanamura, K.; Sato, Y.; Yoshida, T., Compatibility of $\text{Li}_7\text{La}_3\text{Zr}_2\text{O}_{12}$ Solid Electrolyte to All-Solid-State Battery Using Li Metal Anode. *J. Electrochem. Soc.* **2010**, *157* (10), A1076.

107. Fu, K.; Gong, Y.; Dai, J.; Gong, A.; Han, X.; Yao, Y.; Wang, C.; Wang, Y.; Chen, Y.; Yan, C.; Li, Y.; Wachsman, E. D.; Hu, L., Flexible, solid-state, ion-conducting membrane with 3D garnet nanofiber networks for lithium batteries. *Proc. Natl. Acad. Sci.* **2016**, *113* (26), 7094-7099.
108. Li, P.; Dong, X.; Li, C.; Liu, J.; Liu, Y.; Feng, W.; Wang, C.; Wang, Y.; Xia, Y., Anchoring an Artificial Solid–Electrolyte Interphase Layer on a 3D Current Collector for High-Performance Lithium Anodes. *Angew. Chem. Int. Ed. Engl.* **2019**, *58* (7), 2093-2097.
109. Gong, Y.; Fu, K.; Xu, S.; Dai, J.; Hamann, T. R.; Zhang, L.; Hitz, G. T.; Fu, Z.; Ma, Z.; McOwen, D. W.; Han, X.; Hu, L.; Wachsman, E. D., Lithium-ion conductive ceramic textile: A new architecture for flexible solid-state lithium metal batteries. *Mater. Today* **2018**.
110. Jiang, Z.; Xie, H.; Wang, S.; Song, X.; Yao, X.; Wang, H., Perovskite Membranes with Vertically Aligned Microchannels for All-Solid-State Lithium Batteries. *Adv. Energy Mater.* **2018**, *8* (27), 1801433.
111. Wu, B.; Wang, S.; Evans Iv, W. J.; Deng, D. Z.; Yang, J.; Xiao, J., Interfacial behaviours between lithium ion conductors and electrode materials in various battery systems. *J. Mater. Chem. A* **2016**, *4* (40), 15266-15280.
112. Betz, J.; Bieker, G.; Meister, P.; Placke, T.; Winter, M.; Schmuck, R., Theoretical versus Practical Energy: A Plea for More Transparency in the Energy Calculation of Different Rechargeable Battery Systems. *Adv. Energy Mater.* **2018**, 1803170.
113. McOwen, D. W.; Xu, S.; Gong, Y.; Wen, Y.; Godbey, G. L.; Gritton, J. E.; Hamann, T. R.; Dai, J.; Hitz, G. T.; Hu, L.; Wachsman, E. D., 3D-Printing Electrolytes for Solid-State Batteries. *Adv. Mater.* **2018**, *30* (18), e1707132.
114. Inda, Y.; Katoh, T.; Baba, M., Development of all-solid lithium-ion battery using Li-ion conducting glass-ceramics. *J. Power Sources* **2007**, *174* (2), 741-744.

115. Asl, N. M.; Keith, J.; Lim, C.; Zhu, L.; Kim, Y., Inorganic solid/organic liquid hybrid electrolyte for use in Li-ion battery. *Electrochimica Acta* **2012**, *79*, 8-16.
116. Liu, Y.; Li, C.; Li, B.; Song, H.; Cheng, Z.; Chen, M.; He, P.; Zhou, H., Germanium Thin Film Protected Lithium Aluminum Germanium Phosphate for Solid-State Li Batteries. *Adv. Energy Mater.* **2018**, *8* (16), 1702374.
117. Bae, J.; Li, Y.; Zhao, F.; Zhou, X.; Ding, Y.; Yu, G., Designing 3D nanostructured garnet frameworks for enhancing ionic conductivity and flexibility in composite polymer electrolytes for lithium batteries. *Energy Storage Mater.* **2018**, *15*, 46-52.
118. Fu, K.; Gong, Y.; Hitz, G. T.; McOwen, D. W.; Li, Y.; Xu, S.; Wen, Y.; Zhang, L.; Wang, C.; Pastel, G.; Dai, J.; Liu, B.; Xie, H.; Yao, Y.; Wachsman, E. D.; Hu, L., Three-dimensional bilayer garnet solid electrolyte based high energy density lithium metal–sulfur batteries. *Energy Environ. Sci.* **2017**, *10* (7), 1568-1575.
119. Pitawala, H. M. J. C.; Dissanayake, M. A. K. L.; Seneviratne, V. A., Combined effect of Al₂O₃ nano-fillers and EC plasticizer on ionic conductivity enhancement in the solid polymer electrolyte (PEO)₉LiTf. *Solid State Ionics* **2007**, *178* (13), 885-888.
120. Syzdek, J.; Armand, M.; Marcinek, M.; Zalewska, A.; Żukowska, G.; Wieczorek, W., Detailed studies on the fillers modification and their influence on composite, poly(oxyethylene)-based polymeric electrolytes. *Electrochimica Acta* **2010**, *55* (4), 1314-1322.
121. Sheng, O.; Jin, C.; Luo, J.; Yuan, H.; Huang, H.; Gan, Y.; Zhang, J.; Xia, Y.; Liang, C.; Zhang, W.; Tao, X., Mg₂B₂O₅ Nanowire Enabled Multifunctional Solid-State Electrolytes with High Ionic Conductivity, Excellent Mechanical Properties, and Flame-Retardant Performance. *Nano Lett.* **2018**, *18* (5), 3104-3112.

122. Zhai, H.; Xu, P.; Ning, M.; Cheng, Q.; Mandal, J.; Yang, Y., A Flexible Solid Composite Electrolyte with Vertically Aligned and Connected Ion-Conducting Nanoparticles for Lithium Batteries. *Nano Lett.* **2017**, *17* (5), 3182-3187.
123. Zheng, J.; Tang, M.; Hu, Y.-Y., Lithium Ion Pathway within $\text{Li}_7\text{La}_3\text{Zr}_2\text{O}_{12}$ -Polyethylene Oxide Composite Electrolytes. *Angew. Chem. Int. Ed. Engl.* **2016**, *55* (40), 12538-12542.
124. Xie, H.; Yang, C.; Fu, K.; Yao, Y.; Jiang, F.; Hitz, E.; Liu, B.; Wang, S.; Hu, L., Flexible, Scalable, and Highly Conductive Garnet-Polymer Solid Electrolyte Templated by Bacterial Cellulose. *Adv. Energy Mater.* **2018**, *8* (18), 1703474.
125. Fan, L.; Wei, S.; Li, S.; Li, Q.; Lu, Y., Recent Progress of the Solid-State Electrolytes for High-Energy Metal-Based Batteries. *Adv. Energy Mater.* **2018**, *8* (11), 1702657.
126. Zhang, W.; Nie, J.; Li, F.; Wang, Z. L.; Sun, C., A durable and safe solid-state lithium battery with a hybrid electrolyte membrane. *Nano Energy* **2018**, *45*, 413-419.
127. Dirican, M.; Yan, C.; Zhu, P.; Zhang, X., Composite solid electrolytes for all-solid-state lithium batteries. *Materials Science and Engineering: R: Reports* **2019**, *136*, 27-46.
128. Zhang, X.; Xie, J.; Shi, F.; Lin, D.; Liu, Y.; Liu, W.; Pei, A.; Gong, Y.; Wang, H.; Liu, K.; Xiang, Y.; Cui, Y., Vertically Aligned and Continuous Nanoscale Ceramic-Polymer Interfaces in Composite Solid Polymer Electrolytes for Enhanced Ionic Conductivity. *Nano Lett.* **2018**, *18* (6), 3829-3838.
129. Blake, A. J.; Kohlmeyer, R. R.; Hardin, J. O.; Carmona, E. A.; Maruyama, B.; Berrigan, J. D.; Huang, H.; Durstock, M. F., 3D Printable Ceramic-Polymer Electrolytes for Flexible High-Performance Li-Ion Batteries with Enhanced Thermal Stability. *Adv. Energy Mater.* **2017**, 1602920.

130. Zekoll, S.; Marriner-Edwards, C.; Hekselman, A. K. O.; Kasemchainan, J.; Kuss, C.; Armstrong, D. E. J.; Cai, D.; Wallace, R. J.; Richter, F. H.; Thijssen, J. H. J.; Bruce, P. G., Hybrid electrolytes with 3D bicontinuous ordered ceramic and polymer microchannels for all-solid-state batteries. *Energy Environ. Sci.* **2018**, *11* (1), 185-201.
131. Cheng, M.; Jiang, Y.; Yao, W.; Yuan, Y.; Deivanayagam, R.; Foroozan, T.; Huang, Z.; Song, B.; Rojaee, R.; Shokuhfar, T.; Pan, Y.; Lu, J.; Shahbazian-Yassar, R., Elevated-Temperature 3D Printing of Hybrid Solid-State Electrolyte for Li-Ion Batteries. *Adv. Mater.* **2018**, *30* (39), 1800615.
132. Morrish, W.; West, P.; Orlando, N.; Klantsataya, E.; Gardner, K.; Lane, S.; Decorby, R.; Francois, A.; Meldrum, A., Refractometric micro-sensor using a mirrored capillary resonator. *Opt. Express* **2016**, *24* (22), 24959-24970.
133. Q. Fang, D. G. C., J. W. Gardner, Micro-gas-sensor with conducting polymers. *Sensors and Actuators B* **2002**, *84*, 66-71.
134. Hines, L.; Petersen, K.; Lum, G. Z.; Sitti, M., Soft Actuators for Small-Scale Robotics. *Adv. Mater.* **2017**, *29* (13).
135. Lee, H. T.; Kim, M. S.; Lee, G. Y.; Kim, C. S.; Ahn, S. H., Shape Memory Alloy (SMA)-Based Microscale Actuators with 60% Deformation Rate and 1.6 kHz Actuation Speed. *Small* **2018**, *14* (23), e1801023.
136. Sinatra, N. R.; Ranzani, T.; Vlassak, J. J.; Parker, K. K.; Wood, R. J., Nanofiber-reinforced soft fluidic micro-actuators. *J. Micromech. Microeng.* **2018**, *28* (8), 084002.
137. Wise, R. M. H. a. K. D., A 3D implantable microsystem for intraocular pressure monitoring using a glass-in-silicon reflow process. *IEEE* **2011**, 23-27.

138. Hodgins, D.; Bertsch, A.; Post, N.; Frischholz, M.; Volckaerts, B.; Spensley, J.; Wasikiewicz, J. M.; Higgins, H.; von Stetten, F.; Kenney, L., Healthy Aims: Developing New Medical Implants and Diagnostic Equipment. *IEEE Pervas. Comput.* **2008**, *7* (1), 14-21.
139. Salian, G. D.; Lebouin, C.; Demoulin, A.; Lepihin, M. S.; Maria, S.; Galeyeva, A. K.; Kurbatov, A. P.; Djenizian, T., Electrodeposition of polymer electrolyte in nanostructured electrodes for enhanced electrochemical performance of thin-film Li-ion microbatteries. *J. Power Sources* **2017**, *340*, 242-246.
140. Sugiawati, V. A.; Vacandio, F.; Knauth, P.; Djenizian, T., Sputter-Deposited Amorphous LiCuPO₄ Thin Film as Cathode Material for Li-ion Microbatteries. *Chem. Select* **2018**, *3* (2), 405-409.
141. Ferrari, S.; Loveridge, M.; Beattie, S. D.; Jahn, M.; Dashwood, R. J.; Bhagat, R., Latest advances in the manufacturing of 3D rechargeable lithium microbatteries. *J. Power Sources* **2015**, *286*, 25-46.
142. Ning, H.; Pikul, J. H.; Zhang, R.; Li, X.; Xu, S.; Wang, J.; Rogers, J. A.; King, W. P.; Braun, P. V., Holographic patterning of high-performance on-chip 3D lithium-ion microbatteries. *Proc. Natl. Acad. Sci.* **2015**, *112* (21), 6573-6578.
143. Kristina Edstrom, D. B., and Leif Nyholm, Electrodeposition as a Tool for 3D Microbattery Fabrication. *Electrochem. Soc. Interface* **2011**, *20* (2), 41-46.
144. Li, W.; Bradley, L. C.; Watkins, J. J., Copolymer Solid-State Electrolytes for 3D Microbatteries via Initiated Chemical Vapor Deposition. *ACS Appl. Mater. Interfaces* **2019**, *11* (6), 5668-5674.
145. Johns, P.; Roberts, M.; Owen, J., Conformal electrodeposition of manganese dioxide onto reticulated vitreous carbon for 3D microbattery applications. *J. Mater. Chem.* **2011**, *21* (27), 10153.

146. Sun, K.; Wei, T. S.; Ahn, B. Y.; Seo, J. Y.; Dillon, S. J.; Lewis, J. A., 3D printing of interdigitated Li-ion microbattery architectures. *Adv. Mater.* **2013**, *25* (33), 4539-43.
147. Fu, K.; Wang, Y.; Yan, C.; Yao, Y.; Chen, Y.; Dai, J.; Lacey, S.; Wang, Y.; Wan, J.; Li, T.; Wang, Z.; Xu, Y.; Hu, L., Graphene Oxide-Based Electrode Inks for 3D-Printed Lithium-Ion Batteries. *Adv. Mater.* **2016**, *28*, 2587-2594.
148. Cao, D.; Xing, Y.; Tantratian, K.; Wang, X.; Ma, Y.; Mukhopadhyay, A.; Cheng, Z.; Zhang, Q.; Jiao, Y.; Chen, L.; Zhu, H., 3D Printed High-Performance Lithium Metal Microbatteries Enabled by Nanocellulose. *Adv. Mater.* **2019**, *31* (14), e1807313.
149. Fu, K.; Wang, Y.; Yan, C.; Yao, Y.; Chen, Y.; Dai, J.; Lacey, S.; Wang, Y.; Wan, J.; Li, T.; Wang, Z.; Xu, Y.; Hu, L., Graphene Oxide-Based Electrode Inks for 3D-Printed Lithium-Ion Batteries. *Adv. Mater.* **2016**, *28* (13), 2587-2594.
150. Lethien, C.; Le Bideau, J.; Brousse, T., Challenges and prospects of 3D micro-supercapacitors for powering the internet of things. *Energy Environ. Sci.* **2019**, *12* (1), 96-115.
151. Gao, W.; Singh, N.; Song, L.; Liu, Z.; Reddy, A. L. M.; Ci, L.; Vajtai, R.; Zhang, Q.; Wei, B.; Ajayan, P. M., Direct laser writing of micro-supercapacitors on hydrated graphite oxide films. *Nat. Nanotech.* **2011**, *6*, 496.
152. El-Kady, M. F.; Kaner, R. B., Scalable fabrication of high-power graphene micro-supercapacitors for flexible and on-chip energy storage. *Nat. Commun.* **2013**, *4*, 1475.
153. Wu, Z. S.; Parvez, K.; Feng, X.; Mullen, K., Graphene-based in-plane micro-supercapacitors with high power and energy densities. *Nat. Commun.* **2013**, *4*, 2487.
154. Liu, W.-W.; Feng, Y.-Q.; Yan, X.-B.; Chen, J.-T.; Xue, Q.-J., Superior Micro-Supercapacitors Based on Graphene Quantum Dots. *Adv. Funct. Mater.* **2013**, *23* (33), 4111-4122.

155. Kyeremateng, N. A.; Brousse, T.; Pech, D., Microsupercapacitors as miniaturized energy-storage components for on-chip electronics. *Nat. Nanotech.* **2017**, *12* (1), 7-15.
156. Qi, D.; Liu, Y.; Liu, Z.; Zhang, L.; Chen, X., Design of Architectures and Materials in In-Plane Micro-supercapacitors: Current Status and Future Challenges. *Adv. Mater.* **2017**, *29* (5).
157. Wang, K.; Zou, W.; Quan, B.; Yu, A.; Wu, H.; Jiang, P.; Wei, Z., An All-Solid-State Flexible Micro-supercapacitor on a Chip. *Adv. Energy Mater.* **2011**, *1* (6), 1068-1072.
158. Kurra, N.; Hota, M. K.; Alshareef, H. N., Conducting polymer micro-supercapacitors for flexible energy storage and Ac line-filtering. *Nano Energy* **2015**, *13*, 500-508.
159. Zhang, C.; Kremer, M. P.; Seral-Ascaso, A.; Park, S.-H.; McEvoy, N.; Anasori, B.; Gogotsi, Y.; Nicolosi, V., Stamping of Flexible, Coplanar Micro-Supercapacitors Using MXene Inks. *Adv. Funct. Mater.* **2018**, *28* (9), 1705506.
160. Shen, K.; Ding, J.; Yang, S., 3D Printing Quasi-Solid-State Asymmetric Micro-Supercapacitors with Ultrahigh Areal Energy Density. *Adv. Energy Mater.* **2018**, *8* (20), 1800408.
161. Yang, Z.; Deng, J.; Chen, X.; Ren, J.; Peng, H., A highly stretchable, fiber-shaped supercapacitor. *Angew. Chem. Int. Ed. Engl.* **2013**, *52* (50), 13453-7.
162. Chen, X.; Lin, H.; Deng, J.; Zhang, Y.; Sun, X.; Chen, P.; Fang, X.; Zhang, Z.; Guan, G.; Peng, H., Electrochromic fiber-shaped supercapacitors. *Adv. Mater.* **2014**, *26* (48), 8126-32.
163. Yu, J.; Lu, W.; Smith, J. P.; Booksh, K. S.; Meng, L.; Huang, Y.; Li, Q.; Byun, J.-H.; Oh, Y.; Yan, Y.; Chou, T.-W., A High Performance Stretchable Asymmetric Fiber-Shaped Supercapacitor with a Core-Sheath Helical Structure. *Adv. Energy Mater.* **2017**, *7* (3), 1600976.

164. Xu, P.; Gu, T.; Cao, Z.; Wei, B.; Yu, J.; Li, F.; Byun, J.-H.; Lu, W.; Li, Q.; Chou, T.-W., Carbon Nanotube Fiber Based Stretchable Wire-Shaped Supercapacitors. *Adv. Energy Mater.* **2014**, *4* (3), 1300759.
165. Jin, H.; Zhou, L.; Mak, C. L.; Huang, H.; Tang, W. M.; Chan, H. L. W., High-performance fiber-shaped supercapacitors using carbon fiber thread (CFT)@polyaniline and functionalized CFT electrodes for wearable/stretchable electronics. *Nano Energy* **2015**, *11*, 662-670.
166. Chen, T.; Hao, R.; Peng, H.; Dai, L., High-performance, stretchable, wire-shaped supercapacitors. *Angew. Chem. Int. Ed. Engl.* **2015**, *54* (2), 618-22.
167. Wang, Q.; Wang, X.; Xu, J.; Ouyang, X.; Hou, X.; Chen, D.; Wang, R.; Shen, G., Flexible coaxial-type fiber supercapacitor based on NiCo₂O₄ nanosheets electrodes. *Nano Energy* **2014**, *8*, 44-51.
168. Fu, Y.; Cai, X.; Wu, H.; Lv, Z.; Hou, S.; Peng, M.; Yu, X.; Zou, D., Fiber supercapacitors utilizing pen ink for flexible/wearable energy storage. *Adv. Mater.* **2012**, *24* (42), 5713-5718.
169. Wang, X.; Liu, B.; Liu, R.; Wang, Q.; Hou, X.; Chen, D.; Wang, R.; Shen, G., Fiber-based flexible all-solid-state asymmetric supercapacitors for integrated photodetecting system. *Angew. Chem. Int. Ed. Engl.* **2014**, *53* (7), 1849-53.
170. Zhang, Q.; Xu, W.; Sun, J.; Pan, Z.; Zhao, J.; Wang, X.; Zhang, J.; Man, P.; Guo, J.; Zhou, Z.; He, B.; Zhang, Z.; Li, Q.; Zhang, Y.; Xu, L.; Yao, Y., Constructing Ultrahigh-Capacity Zinc-Nickel-Cobalt Oxide@Ni(OH)₂ Core-Shell Nanowire Arrays for High-Performance Coaxial Fiber-Shaped Asymmetric Supercapacitors. *Nano Lett.* **2017**, *17* (12), 7552-7560.
171. Wang, Z.; Cheng, J.; Guan, Q.; Huang, H.; Li, Y.; Zhou, J.; Ni, W.; Wang, B.; He, S.; Peng, H., All-in-one fiber for stretchable fiber-shaped tandem supercapacitors. *Nano Energy* **2018**, *45*, 210-219.

172. Su, F.; Lv, X.; Miao, M., High-performance two-ply yarn supercapacitors based on carbon nanotube yarns dotted with Co_3O_4 and NiO nanoparticles. *Small* **2015**, *11* (7), 854-61.
173. Zhao, J.; Zhang, Y.; Huang, Y.; Xie, J.; Zhao, X.; Li, C.; Qu, J.; Zhang, Q.; Sun, J.; He, B.; Li, Q.; Lu, C.; Xu, X.; Lu, W.; Li, L.; Yao, Y., 3D Printing Fiber Electrodes for an All-Fiber Integrated Electronic Device via Hybridization of an Asymmetric Supercapacitor and a Temperature Sensor. *Adv. Sci.* **2018**, *5* (11), 1801114.
174. Li, Y.; Dai, H., Recent advances in zinc–air batteries. *Chem. Soc. Rev.* **2014**, *43* (15), 5257-5275.
175. Zhang, N.; Cheng, F.; Liu, Y.; Zhao, Q.; Lei, K.; Chen, C.; Liu, X.; Chen, J., Cation-Deficient Spinel ZnMn_2O_4 Cathode in $\text{Zn}(\text{CF}_3\text{SO}_3)_2$ Electrolyte for Rechargeable Aqueous Zn-Ion Battery. *J. AM. Chem. Soc.* **2016**, *138* (39), 12894-12901.
176. He, P.; Yan, M.; Zhang, G.; Sun, R.; Chen, L.; An, Q.; Mai, L., Layered VS_2 Nanosheet-Based Aqueous Zn Ion Battery Cathode. *Adv. Energy Mater.* **2017**, *7* (11), 1601920.
177. Zhang, L.; Chen, L.; Zhou, X.; Liu, Z., Towards High-Voltage Aqueous Metal-Ion Batteries Beyond 1.5 V: The Zinc/Zinc Hexacyanoferrate System. *Adv. Energy Mater.* **2015**, *5* (2), 1400930.
178. Xia, C.; Guo, J.; Lei, Y.; Liang, H.; Zhao, C.; Alshareef, H. N., Rechargeable Aqueous Zinc-Ion Battery Based on Porous Framework Zinc Pyrovanadate Intercalation Cathode. *Adv. Energy Mater.* **2018**, *30* (5).
179. Trocoli, R.; La Mantia, F., An aqueous zinc-ion battery based on copper hexacyanoferrate. *Chem.Sus.Chem.* **2015**, *8* (3), 481-5.

180. Chao, D.; Zhu, C. R.; Song, M.; Liang, P.; Zhang, X.; Tiep, N. H.; Zhao, H.; Wang, J.; Wang, R.; Zhang, H.; Fan, H. J., A High-Rate and Stable Quasi-Solid-State Zinc-Ion Battery with Novel 2D Layered Zinc Orthovanadate Array. *Adv. Mater.* **2018**, *30* (32), e1803181.
181. He, P.; Zhang, G.; Liao, X.; Yan, M.; Xu, X.; An, Q.; Liu, J.; Mai, L., Sodium Ion Stabilized Vanadium Oxide Nanowire Cathode for High-Performance Zinc-Ion Batteries. *Adv. Energy Mater.* **2018**, *8* (10), 1702463.
182. Kundu, D.; Adams, B. D.; Duffort, V.; Vajargah, S. H.; Nazar, L. F., A high-capacity and long-life aqueous rechargeable zinc battery using a metal oxide intercalation cathode. *nat. Energy* **2016**, *1* (10).
183. Konarov, A.; Voronina, N.; Jo, J. H.; Bakenov, Z.; Sun, Y.-K.; Myung, S.-T., Present and Future Perspective on Electrode Materials for Rechargeable Zinc-Ion Batteries. *ACS Energy Lett.* **2018**, *3* (10), 2620-2640.
184. Pan, H.; Shao, Y.; Yan, P.; Cheng, Y.; Han, K. S.; Nie, Z.; Wang, C.; Yang, J.; Li, X.; Bhattacharya, P.; Mueller, K. T.; Liu, J., Reversible aqueous zinc/manganese oxide energy storage from conversion reactions. *Nat. Energy* **2016**, *1* (5).
185. Jost, K.; Stenger, D.; Perez, C. R.; McDonough, J. K.; Lian, K.; Gogotsi, Y.; Dion, G., Knitted and screen printed carbon-fiber supercapacitors for applications in wearable electronics. *Energy Environ. Sci.* **2013**, *6* (9), 2698-2705.
186. Tehrani, Z.; Korochkina, T.; Govindarajan, S.; Thomas, D. J.; O'Mahony, J.; Kettle, J.; Claypole, T. C.; Gethin, D. T., Ultra-thin flexible screen printed rechargeable polymer battery for wearable electronic applications. *Organic Electronics* **2015**, *26*, 386-394.
187. Hilder, M.; Winther-Jensen, B.; Clark, N. B., Paper-based, printed zinc-air battery. *J. Power Sources* **2009**, *194* (2), 1135-1141.

188. Berchmans, S.; Bandodkar, A. J.; Jia, W.; Ramírez, J.; Meng, Y. S.; Wang, J., An epidermal alkaline rechargeable Ag–Zn printable tattoo battery for wearable electronics. *J. Mater. Chem. A* **2014**, *2* (38), 15788-15795.
189. Gaikwad, A. M.; Whiting, G. L.; Steingart, D. A.; Arias, A. C., Highly Flexible, Printed Alkaline Batteries Based on Mesh-Embedded Electrodes. *Adv. Mater.* **2011**, *23* (29), 3251-3255.
190. Kumar, R.; Shin, J.; Yin, L.; You, J.-M.; Meng, Y. S.; Wang, J., All-Printed, Stretchable Zn-Ag₂O Rechargeable Battery via Hyperelastic Binder for Self-Powering Wearable Electronics. *Adv. Energy Mater.* **2017**, *7* (8), 1602096.
191. Kumar, R.; Johnson, K. M.; Williams, N. X.; Subramanian, V., Scaling Printable Zn–Ag₂O Batteries for Integrated Electronics. *Adv. Energy Mater.* **2019**, *9* (13), 1803645.

Chapter 2

2 Experimental Methods and Characterization Techniques

2.1 Experimental methods

2.1.1 3D printing of free-standing patterned LiFePO_4 (LFP) thick electrodes

The preparation process includes two steps: LFP ink preparation and 3D printing process. The LFP ink preparation process can be described as follow: Commercialized LFP nanoparticles were used as active materials. Highly concentrated LFP ink was prepared by first mixing 1400 mg of LFP nanoparticles, 200 mg of acetylene black (AB), and 100 mg multi-wall carbon nanotubes (MWCNTs, diameter of 40~60 nm, length of 2 μm) and grinding them well for a few minutes. Then 300 mg PVDF-HFP powder (Mw ~ 400000, Sigma-Aldrich) was dissolved in 1200 mg 1-methyl-2-pyrrolidinone (NMP, Sigma-Aldrich), which was added into the mixed powder as a binder. Afterward, the obtained concentrated LFP gel was further mixed in a conditioning mixer (ARM 310, Thinky) at 2000 rpm for 25 min. Finally, a homogenized LFP paste was obtained for the 3D printing process.



Figure 2.1 ARM 310 Thinky Mixer for ink preparation

For 3D printing process: The as-prepared LFP ink was used to fabricate 3D structured electrodes by using a fused filament fabrication (FFF) DeltaMaker 3D printer modified with a paste extrusion-type tool head. In detail, the as-prepared LFP ink was first loaded into a 3cc syringe. The syringe was subsequently subject to centrifugation at 3000 rpm for 3 min to expel out all air-bubbles in the ink. A metal nozzle with an inner diameter of 200 μm was adopted and a Nordson EFD computer-controlled pneumatic fluid dispenser was used to control the printing extrusion pressures between 30 psi to 50 psi. The printing speed ranges from 6 mm s^{-1} to 10 mm s^{-1} . After printing, the 3D structures were first immersed into a water coagulation bath for few minutes to remove the solvent, followed by freeze-drying for 24 h.

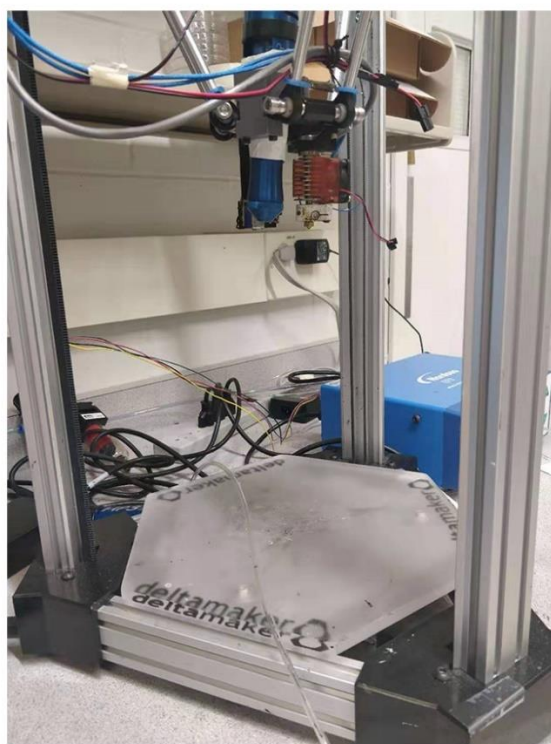


Figure 2.2 Fused filament fabrication (FFF) DeltaMaker 3D printer

2.1.2 3D Printing of Patternable Silicon Electrodes

The fabrication process includes two steps: Silicon (Si) ink preparation and 3D printing process. The Si ink preparation process can be described as follow: Si-SA(Sodium Alginate) ink was prepared by first mixing 350 mg of Si nanoparticles (50nm, Hongwu Nano), 140 mg multi-wall carbon nanotubes (MWCNTs, diameter of 40-60 nm, length of 2 um), and 70 mg of acetylene black (AB) and grinding them well by hand for a few minutes. After that, the SA solution (2.8 g, 5 wt%) was added to the mixed powders as an aqueous binder. After that, the composites were further mixed in a conditioning mixer (ARM, Thinky) at 2000 rpm for 40 minutes to obtain a homogenous and viscous ink. Finally, the obtained Si-SA ink was loaded into a 3cc syringe for printing.



Figure 2.3 Freeze-Drier for drying the printed structures

For 3D printing process: 3D printing process was conducted on a fused filament fabrication (FFF) DeltaMaker 3D printer modified with a paste extrusion-type tool head. The syringe with Si-SA ink was subject to centrifugation at 3000 rpm for 3 minutes to expel out the air-bubbles prior to the printing process. A Nordson EFD computer-controlled pneumatic fluid dispenser provides the

appropriate pressure to extrude the ink through a metal nozzle with an inner diameter of 200 μm and control the flow rate. The printing speed ranges from 6 mm s^{-1} to 10 mm s^{-1} depending on the printing pressure and ink viscosity. The 3D structures were printed directly on the Cu foil. The printed 3D Si electrodes were post-treated in two ways: one was directly dried in air. The other was freeze-dried for 24h to obtain the designed 3D architecture.

2.1.3 3D Printing of Thin Solid-State Electrolyte LAGP ($\text{Li}_{1.5}\text{Al}_{0.5}\text{Ge}_{1.5}\text{P}_3\text{O}_{12}$)

The fabrication process includes two steps: Ink Preparation and 3D printing process. The typical fabrication process of LAGP ink was described as follows: 4.0 g LAGP powders were first mixed with 1.0g of Pluronic F127 solution (10%) to obtain the homogeneous gel. After that, 2g polyvinyl alcohol (PVA) aqueous solution (15%) and 0.6 g sodium alginate (SA) aqueous solution (10%) as binders were added into the obtained gel to increase the viscosity of the ink. Subsequently, the obtained LAGP gel was further mixed well in a conditioning mixer (ARM, Thinky) at 2000 rpm for 10 min to obtain a homogenous and viscous ink for 3D printing.

3D printing process: The as-prepared ink was first loaded into a 3ml syringe. Afterward, the ink was subject to centrifugation for 5min at 3000 rpm to remove the air bubbles. A fused filament fabrication (FFF) DeltaMaker 3D printer modified with a paste extrusion-type tool head was used to fabricate uniform solid electrolyte film. The ink was deposited onto a glass substrate with extrusion pressure controlled by a Nordson EFD fluid dispenser. A metal nozzle with an inner diameter of 150 μm was adopted. The printing speed was adjusted in a range from 6 to 12 mm s^{-1} depending on the ink viscosity. After printing, the 3D-printed structures with glass substrate were aged in the air for drying. The dried structures were then sintered in a muffle furnace at 900°C for 6h with a ramping rate of 2.5°C min^{-1} .

2.1.4 3D Printing of GO/CNT skeleton

The typical fabrication process of GO/CNT ink was described as follows: 50 mg MWCNT (diameter of 40 – 60 nm, length of 2 μm) was dispersed into 50 ml GO aqueous solution (GO ~ 4mg/ml) and the mixture was then ultra-sonicated for 3h to obtain a well-dispersed suspension. Afterward, the GO/CNT suspension was concentrated by centrifugation to form a higher concentration of around 40 mg/ml. The concentrated suspension was further mixed well in a conditioning mixer (ARM, Thinky) at 2000 rpm for 10 min to obtain a homogenous and viscous ink. The 3D printing process was conducted on a fused filament fabrication (FFF) DeltaMaker 3D printer modified with a paste extrusion-type tool head. The syringe with GO/CNT ink was subject to centrifugation at 3000 rpm for 3 minutes to expel out the air-bubbles prior to the printing process. A Nordson EFD computer-controlled pneumatic fluid dispenser provides the appropriate pressure to extrude the ink through a metal nozzle with an inner diameter of 200 μm and control the flow rate. The printing speed ranges from 8 mm s^{-1} to 12 mm s^{-1} depending on the printing pressure and ink viscosity.

2.1.5 Fabrication of 3D Na@rGO/CNT composite electrode

The printed GO/CNT skeleton was used as a 3D Na host. Thermal infusion of Na melting was carried out inside the Ar-filled glove box with both water and O_2 level less than 0.1 ppm. Bulk Na (from Aldrich) was cut into small pieces first and then melted in a stainless-steel boat on a hot plate at ~ 300°C. The GO/CNT skeleton was instantaneously reduced to rGO/CNT by contacting with molten Na. Afterward, Na was slowly absorbed into the rGO/CNT skeleton, and the amount of Na infused can be controlled by controlling the contact time. The Na@rGO/CNT composite was finally obtained and can be directly used as the anode.

2.1.6 Synthesis of O3-NaCu_{1/9}Ni_{2/9}Fe_{3/9}Mn_{3/9}O₂ by Solid-State Reaction Method

The O3-NaCu_{1/9}Ni_{2/9}Fe_{3/9}Mn_{3/9}O₂ (NCNFM) was synthesized by a traditional solid-state reaction. Typically, a stoichiometric mixture of Na₂CO₃ (99%, Sigma-Aldrich), CuO (99%, Sigma-Aldrich), NiO (99%, Sigma-Aldrich), Fe₂O₃ (99%, Sigma-Aldrich), and Mn₂O₃ (99%, Sigma-Aldrich) was ball-milled for 5h in ethanol. An excess of 5% Na₂CO₃ was added to compensate the sodium loss at high temperature. The mixture was dried at 80°C for 10h. The obtained powders were then

pressed into pellets, afterward, the pellets were heated at 850°C for 15h. The heated pellets were cooled to room temperature and then transferred to an argon-filled glovebox until use.



Figure 2.4 Thermal furnace for heating the O3-NCNFM precursor pellet

2.1.7 3D Printing of O3-NCNFM skeleton

The NCNFM ink was prepared by first mixing 900 mg of as-prepared Na-CNFM powders, 200 mg of acetylene black (AB), and 100 mg of MWCNT followed by mixing them well for a few minutes. Then 1500 mg of 20% PVDF-HFP dissolved in NMP (PVDF-HFP 300 mg) was added into the mixed powders as a binder, the mixed gel was then transferred into a conditioning mixer (ARM 310, Thinky) to further mix the ink at 2000 rpm for around 30 min. After that, a homogenous and high viscous ink was obtained for 3D printing. The 3D printing process was conducted on a fused filament fabrication (FFF) DeltaMaker 3D printer modified with a paste extrusion-type tool head. The syringe with NCNFM ink was subject to centrifugation at 3000 rpm for 3 minutes to expel out the air-bubbles prior to the printing process. A Nordson EFD computer-controlled pneumatic fluid dispenser provides the appropriate pressure to extrude the ink through a metal nozzle with an inner diameter of 200 μm and control the flow rate. The printing speed ranges from 8 mm s^{-1} to 12 mm s^{-1} depending on the printing pressure and ink viscosity.

2.1.8 Synthesis of P2-Na_{2/3}Ni_{1/3}Mn_{2/3}O₂ (NMO) by Solid-State Reaction Method

The P2-Na_{2/3}Ni_{1/3}Mn_{2/3}O₂ powders were synthesized by a simple solid-state reaction method. Typically, a stoichiometric mixture of Na₂CO₃ (99%, Sigma-Aldrich), NiO (99%, Sigma-Aldrich), and Mn₂O₃ (99%, Sigma-Aldrich) was ball-milled for 5 h in ethanol. An excess amount of 5% Na₂CO₃ was added to compensate for the sodium loss at high temperature. The mixture was dried at 80°C for 10 h. The obtained powders were then pressed into pellets, afterward, the pellets were heated at 900°C for 12 h. The heated pellets were cooled to room temperature and then transferred to an argon-filled glovebox until use.



Figure 2.5 Ball-milling machine used for preparing P2-Na_{2/3}Ni_{1/3}Mn_{2/3}O₂ precursor

2.1.9 Atomic layer deposition coating of AlPO₄ on P2-Na_{2/3}Ni_{1/3}Mn_{2/3}O₂ Cathode

AlPO₄ was deposited on the P2-Na_{2/3}Ni_{1/3}Mn_{2/3}O₂ powders at 250°C in a Savannah 100 ALD system (Ultratech/Cambridge Nanotech, USA) using trimethylaluminum (TMA, (CH₃)₃Al, 98% STREM Chemicals), trimethyl phosphate (TMPO, (CH₃)₃PO₄, 97% STREM Chemicals), and distilled water (H₂O) as precursors. AlPO₄ was deposited in an exposure model by the sequence of TMA pulse (0.5 s) - exposure (1s) - purge (10 s) - H₂O pulse (1s) - exposure (1s) - purge (15 s) - TMPO pulse (2s) - exposure (1s) - purge (10 s) - H₂O pulse (1s) - exposure (1s) - purge (10s). Nitrogen gas (99.999 %) was used as a carrier gas at a flow rate of 20 sccm. AlPO₄ layers were

directly deposited on the $\text{P2-Na}_{2/3}\text{Ni}_{1/3}\text{Mn}_{2/3}\text{O}_2$ powders by repeating the above ALD cycles. In this work, 2, 5, 10, and 20 ALD cycles were selected to control the coating thickness, each of the sample was denoted as NMO-nAP, where n means the ALD cycle number and AP means AlPO_4 .



Figure 2.6 Savannah 100 ALD system (Cambridge Nanotech, USA)

2.2 Characterization Techniques

2.2.1 Physical Characterization methods

A variety of techniques including SEM, EDX, XRD, RAMAN, TEM, FTIR, and XAS are used to characterize the morphologies, composition, crystal structures, functional groups, and chemical environment of the materials studied. This section will give a brief review of these techniques.

The morphology of the materials was checked by using SEM (Hitachi S-4800). The SEM was operated at 5 kV under high vacuum condition to observe the morphologies of the samples. The SEM was coupled with an EXD which could provide information about elemental distribution and compositions within the samples.



Figure 2.7 High-Resolution Field-Emission SEM (Hitachi 4800)

X-ray diffraction (XRD) is a useful tool for studying the crystal structure of the materials. XRD measurements were conducted using a Bruker D8 Advance (Cu $K\alpha$ source, 40 kV, 40 mA) spectrometer. The digital photo of XRD device is shown in Figure 2.8.



Figure 2.8 X-ray Diffraction System (Bruker D8 Advance)

Raman spectroscopy is a spectroscopic technique used to identify molecules and study the vibration of chemical bonds through detecting the inelastic scattering of incident monochromatic light. The laser light interacts with molecular vibrations, resulting in the energy shift and gives information about the vibration models in the system. The Raman spectra were collected on a HORIBA Scientific LabRAM Raman spectrometer equipped with a 532.03 nm laser as shown in Figure 2.9.

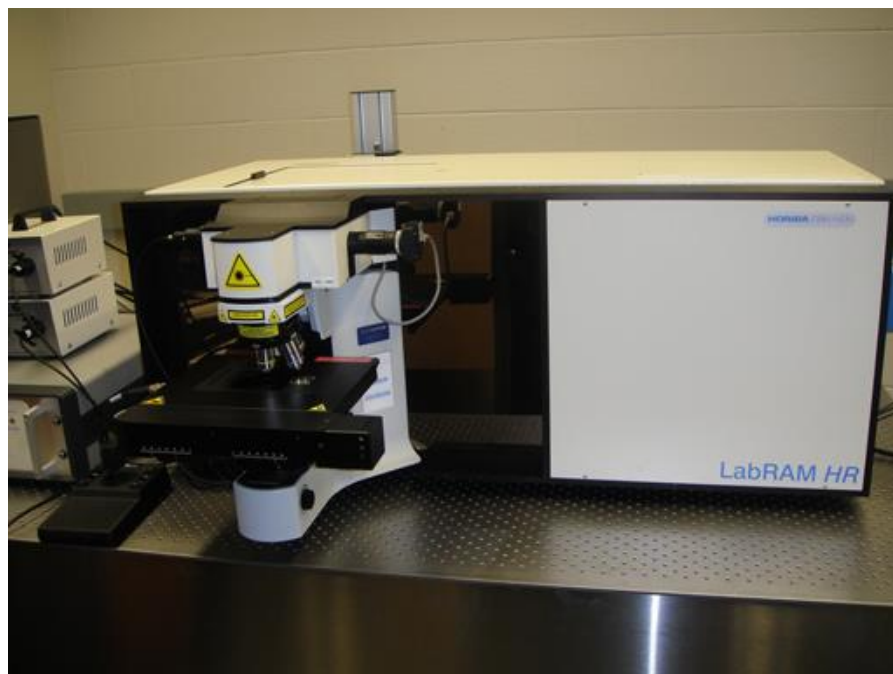


Figure 2.9 Raman Spectroscopy System (HORIBA Scientific LabRAM HR)

TEM is an important technique for studying the detailed morphology of the materials. Compared to SEM, TEM is capable of imaging at a much higher resolution, which could gain several nanometers- and even atomic-resolution information. TEM measurements were carried out on an instrument of FEI Quanta FRG 200F operated at 200 kV.



Figure 2.10 High-Resolution Field-Emission TEM (FEI Quanta FRG 200F)

Fourier-transform infrared spectroscopy (FTIR) is a technique used to obtain the infrared absorption or emission of a sample. FTIR spectra were collected by a Nicolet 6700 FTIR spectrometer.



Figure 2.11 Nicolet 6700 FTIR spectrometer

X-ray absorption spectroscopy is a synchrotron radiation technique, which is used to study the chemical states and local structure of materials through the absorption of X-ray by atoms, where the core-level electrons are ejected and core-holes are left. The absorption energy is determined by the electronic structures of atoms in the samples studied, therefore it can provide detailed information on the chemical states and local structures of materials. Figure 2.11 presents the beamlines at the Canadian Light Source.

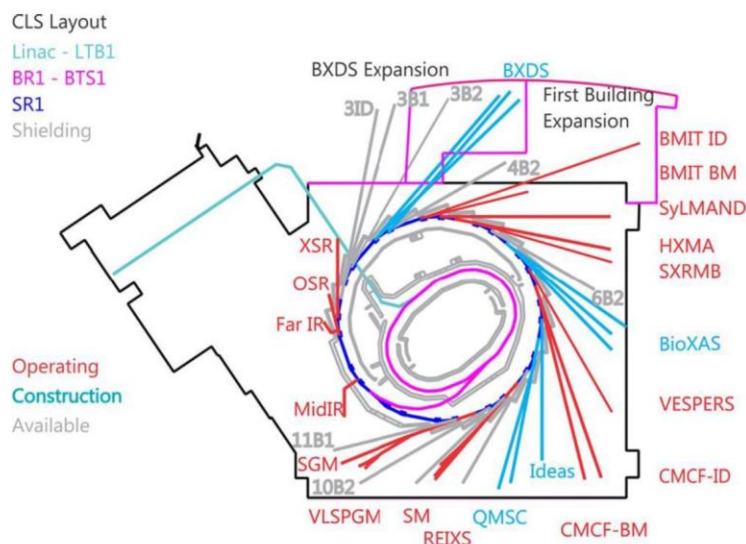


Figure 2.12 Schematic of beamlines at Canadian Light Source

2.2.2 Electrochemical measurements

The electrochemical performances of all the electrodes were measured using CR2032 coin cells. The 3D-printed electrodes (3D-printed LFP, 3D-printed Si, 3D-printed Na@rGO/CNT, and 3D-printed NNCFM) are directly used as the electrodes in various batteries systems without any post-treatment. For the AlPO_4 coated P2-NMO sodium cathode electrode, the electrodes were prepared by mixing active material, acetylene black (AB) and poly (vinylidene fluoride) (PVDF) in a ratio of 80:10:10 in N-methyl-pyrrolidone (NMP). The slurry was then pasted on Al foils and dried at 80°C under vacuum for overnight. The electrolytes used in this thesis are determined by the batteries system and materials studied. For 3D-printed self-supported LFP cathodes: the liquid electrolyte was 1M LiPF_6 dissolved in a mixture of ethylene carbonate (EC), dimethyl carbonate

(DMC), and diethyl carbonate (DEC) with a volume ratio of 1:1:1, and a polyethylene Celgard 2400 was used as the separator. For 3D-printed micro-patterned Si anodes: 1M LiPF₆ dissolved in a mixture of ethylene carbonate (EC) and diethyl carbonate (DEC) (1:1) with 10% FEC as additive was used as the electrolyte, and a polyethylene Celgard 2400 was used as the separator. For 3D-printed thin solid electrolyte LAGP, the printed thin film was directly used as electrolyte and separator without using liquid electrolyte and separator membrane. For 3D-printed Na@rGO/CNT electrodes, the electrolyte used was 1 M sodium hexafluorophosphate (NaFP₆ 98%, Aldrich) dissolved in diglyme (Sigma Aldrich) without any additives. For P2-NMO sodium cathode: 0.5 M sodium hexafluorophosphate (NaFP₆ 98%, Aldrich) dissolved into propylene carbonate (PC, 2% FEC) was used as the electrolyte. Glass fiber (GF) was used as the separator. All the coin cells are assembled in a highly pure Argon-filled glove box with the O₂ and H₂O level less than 0.1 ppm. Figure 2.13 is a digital photo of the Argon-filled glove box. The electrochemical performances of all the coin cells were tested on a LAND test system (Figure 2.14).



Figure 2.13 Argon-filled glove box for coin-cell assembly



Figure 2.14 Digital photo of the LAND battery testing system

Cyclic voltammetry (CV) is an important and widely used electroanalytical technique for studying the electrochemical behaviors of Li/Na batteries. CV is a type of potentiodynamic electrochemical measurement. In a CV experiment, the working electrode's potential is ramped in the opposite direction to return to the initial potential. The current at the working electrode is plotted vs. the applied voltage to give the cyclic voltammogram trace. For Li/Na batteries, the CV curves can reflect potentials where lithium/sodium insertion/desertion or the redox reactions take place. Figure 2.15 shows the optical photo of the Bio-Logic multichannel potentiostat 3/Z (VMP3) for CV measurements.

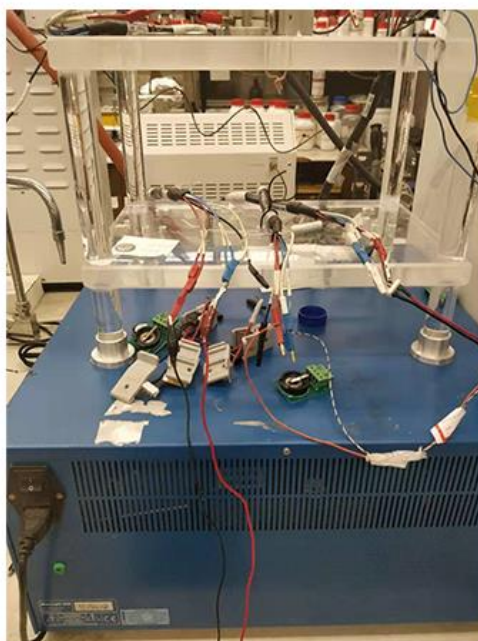


Figure 2.15 Photo of the Bio-Logic multichannel potentiostat 3/Z (VMP3)

Chapter 3

3 Toward High Areal Energy and Power Density Electrode for Li-Ion Batteries via Optimized 3D Printing Approach

High-energy and power density lithium-ion batteries are promising energy storage systems for future portable electronics and electric vehicles. Here, three-dimensional (3D) patterned electrodes are created through the paste extrusion-based 3D printing technique realizing a trade-off between high-energy density and power density. The 3D electrodes possess several distinct merits over traditional flat thick electrodes, such as higher surface area, shorter ion transport path, and improved mechanical strength. Benefiting from these advantages, the 3D-printed thick electrodes present the higher specific capacity and improved cycling stability compared with those of the conventional thick electrodes. Comparing to the previous studies on 3D-printed electrodes, this study investigates the influence and optimization of 3D printed LiFePO_4 (LFP) electrodes with three different geometric shapes to achieve a high rate performance and long-term cycling stability. Accordingly, a series of 3D electrodes with different thickness were created and an ultrathick ($1500\ \mu\text{m}$) 3D-patterned electrode exhibits a high areal capacity of around $7.5\ \text{mA h cm}^{-2}$, presenting remarkable value for state-of-the-art LFP cathodes. This work demonstrates patternable 3D printing as a potential strategy to fabricate thick electrodes toward high areal energy density and power density, which holds great promise for the future development of high-performance energy storage devices.

3.1 Introduction

The advance of portable electronics and electric vehicles has stimulated the development of energy storage devices with increasingly higher energy density and power density during the past decades.¹⁻⁴ To meet the growing demands for advanced energy storage systems, tremendous efforts have been devoted to developing new electrode materials with high capacity.⁵⁻⁷ The design of electrode architectures for achieving higher energy density and power density storage devices is a particular point of focus. Regarding this respect, it is important to have the capability to optimize the electrode architecture design as it greatly affects the transport of ions and electrons, as well as the kinetic reaction.⁸⁻¹² One promising strategy is to create thicker electrodes with higher areal mass loading to meet the high energy density requirement.¹³ Unfortunately, the traditional blade-casted thick electrode limits the transport of ions and electrons across the thick electrode, resulting in poor power density and incomplete utilization of active materials.^{8, 14} Moreover, the active material detaches from the current collector with cycling, leading to a shorter cycle life. Three-dimensional (3D) batteries have been proposed to be a promising alternative approach to achieve a trade-off between high energy density and power density.¹⁵ Batteries with 3D architectures can possess higher energy density by increasing the electrode height to provide more active materials, while the ion diffusion length could be maintained at a constant value, suggesting that the energy density can be improved without sacrificing power density.

3D printing, also known as advanced additive manufacturing (AM), has recently attracted much attention in the energy storage field due to its capability to enable the construction of complex 3D architectures accurately and efficiently.¹⁶⁻²⁰ Importantly, 3D printing techniques can control electrode thickness by simply adjusting the printing layer count, changing the printing nozzle, and modifying the printing speed and pressures.²¹⁻²³ For instance, Lewis and co-workers fabricated the first 3D-printed interdigitated Li-ion micro-battery architectures using a paste-extrusion type printing technique, where the printable cathode and anode inks were composed of LiFePO_4 (LFP) and $\text{Li}_4\text{Ti}_5\text{O}_{12}$ (LTO) nanoparticles dispersed in a highly concentrated slurry.²⁴ Later on, Hu and coworkers successfully fabricated an interdigitated Li-ion micro-battery via a 3D printing technique based on graphene oxide (GO) composite inks consisting of highly concentrated GO suspensions with the cathode (LFP) and anode (LTO) active materials added.²⁵ The printed full cell displayed a relatively stable discharge capacity of 91 mA h g^{-1} , corresponding to a high areal

capacity of $1.64 \text{ mA h cm}^{-2}$ based on the high electrode mass loading of around 18 mg cm^{-2} . More recently, the 3D printed hierarchical porous framework containing graphene/ $\text{Na}_3\text{V}_2(\text{PO}_4)_3$ composite as Na-ion battery cathode was reported and displayed a high specific capacity as well as better cycling stability up to 900 cycles.²⁶ Despite the progress being made on 3D printing for batteries, there has yet been a study that investigates the electrode micro-pattern effects on the electrochemical performance through the 3D printing technique. Meanwhile, great challenges still lie in the pursuit to develop low-cost, facile, and scalable printing processes/inks for practical application in future advanced energy storage systems.

Herein, for the first time, we report the design of various 3D-patterned thick LFP electrodes that achieved high areal energy density performance through an optimized extrusion-based 3D printing approach. The printing ink in this work is quite similar to the general electrode slurry composition used for lithium-ion battery, which consists of LFP nanoparticles active material, acetylene black (AB), and multiwalled carbon nanotubes (MWCNTs) dispersed in a highly concentrated slurry composed of poly (vinylidene fluoride-co-hexafluoropropylene) (PVDF-HFP) dissolved in *n*-methyl-2-pyrrolidone (NMP). The 3D-printed micro-structured electrodes showed several distinct advantages over the conventional slurry-coated thick electrode: 1) The well-designed macro-pores in 3D-patterned architectures could increase the surface area of the electrode and facilitate the penetration of electrolyte into the active materials; 2) The continuous filaments composed of interconnected porous polymer framework and conducting MWCNTs networks with controllable inter-distance are able to accelerate the electron and ion transport. Moreover, the 3D-patterned thick electrode is composed of the filament with a shorter lithium ion diffusion length (less than $150 \text{ }\mu\text{m}$) than that of the conventional slurry coating thick electrode; 3) The mechanical strength of the 3D-printed structures could help mitigate the challenge of deformation in conventional thick electrodes, thus improving the cycling stability of LIBs under high loading. As a result, three types of 3D-printed patterned thick electrodes have been developed; each of them presents a higher specific capacity and improved cycling stability compared with those of the conventional flat thick electrode. Furthermore, we fabricated a series of 3D electrodes with different printing layers and an ultrathick ($1500 \text{ }\mu\text{m}$) 8-layers 3D-patterned electrode with an areal mass loading of around 50 mg cm^{-2} , exhibiting the high areal capacity of around 7.5 mA h cm^{-2} and presenting a desirable value for LFP cathode in practical high energy density LIBs application.

3.2 Experiment Section

3.2.1 Preparation of LFP ink

Commercialized LFP nanoparticles were used as active materials. Highly concentrated LFP ink was prepared by first mixing 1400 mg of LFP nanoparticles, 200 mg of acetylene black (AB), and 100 mg multi-wall carbon nanotubes (MWCNTs, diameter of 40~60 nm, length of 2 μm) and grinding them well for a few minutes. Then 300 mg PVDF-HFP powder ($M_w \sim 400000$, Sigma-Aldrich) was dissolved in 1200 mg 1-methyl-2-pyrrolidinone (NMP, Sigma-Aldrich), which was added into the mixed powder as a binder. Afterward, the obtained concentrated LFP gel was further mixed in a conditioning mixer (ARM 310, Thinky) at 2000 rpm for 25 min. Finally, a homogenized LFP paste was obtained for the 3D printing process.

3.2.2 3D printing process

The as-prepared LFP ink was used to fabricate 3D structured electrodes by using a fused filament fabrication (FFF) DeltaMaker 3D printer modified with a paste extrusion-type tool head. In detail, the as-prepared LFP ink was first loaded into a 3cc syringe. The syringe was subsequently subject to centrifugation at 3000 rpm for 3 min to expel out all air-bubbles in the ink. A metal nozzle with an inner diameter of 200 μm was adopted and a Nordson EFD computer-controlled pneumatic fluid dispenser was used to control the printing extrusion pressures between 30 psi to 50 psi. The printing speed ranges from 6 mm s^{-1} to 10 mm s^{-1} . After printing, the 3D structures were first immersed into a water coagulation bath for few minutes to remove the solvent, followed by freeze-drying for 24 h.

3.2.3 Materials characterizations

The morphologies of all the samples were observed by using a Hitachi S-4800 field-emission scanning electron microscope (SEM). X-ray diffraction (XRD) measurements were conducted using a Bruker D8 Advance (Cu-K α source, 40 kV, 40 mA) spectrometer.

3.2.4 Electrochemical measurements

The electrochemical performance of the 3D-printed LFP electrodes was tested in 2032-coin cells. All cells were assembled in an Ar-filled glovebox with Li foil as counter and reference electrodes.

The liquid electrolyte was 1M LiPF_6 dissolved in a mixture of ethylene carbonate (EC), dimethyl carbonate (DMC), and diethyl carbonate (DEC) with a volume ratio of 1:1:1. The galvanostatic charge-discharge performance was evaluated with a LAND test system in a voltage range of 2.5-4.2 V (vs. Li/Li^+) at room temperature.

3.3 Results and Discussion

3.3.1 Morphology and Structural Characterization

Figure 1a is a schematic illustration of the fabrication process of 3D printing self-supported LFP electrodes. The printable LFP composite ink (**Figure S1a**) was prepared by first adding LFP nanoparticles, AB and MWCNTs into PVDF-HFP/NMP to form the slurry. The high-concentration mixture was then mixed homogeneously by a Thinky mixer prior to the printing process. Subsequently, the obtained LFP ink was loaded into a syringe as shown in **Figure S1b** and then extruded through a metal nozzle with an inner diameter of 200 μm onto a glass slide substrate. The process was controlled by a pre-designed program. The 3D printed object together with the glass slice substrate was then subjected to a water bath for solvent exchange. After soaking in the water bath for few minutes, the printed structure was smoothly peeled off from the glass substrate and a free-standing electrode with a smooth surface and improved mechanical strength was obtained after freeze-drying for 24h. **Figure 1b** shows various 3D-printed complex shapes and structures designed by a 3D-software, demonstrating that 3D printing technique has great ability and potential in fabricating batteries with complex shapes and configurations.

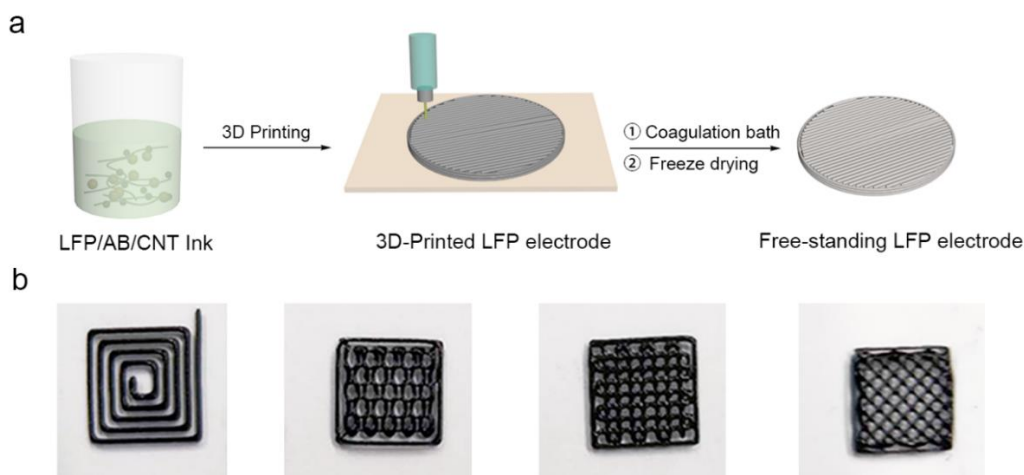


Figure 3.1 a) Schematic illustration of 3D-printed self-supported LFP electrodes, and b) Optical images of 3D-printed LFP structure with various patterns.

Since 3D printing can construct various shapes and structures, three typical circle-shaped patterns were selected for printing LFP electrodes to explore the best electrochemical performance in coin-cell LIBs as shown in **Figure S2**. The microstructures and morphologies of the three types of 3D-printed LFP electrodes were first investigated by scanning electron microscopy (SEM) as shown in **Figure 2**. **Figure 2a, 2e, and 2i** show the schematic of the circle-grid, circle-ring, and circle-line pattern LFP electrodes, respectively. The microstructure of the grid-like pattern is clearly visible in **Figure 2b**. The diameter of the filament is around 100 μm -150 μm , which is a little smaller than that of the metal nozzle used for the printing. The diameter decreasing results from the shrinkage of the polymer binder during the solvent removal step in the drying processes. It should be noted that the decreased diameter of the dried filament might reduce the ion transport length, thereby improving the rate performance of the electrodes. The interval between the two filaments, which could be controlled by the printing procedure, is controlled to be around 500 μm . The well-designed interval space was able to facilitate the diffusion of electrolyte to the active materials. The surface of the filament is very smooth and each filament shows a very dense structure, ensuring a high material loading density. The magnified SEM images in **Figure 2c and 2d** show that the LFP nanoparticles and AB nanoparticles are uniformly wrapped by the PVDF-HFP binder, and the CNTs are interconnected between the LFP and AB nanoparticles, thus forming an interconnected porous framework and continuous conducting network. **Figure 2f and 2j** show the microstructure with a ring-like pattern and line-like pattern, respectively. The diameters of the filaments in these two patterns are similar to that of the grid pattern. The magnified SEM images in **Figure 2h and 2i** also reveal that these two patterned electrodes are constructed by the layered filaments consisting of the active material wrapped by a porous polymer framework and conducting carbon network, thereby facilitating the ion/electron transport.

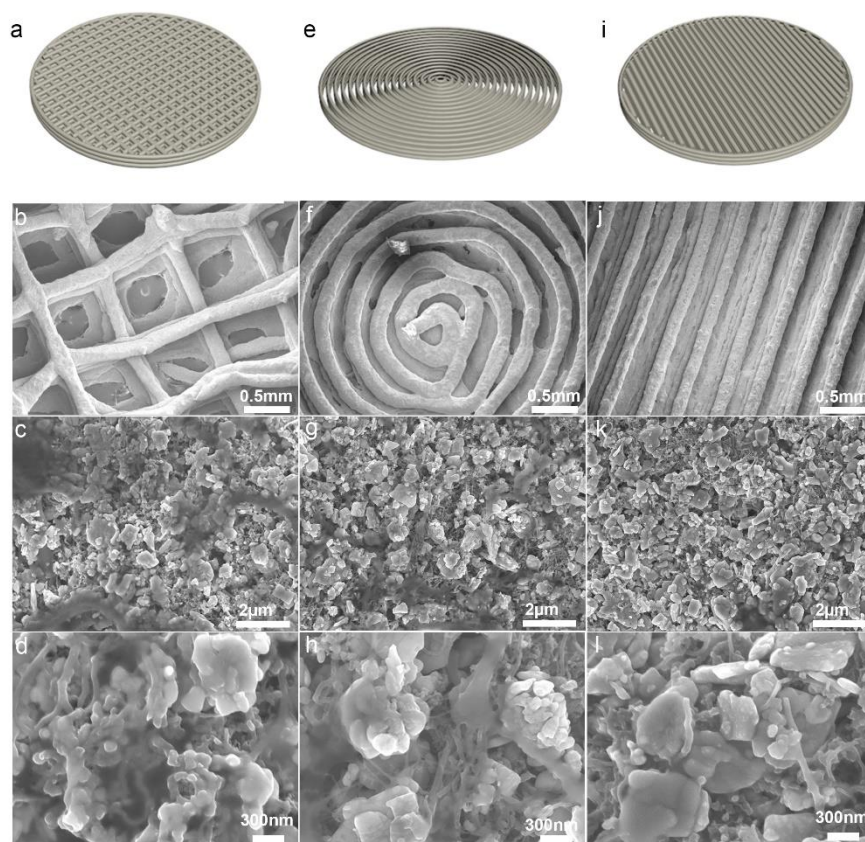


Figure 3.2 Schematic and SEM images of three types of 3D-printed LFP electrodes. a) Schematic illustration and b, c, and d) SEM images of 3D-printed circle-grid pattern LFP electrode. e) Schematic illustration and f, g, and h) SEM images of 3D-printed circle-ring pattern LFP electrode. i) Schematic illustration and j, k, and l) SEM images of 3D-printed circle-line pattern LFP electrode.

To further examine the uniform distribution of LFP nanoparticles into the printed architectures, SEM-EDS elemental mapping was carried out as shown in **Figure S3**. The elemental mapping images suggest a homogeneous distribution of C, F, Fe, P, and O in the whole structure. **Figure S4** shows the EDS spectra and corresponding elemental percentage table of the 3D-printed LFP electrode. The atomic ratio of Fe: P: O in the printed electrode is around 0.94:1:4.3, which is very close to the theoretical atomic ratio of Fe: P: O (1:1:4). To verify the phase stability of the LFP during the ink preparation and freeze-drying process, X-ray diffraction (XRD) measurement was conducted to compare the phase of pristine LFP nanoparticles and that of the 3D-printed LFP electrodes. As presented in **Figure S5**, the LFP powders and 3D-printed LFP electrodes exhibit

the same diffraction peaks, indicating that the ink preparation and post-drying process did not alter the crystal phase of the LFP, which is critical for maintaining desired electrochemical performance.

3.3.2 Electrochemical Characterization

The electrochemical performances of the three types of 3D-printed LFP electrodes were evaluated in coin-cells. All three LFP electrodes have an areal mass loading of around 10 mg cm^{-2} . The rate capabilities of the 3D-printed three types of LFP electrodes were first examined at different rates from 0.1 C to 4.0 C within the voltage window of 2.5-4.2V. As shown in **Figure 3a**, each of the three types of LFP electrodes exhibits the high specific capacity of around 150 mA h g^{-1} at a low current density of 0.1C at the initial cycle, close to the theoretical specific capacity of LFP (170 mA h g^{-1}). It is interesting that the three types of LFP electrodes present similar specific capacities when cycling at lower C-rates such as 0.1 C, 0.5 C, and 1 C, however, the specific capacities show obvious differences at higher C-rates of 2.0 C and 4.0 C among the three patterned LFP electrodes. When the current density changed back to 0.1 C, all of the three patterned LFP electrodes exhibit a specific capacity of around 150 mA h g^{-1} , indicating a good reversibility of the 3D-printed LFP electrode. The rate performance comparison among the three patterned LFP electrodes indicates that the micro-structures of the electrodes have a distinct effect on the battery performance. **Figure 3b, 3c, and 3d** show the charge/discharge curves of the three patterned electrodes at various current densities, revealing a clear pattern on the electrochemical behavior of the cells. The comparison of overpotential at various current densities for the three types of patterned electrodes is presented in **Figure S6**. It should be noted that the line-patterned electrode exhibits much lower overpotential at various cycling rates due to its well-designed micro-structure, facilitating the ion and electron transport, particularly at high current densities.

The cycling stability of the 3D-printed patterned LFP electrodes was further examined at the current density of 1 C with the first six cycles activated at 0.1 C. As shown in **Figure 3e**, the initial discharge capacities of the grid, ring, and line patterned electrodes are 149.3, 145.8, and 144.6 mA h g^{-1} , with the initial Coulombic efficiency of 98.88%, 98.98%, and 98.14%, respectively. Each of the three patterned LFP electrodes displayed the discharge capacity of around 132 mA h g^{-1} after a few cycles at the lower current density of 0.1 C. Moreover, the line-patterned electrode presents an excellent cyclability over 150 cycles without any capacity fading. By contrast, the grid-

patterned and ring-patterned electrodes deliver a discharge capacity of 102.4 and 105 mA h g⁻¹, demonstrating the capacity retention of 77.4% and 79.1%, respectively. This result suggests that the line-pattern microstructure possesses more advantages over the other two patterned microstructures, which is in accordance with the results from the rate performance comparison. For demonstrating the advantages of 3D-printed electrodes in achieving high-performance batteries, conventional slurry-coated thick electrodes were fabricated to compare with 3D patterned electrodes. As observed in **Figure S7a**, the electrode with an areal mass loading of around 10 mg cm⁻² was prepared by using the slurry with the same composition with the printing ink. Some cracks were observed on the electrode. When the thickness of the conventional electrode was further increased, as demonstrated in **Figure S7b**, severe electrode cracking and detachment from the Al current collector was observed. This phenomenon is common in thick electrodes fabricated by a typical slurry coating process, can be attributed to the weak adhesion between the electrode components and metal current collectors and the shrinkage of the electrode materials during the drying process, which causes a failure to maintain the electrode structural integrity.^{11, 27-28} The ease of deformation of the conventional thick electrode leads to the shorter cycle life and poor safety. As shown in **Figure S7c**, the conventional thick electrode with an areal mass loading of around 10 mg cm⁻² exhibits an initial discharge capacity of approximately 124 mA h g⁻¹ with a dramatic capacity fade occurring with a capacity retention of 51.8% after 115 cycles. This comparison clearly indicates that all the 3D-printed patterned electrodes show an improved specific capacity and cycling stability compared to the performance of the conventional thick electrode. The enhanced electrochemical performance of 3D-printed electrodes can be ascribed to the micro-scaled and nano-scaled multi-channeled architecture, which allows for fast lithium ion diffusion and efficient electrolyte penetration. In addition, the superior mechanical structure stability of the 3D-printed patterned electrodes is also a factor that contributes to the enhanced cycling stability.

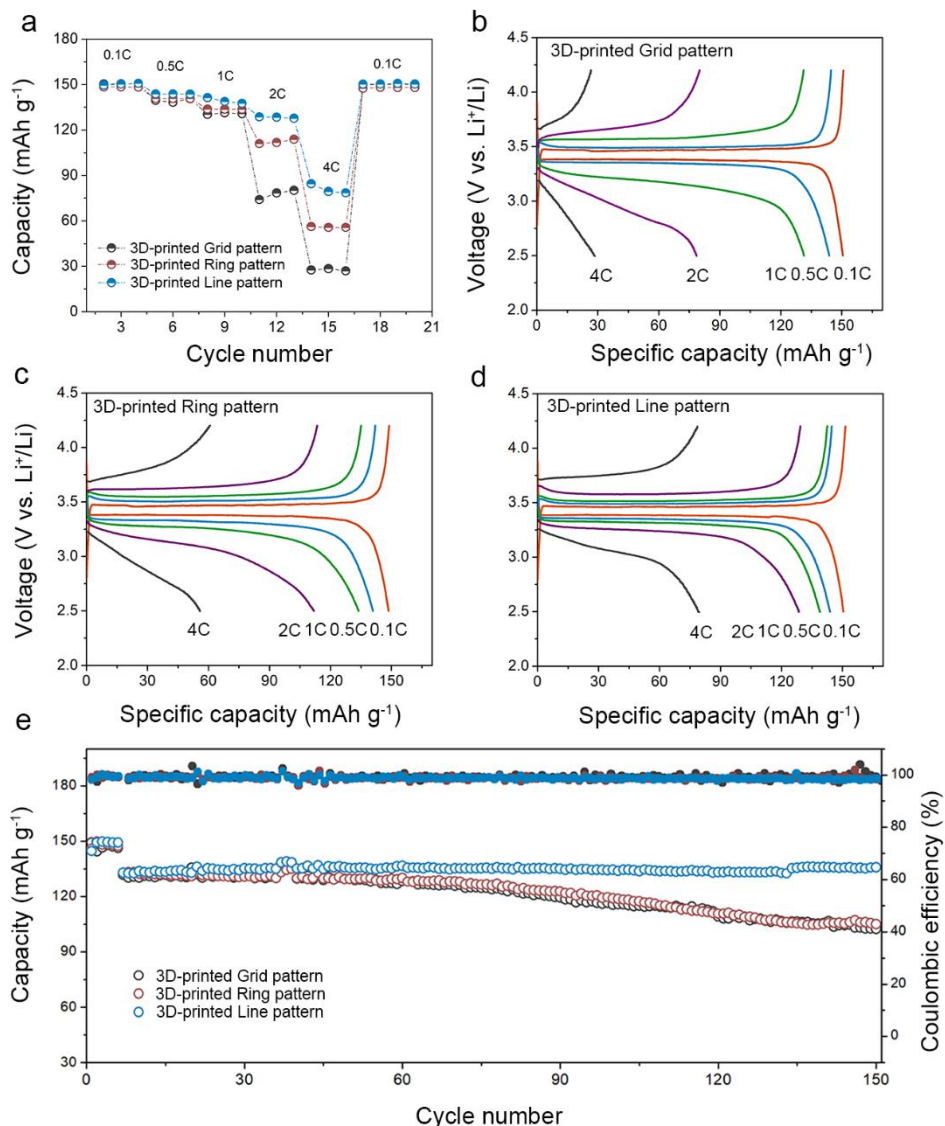


Figure 3.3 Electrochemical performance of the three types of 3D-printed LFP electrodes. a) Comparison of rate performance of the three types of LFP electrodes. Charge-discharge voltage curves of b) 3D-printed grid pattern, c) 3D-printed ring pattern and d) 3D-printed line pattern LFP electrodes at various rates. e) Cycling performance of the three types of LFP electrodes at 1C with the first six cycles activated at 0.1 C.

To further consider the superiorities of the 3D printing technique in building high-performance thick electrodes for LIBs, a series of line-pattern LFP electrodes with different thickness were fabricated by the 3D printing method. **Figure S8** shows four 3D-patterned electrodes with different printing layers (2 layers, 4 layers, 6 layers, and 8 layers) on the same glass slice substrate before

dried. After coagulation in a water bath followed by freeze-drying, free-standing electrodes with increased mechanical strength were obtained and the pre-designed patterned structures were successfully reproduced (inset in **Figure 4a**). Figure 4a presents the comparison of the practical and theoretical thickness of the printed electrodes as a function of printing layer number. The theoretical thickness of one layer is set to be 0.2 mm. It should be noted that the practical value of the electrodes thickness is a little bit smaller than the theoretical value due to above-mentioned shrinking. As shown in **Figure S9**, the thickness of 8 layers of electrode is 1.5 mm, and the printed electrode thickness demonstrates an approximately linear relationship with the printing layer number, which can be ascribed to the uniform features of each printing filament layer. This result also discloses that the bottom filament layer is mechanically strong enough to maintain the structure during the entire layer-by-layer printing process.

The electrochemical performance comparison of the 3D-printed electrodes with different printing layers is displayed in **Figure 4b**. It clearly shows that electrodes with 2 layers, 4 layers, 6 layers, and 8 layers exhibit the high stable areal capacity of around 2.07, 4.3, 6.0, and 7.5 mA h cm⁻², respectively. All these areal capacity values, especially 7.5 mA h cm⁻², demonstrate the practical application for LFP cathodes in LIBs. Moreover, it should be mentioned that the areal capacity values of different layered electrodes reveal an almost linear relationship with the layer number except for the 8-layered electrode. This phenomenon further confirms that the 3D structure is beneficial for ion transportation even within an ultrathick electrode. **Figure 4c** shows the charge/discharge profiles of the 3D-printed LFP electrodes with different layers, all presenting typical charge/discharge plateaus at around 3.5 V. The plotted curve in **Figure 4d** clearly displays the comparison of this work with previously reported data in the literature, in terms of areal energy and power densities.^{11, 13, 22, 24, 29-34} As highlighted with a red star, the 3D-printed 8 layered line-patterned electrode could present the high areal energy density of 69.41 J cm⁻² at the power density of 2.99 mW cm⁻², thereby demonstrating great potential for practical high energy density LIBs application. The superior performance can be ascribed to well-designed 3D architecture that possesses short transport length which facilitates ion and electron diffusion during the cycling process, as well as accommodating substantial amounts of active materials which realizes high areal capacity.

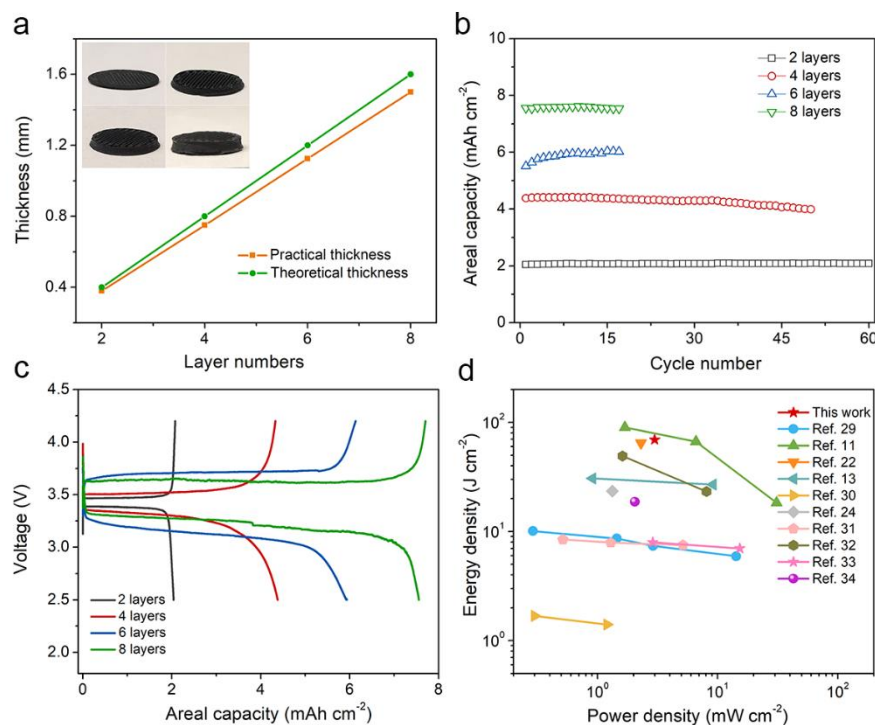


Figure 3.4 a) Practical and theoretical thickness of the 3D-printed electrodes as a function of the printing layer number (inset: optical images of 3D-printed electrodes with different printing layers). b) Comparison of the areal capacity of the LFP electrodes with different layer numbers. c) Charge/discharge profiles of the LFP electrodes with different layer numbers. d) Comparison of power density and energy density of this work with previously reported values.

3D electrodes with well-designed architectures via 3D printing technique has been proven to show many advantages over conventional slurry-coated flat electrodes in terms of delivering enhanced areal energy density, better power density, and cycling stability. As illustrated in **Figure 5**, although high power density can be achieved with a short ion transport distance, conventional thin electrodes can only deliver the low energy density as it lacks active materials. When a thick electrode is constructed by the conventional slurry coating method, the high energy density could be realized, however, the power density would be greatly restricted as the ion transport distance increases substantially. To this end, 3D electrodes can realize a trade-off between the high energy density and power density by maintaining a short and uniform ion diffusion path, ensuring that the

thick electrode can achieve high power density. Compared to previous 3D-printed LFP, this work demonstrates greatly improved power and energy density due to the optimized 3D printing process as well as the geometric considerations. This work also demonstrates that 3D-printed electrodes can realize the highest level of areal loading comparing to other advanced 3D electrode manufacturing methods.

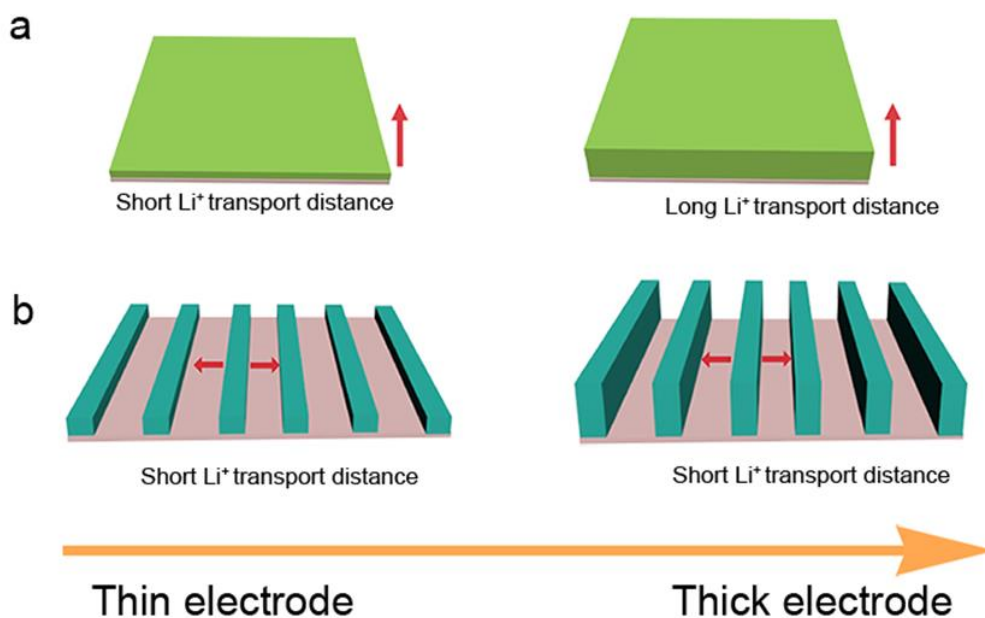


Figure 3.5 Schematic illustration of the comparison between ultra-thick a) traditional electrodes and b) 3D electrodes.

3.4 Conclusion

3D patterned self-supported thick electrodes for high areal energy and power density LIBs were realized by an optimized extrusion-type 3D printing technique. The resulting unique 3D structured electrodes were constructed by continuous layer-by-layer filaments composed of interconnected porous polymer frameworks and continuous conducting carbon networks, thereby greatly improving ion and electron transport. The well-designed 3D micro-structures were demonstrated to increase the surface area and maintain a short ion transport distance even within a thick electrode, facilitating the electrolyte penetration into the active materials as well as ion/electron diffusion. Due to these structural merits, the 3D-patterned electrodes exhibited superior electrochemical performance over conventional thick flat electrodes in terms of specific capacity and cycling stability. Moreover, an ultrathick electrode of 1500 μm 3D electrodes with 8 printed layers was

fabricated and presented a high areal capacity of approximately 7.5 mA h cm^{-2} and energy density of 69.41 J cm^{-2} at a power density of 2.99 mW cm^{-2} , demonstrating comparable values with reported high-performance LFP cathodes fabricated by both 3D printing and other methods in literature. This work thus provides a facile, low cost, and easily scaled way to fabricate high areal loading/thick electrode to achieve high areal energy density with high power density, which holds great promise for future practical application of high energy density lithium-ion batteries.

Acknowledgements

The work was supported by Natural Science Foundation of China (NSFC) (Grant U1432249), the National Key R&D Program of China (Grant 2017YFA0205002), and the Priority Academic Program Development (PAPD) of Jiangsu Higher Education Institutions. This is also a project supported by Jiangsu Key Laboratory for Carbon-Based Functional Materials and Devices and the Collaborative Innovation Center of Suzhou Nano Science & Technology. This work was also supported by the Natural Science and Engineering Research Council of Canada (NSERC), the Canada Research Chair Program (CRC), the Canada Foundation for Innovation (CFI), and the University of Western Ontario (UWO).

3.5 References

1. Lu, L.; Han, X.; Li, J.; Hua, J.; Ouyang, M., A Review On The Key Issues For Lithium-Ion Battery Management In Electric Vehicles. *J. Power Sources* **2013**, *226*, 272-288.
2. Nitta, N.; Wu, F.; Lee, J. T.; Yushin, G., Li-Ion Battery Materials: Present and Future. *Mater. Today* **2015**, *18*, 252-264.
3. Tarascon, J. M.; Armand, M., Issues and Challenges Facing Rechargeable Lithium Batteries. *Nature* **2001**, *414*, 359-367.
4. Wang, J.; Sun, X., Olivine LiFePO_4 : The Remaining Challenges for Future Energy Storage. *Energy Environ. Sci.* **2015**, *8*, 1110-1138.

5. Gao, X.; Wang, J.; Zhang, D.; Nie, K.; Ma, Y.; Zhong, J.; Sun, X., Hollow NiFe₂O₄ Nanospheres on Carbon Nanorods as A Highly Efficient Anode Material for Lithium-Ion Batteries. *J. Mater. Chem. A* **2017**, *5*, 5007-5012.
6. Li, X.; Gu, M.; Hu, S.; Kennard, R.; Yan, P.; Chen, X.; Wang, C.; Sailor, M. J.; Zhang, J.-G.; Liu, J., Mesoporous Silicon Sponge as An Anti-Pulverization Structure for High-Performance Lithium-Ion Battery Anodes. *Nat. Commun.* **2014**, *5*, 4105-4112.
7. Gao, X.; Wang, J.; Zhang, D.; Adair, K.; Feng, K.; Sun, N.; Zheng, H.; Shao, H.; Zhong, J.; Ma, Y.; Sun, X.; Sun, X., Carbon Coated Bimetallic Sulfide Nanodots/Carbon Nanorod Heterostructure Enabling Long-Life Lithium-Ion Batteries. *J. Mater. Chem. A* **2017**, *5*, 25625-25631.
8. Gallagher, K. G.; Trask, S. E.; Bauer, C.; Woehrlle, T.; Lux, S. F.; Tschech, M.; Lamp, P.; Polzin, B. J.; Ha, S.; Long, B.; Wu, Q.; Lu, W.; Dees, D. W.; Jansen, A. N., Optimizing Areal Capacities Through Understanding the Limitations of Lithium-Ion Electrodes. *J. Electrochem. Soc.* **2015**, *163*, A138-A149.
9. Song, J.; Sen, X.; Linjun, W.; Zhenzhen, D.; Lina, C.; Jiafeng, C.; Xianghua, K.; Ming, G.; Junling, L.; Yanwu, Z.; Hengxing, J.; S., R. R., Covalently Connected Carbon Nanostructures for Current Collectors in Both the Cathode and Anode of Li-S Batteries. *Adv. Mater.* **2016**, *28*, 9094-9102.
10. Park, J.; Li, J.; Lu, W.; Sastry, A. M., Geometric Consideration of Nanostructures for Energy Storage Systems. *J. Appl. Phys.* **2016**, *119*, 025101.
11. Chen, C.; Zhang, Y.; Li, Y.; Kuang, Y.; Song, J.; Luo, W.; Wang, Y.; Yao, Y.; Pastel, G.; Xie, J.; Hu, L., Highly Conductive, Lightweight, Low-Tortuosity Carbon Frameworks as Ultrathick 3D Current Collectors. *Adv. Energy Mater.* *7*, 1700595.

12. Lawes, S.; Sun, Q.; Lushington, A.; Xiao, B.; Liu, Y.; Sun, X., Inkjet-Printed Silicon as High Performance Anodes for Li-Ion Batteries. *Nano Energy* **2017**, *36*, 313-321.
13. Zheng, H.; Li, J.; Song, X.; Liu, G.; Battaglia, V. S., A Comprehensive Understanding of Electrode Thickness Effects on The Electrochemical Performances of Li-Ion Battery Cathodes. *Electrochim. Acta* **2012**, *71*, 258-265.
14. Jiang, F.; Peng, P., Elucidating the Performance Limitations of Lithium-ion Batteries Due to Species and Charge Transport through Five Characteristic Parameters. *Sci. Rep.* **2016**, *6*, 32639-32657.
15. Long, J. W.; Dunn, B.; Rolison, D. R.; White, H. S., Three-Dimensional Battery Architectures. *Chem. Rev.* **2004**, *104*, 4463-4492.
16. Chen, L.; Tang, X.; Xie, P.; Xu, J.; Chen, Z.; Cai, Z.; He, P.; Zhou, H.; Zhang, D.; Fan, T., 3D Printing of Artificial Leaf With Tunable Hierarchical Porosity for CO₂ Photoreduction. *Chem. Mater.* **2018**, *30*, 799-806.
17. Teng-Sing, W.; Yeop, A. B.; Julia, G.; A., L. J., 3D Printing of Customized Li-Ion Batteries with Thick Electrodes. *Adv. Mater.* **2018**, *30*, 1703027.
18. Hu, J.; Jiang, Y.; Cui, S.; Duan, Y.; Liu, T.; Guo, H.; Lin, L.; Lin, Y.; Zheng, J.; Amine, K.; Pan, F., 3D-Printed Cathodes of LiMn_{1-x}Fe_xPO₄ Nanocrystals Achieve Both Ultrahigh Rate and High Capacity for Advanced Lithium-Ion Battery. *Adv. Energy Mater.* **2016**, *6*, 1600856.
19. Jiang, Y.; Xu, Z.; Huang, T.; Liu, Y.; Guo, F.; Xi, J.; Gao, W.; Gao, C., Direct 3D Printing of Ultralight Graphene Oxide Aerogel Microlattices. *Adv. Funct. Mater.* **2018**, *28*, 1707024.
20. Lawes, S.; Riese, A.; Sun, Q.; Cheng, N.; Sun, X., Printing Nanostructured Carbon for Energy Storage and Conversion Applications. *Carbon* **2015**, *92*, 150-176.

21. Collin, L.; Ju-Hee, S.; John, M.; D., D. M., 3D Printing of Free Standing Liquid Metal Microstructures. *Adv. Mater.* **2013**, *25*, 5081-5085.
22. Li, J.; Leu, M. C.; Panat, R.; Park, J., A Hybrid Three-Dimensionally Structured Electrode for Lithium-Ion Batteries via 3D Printing. *Mater. Design* **2017**, *119*, 417-424.
23. Choi, K.-H.; Ahn, D. B.; Lee, S.-Y., Current Status and Challenges in Printed Batteries: Toward Form Factor-Free, Monolithic Integrated Power Sources. *ACS Energy Lett.* **2017**, *3*, 220-236.
24. Sun, K.; Wei, T. S.; Ahn, B. Y.; Seo, J. Y.; Dillon, S. J.; Lewis, J. A., 3D printing of Interdigitated Li-Ion Microbattery Architectures. *Adv. Mater.* **2013**, *25*, 4539-4543.
25. Fu, K.; Wang, Y.; Yan, C.; Yao, Y.; Chen, Y.; Dai, J.; Lacey, S.; Wang, Y.; Wan, J.; Li, T.; Wang, Z.; Xu, Y.; Hu, L., Graphene Oxide-Based Electrode Inks for 3D-Printed Lithium-Ion Batteries. *Adv. Mater.* **2016**, *28*, 2587-2594.
26. Ding, J.; Shen, K.; Du, Z.; Li, B.; Yang, S., 3D-Printed Hierarchical Porous Frameworks for Sodium Storage. *ACS Appl. Mater. Interfaces* **2017**, *9*, 41871-41877.
27. Sung-Ju, C.; Keun-Ho, C.; Jong-Tae, Y.; Jeong-Hun, K.; Yong-Hyeok, L.; Sang-Jin, C.; Sang-Bum, P.; Don-Ha, C.; Qinglin, W.; Sun-Young, L.; Sang-Young, L., Hetero-Nanonet Rechargeable Paper Batteries: Toward Ultrahigh Energy Density and Origami Foldability. *Adv. Funct. Mater.* **2015**, *25*, 6029-6040.
28. Evanoff, K.; Khan, J.; Balandin, A. A.; Magasinski, A.; Ready, W. J.; Fuller, T. F.; Yushin, G., Towards Ultrathick Battery Electrodes: Aligned Carbon Nanotube-Enabled Architecture. *Adv. Mater.* **2012**, *24*, 533-537.

29. Liu, C.; Cheng, X.; Li, B.; Chen, Z.; Mi, S.; Lao, C., Fabrication and Characterization of 3D-Printed Highly-Porous 3D LiFePO₄ Electrodes by Low Temperature Direct Writing Process. *Materials* **2017**, *10*, 934-947.
30. Shaijumon, M. M.; Perre, E.; Daffos, B.; Taberna, P. L.; Tarascon, J. M.; Simon, P., Nanoarchitected 3D Cathodes for Li-Ion Microbatteries. *Adv. Mater.* **2010**, *22*, 4978-4981.
31. Kohlmeyer, R. R.; Blake, A. J.; Hardin, J. O.; Carmona, E. A.; Carpena-Núñez, J.; Maruyama, B.; Daniel Berrigan, J.; Huang, H.; Durstock, M. F., Composite Batteries: A Simple yet Universal Approach to 3D Printable Lithium-Ion Battery Electrodes. *J. Mater. Chem. A* **2016**, *4*, 16856-16864.
32. Li, J.; Liang, X.; Liou, F.; Park, J., Macro-/Micro-Controlled 3D Lithium-Ion Batteries via Additive Manufacturing and Electric Field Processing. *Sci. Rep.* **2018**, *8*, 1846-1857.
33. Gao, L.; Jin, Y.; Liu, X.; Xu, M.; Lai, X.; Shui, J., A Rationally Assembled Graphene Nanoribbon/Graphene Framework for High Volumetric Energy and Power Density Li-Ion Batteries. *Nanoscale* **2018**, *10*, 7676-7684.
34. Hur, J. I.; Smith, L. C.; Dunn, B., High Areal Energy Density 3D Lithium-Ion Microbatteries. *Joule* **2018**, *2*, 1187-1201.

Supporting Information

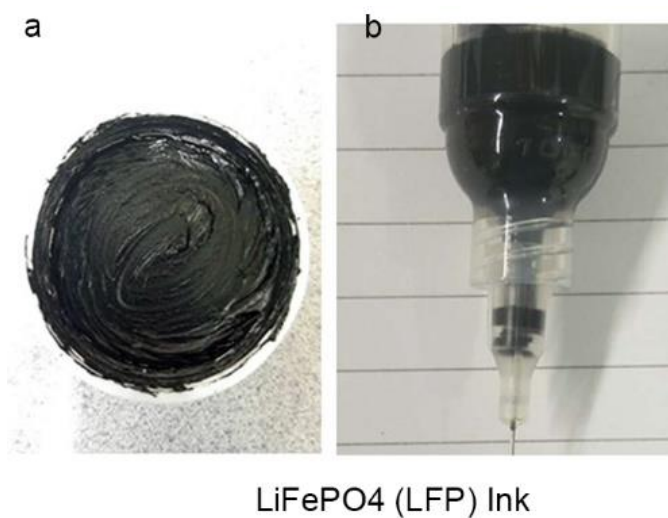


Figure S 3.1 a) The as-prepared LFP ink, b) The LFP ink loaded into a 3cc syringe

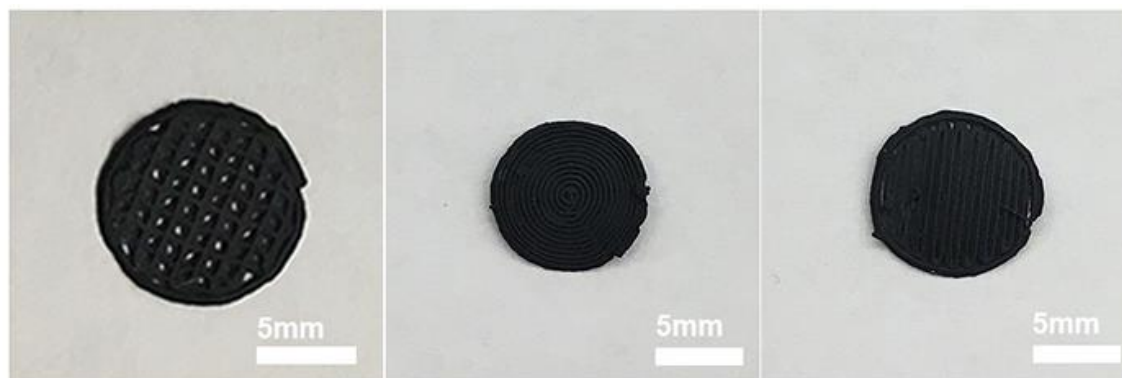


Figure S3.2 The optical images of the 3D-Printed three patterns of LFP electrodes

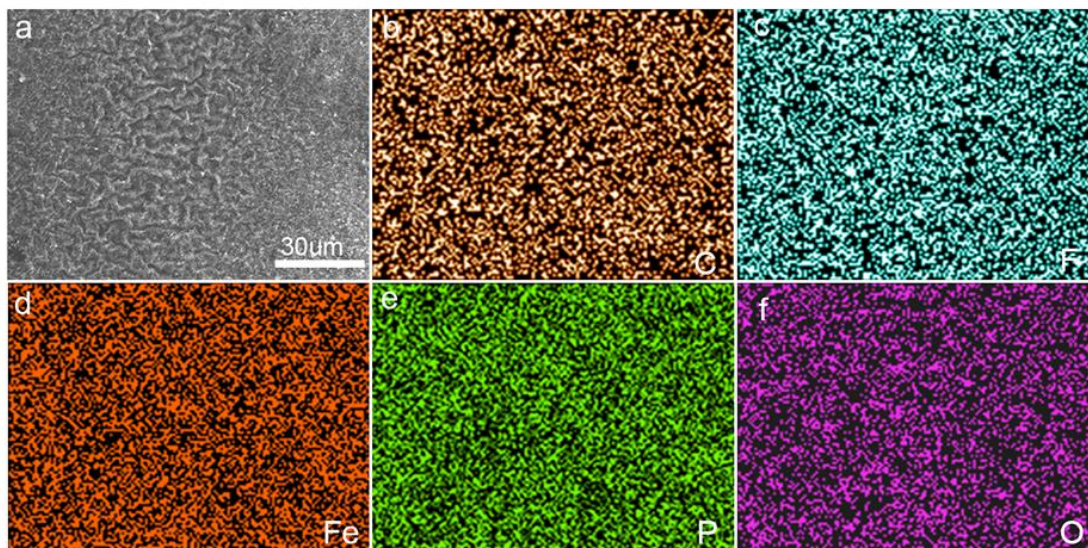


Figure S3.3 (a) SEM image and (b-f) corresponding C, F, Fe, P, and O element mapping images of the 3D-printed LFP electrode

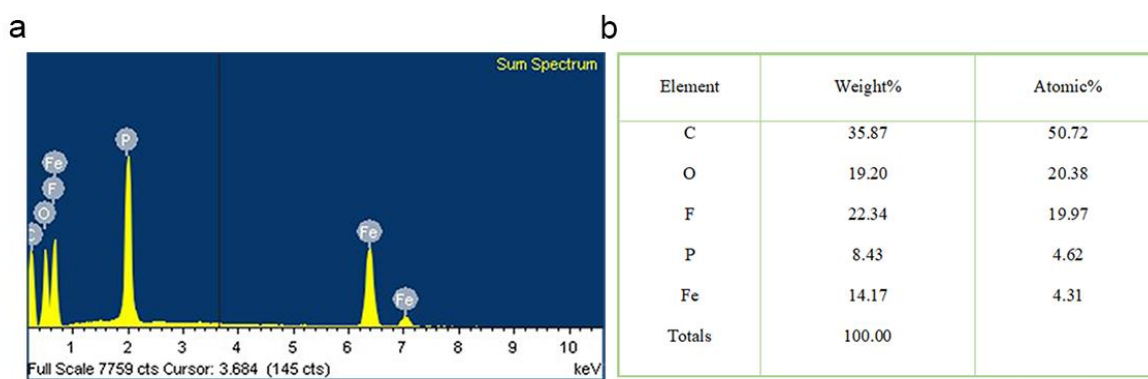


Figure S3.4 a) EDS spectra of the 3D-printed LFP electrode and its corresponding b) EDS elemental percentage table

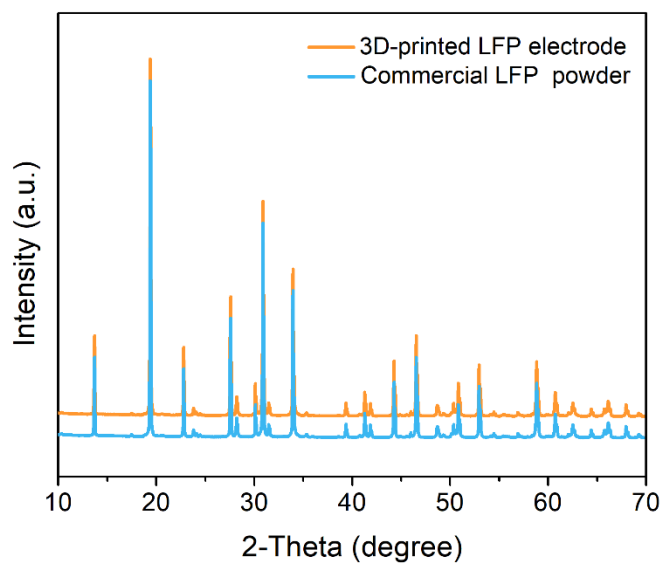


Figure S3.5 XRD patterns of commercial LFP nanoparticles and 3D-printed LFP electrode

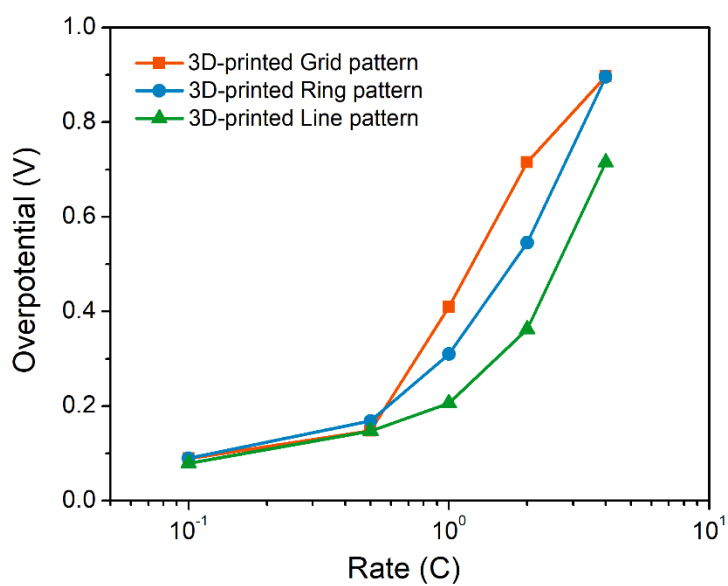


Figure S3.6 Overpotential-rate plots for the three types of 3D-printed patterned electrodes

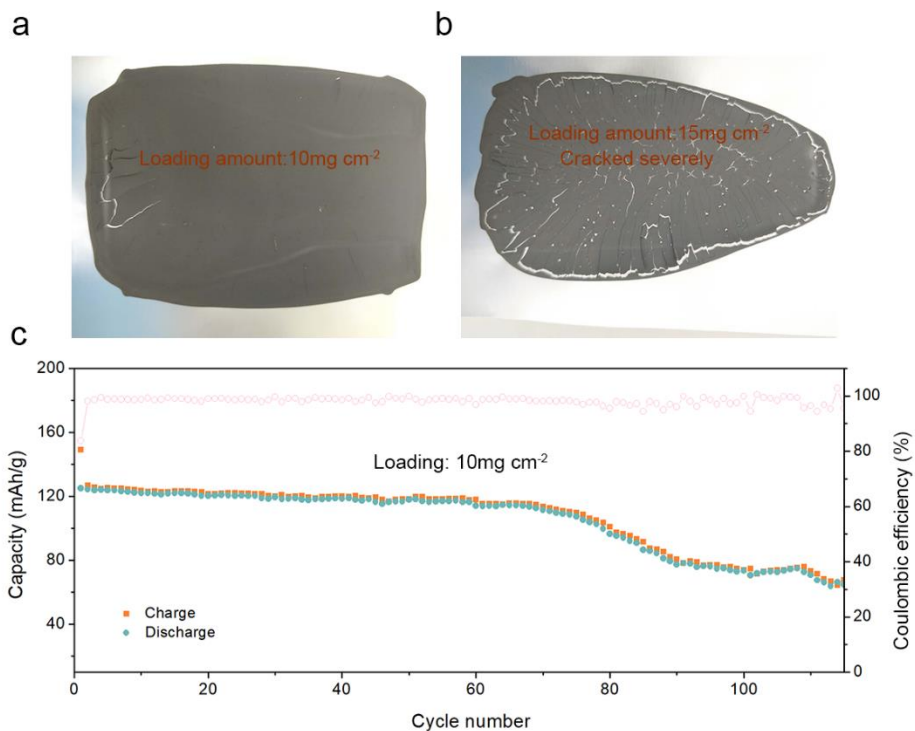


Figure S3.7 a) LFP electrode with a loading amount of around 10 mg cm^{-2} , b) LFP electrode with a loading amount of around 15 mg cm^{-2} prepared by a traditional blade-casting method, and c) LFP cycling performance at a current of 1C rate

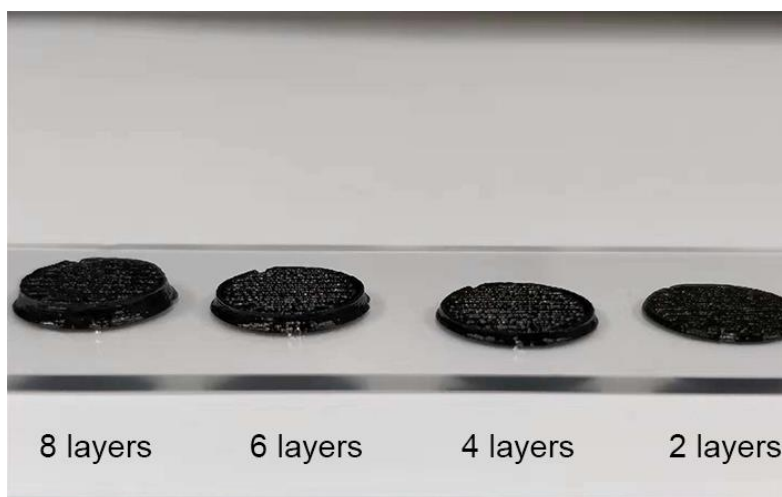


Figure S3.8 3D-printed LFP electrodes with different layers on a glass-slice substrate before dried



Figure S3.9 Measurement of the thickness of 8-layers patterned electrode

Chapter 4

4 3D Printing of Vertically Aligned and Patternable Silicon Anodes for High Areal Capacity Li-Ion Batteries

Silicon has been regarded as one of the most promising anode materials because of its high specific capacity. However, the main challenges associated with Si anodes: namely the huge volume expansion of Si and poor electrical conductivity, can result in a short battery cycle life. Moreover, the fatal disadvantage caused by large volume change is exacerbated under high Si mass loading. Herein for the first time, we developed a facile 3D printing approach to rapidly construct patternable and hierarchically porous Si architecture. The 3D-printed Si electrodes designed possess vertically aligned mass/ionic transport pathways and macro/micro-scaled porosities, which can facilitate electron/ion transport within the entire electrodes and effectively mitigates the huge volume expansion expected during cycling. As a result, these electrodes exhibited a reversible high areal capacity of around 3 mAh cm^{-2} (corresponding to a specific capacity of 1450 mAh g^{-1}). Moreover, even under a high mass loading of 3.81 mg cm^{-2} , the electrodes display an extremely high initial areal capacity of $10.31 \text{ mAh cm}^{-2}$ (corresponding to a specific capacity of $2706.04 \text{ mAh g}^{-1}$). This work thus opens a new and promising avenue for constructing novel 3D architectures for advanced energy systems.

4.1 Introduction

Nowadays, lithium-ion batteries (LIBs) with high energy densities are highly desired for powering consumer electronics and electric vehicles.¹⁻³ Silicon (Si) anodes have thus attracted tremendous interest in the past decades due to their high specific capacity (around 4200 mAh g⁻¹), low cost, and relatively low discharge potential ($\approx 0.4\text{V}$ versus Li⁺/Li). Despite possessing these distinguishing features, Si anodes have several intrinsic obstacles, namely huge volume expansion (nearly 400%) during the cycling process and poor electrical conductivity, which cause fast capacity fading, thereby greatly restricting their practical application.⁴⁻⁵

Hitherto, numerous efforts have been made to address the aforementioned challenges, which can be classified into three main categories: 1) design of various nanostructured and porous silicon to alleviate the large volume change such as Si nanowire,⁶⁻⁷ Si nanotubes,⁸ mesoporous Si,⁹ and hollow particles.¹⁰ 2) Development of varied carbon-based composites (graphene-Si, CNT-Si, carbon nanosheets-Si) to enhance the overall electrical conductivity.¹¹⁻¹² 3) Design of multi-functional binders to enhance structural integrity.¹³⁻¹⁴ However, these strategies are either too complex and expensive or can hardly realize a desirable areal capacity. It is critical to develop a facile and low-cost approach in order to realize stable and high areal capacity Si anodes that can meet the requirements for practical application.

Recently 3D printing, as an advanced additive manufacturing (AM) technique, has gained large scale attention for its capabilities in the fabrication of complex 3D structures and geometric shapes from various materials - and has been widely used in a wide range of areas, including biomedical fields¹⁵⁻¹⁶ as well as the fabrication of electronics¹⁷⁻¹⁸, catalysis¹⁹⁻²¹, and energy storage and conversion devices²²⁻²³. For instance, Hu and co-workers²⁴ constructed a 3D holey graphene oxide (hGO) mesh with multiple levels of porosity (macroscale to nanoscale) through an extrusion-based printing technique. The printed 3D hGO electrode exhibited superior Li-O₂ battery performance due to the designed hierarchical porous architectures. More recently, Fan and co-workers²⁵ employed 3D-printing in constructing a leaf-inspired architected graphene/Ni_{0.33}Co_{0.66}S₂ aerogel where the resultant structures allowed rapid electron/ion transport, thus leading to superior electrochemical performance. These previous works demonstrate that 3D printing shows a

promising role in the manufacture of novel 3D architectures, which could provide new avenues for solving the major challenges associated with Si anodes.

Herein, for the first time, we construct a 3D vertically aligned structure with multi-scaled porosities (denoted as 3D-VLMP) for silicon anodes using extrusion-based direct-ink-writing (DIW) 3D printing techniques, assisted with a freeze-drying post-treatment. The designed structure has multiple strengths: (1) the hierarchically porous 3D architecture enables electrode structural integrity, (2) the multiple levels of porosity (macro to micro) provides free space to accommodate the huge volume expansion of Si during repeated cycles and facilitates the access of electrolyte into the active materials, (3) the vertical walls constructing the micropores allows continuous and fast electron/ion transport pathways, (4) the interwoven filaments consisting of CNTs act as a high-performance electrical network. Thus, the 3D-VLMP Si electrode is able to exhibit a high areal capacity of around 3 mAh cm^{-2} (corresponding to a specific capacity of 1450 mAh g^{-1}) after 60 cycles. Moreover, even under a high mass loading of 3.81 mg cm^{-2} , the electrode can display an extremely high initial areal capacity of $10.31 \text{ mAh cm}^{-2}$ (corresponding to a specific capacity of $2706.04 \text{ mAh g}^{-1}$). This work thus opens a new and promising avenue for constructing novel 3D architectures for advanced energy systems.

4.2 Experimental Section

4.2.1 Si-SA Ink Preparation

Si-SA ink was prepared by mixing 350 mg of Si nanoparticles, 140 mg of multi-wall carbon nanotubes (MWCNTs, the diameter of 40-60 nm, length of 2 μm), and 70 mg of acetylene black (AB) and then grinding them well by hand for a few minutes. Sodium alginate (SA) solution (2.8 g, 5 wt%) was then added to the mixed powders as an aqueous binder. After that, the composites were further mixed in a conditioning mixer (ARM, Thinky) at 2000 rpm for 40 minutes to obtain a homogenous and viscous ink. Finally, the obtained Si-SA ink was loaded into a 3cc syringe for printing.

4.2.2 3D Printing Process

The 3D printing process was conducted on a fused filament fabrication (FFF) DeltaMaker 3D printer modified with a paste extrusion-type tool head. The syringe with Si-SA ink was subject to centrifugation at 3000 rpm for 3 minutes to expel out the air-bubbles prior to the printing process. A Nordson EFD computer-controlled pneumatic fluid dispenser provides the appropriate pressure to extrude the ink through a metal nozzle with an inner diameter of 200 μm and control the flow rate. The printing speed ranges from 6 mm s^{-1} to 10 mm s^{-1} depending on the printing pressure and ink viscosity. The 3D structures were printed directly on the Cu foil. The printed 3D Si electrodes were post-treated in two ways: one was directly dried in air. The other was freeze-dried for 24h to obtain the designed 3D architecture.

4.2.3 Materials characterizations

The morphologies of all the samples were observed by using a Hitachi S-4800 field-emission scanning electron microscope (SEM). Fourier-transform infrared spectroscopy (FTIR) spectra were collected by a Nicolet 6700 FTIR spectrometer. Raman spectra were collected on a HORIBA Scientific LabRAM Raman spectrometer equipped with a 532.03 nm laser.

4.2.4 Electrochemical Measurements

The electrochemical performance of the 3D-printed Si electrodes was tested in CR 2032-coin cells. All cells were assembled in an Ar-filled glovebox with Li foil as the counter and reference electrodes. The liquid electrolyte was 1M LiPF_6 dissolved in a mixture of ethylene carbonate (EC) and diethyl carbonate (DEC) (1:1, by volume) containing 10% fluoroethylene carbonate (FEC). The galvanostatic charge-discharge performance was evaluated with a LAND test system within a voltage range of 0.01-1.5 V (vs. Li/Li^+) at room temperature.

4.3 Results and Discussion

4.3.1 Morphology and Structure Characterization

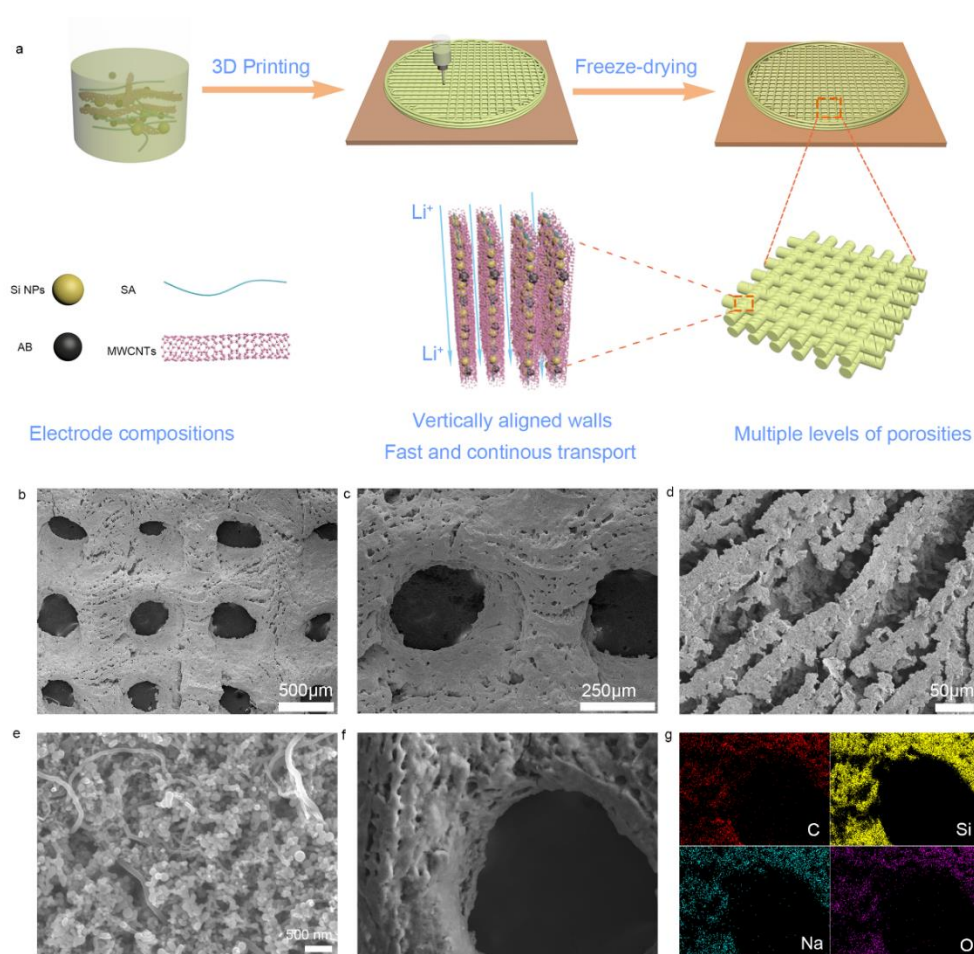


Figure 4.1. Fabrication process and material characterization of the 3D-VLMP Si electrode. (a) Schematic illustration of 3D printing of vertically aligned silicon electrodes with multiple levels of porosities. (b to e) SEM images of the 3D-VLMP Si electrodes under different magnifications; (f and g) SEM image and corresponding EDX mappings of the 3D-VLMP Si electrode.

The 3D patterned silicon electrodes with vertically aligned architecture and multiple levels of porosities were fabricated through a paste-extrusion type 3D printing method combined with a freeze-drying post-printing treatment as illustrated in **Figure 4.1a**. To obtain a printable ink for the DIW process, highly concentrated sodium alginate (SA) solution (5 wt %) was used as an aqueous binder to get a proper Si-SA ink with a suitable viscosity. The detailed ink preparation process can be found in the experimental section. The obtained homogeneous and highly viscous Si-SA ink was then transferred into a 3cc syringe for printing (**Figure S4.1**). The ink was then extruded through a metal nozzle onto the Cu foil controlled by a pre-designed program.

Subsequently, the as-printed Si electrode was freeze-dried for 24h to obtain the desired 3D microstructure.

The microstructures and morphologies of the as-printed vertically aligned Si electrodes were first investigated by scanning electron microscopy (SEM). **Figure 4.1b** is a top-down SEM image of the 3D-VLMP Si electrode taken directly after the printing and freeze-drying procedures. It is clear that the 3D architecture with well-defined and interconnected macropores was well maintained. The 3D architecture was constructed from continuous and interwoven filaments with a diameter of around 150-200 μm . 3D architecture can enable excellent structural integrity without cracking. In contrast, as shown in **Figure S4.2**, the conventional slurry-coated 2D flat Si electrodes demonstrated severe cracking due to the huge amounts of stresses generated during the drying process. **Figure 4.1c** is an enlarged SEM image where it can be seen that the size of a macropore is around 150 μm (from 3D design) and numerous micropores (tens of micrometers) were generated from the freeze-drying process as observable on the filaments of the 3D architecture. More interestingly, the micropores are formed out of the vertical-wall structures consisting of 1D carbon nanotubes, 0D Si nanoparticles, and aqueous-based SA binder, as displayed in **Figure 4.1d**. **Figure 4.1e** shows the detailed morphology of the filaments. As observed from the magnified SEM image, CNTs are interconnected with Si and AB nanoparticles, forming nano-scaled pores and a continuous conducting network, which is beneficial for the electron/ion transport within the whole electrode. SEM elemental mapping was carried out to determine the distribution of Si nanoparticles in the printed architectures, as shown in **Figure 4.1f and 4.1g**. The elemental mapping images of the printed Si electrode display a uniform distribution of Si, C, Na, and O throughout the whole structure.

Raman spectroscopy measurement was further conducted to gain insight into the composition of the printed Si electrodes. As depicted in **Figure S4.3**, Raman spectroscopy shows four characteristic peaks, the sharp peak located at 505 cm^{-1} is attributed to the Si-Si vibrational stretching mode in crystalline Si. Another two peaks (demonstrated in the inset image, Figure S3) at around 1338 and 1597 cm^{-1} can be assigned to the D and G bands of CNT. The peak intensity ratio of the IG/ID is around 1.02, indicating the CNT has a crystalline structure.²⁶ **Figure S4.4** is the FTIR spectra of the printed Si electrodes, which shows typical bands of around 3440 and 1615

cm^{-1} attributed to the stretching of the $-\text{OH}$, and $-\text{COO}^-$, indicating the presence of sodium alginate binder.²⁷

4.3.2 Electrochemical Characterization

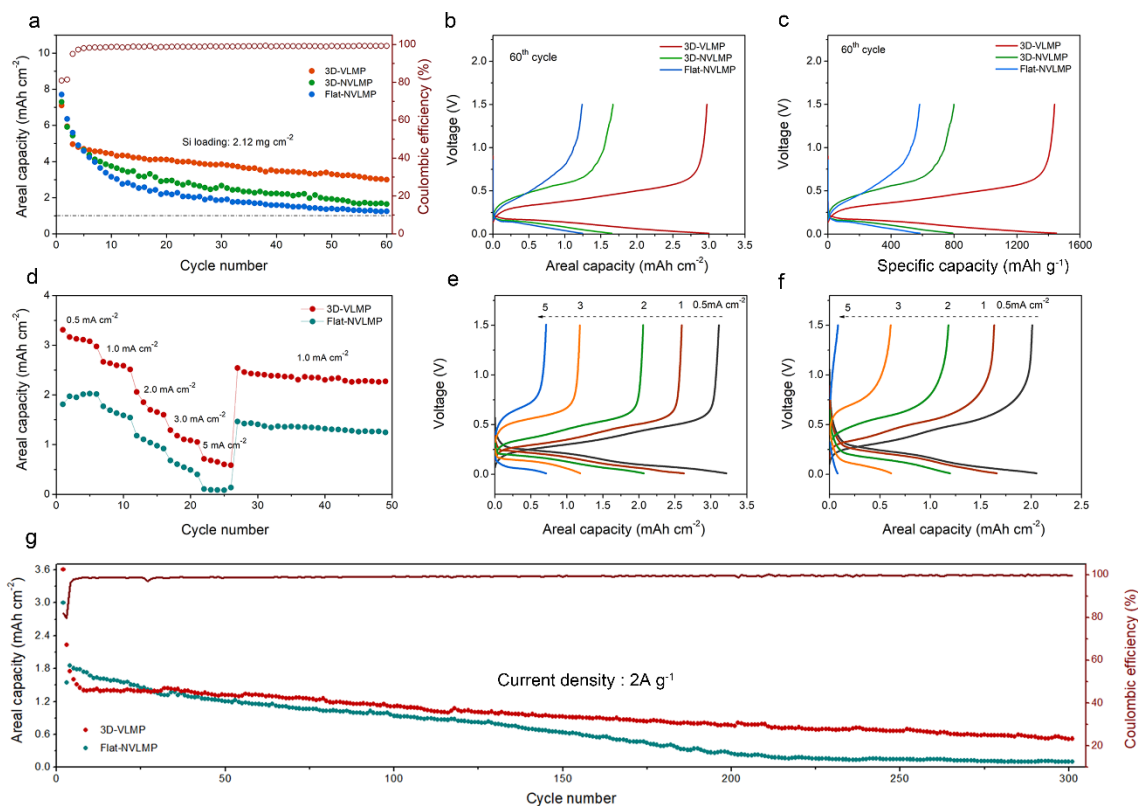


Figure 4.2. Electrochemical performances comparison of the Si electrodes with different structures. (a) Areal capacity vs. cycle number at a current of 1 Ag⁻¹ for 60 cycles; (b and c) Charge-discharge profiles of the various Si electrodes at their 60th cycle; (d) Rate capability of the 3D-VLMP and Flat-NVLMP Si electrodes at various current densities from 0.5 to 5 mA cm⁻²; (e and f) Charge-discharge profiles of the 3D-VLMP and Flat-NVLMP Si electrodes at various current densities from 0.5 to 5 mA cm⁻²; (g) The capacity retentions of the 3D-VLMP and Flat-NVLMP Si electrodes at a current density of 2 Ag⁻¹, along with the Coulombic efficiency of the 3D-VLMP Si electrode over 300 cycles.

The advantages of the uniquely designed structures in respect to battery performance were systematically evaluated by testing coin-cells with Li metal as the counter/reference electrode and

the 3D printed Si electrode as the working electrode. **Figure 4.2a and Figure S4.6** shows the cycling performance comparison of the Si electrodes among three different structures. All three Si electrodes were prepared under an areal mass loading of around 2.12 mg cm^{-2} to meet the performance level of commercial lithium-ion batteries (over 3 mAh cm^{-2}). In the first cycle, each Si electrode exhibited a high areal capacity of over 7 mAh cm^{-2} at a lower current density of 0.3 A g^{-1} . However, the capacity retention from the 2nd cycle to the 60th cycle was distinctly different among the three Si electrodes. As shown in **Figure 4.2c and 4.2c**, the 3D-VLMP Si electrode displayed the highest areal capacity of around 3.01 mAh cm^{-2} ($1467.2 \text{ mAh g}^{-1}$) after 60 cycles. In contrast, the 3D printed and non-vertically aligned Si electrode without micro-pore structures (denoted as 3D-NVLMP Si) delivered relatively lower areal capacity of 1.67 mAh cm^{-2} (814.4 mAh g^{-1}), whereas the conventional slurry-coated non-vertically aligned Si electrode without pores (Flat-NVLMP Si) only obtained an areal capacity of 1.24 mAh cm^{-2} (582.5 mAh g^{-1}) corresponding to a capacity retention of only 16.07% against the initial cycle. This comparison suggests that the 3D vertically aligned and macro/micro porous architecture can effectively help accommodate the severe volume change during the lithiation/delithiation process, leading to superior cycling stability. To further demonstrate the benefits of the designed 3D-VLMP structures, we compared the rate capabilities of the 3D-VLMP and Flat-NVLMP Si electrodes at various current densities from 0.5 to 5 mA cm^{-2} . As displayed in **Figure 4.2d and Figure S4.7**, the 3D-VLMP Si electrode exhibited superb rate capabilities compared to that of the Flat-NVLMP Si electrode as the current density was varied from 0.5 to 5 mA cm^{-2} . Even at a high current density of 5 mA cm^{-2} , the 3D-VLMP Si electrode was able to deliver an areal capacity of 0.68 mAh cm^{-2} (579.5 mAh g^{-1}) while the Flat-NVLMP Si only achieved an areal capacity of 0.09 mAh cm^{-2} (103 mAh g^{-1}). Moreover, when the current density changed back to 1 mA cm^{-2} , the 3D-VLMP Si exhibited an excellent specific capacity of around 2000 mAh g^{-1} (corresponding to 2.35 mAh cm^{-2}), whereas the specific capacity of the Flat-NVLMP Si is less than 1600 mAh g^{-1} . **Figure 4.2e and 4.2f** are the voltage profiles of the 3D-VLMP and Flat-NVLMP Si electrodes, respectively. It is clear that the 3D-VLMP Si obtained a smaller overpotential, especially at high current densities compared to that of the Flat-NVMP Si, indicating that the designed 3D-VLMP architecture could greatly help facilitate the Li^+ transport within the whole electrode. Furthermore, as shown in **Figure 4.2g**, the 3D-VLMP Si electrodes exhibited superior capacity retention at a high current density of 2 A g^{-1} after 300 cycles.

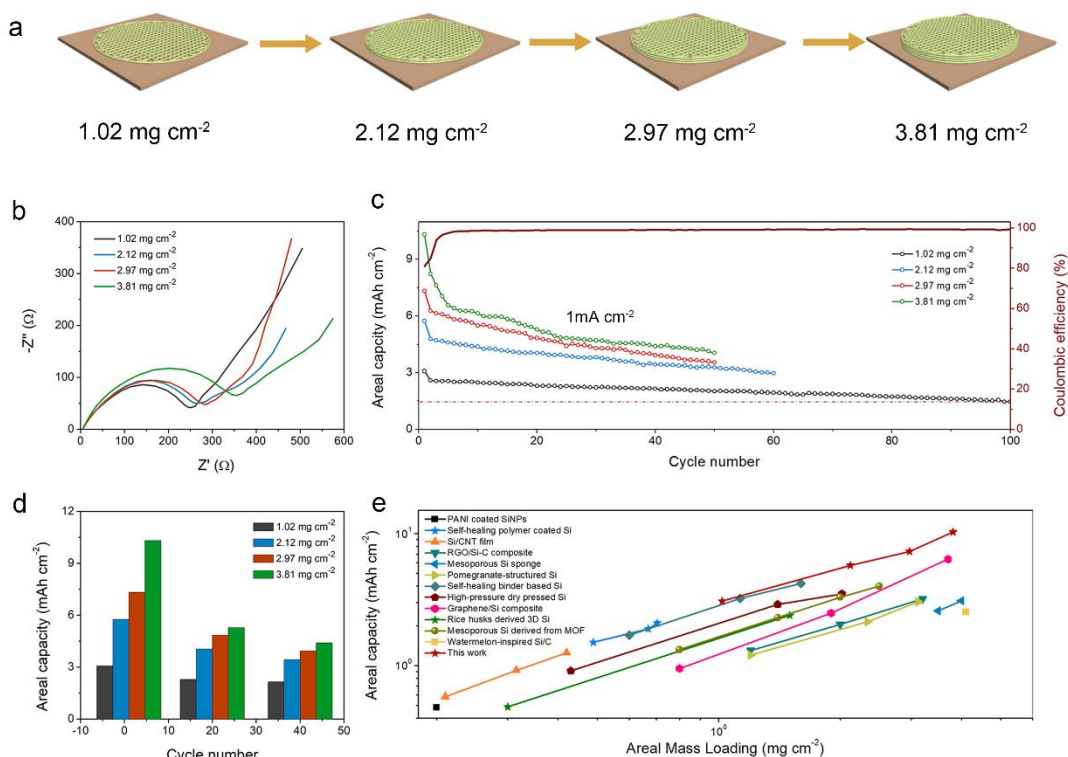


Figure 4.3. Performance metrics for 3D-VLMP Si electrodes with high areal mass loading. (a) Schematic illustration of the 3D-printed VLMP Si electrodes with different thickness and mass loadings; (b) Comparison of the electrochemical impedance of the 3D-VLMP Si electrodes with different mass loadings; (c). Various areal mass loading tests (up to 3.81 mg cm^{-2}) of the printed 3D-VLMP Si electrodes. All electrodes were cycled at 0.3 mA cm^{-2} for the initial cycle up to 1.0 mA cm^{-2} for the later cycles. (d). Areal capacity of the 3D-VLMP Si electrodes with different mass loading at the 1st, 20th, and 40th cycle, respectively; (e). Comparison of areal performance between the 3D VLMP Si electrodes with Si anodes as reported in other works, as noted.

High areal mass loading is crucial to achieving high-performance EES systems in practical application. However, many reported works only studied the low-Si mass loadings in order to achieve a long cycling life of their Si electrodes,²⁸⁻²⁹ hence, it can be deduced that there is a considerable challenge to realize a desirable performance under high areal mass loading. We therefore fabricated a series of 3D-VLMP Si electrodes with different areal mass loadings up to

3.81 mg cm⁻² via 3D printing as illustrated in **Figure 4.3a**. To demonstrate the benefits of the designed 3D vertical architecture for ion/electron transport kinetics, electrochemical impedance spectroscopy (EIS) measurements were conducted on the various 3D-VLMP Si electrodes as shown in **Figure 4.3b**. All the curves exhibited a semicircle path in the high-frequency range and a straight line in the low-frequency range. It is obvious that the charge transfer resistance showed negligible increase as the mass loading was increased from 1.02 mg cm⁻² to 3.81 mg cm⁻². This can be attributed to the 3D architecture which enabled fast electron/ion transport along the pathways, allowing for easy penetration of electrolyte into the active materials. **Figure 4.3c** shows the areal capacity of the 3D-VLMP Si electrodes under different areal mass loadings cycled at 0.3 mA cm⁻² for the initial cycle, and 1.0 mA cm⁻² for the later cycles. The 3D-VLMP Si electrodes show an almost linear increase of areal capacity from 3.07 mAh cm⁻² to 10.32 mAh cm⁻² with the areal mass loadings increasing from 1.02 mg cm⁻² to 3.87 mg cm⁻² (**Figure 4.3d and Figure S4.8**). Each of the four Si electrodes delivered a high initial specific capacity of around 3000 mAh g⁻¹, suggesting that the 3D vertically aligned and multi-scaled porous structures can provide fast and continuous Li⁺ pathways, even under high areal mass loading. Moreover, the 3D-VLMP Si electrode with an areal loading of 1.02 mg cm⁻² delivered a high areal capacity of 1.47 mAh cm⁻² (corresponding to specific capacity of 1444.56 mAh g⁻¹) after 100 cycles. Even under an incredibly high areal loading of 3.87 mg cm⁻², the 3D-VLMP Si electrode exhibited an areal capacity of 4.40 mAh cm⁻² (corresponding to 1136.95 mAh g⁻¹) after 40 cycles.

Figure 4.3e shows the comparison of the areal capacity versus areal mass loading between our 3D-VLMP Si electrodes and other Si anodes reported in literature³⁰⁻⁴¹. As highlighted, our 3D-VLMP Si electrodes outperformed most of the reported works in terms of the areal capacity and mass loadings. The achievement of high areal capacity under high areal mass loading demonstrates great potential for application in high-energy-density LIBs.

4.3.3 Post-cycled Electrode Morphology Characterization

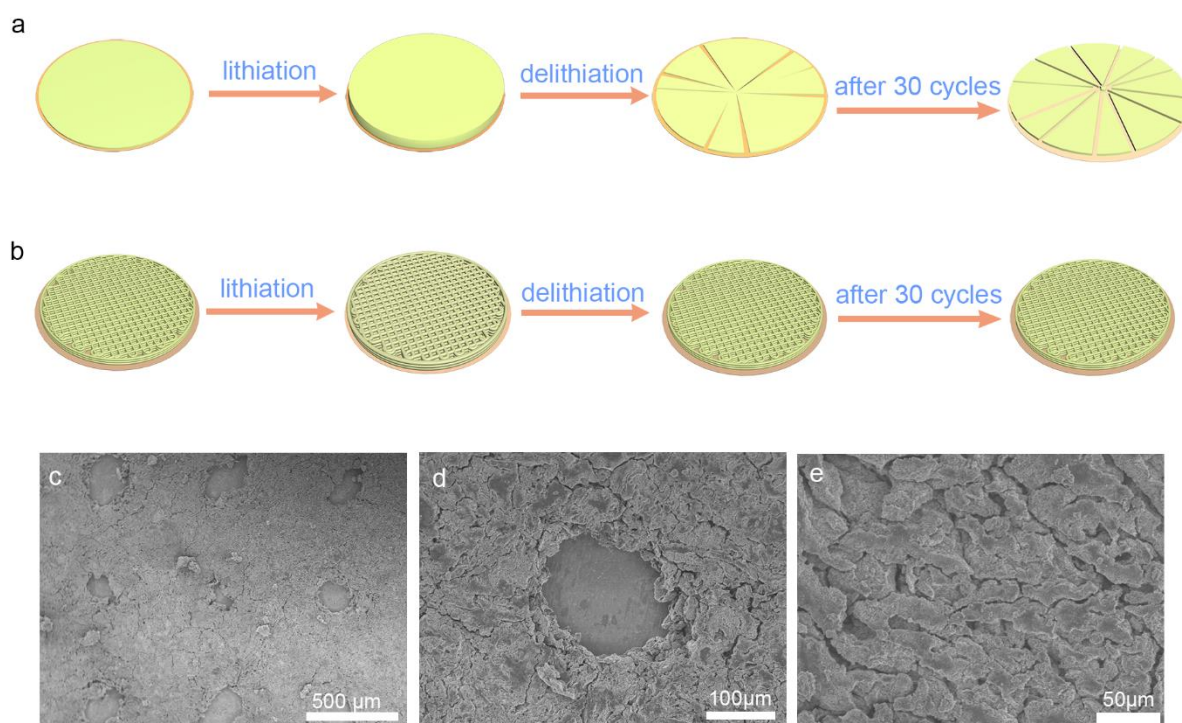


Figure 4.4. (a) Schematic illustration of cyclic pulverization of the Flat-NVLMP Si electrode; (b) Schematic illustration of the volume expansion mitigation of the 3D-VLMP Si electrode cycling (c-e) SEM images of the 3D-VLMP Si electrode after 30 cycles.

Large volume expansion of Si during the repeated cycling process is the main origin of the Si electrode capacity decay. As illustrated in **Figure 4.4a**, the conventional Flat-NVLMP Si electrode is expanded during lithiation. Upon subsequent delithiation, the volume change will cause cracks to form and propagate on the Si electrode. After several cycles of continuous volume expansion, the Si electrode will be severely pulverized. In contrast, as depicted in **Figure 4.4b**, the printed 3D-VLMP Si electrode demonstrated superior structural stability due to the macro/micropores which effectively mitigated the large volume expansion during the repeated lithiation/delithiation process. **Figure S4.9** displays the optical images of the 3D-VLMP Si and Flat-NVLMP Si electrodes after 30 cycles, where it is evident that the 3D-VLMP Si electrode remained the patterned architecture well, whereas the Flat-NVLMP Si electrode was pulverized severely and almost all the materials detached from the current collector. The cycled electrode morphologies were further studied through SEM imaging to ascertain the effect of the 3D-VLMP architecture on

the electrochemical performance. As shown in **Figure 4.4c**, the designed macropores were able to be well maintained after 30 cycles. The enlarged SEM image (**Figure 4.4d**) demonstrated that the size of the macropore became smaller compared to that of the pristine 3D-VLMP Si electrode, suggesting that the macropores provided free space for accommodating the volume expansion of Si during the cycling process. Moreover, as displayed in **Figure 4.4e**, the vertically aligned structures were still able to be observed although the spacing between the sheet-like structures was reduced due to the volume expansion of Si. The micro-scaled interval was able to release the huge stress caused by the large volume change and also facilitate the penetration of the electrolyte into the active materials, ensuring fast Li^+ transport and stable cycling performance.

4.4 Conclusion

We developed a novel facile 3D printing approach to rapidly construct patterned Si electrodes with vertically aligned and multi-scaled porous structures to achieve high areal capacity LIBs. Compared to the conventional flat 2D Si electrodes, the 3D-printed Si electrodes possessed vertically aligned mass/ionic transport pathways and macro/micro-scaled porosities, which helped facilitate the electron/ion transport within the whole electrodes and effectively helped mitigate the large volume expansion during cycling by providing extra negative space. From the structural advantages, the 3D-printed Si was able to exhibit a superior areal capacity of around 3 mAh cm^{-2} (corresponding to a specific capacity of 1450 mAh g^{-1}) after 60 cycles. Moreover, the 3D-printed Si delivered excellent performance merits under different areal mass loadings. Even under a high mass loading of 3.81 mg cm^{-2} , the 3D-printed Si displayed an extremely high areal capacity of $10.31 \text{ mAh cm}^{-2}$ ($2706.04 \text{ mAh g}^{-1}$). This work demonstrated a facile 3D printing approach to design unique architecture for realizing a high-performance Si anode. These techniques hence open a promising avenue for developing other advanced energy systems in the future.

Acknowledgements

The work was supported by Natural Science Foundation of China (NSFC) (Grant U1432249), the National Key R&D Program of China (Grant 2017YFA0205002), and the Priority Academic Program Development (PAPD) of Jiangsu Higher Education Institutions. This is also a project supported by Jiangsu Key Laboratory for Carbon-Based Functional Materials and Devices and the

Collaborative Innovation Center of Suzhou Nano Science & Technology. This work was also supported by the Natural Science and Engineering Research Council of Canada (NSERC), the Canada Research Chair Program (CRC), the Canada Foundation for Innovation (CFI), and the University of Western Ontario (UWO).

4.5 References

1. Tarascon, J. M.; Armand, M., Issues and Challenges Facing Rechargeable Lithium Batteries. *Nature* **2001**, *414*, 359-367.
2. Gao, X.; Wang, J.; Zhang, D.; Adair, K.; Feng, K.; Sun, N.; Zheng, H.; Shao, H.; Zhong, J.; Ma, Y.; Sun, X.; Sun, X., Carbon Coated Bimetallic Sulfide Nanodots/Carbon Nanorod Heterostructure Enabling Long-Life Lithium-Ion Batteries. *J. Mater. Chem. A* **2017**, *5*, 25625-25631.
3. Gao, X.; Wang, J.; Zhang, D.; Nie, K.; Ma, Y.; Zhong, J.; Sun, X., Hollow NiFe₂O₄ Nanospheres on Carbon Nanorods as A Highly Efficient Anode Material for Lithium-Ion Batteries. *J. Mater. Chem. A* **2017**, *5*, 5007-5012.
4. Chae, S.; Ko, M.; Kim, K.; Ahn, K.; Cho, J., Confronting Issues of the Practical Implementation of Si Anode in High-Energy Lithium-Ion Batteries. *Joule* **2017**, *1* (1), 47-60.
5. Li, P.; Zhao, G.; Zheng, X.; Xu, X.; Yao, C.; Sun, W.; Dou, S. X., Recent Progress on Silicon-Based Anode Materials for Practical Lithium-ion Battery Applications. *Energy Storage Mater.* **2018**, *15*, 422-446.
6. Chockla, A. M.; Harris, J. T.; Akhavan, V. A.; Bogart, T. D.; Holmberg, V. C.; Steinhagen, C.; Mullins, C. B.; Stevenson, K. J.; Korgel, B. A., Silicon nanowire fabric as a lithium ion battery electrode material. *J. AM. Chem. Soc.* **2011**, *133* (51), 20914-21.

7. Liu, X. H.; Fan, F.; Yang, H.; Zhang, S.; Huang, J. Y.; Zhu, T., Self-limiting lithiation in silicon nanowires. *ACS Nano* **2013**, *7* (2), 1495-503.
8. Song, T.; Xia, J.; Lee, J. H.; Lee, D. H.; Kwon, M. S.; Choi, J. M.; Wu, J.; Doo, S. K.; Chang, H.; Park, W. I.; Zang, D. S.; Kim, H.; Huang, Y.; Hwang, K. C.; Rogers, J. A.; Paik, U., Arrays of sealed silicon nanotubes as anodes for lithium ion batteries. *Nano Lett.* **2010**, *10* (5), 1710-6.
9. Xiao, Q.; Gu, M.; Yang, H.; Li, B.; Zhang, C.; Liu, Y.; Liu, F.; Dai, F.; Yang, L.; Liu, Z.; Xiao, X.; Liu, G.; Zhao, P.; Zhang, S.; Wang, C.; Lu, Y.; Cai, M., Inward lithium-ion breathing of hierarchically porous silicon anodes. *Nat. Commun.* **2015**, *6*, 8844.
10. Du, F.-H.; Li, B.; Fu, W.; Xiong, Y.-J.; Wang, K.-X.; Chen, J.-S., Surface Binding of Polypyrrole on Porous Silicon Hollow Nanospheres for Li-Ion Battery Anodes with High Structure Stability. *Adv.Mater.* **2014**, *26* (35), 6145-6150.
11. Wang, B.; Li, X.; Zhang, X.; Luo, B.; Jin, M.; Liang, M.; Dayeh, S. A.; Picraux, S. T.; Zhi, L., Adaptable silicon-carbon nanocables sandwiched between reduced graphene oxide sheets as lithium ion battery anodes. *ACS Nano* **2013**, *7* (2), 1437-45.
12. Li, W.; Tang, Y.; Kang, W.; Zhang, Z.; Yang, X.; Zhu, Y.; Zhang, W.; Lee, C.-S., Core-Shell Si/C Nanospheres Embedded in Bubble Sheet-like Carbon Film with Enhanced Performance as Lithium Ion Battery Anodes. *Small* **2015**, *11* (11), 1345-1351.
13. Liu, D.; Zhao, Y.; Tan, R.; Tian, L.-L.; Liu, Y.; Chen, H.; Pan, F., Novel conductive binder for high-performance silicon anodes in lithium ion batteries. *Nano Energy* **2017**, *36*, 206-212.
14. Zeng, W.; Wang, L.; Peng, X.; Liu, T.; Jiang, Y.; Qin, F.; Hu, L.; Chu, P. K.; Huo, K.; Zhou, Y., Enhanced Ion Conductivity in Conducting Polymer Binder for High-Performance Silicon Anodes in Advanced Lithium-Ion Batteries. *Adv. Energy Mater.* **2018**, *8* (11), 1702314.

15. Qian, F.; Zhu, C.; Knipe, J. M.; Ruelas, S.; Stolaroff, J. K.; DeOtte, J. R.; Duoss, E. B.; Spadaccini, C. M.; Henard, C. A.; Guarnieri, M. T.; Baker, S. E., Direct Writing of Tunable Living Inks for Bioprocess Intensification. *Nano Lett.* **2019**.
16. Wang, X.; Li, T.; Ma, H.; Zhai, D.; Jiang, C.; Chang, J.; Wang, J.; Wu, C., A 3D-printed scaffold with MoS₂ nanosheets for tumor therapy and tissue regeneration. *Npg Asia Mater.* **2017**, *9*, e376.
17. Valentine, A. D.; Busbee, T. A.; Boley, J. W.; Raney, J. R.; Chortos, A.; Kotikian, A.; Berrigan, J. D.; Durstock, M. F.; Lewis, J. A., Hybrid 3D Printing of Soft Electronics. *Adv. Mater.* **2017**, *29* (40), 1703817.
18. Yang, H.; Leow, W. R.; Chen, X., 3D Printing of Flexible Electronic Devices. *Small Methods* **2018**, *2* (1), 1700259.
19. Díaz-Marta, A. S.; Tubío, C. R.; Carbajales, C.; Fernández, C.; Escalante, L.; Sotelo, E.; Guitián, F.; Barrio, V. L.; Gil, A.; Coelho, A., Three-Dimensional Printing in Catalysis: Combining 3D Heterogeneous Copper and Palladium Catalysts for Multicatalytic Multicomponent Reactions. *ACS Catal.* **2017**, *8* (1), 392-404.
20. Chen, L.; Tang, X.; Xie, P.; Xu, J.; Chen, Z.; Cai, Z.; He, P.; Zhou, H.; Zhang, D.; Fan, T., 3D Printing of Artificial Leaf With Tunable Hierarchical Porosity for CO₂ Photoreduction. *Chem. Mater.* **2018**, *30*, 799-806.
21. Zhang, Y.; Sun, X.; Nomura, N.; Fujita, T., Hierarchical Nanoporous Copper Architectures via 3D Printing Technique for Highly Efficient Catalysts. *Small* **2019**, *15* (22), 1805432.
22. Gao, X.; Sun, Q.; Yang, X.; Liang, J.; Koo, A.; Li, W.; Liang, J.; Wang, J.; Li, R.; Holness, F. B.; Price, A. D.; Yang, S.; Sham, T.-K.; Sun, X., Toward a Remarkable Li-S battery via 3D Printing. *Nano Energy* **2019**, *56*, 595-603.

23. Wang, J.; Sun, Q.; Gao, X.; Wang, C.; Li, W.; Holness, F. B.; Zheng, M.; Li, R.; Price, A. D.; Sun, X.; Sham, T. K.; Sun, X., Toward High Areal Energy and Power Density Electrode for Li-Ion Batteries via Optimized 3D Printing Approach. *ACS Appl. Mater. Interfaces* **2018**, *10* (46), 39794-39801.
24. Lacey, S. D.; Kirsch, D. J.; Li, Y.; Morgenstern, J. T.; Zarket, B. C.; Yao, Y.; Dai, J.; Garcia, L. Q.; Liu, B.; Gao, T.; Xu, S.; Raghavan, S. R.; Connell, J. W.; Lin, Y.; Hu, L., Extrusion-Based 3D Printing of Hierarchically Porous Advanced Battery Electrodes. *Adv. Mater.* **2016**, 1705651-n/a.
25. Tang, X.; Zhu, C.; Cheng, D.; Zhou, H.; Liu, X.; Xie, P.; Zhao, Q.; Zhang, D.; Fan, T., Architected Leaf-Inspired Ni_{0.33}Co_{0.66}S₂/Graphene Aerogels via 3D Printing for High-Performance Energy Storage. *Adv. Funct. Mater.* **2018**, *28* (51), 1805057.
26. Fu, K.; Yildiz, O.; Bhanushali, H.; Wang, Y.; Stano, K.; Xue, L.; Zhang, X.; Bradford, P. D., Aligned carbon nanotube-silicon sheets: a novel nano-architecture for flexible lithium ion battery electrodes. *Adv. Mater.* **2013**, *25* (36), 5109-14.
27. Liu, J.; Zhang, Q.; Wu, Z. Y.; Wu, J. H.; Li, J. T.; Huang, L.; Sun, S. G., A high-performance alginate hydrogel binder for the Si/C anode of a Li-ion battery. *Chem. Commun.* **2014**, *50* (48), 6386-9.
28. Wen, Y.; Zhu, Y.; Langrock, A.; Manivannan, A.; Ehrman, S. H.; Wang, C., Graphene-Bonded and -Encapsulated Si Nanoparticles for Lithium Ion Battery Anodes. *Small* **2013**, *9* (16), 2810-2816.
29. Cao, F.-F.; Deng, J.-W.; Xin, S.; Ji, H.-X.; Schmidt, O. G.; Wan, L.-J.; Guo, Y.-G., Cu-Si Nanocable Arrays as High-Rate Anode Materials for Lithium-Ion Batteries. *Adv. Mater.* **2011**, *23* (38), 4415-4420.

30. Wu, H.; Yu, G.; Pan, L.; Liu, N.; McDowell, M. T.; Bao, Z.; Cui, Y., Stable Li-ion battery anodes by in-situ polymerization of conducting hydrogel to conformally coat silicon nanoparticles. *Nat. Commun.* **2013**, *4*, 1943.
31. Wang, C.; Wu, H.; Chen, Z.; McDowell, M. T.; Cui, Y.; Bao, Z., Self-healing chemistry enables the stable operation of silicon microparticle anodes for high-energy lithium-ion batteries. *Nat. Chem.* **2013**, *5* (12), 1042-8.
32. Xiao, Q.; Fan, Y.; Wang, X.; Susantyoko, R. A.; Zhang, Q., A multilayer Si/CNT coaxial nanofiber LIB anode with a high areal capacity. *Energy Environ. Sci.* **2014**, *7* (2), 655-661.
33. Yi, R.; Zai, J.; Dai, F.; Gordin, M. L.; Wang, D., Dual conductive network-enabled graphene/Si-C composite anode with high areal capacity for lithium-ion batteries. *Nano Energy* **2014**, *6*, 211-218.
34. Li, X.; Gu, M.; Hu, S.; Kennard, R.; Yan, P.; Chen, X.; Wang, C.; Sailor, M. J.; Zhang, J. G.; Liu, J., Mesoporous silicon sponge as an anti-pulverization structure for high-performance lithium-ion battery anodes. *Nat. Commun.* **2014**, *5*, 4105.
35. Liu, N.; Lu, Z.; Zhao, J.; McDowell, M. T.; Lee, H.-W.; Zhao, W.; Cui, Y., A pomegranate-inspired nanoscale design for large-volume-change lithium battery anodes. *Nat. Nanotech.* **2014**, *9* (3), 187-192.
36. Chen, Z.; Wang, C.; Lopez, J.; Lu, Z.; Cui, Y.; Bao, Z., High-Areal-Capacity Silicon Electrodes with Low-Cost Silicon Particles Based on Spatial Control of Self-Healing Binder. *Adv. Energy Mater.* **2015**, *5* (8), 1401826.
37. Lin, D.; Lu, Z.; Hsu, P.-C.; Lee, H. R.; Liu, N.; Zhao, J.; Wang, H.; Liu, C.; Cui, Y., A high tap density secondary silicon particle anode fabricated by scalable mechanical pressing for lithium-ion batteries. *Energy Environ. Sci.* **2015**, *8* (8), 2371-2376.

38. Zhou, M.; Li, X.; Wang, B.; Zhang, Y.; Ning, J.; Xiao, Z.; Zhang, X.; Chang, Y.; Zhi, L., High-Performance Silicon Battery Anodes Enabled by Engineering Graphene Assemblies. *Nano Lett.* **2015**, *15* (9), 6222-8.
39. Jung, D. S.; Ryou, M. H.; Sung, Y. J.; Park, S. B.; Choi, J. W., Recycling rice husks for high-capacity lithium battery anodes. *Proc. Natl. Acad. Sci.* **2013**, *110* (30), 12229-34.
40. Yoon, T.; Bok, T.; Kim, C.; Na, Y.; Park, S.; Kim, K. S., Mesoporous Silicon Hollow Nanocubes Derived from Metal-Organic Framework Template for Advanced Lithium-Ion Battery Anode. *ACS Nano* **2017**, *11* (5), 4808-4815.
41. Xu, Q.; Li, J.-Y.; Sun, J.-K.; Yin, Y.-X.; Wan, L.-J.; Guo, Y.-G., Watermelon-Inspired Si/C Microspheres with Hierarchical Buffer Structures for Densely Compacted Lithium-Ion Battery Anodes. *Adv. Energy Mater.* **2017**, *7* (3), 1601481.

Supporting Information



Figure S4.1 The Si-SA ink loaded in a 3cc syringe.

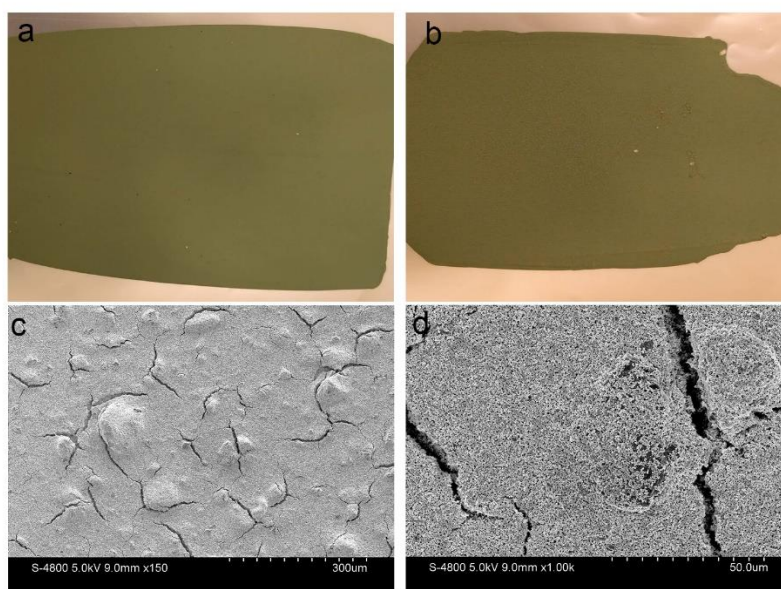


Figure S4.2 (a) Slurry-casted Si electrode under low areal loading (around 1.0 mg cm^{-2}); (b) Slurry-casted Si electrode under high areal loading (around 2.0 mg cm^{-2}); (c) and (d) SEM images of the low areal loading Si electrode.

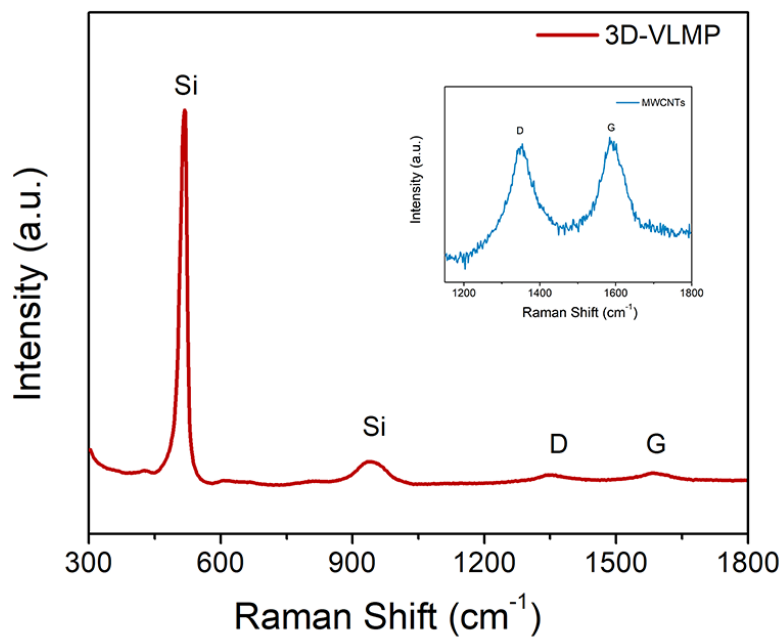


Figure S4.3 Raman spectra of the 3D-VLMP Si electrodes (Inset: enlarged Raman peaks of MWCNTs).

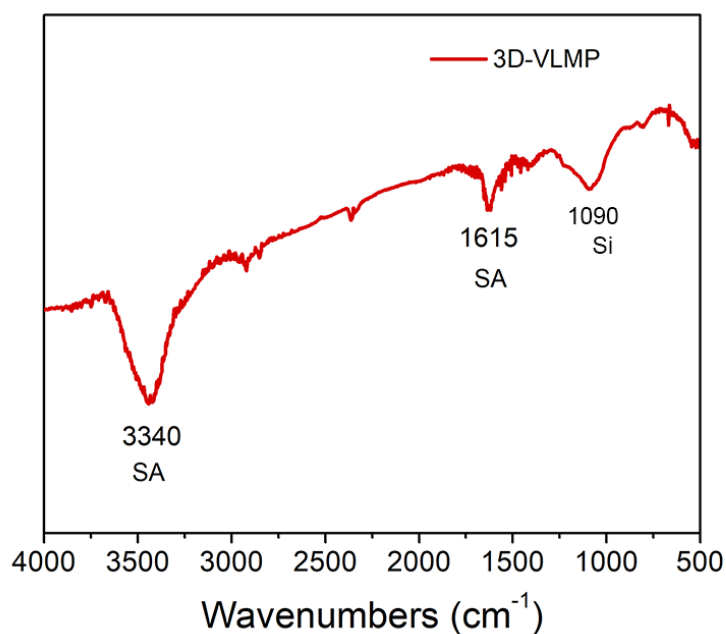


Figure S4.4 FTIR Spectra of the 3D-VLMP Si electrodes

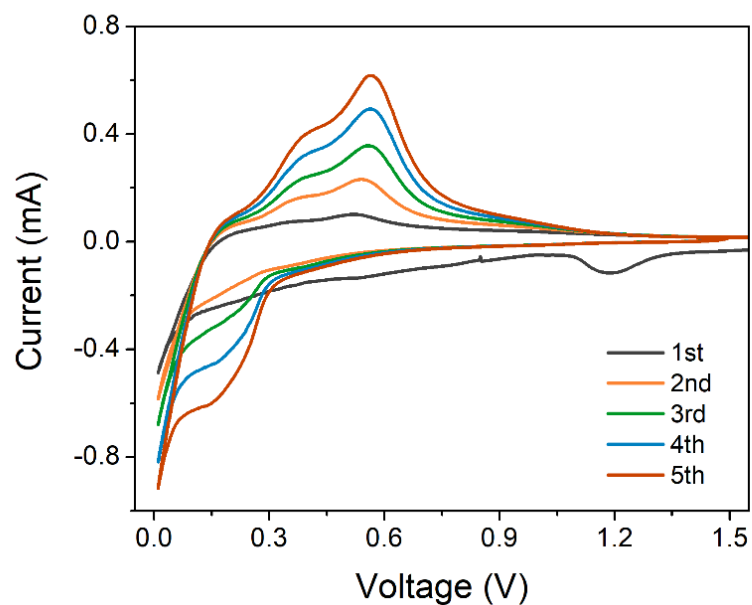


Figure S4.5 CV curves of the 3D-VLMP Si electrode at a scanning rate of 0.2 mV S⁻¹

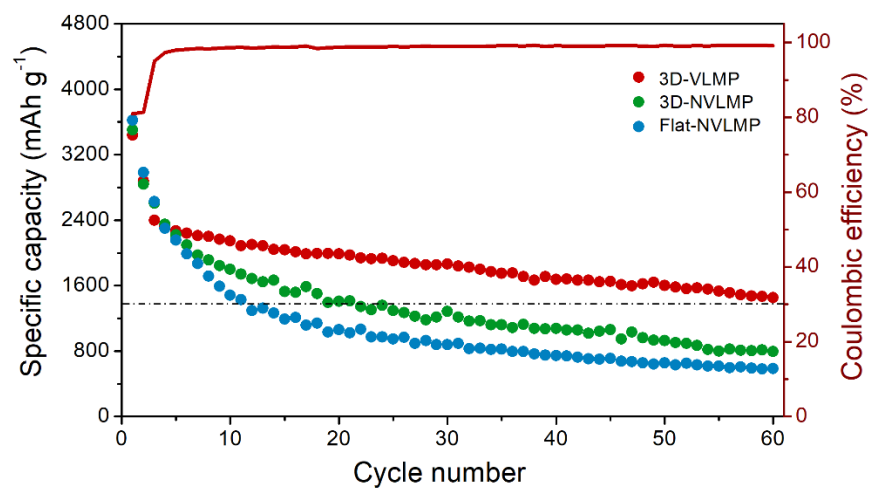


Figure S4.6 Specific capacity vs. cycle at a current density of 1 Ag⁻¹ for 60 cycles.

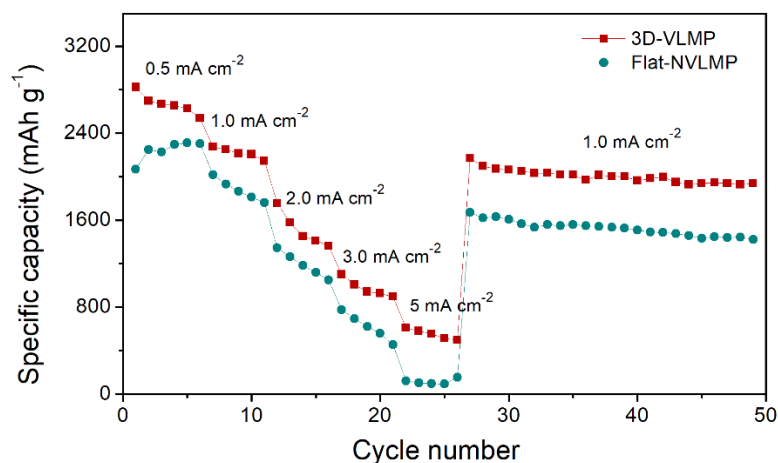


Figure S4.7 Rate capability of the 3D-VLMP and Flat-NVLMP Si electrodes at various current densities from 0.5 to 5 mA cm⁻².

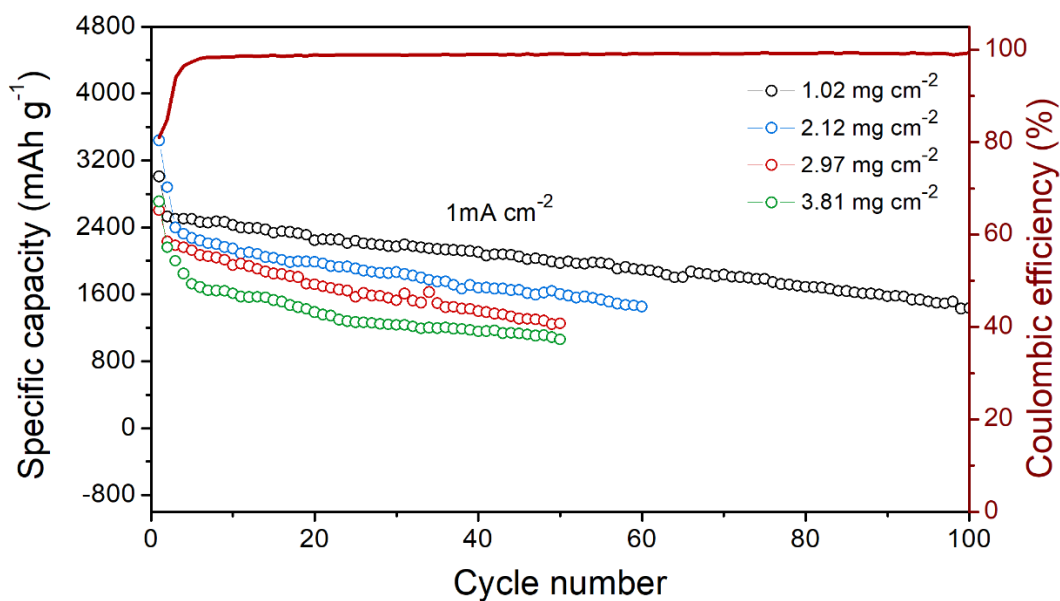


Figure S4.8 Various areal mass loading tests (up to 3.81 mg cm⁻²) of the printed 3D-VLMP Si electrodes. All electrodes were cycled at 0.3 mA cm⁻² for the initial cycle, and 1.0 mA cm⁻² for the late cycles.

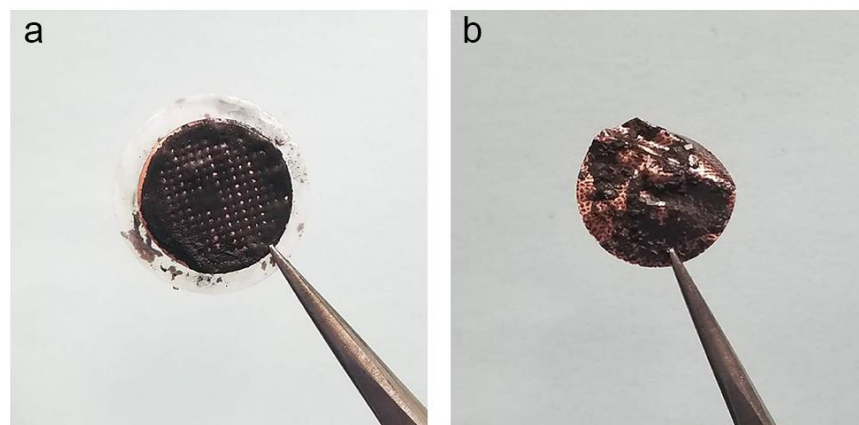


Figure S4.9 Optical images of the 3D-VLMP and Flat-NVLMP Si electrodes after 30 cycles.

Chapter 5

5 3D Printing of Shape-Versatile and Thin Solid Electrolyte for High-Performance Solid-State Li-Metal Batteries

Solid-state Li-metal batteries have recently received considerable interests due to their high safety and high energy density. However, it is of great challenge to fabricate a thin solid electrolyte through a low-cost and facile approach. Herein, we successfully fabricate a LAGP thin film with a thickness of around 70 μm via a low-cost and efficient extrusion-based 3D printing approach. Compared with the conventional pressed thick solid-state electrolyte pellets, the printed thin solid-state electrolyte can not only reduce the total weight of a cell but also shorten the Li^+ transport distance, which could increase the energy density and power density of a solid battery. Moreover, various 3D LAGP architectures are constructed by using the same ink, which could broaden the diversity of solid batteries with different size and shapes. This study thus demonstrates a low-cost and facile strategy to fabricate shape-versatile and thin solid electrolytes for high-energy-density solid-state energy storage systems.

5.1 Introduction

Rechargeable Li-ion batteries have dominated the energy storage power source market for the past few decades due to their high specific energy density and long cycle life.¹⁻² However, the current Li-ion batteries with graphite as the anode cannot meet the rapidly growing demand for high-energy-density storage devices. Developing high-performance Li-metal batteries is necessary to meet the needs of future electronics and electric vehicles.³⁻⁴ However, traditional liquid electrolytes have the risks of leakage and flammability, which will cause serious safety hazards. Moreover, the usage of Li metal can further aggravate these potential safety issues. Solid-state electrolytes are thus considered as a promising strategy for solving the safety issues.⁵⁻⁷

Various solid electrolytes have been studied in the last decade, such as sulfide electrolytes,⁸⁻⁹ garnet-type solid electrolytes,¹⁰⁻¹¹ NASICON-type solid electrolytes,¹²⁻¹⁴ and solid polymer electrolytes.¹⁵⁻¹⁷ Among these solid electrolytes, NASICON-type solid electrolyte LAGP ($\text{Li}_{1.5}\text{Al}_{0.5}\text{Ge}_{1.5}\text{P}_3\text{O}_{12}$) has received considerable attention since it has a relatively high lithium ionic conductivity (10^{-4} to 10^{-3} S cm^{-1}), a wide electrochemical window (6 V), and superior stability in air and moisture.¹⁸⁻¹⁹ However, one critical challenge for practical application is to fabricate LAGP thin films with desirable ionic conductivity through a simple and low-cost approach. The traditional cold sintering method is to adopt a metal mold to integrate the bulk materials into a pellet under a high pressure, which is generally hard to fabricate thin solid electrolyte films.²⁰ The thick solid electrolyte can lead to a lower energy density and power density as it increases the mass of a battery and prolongs Li^+ transport distance. Moreover, the mold for preparing solid electrolyte pellets could limit the diversity of solid batteries with respect to the size and shapes. Some other fabrication strategies, like atomic layer deposition,²¹ frequency magnetron sputtering,²² or pulsed laser deposition,²³ can indeed fabricate ultrathin films, however, these techniques are too expensive and require special conditions, which are undesirable for practical application. Therefore, a facile, cost-effective and scalable manufacturing approach is in an urgent need for fabricating thin solid electrolyte films with ideal ionic conductivity.

Additive manufacturing (AM) techniques, such as 3D printing, have shown great efficiency in fabricating products with complex geometric shapes and composition through a layer-by-layer fabrication process.²⁴⁻²⁵ Among various 3D printing techniques, extrusion-type direct-ink writing

(DIW) 3D printing has gained tremendous interest due to its simple printing mechanisms and inexpensive fabrication processes. Moreover, DIW technique can be employed to design unique architectures with multiple functional materials by selecting different printable inks, such as ceramics,²⁶ polymers,²⁷⁻²⁸ and metal alloys.²⁹⁻³⁰ More importantly, this printing technique can well control the structures and thickness by simply changing printing nozzles, adjusting printing layer numbers, and optimizing printing speed and pressure. This printing technique has thus attracted much attention and been widely used in the fields of electronics,³¹⁻³⁴ medical science,³⁵⁻³⁷ and energy storage.³⁸⁻⁴³

In this study, we successfully fabricate a homogenous LAGP thin film with a thickness of around 70 μm via a facile and efficient DIW 3D printing approach. The printed thin solid-state electrolyte can not only reduce the total weight of a cell but also shorten the Li^+ transport distance, which could increase the energy density and power density of a solid battery. Benefiting from these merits, a $\text{LiFePO}_4(\text{LFP})/\text{Li}$ solid battery with the 3D-printed LAGP (denoted as 3DP-LAGP) thin film as the electrolyte delivers a superior specific capacity of around 130 mAh g^{-1} even at a high rate of 5C, which is much higher than that of the battery with a thick LAGP pellet fabricated by conventional cold-sintering technique. Moreover, various 3D LAGP architectures are constructed by 3D printing method based on the same ink, which could broaden the diversity of solid batteries with different size and shapes. This study demonstrates a low-cost and facile strategy to fabricate shape-versatile and thin solid electrolytes for high-energy-density solid-state energy storage systems.

5.2 Experimental Section

5.2.1 Ink Preparation

The typical fabrication process of LAGP ink was described as follows: 4.0 g LAGP powders were first mixed with 1.0g of Pluronic F127 solution (10%) to obtain the homogeneous gel. After that, 2g polyvinyl alcohol (PVA) aqueous solution (15%) and 0.6 g sodium alginate (SA) aqueous solution (10%) as binders were added into the obtained gel to increase the viscosity of the ink. Subsequently, the obtained LAGP gel was further mixed well in a conditioning mixer (ARM, Thinky) at 2000 rpm for 10 min to obtain a homogenous and viscous ink for 3D printing.

5.2.2 3D printing process

The as-prepared ink was first loaded into a 3ml syringe. Afterward, the ink was subject to centrifugation for 5min at 3000 rpm to remove the air bubbles. A fused filament fabrication (FFF) DeltaMaker 3D printer modified with a paste extrusion-type tool head was used to fabricate uniform solid electrolyte film. The ink was deposited onto a glass substrate with extrusion pressure controlled by a Nordson EFD fluid dispenser. A metal nozzle with an inner diameter of 150 μm was adopted. The printing speed was adjusted in a range from 6 to 12 mm s^{-1} depending on the ink viscosity. After printing, the 3D-printed structures with glass substrate were aged in the air for drying. The dried structures were then sintered in a muffle furnace at 900°C for 6h with a ramping rate of 2.5°C min^{-1} .

5.2.3 Materials Characterizations

The morphologies were determined by using a Hitachi s-4800 field-emission scanning electron microscopy. X-ray diffraction (XRD) measurements were conducted using a Bruker D8 Advanced (Cu $K\alpha$ source, 40 kV, 40 mA) spectrometer.

5.2.4 Electrochemical Measurements

LiFePO_4 electrodes were prepared by mixing active materials, acetylene black (AB) and poly (vinylidene fluoride) (PVDF) in a ratio of 80:10:10 in N-methyl-pyrrolidone (NMP). The slurry was then pasted on Al foils and dried at 120°C under vacuum for overnight. The as-prepared LiFePO_4 electrode was then cut into a disc with a diameter of 10 mm and used as the cathode. The mass loading of LiFePO_4 is around 1.0-1.5 mg cm^{-2} . Electrochemical performances of the LiFePO_4 were examined in a coin cell assembled in an argon-filled glove box with moisture and oxygen contents less than 1 ppm. Printed LAGP film and conventional thick LAGP pellet were used as solid electrolytes. A PVDF-HFP gel polymer was added at both sides of the LAGP for improving the interfacial contact between the solid electrolyte and electrodes. Electrochemical impedance spectroscopic (EIS) measurements were performed on a Bio-Logic multichannel potentiostat 3/Z (VMP3). The galvanostatic charge/discharge performance was evaluated with a LAND test system in the voltage range of 2.5-4.2 V (vs. Li^+/Li) at room temperature.

5.3 Results and Discussion

5.3.1 Morphology and Structure Characterization

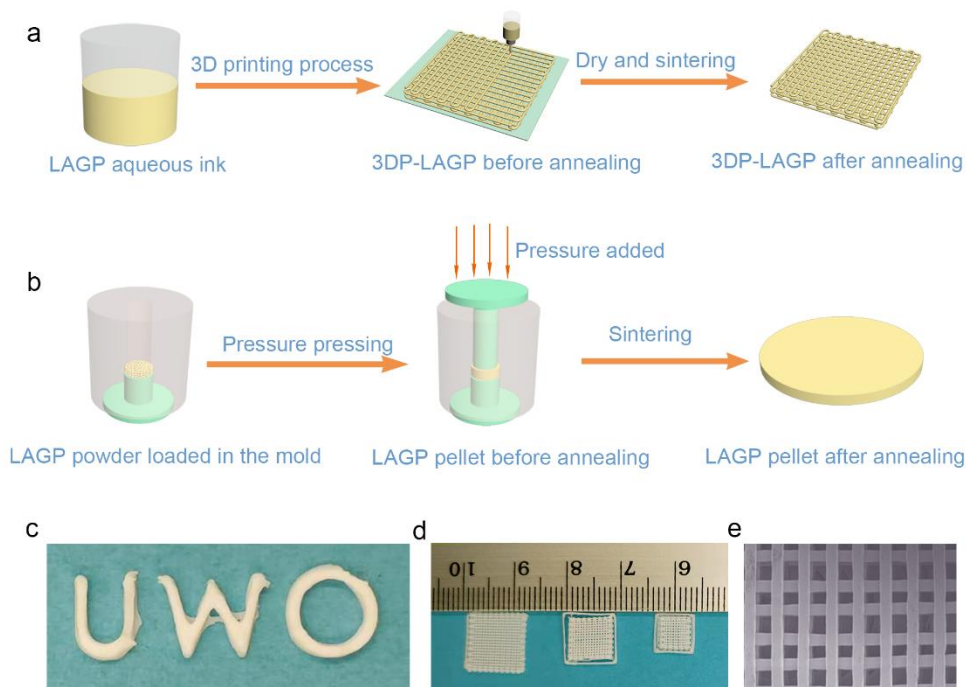


Figure 5.1 (a) Schematic illustration of 3D printing of LAGP solid electrolytes. (b) Schematic illustration of the procedure for the synthesis of the thick LAGP pellet with a conventional method. Optical images of 3D-printed LAGP with (c) unique letter shapes and (d) micro lattice structures in different sizes. (e) Top-view SEM image of the microlattice structured LAGP.

Figure 5.1a illustrates the LAGP solid electrolyte fabrication process by an extrusion-type 3D printing method. This method is capable of fabricating LAGP solid electrolyte with controllable thickness and shapes. In order to obtain fine printing LAGP structures, it is critically important to prepare an ink with suitable viscosity and shear-thinning features. Specifically, a self-supported printable LAGP ink was prepared by two steps: (1) LAGP powder was mixed with a small amount of Pluronic F127 solution (10%) to obtain homogeneous gel, and (2) Polyvinyl alcohol (PVA) and sodium alginate (SA) aqueous solution as binders were added into the obtained gel to increase the viscosity of the ink. The mixture was then transferred into a Think mixer to get desirable printing ink. Subsequently, the LAGP ink was loaded into a syringe (**Figure S5.1**) and extruded layer-by-

layer through a metal nozzle onto a glass slide controlled by a pre-designed program. The printed structures were dried at room temperature and then sintered in a muffle furnace to remove the binders and obtain fine LAGP structures. For obtaining a thin LAGP film, a single-layer dense LAGP film was printed and sintered, the printed height was adjusted to 150 μm . **Figure 5.1b** shows the fabrication process of a thick LAGP pellet (denoted as Con-LAGP) with a conventional method, where the thickness and size of the LAGP are greatly limited by the mold (**Figure S5.2**) used for fabricating pellets. Compared with the printed LAGP, the conventional pressed LAGP pellet is too thick, which will undoubtedly increase the total weight of a battery and reduce the energy density of the solid battery. Interestingly, LAGP with various patterns, such as unique letters and microlattice structures with different sizes as shown in **Figure S5.3 and S5.4**, can be printed based on the prepared ink. **Figure 5.1c and 5.1d** display that the printed various patterned LAGP can maintain the shape very well with fine and smooth surface after the thermal annealing process (**Figure 5.1e**). This thus demonstrates that 3D printing has potential in fabricating 3D solid batteries with controllable sizes and shapes.

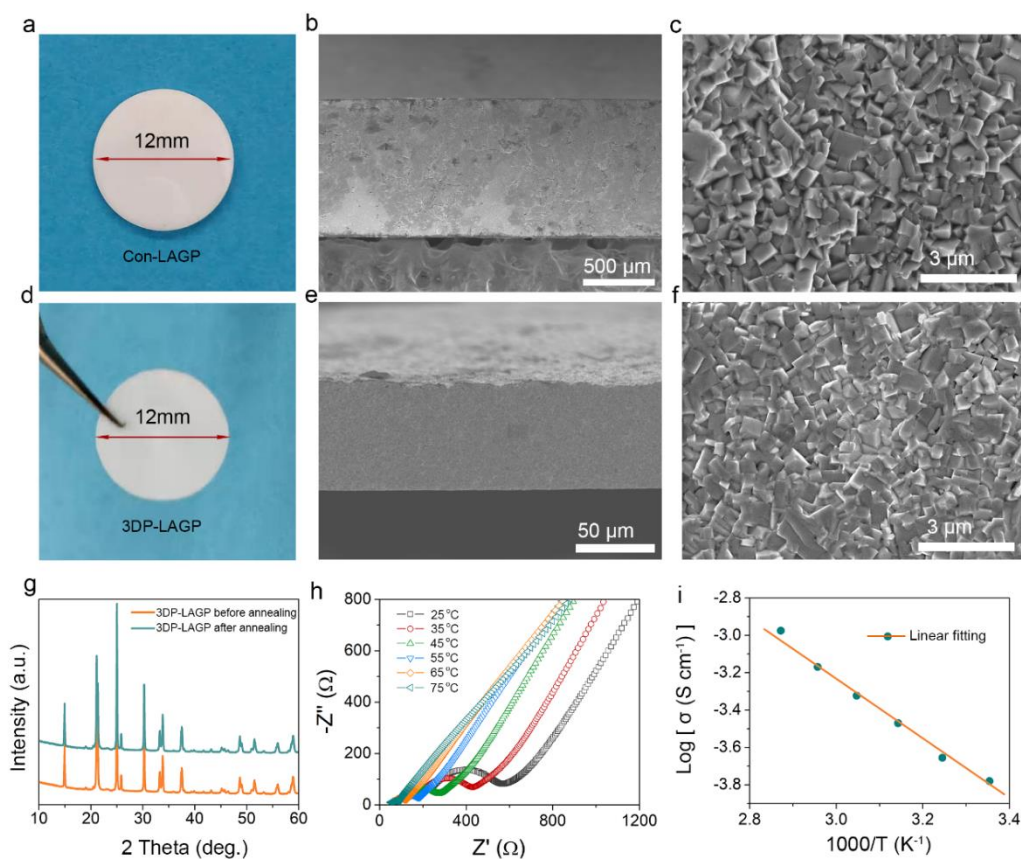


Figure 5.2. Digital photos of (a) the Con-LAGP thick pellet and (d) the 3DP-LAGP thin film. (b-c) Cross-sectional SEM images of (b-c) the Con-LAGP and (e-f) the 3DP-LAGP at different magnifications, respectively. (g) XRD patterns of 3DP-LAGP before and after thermal annealing. (h) EIS plots of the 3DP-LAGP at different temperatures of 25-75°C. (i) Conductivity vs. 1000/T of 3DP-LAGP electrolyte.

Figure 5.2a and 5.2d show the digital photos of the Con-LAGP thick electrolyte and 3DP-LAGP thin electrolyte after thermal annealing, respectively. Both LAGP films display a smooth surface and a diameter of around 12 mm, which is suitable for acting as electrolytes in the coin-cell. SEM images were applied to figure out the exact thickness and microstructures of the two LAGP films. **Figure 5.2b** presents the cross-sectional SEM image of the Con-LAGP with a thickness of approximately 0.95 mm. **Figure 5.2c** is a higher magnification SEM image of the cross-section, which reveals that most of the particles with the size of around 0.5-1.0 μm are closely connected, although a few voids are found between the grain boundaries of the LAGP. On the other hand, the cross-sectional SEM image of the 3DP-LAGP film is displayed in **Figure 5.2e**, it can be clearly observed that the 3DP-LAGP film presents a thickness of around 70 μm , which is much thinner than that of the Con-LAGP pellet. **Figure 5.2f and Figure S5.5** show the enlarged cross-sectional SEM images of the 3DP-LAGP. It can be found that all the particles are uniformly distributed and closely connected, presenting a smooth surface without any impurities. The microstructure of the 3DP-LAGP film displays similar features with that of the Con-LAGP thick pellet, suggesting a desirable ionic conductivity of the printed thin LAGP film.

X-ray diffraction (XRD) was conducted to determine the phase of the printed LAGP before and after thermal annealing. As shown in **Figure 5.2g**, there were no impurity diffraction peaks can be found in both samples and the XRD patterns of both samples can be well indexed to pure LAGP phase with NASICON structure, suggesting that the ink preparation and thermal treatment processes did not affect the phase and structure of the LAGP. The ionic conductivity of the obtained LAGP was investigated using electrochemical impedance spectroscopy (EIS). **Figure 5.2h** shows the EIS profiles of LAGP at various temperature, it can be found that the ionic conductivity of LAGP is $1.67 \times 10^{-4} \text{ S cm}^{-1}$ at the room temperature. **Figure 5.2i** presents the

temperature dependence of the ionic conductivity of the LAGP, which displayed an Arrhenius behavior according to the Arrhenius equation $\sigma(T) = A\exp(-E_a/k_B T)$, where σ is the ionic conductivity, T is the temperature in Kelvin, k_B is the Boltzmann constant, A is the pre-exponential factor, and E_a is the activation energy for Li^+ hopping between two adjacent sites. The activation energy of the LAGP was determined to be $32.15 \text{ kJ mol}^{-1}$, which is comparable with other reported values.⁴⁴

5.3.2 Electrochemical Characterization

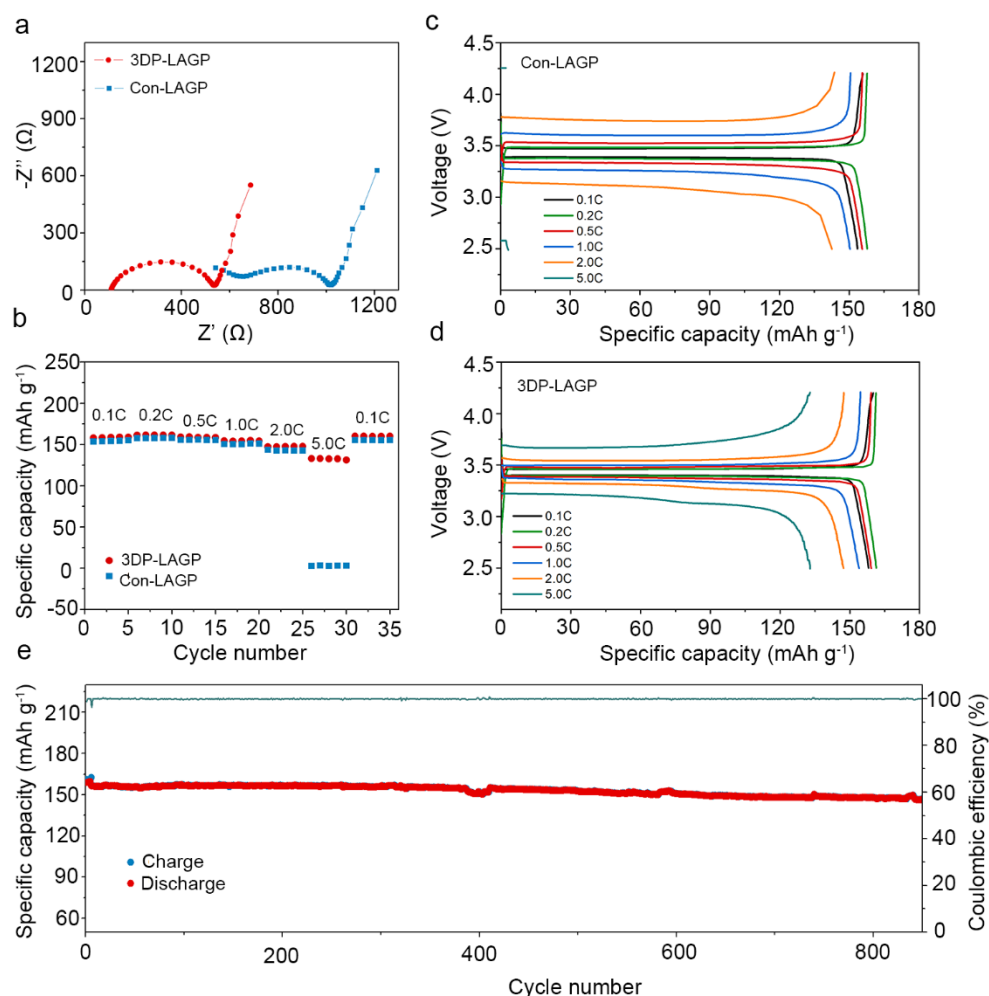


Figure 5.3 Electrochemical performance characterization of the printed LAGP thin film. (a) EIS of the $\text{LiFePO}_4/\text{Li}$ batteries with 3DP-LAGP and Con-LAGP as the electrolytes, respectively (b) Rate capabilities of 3DP-LAGP based solid Li-battery and Con-LAGP based solid Li-battery at a current density range of 0.1C to 5C. Typical charge/discharge voltage

profiles of (c) Con-LAGP based solid Li-battery and (d) 3DP-LAGP based solid Li-battery at various current densities. (e) Long-term cycling performance of 3DP-LAGP based solid Li-battery at a current density of 0.5 C.

To evaluate the advantages of the printed thin solid electrolyte, we assembled the solid-state Li batteries with Li metal and LiFePO₄ (LFP) as the anode and cathode, respectively. The 3DP-LAGP thin film and Con-LAGP thick pellet were used as solid electrolytes for comparison. In order to improve the interface contact between the electrodes and solid-state electrolytes, a PVDF-HFP gel polymer was added at both anode and cathode sides of the solid battery as the interlayer. **Figure 5.3a** depicts the impedance plots of the batteries with 3DP-LAGP thin electrolyte and Con-LAGP thick electrolyte. It reveals that both batteries present a smaller interfacial resistance due to the existence of gel polymer buffer layers. However, the battery with 3DP-LAGP thin electrolyte displays a greatly decreased bulk resistance compared to that of the battery with Con-LAGP thick electrolyte. **Figure 5.3b** shows the rate capabilities of the solid-state Li batteries with 3DP-LAGP and Con-LAGP as solid electrolytes. It is found that both solid-state Li batteries exhibited superior specific capacities when current densities changed from 0.1C to 2.0C, and 3DP-LAGP based solid battery shows a little bit higher capacity than that of the Con-LAGP based solid battery. However, at a current density of 5C, the Con-LAGP based solid battery displays an extremely poor capacity. By contrast, the 3DP-LAGP based solid battery can exhibit a high specific capacity of around 130 mAh g⁻¹ even at 5C. When current density changed back to 0.1C, both batteries could deliver a specific capacity of around 155 mAh g⁻¹, demonstrating good reversibility of the LAGP based solid batteries. **Figure 5.3c and 5.3d** show the charge/discharge profiles of the batteries with Con-LAGP and 3DP-LAGP as electrolytes, respectively. Although both batteries deliver similar capacities at lower current densities, it can be easily found that the 3DP-LAGP based solid battery shows much lower overpotential than that of the Con-LAGP based solid battery. For instance, the Con-LAGP based solid battery exhibits a large overpotential of around 350 mV and 640 mV at 1C and 2C, respectively. By contrast, the 3DP-LAGP based solid battery shows a much smaller overpotential of 160 mV and 270 mV at 1C and 2C. The results demonstrate that the printed thin electrolyte can ensure fast ion transport, thus improving the power density of a solid battery. **Figure 5.3e** displays the long-term cycling performance of LiFePO₄ with the 3DP-LAGP thin electrolyte. The 3DP-LAGP based LiFePO₄ shows a high specific capacity of 155 mAh g⁻¹ and

remains as high as 146 mAh g^{-1} even over 850 cycles, which gives an extremely stable cycling performance with a lower capacity decay rate of 0.0068% per cycle. However, the LiFePO_4 with the pure gel polymer electrolyte undergoes a fast capacity decay and only shows a capacity of around 72 mAh g^{-1} after 850 cycles with a capacity retention of 46% as presented in **Figure S5.6**. By contrast, the Con-LAGP based LiFePO_4 delivers high cycling stability (**Figure S5.7**), which is similar to the cycling performance of the 3DP-LAGP based LiFePO_4 . The excellent cycling performance suggests that the LAGP solid electrolyte can suppress the lithium dendrite growth, thereby leading to a highly safe Li-metal battery.

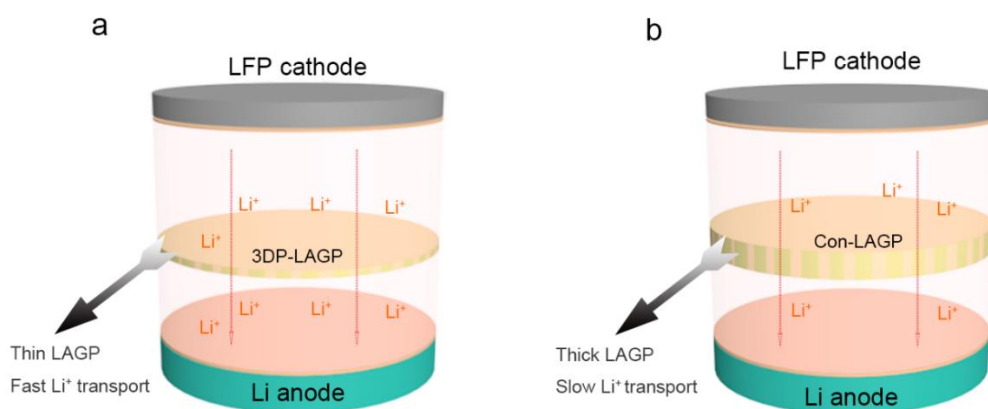


Figure 5.4 Schematic illustration of Li^+ transport kinetics in solid-state Li batteries with (a) 3D-printed thin LAGP and (b) conventional thick LAGP as solid electrolytes.

The superior rate performance of $\text{LiFePO}_4/\text{Li}$ batteries with 3DP-LAGP as the solid electrolyte can be attributed to the reduced Li^+ transport path as illustrated in **Figure 5.4**. In a solid-state Li battery, the Li^+ will transport from the cathode to the Li anode upon cycling, where the Li^+ transport kinetic is mainly determined by the solid-state electrolyte between the anode and the cathode. To this end, the 3DP-LAGP thin film with desirable ionic conductivity could greatly shorten the transport distance, thus leading to a fast Li^+ transport (**Figure 5.4a**). By contrast, the Con-LAGP thick pellet based solid batteries exhibit a prolonged Li^+ transport path (**Figure 5.4b**), resulting in poor rate capabilities, especially at a high current density. Therefore, the printed thin electrolyte could ensure an improved energy density and power density of the solid battery due to the reduced total weight of a cell and fast Li^+ transport upon cycling. This work is thus expected

to open a new avenue to design high-performance solid batteries with high energy density and power density through 3D printing technologies.

5.4 Conclusion

We have developed a low-cost aqueous-based printable ink for fabricating uniform LAGP thin films via an advanced extrusion-type 3D printing approach. Compared with the conventional pressed thick LAGP pellets, the printed thin LAGP can not only reduce the total weight of a cell but also shorten the Li^+ transport distance, which could increase the energy density and power density of a solid battery. This method offers the flexibility of fabricating thin solid-state electrolytes with controllable thickness in a low-cost and efficient way. In addition, various patterned LAGP architectures are easily fabricated, broadening the diversity of solid batteries with various size and shapes. This work thus would shed light on fabricating desirable solid-state electrolytes for next-generation high energy density solid-state batteries.

Acknowledgements

The work was supported by Natural Science Foundation of China (NSFC) (Grant U1432249), the National Key R&D Program of China (Grant 2017YFA0205002), and the Priority Academic Program Development (PAPD) of Jiangsu Higher Education Institutions. This is also a project supported by Jiangsu Key Laboratory for Carbon-Based Functional Materials and Devices and Collaborative Innovation Center of Suzhou Nano Science & Technology. This work was also supported by the Natural Science and Engineering Research Council of Canada (NSERC), the Canada Research Chair Program (CRC), the Canada Foundation for Innovation (CFI), and the University of Western Ontario (UWO).

5.5 References

1. Tarascon, J. M.; Armand, M., Issues and challenges facing rechargeable lithium batteries. *Nature* **2001**, *414*, 359.
2. Gao, X.; Wang, J.; Zhang, D.; Adair, K.; Feng, K.; Sun, N.; Zheng, H.; Shao, H.; Zhong, J.; Ma, Y.; Sun, X.; Sun, X., Carbon coated bimetallic sulfide nanodots/carbon nanorod

heterostructure enabling long-life lithium-ion batteries. *J. Mater. Chem. A* **2017**, *5* (48), 25625-25631.

3. Lin, D.; Liu, Y.; Cui, Y., Reviving the lithium metal anode for high-energy batteries. *Nat. Nanotech.* **2017**, *12* (3), 194-206.

4. Zhang, R.; Li, N.-W.; Cheng, X.-B.; Yin, Y.-X.; Zhang, Q.; Guo, Y.-G., Advanced Micro/Nanostructures for Lithium Metal Anodes. *Adv. Sci.* **2017**, *4* (3), 1600445-n/a.

5. Manthiram, A.; Yu, X.; Wang, S., Lithium battery chemistries enabled by solid-state electrolytes. *Nat. Rev. Mater.* **2017**, *2*, 16103.

6. Zheng, F.; Kotobuki, M.; Song, S.; Lai, M. O.; Lu, L., Review on solid electrolytes for all-solid-state lithium-ion batteries. *J. Power Sources* **2018**, *389*, 198-213.

7. Gao, Z.; Sun, H.; Fu, L.; Ye, F.; Zhang, Y.; Luo, W.; Huang, Y., Promises, Challenges, and Recent Progress of Inorganic Solid-State Electrolytes for All-Solid-State Lithium Batteries. *Adv. Mater.* **2018**, *30* (17), e1705702.

8. Lau, J.; DeBlock, R. H.; Butts, D. M.; Ashby, D. S.; Choi, C. S.; Dunn, B. S., Sulfide Solid Electrolytes for Lithium Battery Applications. *Adv. Energy Mater.* **2018**, *8* (27), 1800933.

9. Wang, C.; Adair, K. R.; Liang, J.; Li, X.; Sun, Y.; Li, X.; Wang, J.; Sun, Q.; Zhao, F.; Lin, X.; Li, R.; Huang, H.; Zhang, L.; Yang, R.; Lu, S.; Sun, X., Solid-State Plastic Crystal Electrolytes: Effective Protection Interlayers for Sulfide-Based All-Solid-State Lithium Metal Batteries. *Adv. Funct. Mater.* **2019**, 1900392.

10. Bae, J.; Li, Y.; Zhao, F.; Zhou, X.; Ding, Y.; Yu, G., Designing 3D nanostructured garnet frameworks for enhancing ionic conductivity and flexibility in composite polymer electrolytes for lithium batteries. *Energy Storage Mater.* **2018**, *15*, 46-52.

11. Wang, D.; Sun, Q.; Luo, J.; Liang, J.; Sun, Y.; Li, R.; Adair, K.; Zhang, L.; Yang, R.; Lu, S.; Huang, H.; Sun, X., Mitigating the Interfacial Degradation in Cathodes for High-Performance Oxide-Based Solid-State Lithium Batteries. *ACS Appl. Mater. Interfaces* **2019**, *11* (5), 4954-4961.
12. Wang, C.; Sun, Q.; Liu, Y.; Zhao, Y.; Li, X.; Lin, X.; Banis, M. N.; Li, M.; Li, W.; Adair, K. R.; Wang, D.; Liang, J.; Li, R.; Zhang, L.; Yang, R.; Lu, S.; Sun, X., Boosting the performance of lithium batteries with solid-liquid hybrid electrolytes: Interfacial properties and effects of liquid electrolytes. *Nano Energy* **2018**, *48*, 35-43.
13. Liu, Y.; Li, C.; Li, B.; Song, H.; Cheng, Z.; Chen, M.; He, P.; Zhou, H., Germanium Thin Film Protected Lithium Aluminum Germanium Phosphate for Solid-State Li Batteries. *Adv. Energy Mater.* **2018**, *8* (16), 1702374.
14. Liang, J.; Sun, Q.; Zhao, Y.; Sun, Y.; Wang, C.; Li, W.; Li, M.; Wang, D.; Li, X.; Liu, Y.; Adair, K.; Li, R.; Zhang, L.; Yang, R.; Lu, S.; Huang, H.; Sun, X., Stabilization of all-solid-state Li-S batteries with a polymer-ceramic sandwich electrolyte by atomic layer deposition. *J. Mater. Chem. A* **2018**, *6* (46), 23712-23719.
15. Sheng, O.; Jin, C.; Luo, J.; Yuan, H.; Huang, H.; Gan, Y.; Zhang, J.; Xia, Y.; Liang, C.; Zhang, W.; Tao, X., Mg₂B₂O₅ Nanowire Enabled Multifunctional Solid-State Electrolytes with High Ionic Conductivity, Excellent Mechanical Properties, and Flame-Retardant Performance. *Nano Lett.* **2018**, *18* (5), 3104-3112.
16. Zhai, H.; Xu, P.; Ning, M.; Cheng, Q.; Mandal, J.; Yang, Y., A Flexible Solid Composite Electrolyte with Vertically Aligned and Connected Ion-Conducting Nanoparticles for Lithium Batteries. *Nano Lett.* **2017**, *17* (5), 3182-3187.
17. Zhang, X.; Xie, J.; Shi, F.; Lin, D.; Liu, Y.; Liu, W.; Pei, A.; Gong, Y.; Wang, H.; Liu, K.; Xiang, Y.; Cui, Y., Vertically Aligned and Continuous Nanoscale Ceramic-Polymer Interfaces in

Composite Solid Polymer Electrolytes for Enhanced Ionic Conductivity. *Nano Lett.* **2018**, *18* (6), 3829-3838.

18. Fu, J., Fast Li⁺ ion conducting glass-ceramics in the system Li₂O-Al₂O₃-GeO₂-P₂O₅. *Solid State Ionics* **1997**, *104*, 191-194.

19. Wang, S.; Wang, J.; Liu, J.; Song, H.; Liu, Y.; Wang, P.; He, P.; Xu, J.; Zhou, H., Ultra-fine surface solid-state electrolytes for long cycle life all-solid-state lithium-air batteries. *J. Mater. Chem. A* **2018**, *6* (43), 21248-21254.

20. Liu, Y.; Sun, Q.; Wang, D.; Adair, K.; Liang, J.; Sun, X., Development of the cold sintering process and its application in solid-state lithium batteries. *J. Power Sources* **2018**, *393*, 193-203.

21. Wang, B.; Liu, J.; Norouzi Banis, M.; Sun, Q.; Zhao, Y.; Li, R.; Sham, T. K.; Sun, X., Atomic Layer Deposited Lithium Silicates as Solid-State Electrolytes for All-Solid-State Batteries. *ACS Appl. Mater. Interfaces* **2017**, *9* (37), 31786-31793.

22. Choi, C. H.; Cho, W. I.; Cho, B. W.; Kim, H. S.; Yoon, Y. S.; Tak, Y. S., Radio-Frequency Magnetron Sputtering Power Effect on the Ionic Conductivities of Lipon Films. *Electrochem. Solid-State Lett.* **2002**, *5* (1), A14.

23. Saccoccio, M.; Yu, J.; Lu, Z.; Kwok, S. C. T.; Wang, J.; Yeung, K. K.; Yuen, M. M. F.; Ciucci, F., Low temperature pulsed laser deposition of garnet Li_{6.4}La₃Zr_{1.4}Ta_{0.6}O₁₂ films as all solid-state lithium battery electrolytes. *J. Power Sources* **2017**, *365*, 43-52.

24. Ruiz-Morales, J. C.; Tarancón, A.; Canales-Vázquez, J.; Méndez-Ramos, J.; Hernández-Afonso, L.; Acosta-Mora, P.; Marín Rueda, J. R.; Fernández-González, R., Three dimensional printing of components and functional devices for energy and environmental applications. *Energy Environ. Sci.* **2017**.

25. Tian, X.; Jin, J.; Yuan, S.; Chua, C. K.; Tor, S. B.; Zhou, K., Emerging 3D-Printed Electrochemical Energy Storage Devices: A Critical Review. *Adv. Energy Mater.* **2017**, *7* (17), 1700127.
26. Nguyen, D. T.; Meyers, C.; Yee, T. D.; Dudukovic, N. A.; Destino, J. F.; Zhu, C.; Duoss, E. B.; Baumann, T. F.; Suratwala, T.; Smay, J. E.; Dylla-Spears, R., 3D-Printed Transparent Glass. *Adv. Mater.* **2017**, *29* (26), 1701181-n/a.
27. Dizon, J. R. C.; Espera, A. H.; Chen, Q.; Advincula, R. C., Mechanical Characterization of 3D-Printed Polymers. *Addit. Manuf.* **2018**, *20*, 44-67.
28. Guo, S. Z.; Qiu, K.; Meng, F.; Park, S. H.; McAlpine, M. C., 3D Printed Stretchable Tactile Sensors. *Adv. Mater.* **2017**, *29* (27).
29. Jakus, A. E.; Taylor, S. L.; Geisendorfer, N. R.; Dunand, D. C.; Shah, R. N., Metallic Architectures from 3D-Printed Powder-Based Liquid Inks. *Adv. Funct. Mater.* **2015**, *25* (45), 6985-6995.
30. Yan, P.; Brown, E.; Su, Q.; Li, J.; Wang, J.; Xu, C.; Zhou, C.; Lin, D., 3D Printing Hierarchical Silver Nanowire Aerogel with Highly Compressive Resilience and Tensile Elongation through Tunable Poisson's Ratio. *Small* **2017**, 1701756-n/a.
31. Mohammed, M. G.; Kramer, R., All-Printed Flexible and Stretchable Electronics. *Adv. Mater.* **2017**, *29* (19), 1604965.
32. Shin, S. R.; Farzad, R.; Tamayol, A.; Manoharan, V.; Mostafalu, P.; Zhang, Y. S.; Akbari, M.; Jung, S. M.; Kim, D.; Comotto, M.; Annabi, N.; Al-Hazmi, F. E.; Dokmeci, M. R.; Khademhosseini, A., A Bioactive Carbon Nanotube-Based Ink for Printing 2D and 3D Flexible Electronics. *Adv. Mater.* **2016**, *28* (17), 3280-3289.

33. Valentine, A. D.; Busbee, T. A.; Boley, J. W.; Raney, J. R.; Chortos, A.; Kotikian, A.; Berrigan, J. D.; Durstock, M. F.; Lewis, J. A., Hybrid 3D Printing of Soft Electronics. *Adv. Mater.* **2017**, *29* (40), 1703817.
34. Yang, H.; Leow, W. R.; Chen, X., 3D Printing of Flexible Electronic Devices. *Small Methods* **2018**, *2* (1), 1700259.
35. Forget, A.; Blaeser, A.; Miessmer, F.; Kopf, M.; Campos, D. F. D.; Voelcker, N. H.; Blencowe, A.; Fischer, H.; Shastri, V. P., Mechanically Tunable Bioink for 3D Bioprinting of Human Cells. *Adv. Healthc. Mater.* **2017**, *6* (20).
36. Gao, F.; Xu, Z.; Liang, Q.; Liu, B.; Li, H.; Wu, Y.; Zhang, Y.; Lin, Z.; Wu, M.; Ruan, C.; Liu, W., Direct 3D Printing of High Strength Biohybrid Gradient Hydrogel Scaffolds for Efficient Repair of Osteochondral Defect. *Adv. Funct. Mater.* **2018**, 1706644-n/a.
37. Qian, F.; Zhu, C.; Knipe, J. M.; Ruelas, S.; Stolaroff, J. K.; DeOtte, J. R.; Duoss, E. B.; Spadaccini, C. M.; Henard, C. A.; Guarnieri, M. T.; Baker, S. E., Direct Writing of Tunable Living Inks for Bioprocess Intensification. *Nano Lett.* **2019**.
38. Díaz-Marta, A. S.; Tubío, C. R.; Carbajales, C.; Fernández, C.; Escalante, L.; Sotelo, E.; Guitián, F.; Barrio, V. L.; Gil, A.; Coelho, A., Three-Dimensional Printing in Catalysis: Combining 3D Heterogeneous Copper and Palladium Catalysts for Multicatalytic Multicomponent Reactions. *ACS Catal.* **2017**, *8* (1), 392-404.
39. Gao, X.; Sun, Q.; Yang, X.; Liang, J.; Koo, A.; Li, W.; Liang, J.; Wang, J.; Li, R.; Holness, F. B.; Price, A. D.; Yang, S.; Sham, T.-K.; Sun, X., Toward a Remarkable Li-S battery via 3D Printing. *Nano Energy* **2019**, *56*, 595-603.
40. Lacey, S. D.; Kirsch, D. J.; Li, Y.; Morgenstern, J. T.; Zarket, B. C.; Yao, Y.; Dai, J.; Garcia, L. Q.; Liu, B.; Gao, T.; Xu, S.; Raghavan, S. R.; Connell, J. W.; Lin, Y.; Hu, L., Extrusion-Based

3D Printing of Hierarchically Porous Advanced Battery Electrodes. *Adv. Mater.* **2016**, 1705651-n/a.

41. Sun, K.; Wei, T. S.; Ahn, B. Y.; Seo, J. Y.; Dillon, S. J.; Lewis, J. A., 3D printing of interdigitated Li-ion microbattery architectures. *Adv. Mater.* **2013**, 25 (33), 4539-43.

42. Wang, J.; Sun, Q.; Gao, X.; Wang, C.; Li, W.; Holness, F. B.; Zheng, M.; Li, R.; Price, A. D.; Sun, X.; Sham, T. K.; Sun, X., Toward High Areal Energy and Power Density Electrode for Li-Ion Batteries via Optimized 3D Printing Approach. *ACS Appl. Mater. Interfaces* **2018**, 10 (46), 39794-39801.

43. Yao, B.; Chandrasekaran, S.; Zhang, J.; Xiao, W.; Qian, F.; Zhu, C.; Duoss, E. B.; Spadaccini, C. M.; Worsley, M. A.; Li, Y., Efficient 3D Printed Pseudocapacitive Electrodes with Ultrahigh MnO₂ Loading. *Joule* **2019**, 3 (2), 459-470.

44. Wang, C.; Zhao, Y.; Sun, Q.; Li, X.; Liu, Y.; Liang, J.; Li, X.; Lin, X.; Li, R.; Adair, K. R.; Zhang, L.; Yang, R.; Lu, S.; Sun, X., Stabilizing interface between Li₁₀SnP₂S₁₂ and Li metal by molecular layer deposition. *Nano Energy* **2018**, 53, 168-174.

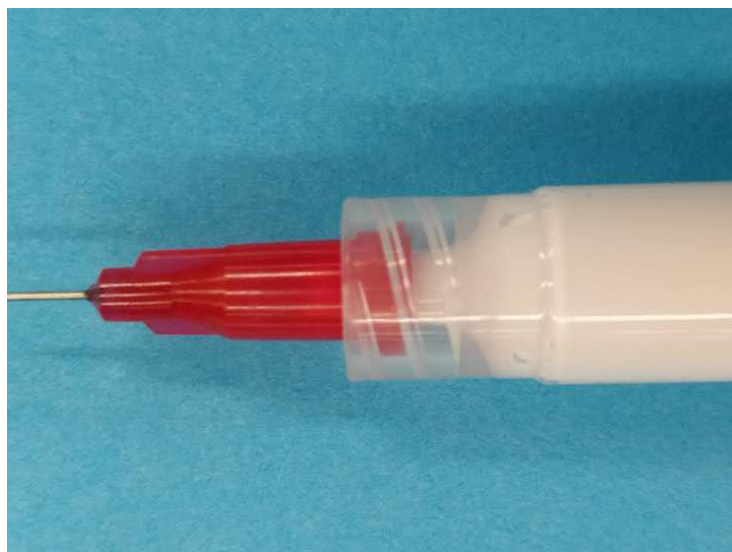
Supporting information

Figure S5.1 LAGP ink loaded into a 3cc syringe



Figure 5.2 Metal mold used for fabricating LAGP pellets



Figure S5.3 3D-printed LAGP with unique “UWO” letters before annealing

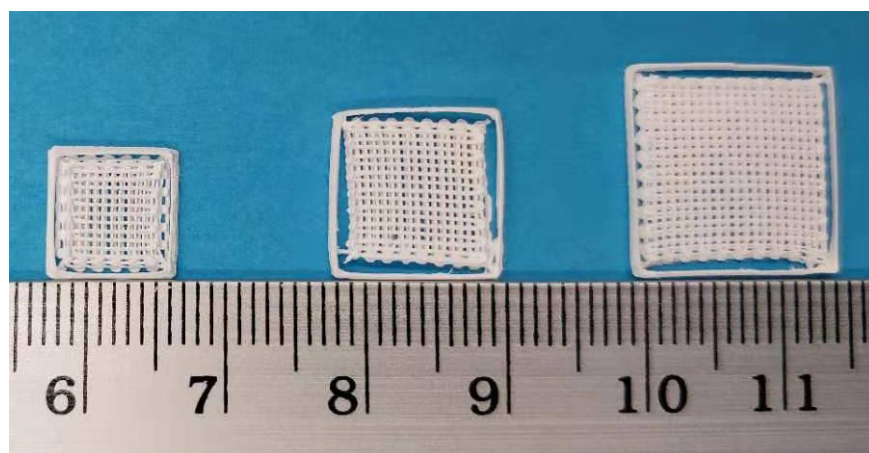


Figure S5.4 3D-printed LAGP micro-lattices with different size before annealing

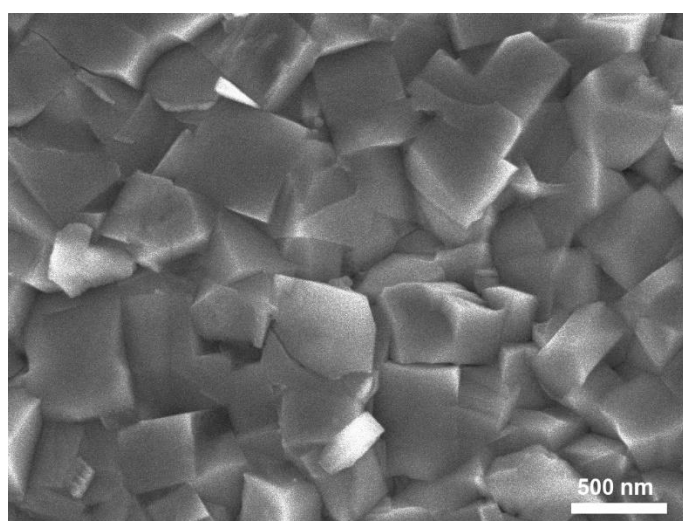


Figure S5.5 Enlarged cross-sectional SEM image of the 3DP-LAGP film.

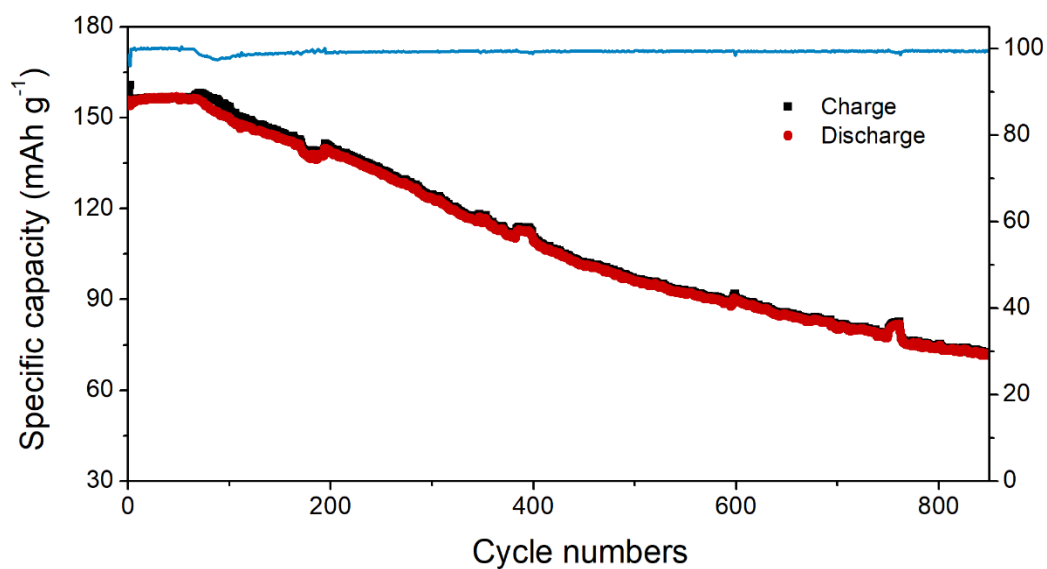


Figure S5.6 Cycling performance of the Li/gel polymer/ LFP cell without using LAGP as the electrolyte at 0.5C.

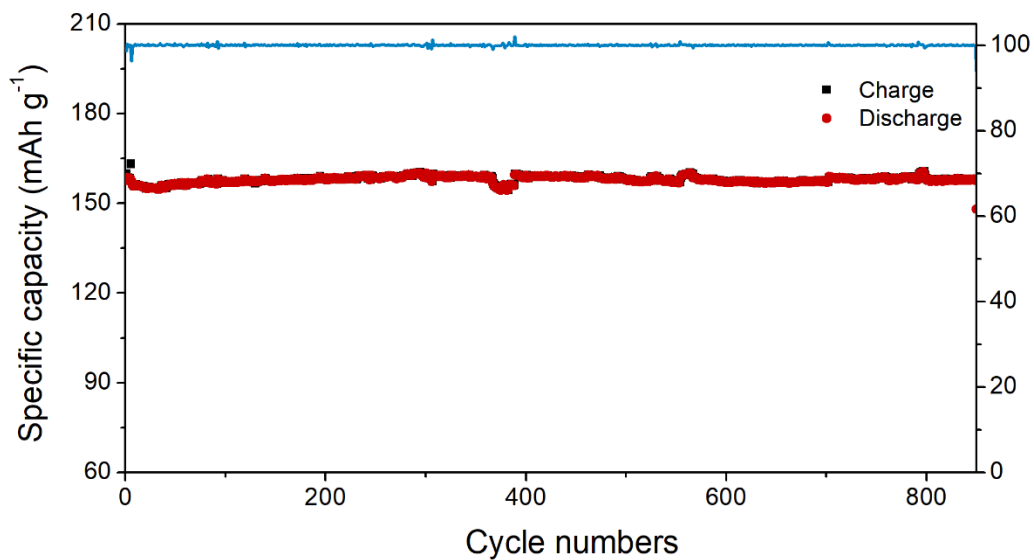


Figure S5.7 Cycling performance of the Li/ LFP cell with Con-pressed 1mm LAGP as the electrolyte at 0.5C.

Chapter 6

6 3D Printing of High-Performance Sodium Metal Batteries

Extrusion-based 3D printing is becoming a promising approach to construct high-performance energy storage devices with various shapes and form factors. However, 3D printing technique has not been applied to fabricate high-energy-density sodium metal batteries (SMBs) as great challenge lies at the printing of highly reactive sodium metal. Here, for the first time, an extrusion-based 3D printing approach was developed to construct a high-performance SMB consisting of a printed Na@rGO/CNT anode and a printed O3-NaCu_{1/9}Ni_{2/9}Fe_{3/9}Mn_{3/9}O₂ (denoted as NCNFM) cathode. The 3D-printed Na@rGO/CNT anode possesses multiple porosities, which could provide abundant active reaction sites and enable fast Na⁺ transport. Moreover, the resultant 3D structured Na@rGO/CNT can effectively suppress the Na dendrite growth by decreasing the local current density and releasing the huge volume change of Na during cycling. On the other hand, the 3D-printed micro-structured NCNFM cathode composed of interconnected CNTs and porous polymer framework can enable fast electron and ion transport as well as facilitated electrolyte penetration within the whole electrode. This work offers a promising approach to construct high-energy-density SMBs, which can also be extended to the developing of next-generation Na-S and Na-O₂ batteries.

6.1 Introduction

3D printing, also known as additive manufacturing (AM), has recently attracted tremendous interest in myriad different fields from medical science¹⁻² to electronics,³⁻⁴ robotics,⁵ and energy storage and conversion devices.⁶⁻⁸ This technique is considered to be an ideal manufacturing method since it can create complex 3D architectures accurately and efficiency and significantly reduce the manufacturing cost by eliminating the materials wastage. Up to now, various 3D printing techniques have been developed and employed in industry and academic for fabricating 3D structures.⁹⁻¹¹ Among them, extrusion-type 3D printing, known as robocasting or direct ink writing, is the most popular and used in a broad range of applications due to its simple printing mechanisms and inexpensive fabrication processes. Moreover, extrusion-type 3D printing can be applied to a wide range of materials including polymers,¹² ceramics,¹³ metal alloys,¹⁴ and electronically functional materials,¹⁵⁻¹⁶ which greatly broadens its applicability in a wide range of fields.

In recent years, extrusion-type 3D printing technique has been employed to construct various 3D structured electrodes or other components with controlled shapes, and periodic or aligned pores for energy storage systems. For instance, extrusion-based 3D printing has been applied to fabricate advanced electrodes for Li-ion batteries,¹⁷⁻¹⁹ Li-O₂/CO₂ batteries,²⁰⁻²² Li-S batteries,²³⁻²⁵ and supercapacitors.²⁶⁻²⁷ Apart from the electrode fabrication, 3D printing has also found applications in the fabrication of high-energy-density micro-batteries, which provides new possibilities for constructing customized energy storage devices. Lewis and co-workers first reported the fabrication of a 3D interdigitated Li-ion micro-battery using the 3D printing technique with the printed LiFePO₄ (LFP) and Li₄Ti₅O₁₂ (LTO) as the cathode and anode, respectively.²⁸ Following this work, Hu et al. successfully printed a micro-battery with enhanced performance based on highly concentrated graphene oxide composite inks.²⁹ Very recently, 3D printing technique has been employed to fabricate high-performance Li metal batteries (LMBs) with a 3D-printed Li anode and a 3D-printed LFP cathode by using cellulose nanofiber (CNF)-based inks,³⁰ which significantly improved the energy density due to the utilization of the printed Li metal anode. To the best of our knowledge, extrusion-based 3D printing technology has not been applied to fabricate sodium metal batteries (SMBs). SMBs are attracting much research interest due to the high capacity, low cost, and abundant natural source of Na metal.³¹⁻³² However, Na metal is highly

chemically reactive, forming dendrite easily during the repetitive electrochemical cycling. Despite various 3D hosts, such as metal foam,³³⁻³⁴ carbon felt,³⁵⁻³⁶ and graphene foam,³⁷ have been employed to suppress the Na dendrite growth, the fabrication procedures of these 3D hosts are usually time-consuming and considerably expensive, which are hardly realizing scalable application. Additionally, it is a great challenge to control the shapes and thickness of Na metal-based electrodes with traditional manufacturing methods. Therefore, SMBs with conventional Na metal electrodes have limited form factors, which have limitations in customization and integration with other complex-shaped electronics. It is thus urgent to develop Na-based electrodes with tunable shape and thickness for high-energy-density customizable SMBs.

Herein, we for the first time successfully fabricated self-supported 3D structured Na@rGO/CNT composite anodes and O₃-NaCu_{1/9}Ni_{2/9}Fe_{3/9}Mn_{3/9}O₂ (denoted as NCFM) cathodes using the layer-by-layer extrusion-type 3D printing approach for high-energy-density SMBs. The 3D-printed Na@rGO/CNT composite electrodes were created in two steps. First, a GO/CNT scaffold with tunable thickness was printed into designed 3D architectures based on a GO/CNT aqueous ink with suitable viscosity and shear-thinning feature, and the Na@rGO/CNT composite was then prepared by infusing Na into the GO/CNT scaffold, which is similar to the process of melting Li into graphene oxide (GO).³⁸ The 3D-printed Na@rGO/CNT composite electrodes with multiple porosities could provide abundant active reaction sites and enable fast Na⁺ transport. Moreover, the resultant 3D structured Na composite can effectively suppress the Na dendrite growth by decreasing the local current density and releasing the volume change during the sodiation/desodiation process. For the cathode part, the 3D structured self-supported NCFM electrodes were successfully fabricated with designed architecture based on a high viscosity ink consisting of NCFM particles as active materials, acetylene black (AB) and multiwalled carbon nanotubes (CNTs) as the conducting agent, and poly(vinylidene fluoride-co-hexafluoropropylene) (PVDF-HFP) as the binder dissolved in N-methyl-2-pyrrolidone (NMP). The 3D-printed microstructured NCFM electrodes possess several advantages, such as increased surface area and facilitated electrolyte penetration. Additionally, the continuous filaments composed of interconnected CNTs and porous polymer framework are forming a continuous conducting network, which could enable fast electron and ion transport within the whole electrode. Our work demonstrates that extrusion-type 3D printing is a powerful strategy for the fabrication of high-

performance SMBs. This work will also shed light on the fabrication of advanced energy storage devices with customized designs.

6.2 Experimental Section

6.2.1 Material synthesis

The O3-NCNFM was synthesized by a traditional solid-state reaction. Typically, a stoichiometric mixture of Na_2CO_3 (99%, Sigma-Aldrich), CuO (99%, Sigma-Aldrich), NiO (99%, Sigma-Aldrich), Fe_2O_3 (99%, Sigma-Aldrich), and Mn_2O_3 (99%, Sigma-Aldrich) was ball-milled for 5h in ethanol. An excess of 5% Na_2CO_3 was added to compensate the sodium loss at high temperature. The mixture was dried at 80°C for 10h. The obtained powders were then pressed into pellets, afterward, the pellets were heated at 850°C for 15h. The heated pellets were cooled to room temperature and then transferred to argon- filled glovebox until use.

6.2.2 Preparation of GO/CNT ink

The typical fabrication process of GO/CNT ink was described as follows: 50 mg MWCNT (diameter of 40 – 60 nm, length of 2 μm) was dispersed into 50 ml GO aqueous solution (GO ~ 4mg/ml) and the mixture was then ultra-sonicated for 3h to obtain a well-dispersed suspension. Afterward, the GO/CNT suspension was concentrated by centrifugation to form a higher concentration of around 40 mg/ml. The concentrated suspension was further mixed well in a conditioning mixer (ARM, Thinky) at 2000 rpm for 10 min to obtain a homogenous and viscous ink.

6.2.3 Preparation of NCNFM ink

The NCNFM ink was prepared by first mixing 900 mg of as-prepared Na-CNFM powders, 200 mg of acetylene black (AB), and 100 mg of MWCNT followed by mixing them well for a few minutes. Then 1500 mg of 20% PVDF-HFP dissolved in NMP (PVDF-HFP 300 mg) was added into the mixed powders as a binder, the mixed gel was then transferred into a conditioning mixer (ARM 310, Thinky) to further mix the ink at 2000 rpm for around 30 min. After that, a homogenous and high viscous ink was obtained for 3D printing.

6.2.4 3D printing process

The 3D printing process was conducted on a fused filament fabrication (FFF) DeltaMaker 3D printer modified with a paste extrusion-type tool head. The syringe with GO/CNT or NCNFM ink was subject to centrifugation at 3000 rpm for 3 minutes to expel out the air-bubbles prior to the printing process. A Nordson EFD computer-controlled pneumatic fluid dispenser provides the appropriate pressure to extrude the ink through a metal nozzle with an inner diameter of 200 μm and control the flow rate. The printing speed ranges from 6 mm s^{-1} to 12 mm s^{-1} depending on the printing pressure and ink viscosity. The as-printed structures were freeze-dried for 24h.

6.2.5 Fabrication of Na@rGO/CNT composite electrodes

The printed GO/CNT skeleton was used as a 3D Na host. Thermal infusion of Na melting was carried out inside the Argon-filled glove box with both water and O_2 level less than 0.1 ppm. Bulk Na (from Aldrich) was cut into small pieces first and then melted in a stainless-steel boat on a hot plate at $\sim 300^\circ\text{C}$. The GO/CNT skeleton was instantaneously reduced to rGO/CNT by contacting with molten Na. Afterward, Na was slowly absorbed into the rGO/CNT skeleton, and the amount of Na infused can be controlled by controlling the contact time. The Na@rGO/CNT composite was finally obtained and can be directly used as the anode.

6.2.6 Materials Characterizations:

The morphologies of the GO/CNT and Na@rGO/CNT composites were checked by using a Hitachi 3400N Environmental scanning electron microscopy at an acceleration voltage of 5 kV. The morphologies of the printed NCNFM electrode were determined by using a Hitachi s-4800 field-emission scanning electron microscopy.

6.2.7 Electrochemical Measurements:

Symmetric coin cells were used for studying the plating/stripping processes with the printed Na@rGO/CNT composites electrodes as the working electrode and the counter electrode. The electrolyte used in this study was 1 M sodium hexafluorophosphate (NaFP_6 98%, Aldrich) dissolved in diglyme (Sigma Aldrich) without any additives. The symmetric cell of Na foil was used to compare with printed Na@rGO/CNT. Constant current densities were applied to the

electrodes during repeated plating/stripping process while transient potential was recorded over time. The full cell was assembled in a CR2032-type coin cell, where the printed planar Na@rGO/CNT and NCNFM electrodes were used as the anode and cathode, respectively. The specific capacity was calculated based on the weight of the printed NCNFM electrode. The galvanostatic charge/discharge performance was evaluated with a LAND test system in the voltage range of 2.0-4.0 V (vs. Na⁺/Na) at room temperature.

6.3 Results and Discussions

6.3.1 Morphology and Structure Characterization

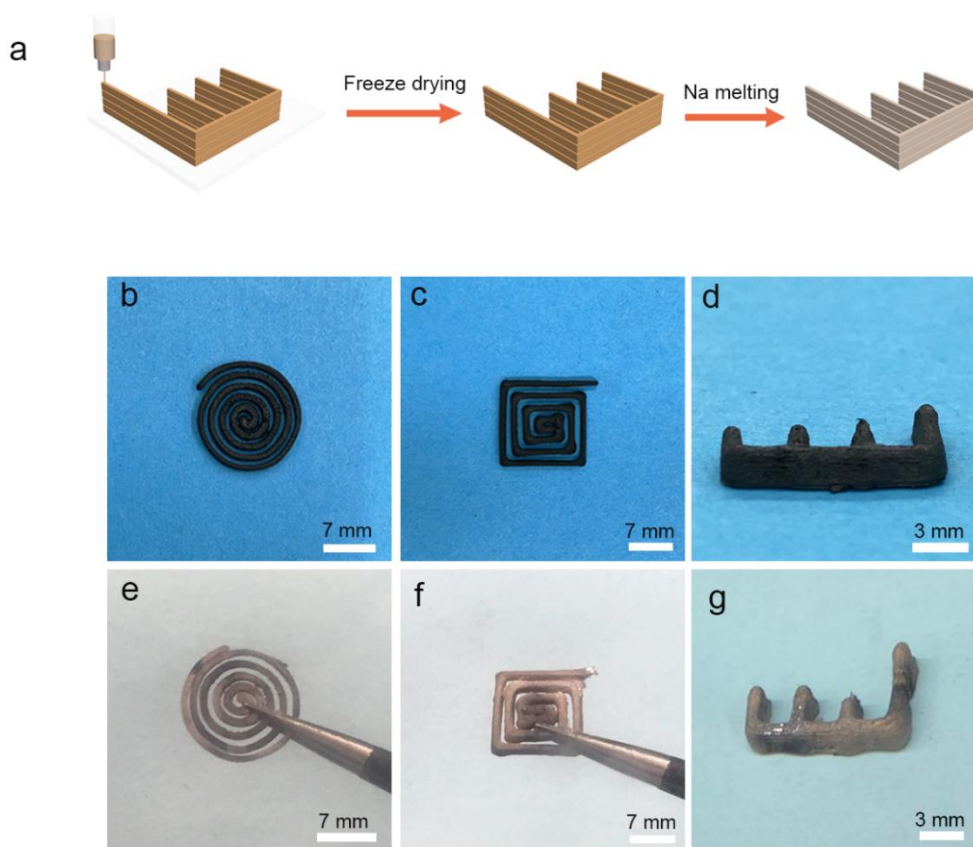


Figure 6.1 Fabrication of the 3D micro-structured Na@rGO/CNT anodes. (a) Schematic process of a typical 3D-printed Na@rGO/CNT electrode. (b-d) Optical images of the GO/CNT skeletons with different 3D-printing patterns. (e-g) Corresponding optical images of 3D-printed Na@rGO/CNT electrodes after Na infusion into the different 3D-printed skeletons.

The fabrication process for the 3D micro-structured Na@rGO/CNT anodes is illustrated in **Figure 6.1a**. Typically, a 3D interdigitated GO/CNT structure was first printed through an extrusion-based direct ink writing (DIW) method (detailed information seen from Experimental section) by using a homogenous and concentrated GO-based suspension. The 3D printed interdigitated structure was subsequently freeze-dried to obtain the GO/CNT aerogel skeleton. Due to the mechanically robust properties of the 3D printed GO/CNT aerogel, 3D micro-structured Na@rGO/CNT electrodes can be prepared after Na infusion into the space between the rGO sheets and the interdigitated skeleton can be well maintained.³⁹ The porous structure of the 3D Na@ rGO/CNT composite induced from the freeze-drying process not only enabled the 3D Na electrodes with high-aspect-ratio, but also reduced local current density, and mitigated the large volume expansion of the Na during the plating/stripping process, which can effectively suppress the Na dendrite growth. **Figure 6.1b-6.1d** shows the optical images of the 3D-printed GO/CNT skeletons with different patterns. **Figure 6.1e-6.1f** are the optical images of the obtained Na@rGO/CNT composite electrodes after Na infusion into the different 3D-printed skeletons. It should be noted that all the Na@rGO/CNT composite electrodes can maintain the shape of the GO/CNT skeleton very well.

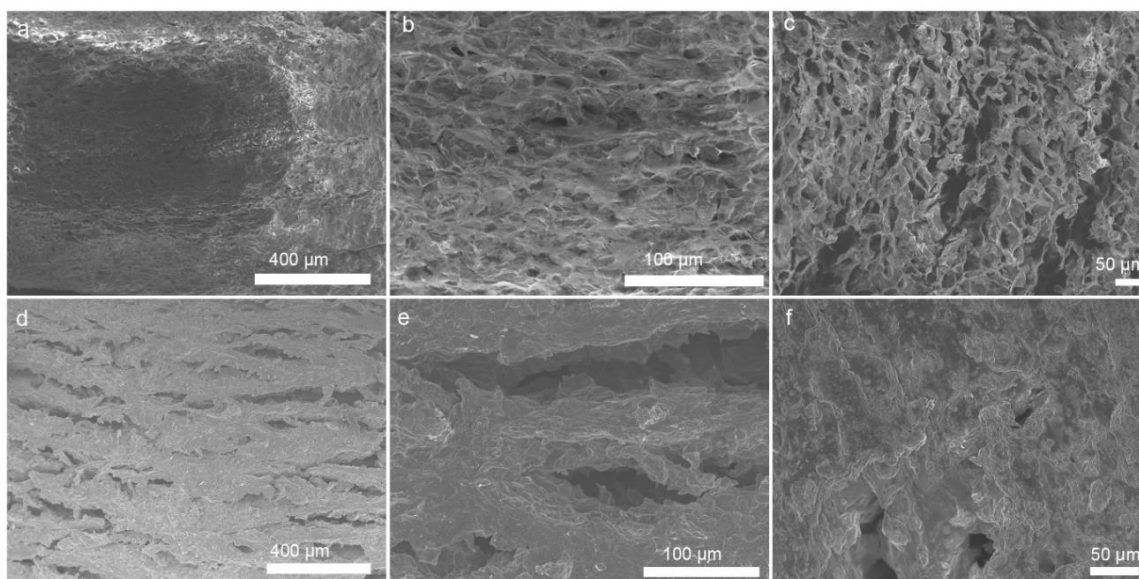


Figure 6.2 Morphological characterizations of the 3D-printed architectures. Top-view SEM images of the 3D-printed GO/CNT skeleton (a and b) and the 3D-printed Na@rGO/CNT composite electrode (d and e). Cross-sectional SEM images of (c) 3D-printed GO/CNT and (f) Na@rGO/CNT.

The morphologies and microstructures of the 3D-printed GO/CNT skeleton before and after Na infusion were studied by scanning electron microscopy (SEM). **Figure 6.2a** shows the top-view SEM of the printed GO/CNT interdigitated skeleton with a clear layer-by-layer structure, in which each filament has the same diameter of around 200 μm . The adjacent filaments were closely connected which was beneficial for maintaining the structure during the Na melting process. The enlarged top-view SEM (**Figure 6.2b**) and cross-sectional SEM (**Figure 6.2c**) of the printed GO/CNT skeleton showing a highly porous structure, where the pores with a diameter of tens of micrometer are derived from the removal of water during the freeze-drying process. **Figure 6.2d** and **6.2e** displays the top-view SEM image of the Na@rGO/CNT skeleton after Na infused into the GO/CNT. It can be clearly found that the Na uniformly covered the whole surface of the skeleton, where the boundary of the filaments was disappeared because of the expansion of graphene oxide and continuous coverage of the Na on the boundary during infusion process. More importantly, the obtained Na@rGO/CNT skeleton still maintained the porous structure well, which is essential for mitigating the huge volume change of Na during the plating/stripping process. **Figure 6.2f** displays the cross-sectional SEM image of the Na@rGO/CNT. It can be observed that the infused Na has partially filled the pores of GO/CNT skeleton, which could ensure a high amount of Na in the composite and provide high areal capacity.

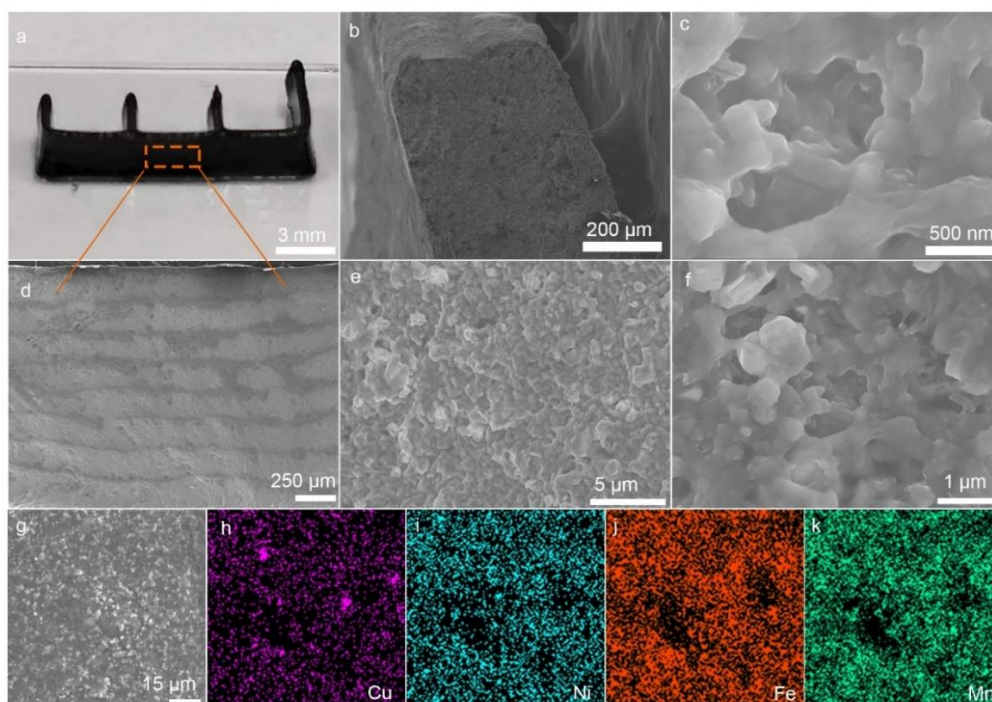


Figure 6.3 Morphology characterizations of the 3D-printed NCNFM cathode architectures. a) Optical image of the 3D-printed interdigital patterned cathode. b) Cross-sectional SEM image of the cathode electrode. c) High-magnification cross-sectional SEM image of the electrode, indicating an internally porous structure. (d-f) Top-view SEM images of the cathode electrode. (g-k) Elemental mappings of the Cu, Ni, Fe, and Mn distributed in the cathode electrode.

After successfully printed the micro-structured Na composite electrode, we further fabricated micro-structured cathode electrodes via the DIW method. Cu doped O₃-NaCu_{1/9}Ni_{2/9}Fe_{3/9}Mn_{3/9}O₂ (denoted as NCNFM) was used as the cathode material due to its high capacity, structural stability, and moisture stability.⁴⁰⁻⁴¹ The ink preparation process was based on our previous work,¹⁹ the detailed information can be found from the experimental section (preparation of NCNFM ink). **Figure 6.3a** shows the optical image of 3D printed interdigital patterned NCNFM cathode after freeze-dried. The NCNFM electrode contained 12 layers and maintained the as-printed shape very well with adjacent layers stacked together tightly. The morphologies of the printed NCNFM were investigated by SEM. As seen from the cross-sectional SEM image in **Figure 6.3b**, the width of the filament was approximately 200 μm, which is a little smaller than that of the printing nozzle. The skeleton was constructed from two closely stacked layers, which can increase the structural integrity of the whole electrode compared to one layer. The magnified SEM (**Figure 6.3c**) displayed the detailed morphology within the filament. It can be found that the NCNFM particles and conducting carbon were interconnected and forming a hierarchical porous structure after the phase-inversion and removal of water during the freeze-drying process. From the surface-view SEM image (**Figure 6.3d**), the printed NCNFM electrode presents an obvious layered structure, in which the height of each filament is around 200 μm, and each layer is stacked tightly with a clear boundary. The enlarged SEM images (**Figure 6.3e and 6.3f**) further revealed the porous and interconnected conducting framework, which can facilitate the ion/electron transport within the whole electrode.

6.3.2 Electrochemical Characterization

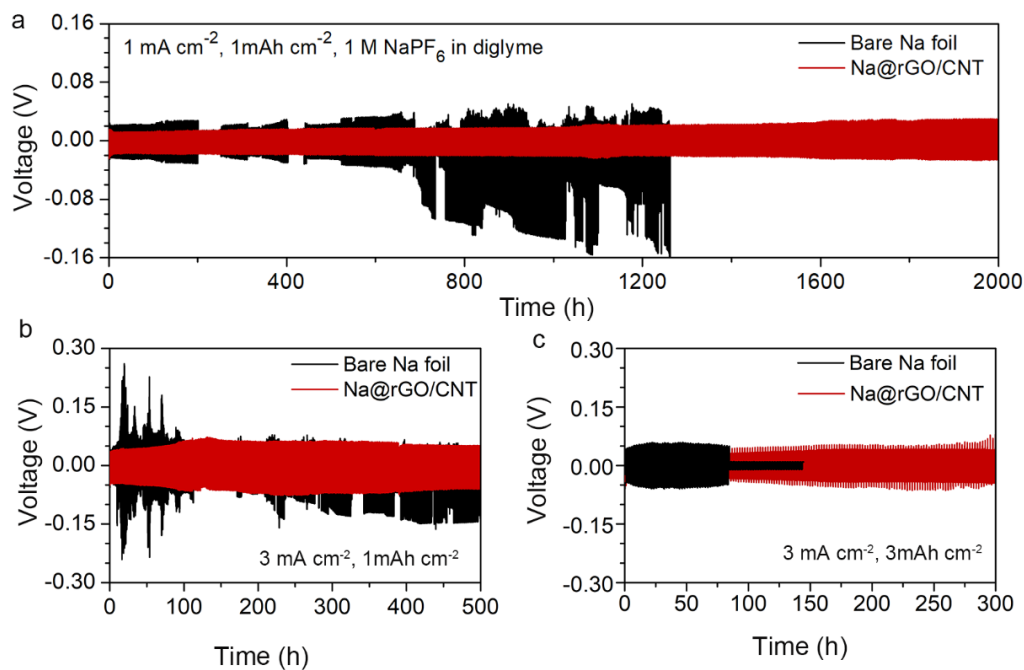


Figure 6.4 Cycling performance of symmetric cells with the 3D-printed rGO/CNT-Na and Na foil electrodes at current densities of (a) 1 mA cm^{-2} and (b) 3 mA cm^{-2} with an areal capacity of 1 mAh cm^{-2} . (c) Symmetric cell cycling performance at a current density of 3 mA cm^{-2} with a high areal capacity of 3 mAh cm^{-2} .

To investigate the cycling stability of the printed Na composite anodes, the 3D-printed Na@rGO/CNT electrode with a planar structure was fabricated and symmetric cells were used to determine the cycling performance of the 3D-printed Na@rGO/CNT composite anode at different current densities and charge/discharge time. Bare Na foil symmetric cells served as the control group. **Figure 6.4a** displays the extended voltage profiles of the symmetric cells at a current density of 1 mA cm^{-2} with an areal capacity of 1 mAh cm^{-2} . As depicted, the 3D-printed Na@rGO/CNT electrode exhibited a more stable voltage curve with a low voltage hysteresis for more than 2000 h. In contrast, the voltage profile of the bare Na foil showed a gradually increased voltage hysteresis and was only stable for over 200 h, which was caused by the formation of Na dendrite. Further increasing the current density to 3 mA cm^{-2} , the voltage hysteresis of bare Na foil began increasing after 30 h and severe fluctuating voltage profiles occurs with overpotential rising to around 150 mV after 230h as presented in **Figure 6.4b**. The increasing of voltage hysteresis and

appearance of fluctuating voltage profiles can be ascribed to the detrimental Na dendrite growth and formation of dead Na, leading to short-circuiting. However, 3D-printed Na@rGO/CNT composites can be stably cycled at this elevated current density with a lower overpotential of less than 50 mV even after 500 h, suggesting an improved plating/stripping performance of 3D-printed Na@rGO/CNT composites. To further demonstrate the advantages of the 3D porous structured Na composites, the cycling performance of symmetric cells with 3D-printed Na@rGO/CNT and bare Na foil electrodes was tested with a high areal capacity of 3 mAh cm⁻². It should be noted that high areal capacity is crucial for practical application, however, more reported Na electrodes are tested with a low areal capacity of 1mAh cm⁻² or even lower for achieving a stable cycling performance in symmetric cells, and it is of great challenge to achieve stable performance with a high areal capacity. **Figure 6.4c** presents the cycling stability and voltage profiles of 3D-printed Na@rGO/CNT and bare Na foil electrodes at a high current density of 3 mA cm⁻² with a high capacity of 3mAh cm⁻². The Na@rGO/CNT electrode displayed a smaller initial overpotential compared to the Na foil. Moreover, the bare Na foil showed poor cycling stability with a short-circuiting happened after 75h. Notably, the 3D-printed Na@rGO/CNT electrode displayed a much more stable plating/stripping process with no obviously increased voltage hysteresis after 300 h. This result demonstrates that the 3D-printed Na@rGO/CNT composites could meet the level of high capacity for practical application.

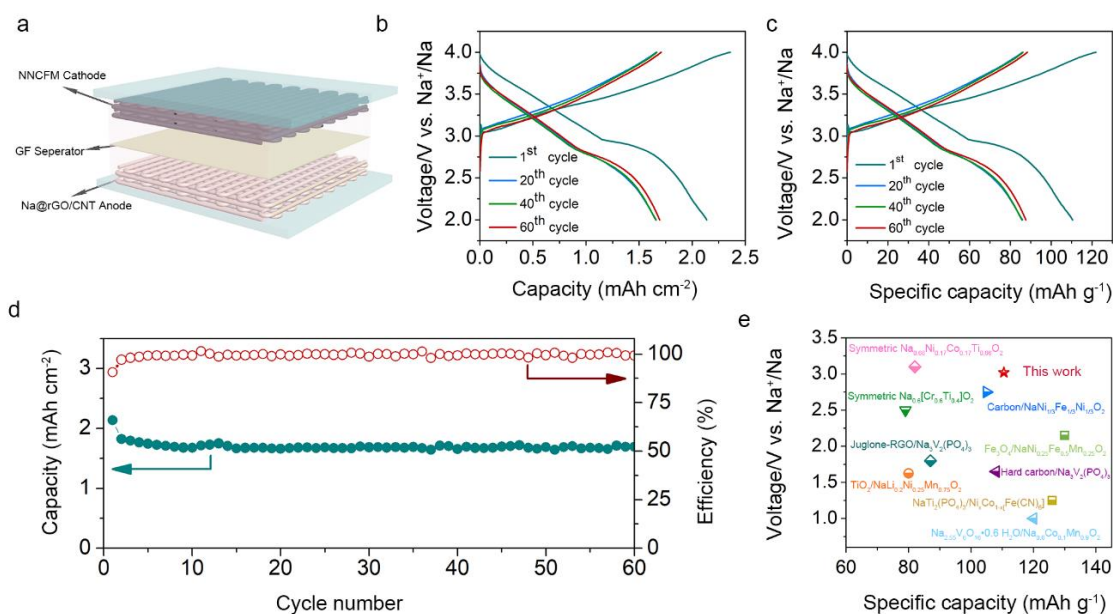


Figure 6.5 Electrochemical performance of the sodium metal full cell (a) Schematic illustrating the assembled cell structure with printed Na@rGO/CNT anode and printed NCNFM cathode. (b and c) The 1st, 20th, 40th, and 60th charge/discharge profiles of the full cell with Na@rGO/CNT anode and NCNFM cathode. (d) Cycling performance of the full cell with Na@rGO/CNT anode and NCNFM cathode. at 0.2C over 60 cycles. (e) Comparison of current sodium metal full cell with those reported in literatures.

To further estimate the structural advantages of the printed electrodes in the full cell, we investigated the electrochemical performance of the sodium metal full cell assembled with printed electrodes. **Figure 6.5a** illustrate the full cell structure with printed Na@rGO/CNT and printed NCNFM as the anode and the cathode, respectively. The current and capacity of the full cell were determined by the mass of NCNFM in the printed cathode. In order to achieve high areal capacity, a printed NCNFM electrode with mass loading of around 20 mg cm⁻² was adopted as the cathode in the full cell. **Figure 6.5b and 6.5c** present the charge/discharge profiles of the Na@rGO/CNT||NCNFM full cell in different cycles. The initial cycle was measured at a lower current density of 0.05C for activation and it could deliver a high specific capacity of 110.5 mAh g⁻¹ (corresponding to an areal capacity of 2.2 mAh cm⁻²). The subsequent cycles were examined at 0.2C. As observed from the curves, it exhibited a higher capacity of 87.5 mAhg⁻¹(corresponding to an areal capacity of 1.7 mAh cm⁻²) even after 60 cycles. **Figure 6.5d** shows the cycling performance of the full cell tested at 0.2 C over 60 cycles, which suggests impressive capacity retention of approximately 93% (calculated based on the capacity in the 2nd cycle). The extremely stable cycling performance of the full cell can be attributed the structural superiorities of the printed electrodes. First, the printed micro-structured NCNFM cathode possesses a 3D porous conducting network, which can enable fast electron and ion transport as well as facilitated electrolyte penetration within the whole electrode. Second, the printed Na@rGO/CNT composite anode with multiple porosities can effectively suppress the Na dendrite growth by decreasing the local current density and releasing the volume change during the sodiation/desodiation process. To estimate the standing of our Na@rGO/CNT||NCNFM full cell, we compare the electrochemical performance of the printed Na@rGO/CNT||NCNFM full cell with that of other full cells recently reported in the literature in terms of specific capacity and output voltage as shown in **Figure 6.5e**.^{40, 42-49} It clearly presents that our printed full cell outperforms most of the reported full cells with

regard to specific capacity and voltage. The results suggest that 3D printing provides a promising strategy in fabricating 3D structured electrodes for achieving high-energy-density storage devices.

6.4 Conclusions

In summary, an extrusion-type 3D printing approach was first developed to construct a high-performance SMB which was assembled by a printed Na@rGO/CNT anode and a printed NCNFM cathode. The 3D-printed Na@rGO/CNT anode possesses multiple porosities, which could provide abundant active reaction sites and enable fast Na⁺ transport. Moreover, the resultant 3D structured Na@rGO/CNT can effectively suppress the Na dendrite growth by decreasing the local current density and releasing the huge volume change of Na during cycling. As a result, the printed Na@rGO/CNT composite can deliver extremely stable performance over 2000 h (~1000 cycles) at a current density of 1 mA cm⁻². Even with a high capacity of 3mAh cm⁻², the Na@rGO/CNT composite can still exhibit a long-lifetime of 300 h at a current density of 3 mA cm⁻², which is almost three times higher than that of the bare Na foil. On the other hand, the 3D-printed microstructured NCNFM cathode composed of interconnected CNTs and porous polymer framework can enable fast electron and ion transport as well as facilitated electrolyte penetration within the whole electrode. When the 3D-printed Na@rGO/CNT anode and the 3D-printed NCNFM cathode were tested in a full cell, it delivered a higher initial specific capacity of 110.5 mAh g⁻¹ (corresponding to an areal capacity of 2.2 mAh cm⁻²) and maintained impressive capacity retention of approximately 93%. This work thus offers a promising approach to construct high-performance Na-metal batteries, which can also be extended to develop next-generation high energy density Na-S and Na-O₂ batteries.

Acknowledgements

The work was supported by Natural Science Foundation of China (NSFC) (Grant U1432249), the National Key R&D Program of China (Grant 2017YFA0205002), and the Priority Academic Program Development (PAPD) of Jiangsu Higher Education Institutions. This is also a project supported by Jiangsu Key Laboratory for Carbon-Based Functional Materials and Devices and Collaborative Innovation Center of Suzhou Nano Science & Technology. This work was also supported by the Natural Science and Engineering Research Council of Canada (NSERC), the

Canada Research Chair Program (CRC), the Canada Foundation for Innovation (CFI), and the University of Western Ontario (UWO).

6.5 References

1. Forget, A.; Blaeser, A.; Miessmer, F.; Kopf, M.; Campos, D. F. D.; Voelcker, N. H.; Blencowe, A.; Fischer, H.; Shastri, V. P., Mechanically Tunable Bioink for 3D Bioprinting of Human Cells. *Adv. Healthc. Mater.* **2017**, *6* (20).
2. Qian, F.; Zhu, C.; Knipe, J. M.; Ruelas, S.; Stolaroff, J. K.; DeOtte, J. R.; Duoss, E. B.; Spadaccini, C. M.; Henard, C. A.; Guarnieri, M. T.; Baker, S. E., Direct Writing of Tunable Living Inks for Bioprocess Intensification. *Nano Lett.* **2019**.
3. Valentine, A. D.; Busbee, T. A.; Boley, J. W.; Raney, J. R.; Chortos, A.; Kotikian, A.; Berrigan, J. D.; Durstock, M. F.; Lewis, J. A., Hybrid 3D Printing of Soft Electronics. *Adv. Mater.* **2017**, *29* (40), 1703817.
4. Yang, H.; Leow, W. R.; Chen, X., 3D Printing of Flexible Electronic Devices. *Small Methods* **2018**, *2* (1), 1700259.
5. Gul, J. Z.; Sajid, M.; Rehman, M. M.; Siddiqui, G. U.; Shah, I.; Kim, K. H.; Lee, J. W.; Choi, K. H., 3D Printing for Soft Robotics - A Review. *Sci. Tech. Adv. Mater.* **2018**, *19* (1), 243-262.
6. Liu, Y.; Zhang, B.; Xu, Q.; Hou, Y.; Seyedin, S.; Qin, S.; Wallace, G. G.; Beirne, S.; Razal, J. M.; Chen, J., Development of Graphene Oxide/Polyaniline Inks for High Performance Flexible Microsupercapacitors via Extrusion Printing. *Adv. Funct. Mater.* **2018**, *28* (21), 1706592.
7. Tang, X.; Zhu, C.; Cheng, D.; Zhou, H.; Liu, X.; Xie, P.; Zhao, Q.; Zhang, D.; Fan, T., Architected Leaf-Inspired $\text{Ni}_{0.33}\text{Co}_{0.66}\text{S}_2$ /Graphene Aerogels via 3D Printing for High-Performance Energy Storage. *Adv. Funct. Mater.* **2018**, *28* (51), 1805057.

8. Díaz-Marta, A. S.; Tubío, C. R.; Carbajales, C.; Fernández, C.; Escalante, L.; Sotelo, E.; Guitián, F.; Barrio, V. L.; Gil, A.; Coelho, A., Three-Dimensional Printing in Catalysis: Combining 3D Heterogeneous Copper and Palladium Catalysts for Multicatalytic Multicomponent Reactions. *ACS Catal.* **2017**, *8* (1), 392-404.
9. Ruiz-Morales, J. C.; Tarancón, A.; Canales-Vázquez, J.; Méndez-Ramos, J.; Hernández-Afonso, L.; Acosta-Mora, P.; Marín Rueda, J. R.; Fernández-González, R., Three dimensional printing of components and functional devices for energy and environmental applications. *Energy Environ. Sci.* **2017**.
10. Choi, K.-H.; Ahn, D. B.; Lee, S.-Y., Current Status and Challenges in Printed Batteries: Toward Form Factor-Free, Monolithic Integrated Power Sources. *ACS Energy Lett.* **2017**, *3* (1), 220-236.
11. Tay, Y. W. D.; Panda, B.; Paul, S. C.; Noor Mohamed, N. A.; Tan, M. J.; Leong, K. F., 3D Printing Trends in Building and Construction Industry: A Review. *Virtual Phys. Prototy.* **2017**, *12* (3), 261-276.
12. Dizon, J. R. C.; Espera, A. H.; Chen, Q.; Advincula, R. C., Mechanical Characterization of 3D-Printed Polymers. *Addit. Manuf.* **2018**, *20*, 44-67.
13. Nguyen, D. T.; Meyers, C.; Yee, T. D.; Dudukovic, N. A.; Destino, J. F.; Zhu, C.; Duoss, E. B.; Baumann, T. F.; Suratwala, T.; Smay, J. E.; Dylla-Spears, R., 3D-Printed Transparent Glass. *Adv. Mater.* **2017**, *29* (26), 1701181-n/a.
14. Yan, P.; Brown, E.; Su, Q.; Li, J.; Wang, J.; Xu, C.; Zhou, C.; Lin, D., 3D Printing Hierarchical Silver Nanowire Aerogel with Highly Compressive Resilience and Tensile Elongation through Tunable Poisson's Ratio. *Small* **2017**, 1701756-n/a.

15. Guo, S. Z.; Qiu, K.; Meng, F.; Park, S. H.; McAlpine, M. C., 3D Printed Stretchable Tactile Sensors. *Adv. Mater.* **2017**, *29* (27).
16. Ota, H.; Emaminejad, S.; Gao, Y.; Zhao, A.; Wu, E.; Challa, S.; Chen, K.; Fahad, H. M.; Jha, A. K.; Kiriya, D.; Gao, W.; Shiraki, H.; Morioka, K.; Ferguson, A. R.; Healy, K. E.; Davis, R. W.; Javey, A., Application of 3D Printing for Smart Objects with Embedded Electronic Sensors and Systems. *Adv. Mater. Tech.* **2016**, *1* (1), 1600013.
17. Zhang, C.; Shen, K.; Li, B.; Li, S.; Yang, S., Continuously 3D printed quantum dot-based electrodes for lithium storage with ultrahigh capacities. *J. Mater. Chem. A* **2018**, *6* (41), 19960-19966.
18. Saleh, M. S.; Li, J.; Park, J.; Panat, R., 3D printed hierarchically-porous microlattice electrode materials for exceptionally high specific capacity and areal capacity lithium ion batteries. *Addit. Manuf.* **2018**, *23*, 70-78.
19. Wang, J.; Sun, Q.; Gao, X.; Wang, C.; Li, W.; Holness, F. B.; Zheng, M.; Li, R.; Price, A. D.; Sun, X.; Sham, T. K.; Sun, X., Toward High Areal Energy and Power Density Electrode for Li-Ion Batteries via Optimized 3D Printing Approach. *ACS Appl. Mater. Interfaces* **2018**, *10* (46), 39794-39801.
20. Qiao, Y.; Liu, Y.; Chen, C.; Xie, H.; Yao, Y.; He, S.; Ping, W.; Liu, B.; Hu, L., 3D-Printed Graphene Oxide Framework with Thermal Shock Synthesized Nanoparticles for Li-CO₂ Batteries. *Adv. Funct. Mater.* **2018**, *28* (51), 1805899.
21. Lyu, Z.; Lim, G. J. H.; Guo, R.; Kou, Z.; Wang, T.; Guan, C.; Ding, J.; Chen, W.; Wang, J., 3D-Printed MOF-Derived Hierarchically Porous Frameworks for Practical High-Energy Density Li-O₂ Batteries. *Adv. Funct. Mater.* **2019**, *29* (1), 1806658.

22. Lacey, S. D.; Kirsch, D. J.; Li, Y.; Morgenstern, J. T.; Zarket, B. C.; Yao, Y.; Dai, J.; Garcia, L. Q.; Liu, B.; Gao, T.; Xu, S.; Raghavan, S. R.; Connell, J. W.; Lin, Y.; Hu, L., Extrusion-Based 3D Printing of Hierarchically Porous Advanced Battery Electrodes. *Adv. Mater.* **2016**, 1705651-n/a.
23. Shen, K.; Mei, H.; Li, B.; Ding, J.; Yang, S., 3D Printing Sulfur Copolymer-Graphene Architectures for Li-S Batteries. *Adv. Energy Mater.* **2018**, 8 (4), 1701527.
24. Gao, X.; Sun, Q.; Yang, X.; Liang, J.; Koo, A.; Li, W.; Liang, J.; Wang, J.; Li, R.; Holness, F. B.; Price, A. D.; Yang, S.; Sham, T.-K.; Sun, X., Toward a Remarkable Li-S battery via 3D Printing. *Nano Energy* **2019**, 56, 595-603.
25. Milroy, C.; Manthiram, A., Printed Microelectrodes for Scalable, High-Areal-Capacity Lithium–Sulfur Batteries. *Chem. Commun.* **2016**, 52 (23), 4282-4285.
26. Yao, B.; Chandrasekaran, S.; Zhang, J.; Xiao, W.; Qian, F.; Zhu, C.; Duoss, E. B.; Spadaccini, C. M.; Worsley, M. A.; Li, Y., Efficient 3D Printed Pseudocapacitive Electrodes with Ultrahigh MnO₂ Loading. *Joule* **2019**, 3 (2), 459-470.
27. Jiang, Y.; Xu, Z.; Huang, T.; Liu, Y.; Guo, F.; Xi, J.; Gao, W.; Gao, C., Direct 3D Printing of Ultralight Graphene Oxide Aerogel Microlattices. *Adv. Funct. Mater.* **2018**, 28 (16), 1707024.
28. Sun, K.; Wei, T. S.; Ahn, B. Y.; Seo, J. Y.; Dillon, S. J.; Lewis, J. A., 3D printing of interdigitated Li-ion microbattery architectures. *Adv. Mater.* **2013**, 25 (33), 4539-43.
29. Fu, K.; Wang, Y.; Yan, C.; Yao, Y.; Chen, Y.; Dai, J.; Lacey, S.; Wang, Y.; Wan, J.; Li, T.; Wang, Z.; Xu, Y.; Hu, L., Graphene Oxide-Based Electrode Inks for 3D-Printed Lithium-Ion Batteries. *Adv. Mater.* **2016**, 28 (13), 2587-2594.

30. Cao, D.; Xing, Y.; Tantratian, K.; Wang, X.; Ma, Y.; Mukhopadhyay, A.; Cheng, Z.; Zhang, Q.; Jiao, Y.; Chen, L.; Zhu, H., 3D Printed High-Performance Lithium Metal Microbatteries Enabled by Nanocellulose. *Adv. Mater.* **2019**, *31* (14), e1807313.
31. Zhao, Y.; Adair, K. R.; Sun, X., Recent Developments and Insights into the Understanding of Na Metal Anodes for Na-Metal Batteries. *Energy Environ. Sci.* **2018**, *11* (10), 2673-2695.
32. Zheng, X.; Bommier, C.; Luo, W.; Jiang, L.; Hao, Y.; Huang, Y., Sodium Metal Anodes for Room-Temperature Sodium-Ion Batteries: Applications, Challenges and Solutions. *Energy Storage Mater.* **2019**, *16*, 6-23.
33. Wang, T.-S.; Liu, Y.; Lu, Y.-X.; Hu, Y.-S.; Fan, L.-Z., Dendrite-free Na Metal Plating/Stripping onto 3D Porous Cu Hosts. *Energy Storage Mater.* **2018**, *15*, 274-281.
34. Liu, S.; Tang, S.; Zhang, X.; Wang, A.; Yang, Q.-H.; Luo, J., Porous Al Current Collector for Dendrite-Free Na Metal Anodes. *Nano Lett.* **2017**, *17* (9), 5862-5868.
35. Chi, S.-S.; Qi, X.-G.; Hu, Y.-S.; Fan, L.-Z., 3D Flexible Carbon Felt Host for Highly Stable Sodium Metal Anodes. *Adv. Energy Mater.*, 1702764-n/a.
36. Luo, W.; Zhang, Y.; Xu, S.; Dai, J.; Hitz, E.; Li, Y.; Yang, C.; Chen, C.; Liu, B.; Hu, L., Encapsulation of Metallic Na in an Electrically Conductive Host with Porous Channels as a Highly Stable Na Metal Anode. *Nano Lett.* **2017**, *17* (6), 3792-3797.
37. Deng, W.; Zhou, X.; Fang, Q.; Liu, Z., Microscale Lithium Metal Stored inside Cellular Graphene Scaffold toward Advanced Metallic Lithium Anodes. *Adv. Energy Mater.*, 1703152-n/a.
38. Lin, D.; Liu, Y.; Liang, Z.; Lee, H. W.; Sun, J.; Wang, H.; Yan, K.; Xie, J.; Cui, Y., Layered reduced graphene oxide with nanoscale interlayer gaps as a stable host for lithium metal anodes. *Nat. Nanotech.* **2016**, *11* (7), 626-32.

39. Wang, A.; Hu, X.; Tang, H.; Zhang, C.; Liu, S.; Yang, Y.-W.; Yang, Q.-H.; Luo, J., Processable and Moldable Sodium-Metal Anodes. *Angew. Chem. Int. Ed. Engl.* **2017**, *56* (39), 11921-11926.
40. Kim, D.; Lee, E.; Slater, M.; Lu, W.; Rood, S.; Johnson, C. S., Layered $\text{Na}[\text{Ni}_{1/3}\text{Fe}_{1/3}\text{Mn}_{1/3}]\text{O}_2$ Cathodes for Na-ion Battery Application. *Electrochem. Commun.* **2012**, *18*, 66-69.
41. Li, Y.; Yang, Z.; Xu, S.; Mu, L.; Gu, L.; Hu, Y.-S.; Li, H.; Chen, L., Air-Stable Copper-Based $\text{P2-Na}_{7/9}\text{Cu}_{2/9}\text{Fe}_{1/9}\text{Mn}_{2/3}\text{O}_2$ as a New Positive Electrode Material for Sodium-Ion Batteries. *Adv. Sci.* **2015**, *2* (6), 1500031-n/a.
42. Xiong, H.; Slater, M. D.; Balasubramanian, M.; Johnson, C. S.; Rajh, T., Amorphous TiO_2 Nanotube Anode for Rechargeable Sodium Ion Batteries. *J. Phys. Chem. Lett.* **2011**, *2* (20), 2560-2565.
43. Oh, S. M.; Myung, S. T.; Yoon, C. S.; Lu, J.; Hassoun, J.; Scrosati, B.; Amine, K.; Sun, Y. K., Advanced $\text{Na}[\text{Ni}_{0.25}\text{Fe}_{0.5}\text{Mn}_{0.25}]\text{O}_2/\text{C-Fe}_3\text{O}_4$ sodium-ion batteries using EMS electrolyte for energy storage. *Nano Lett.* **2014**, *14* (3), 1620-6.
44. Guo, S.; Liu, P.; Sun, Y.; Zhu, K.; Yi, J.; Chen, M.; Ishida, M.; Zhou, H., A High-Voltage and Ultralong-Life Sodium Full Cell for Stationary Energy Storage. *Angew. Chem. Int. Ed. Engl.* **2015**, *54* (40), 11701-5.
45. Wang, H.; Hu, P.; Yang, J.; Gong, G.; Guo, L.; Chen, X., Renewable-juglone-based high-performance sodium-ion batteries. *Adv. Mater.* **2015**, *27* (14), 2348-54.
46. Wang, Y.; Xiao, R.; Hu, Y.-S.; Avdeev, M.; Chen, L., $\text{P2-Na}_{0.6}[\text{Cr}_{0.6}\text{Ti}_{0.4}]\text{O}_2$ cation-disordered electrode for high-rate symmetric rechargeable sodium-ion batteries. *Nat. Commun.* **2015**, *6*, 6954.

47. Yuan, Z.; Si, L.; Zhu, X., Three-dimensional hard carbon matrix for sodium-ion battery anode with superior-rate performance and ultralong cycle life. *J. Mater. Chem. A* **2015**, *3* (46), 23403-23411.
48. Peng, J.; Wang, J.; Yi, H.; Hu, W.; Yu, Y.; Yin, J.; Shen, Y.; Liu, Y.; Luo, J.; Xu, Y.; Wei, P.; Li, Y.; Jin, Y.; Ding, Y.; Miao, L.; Jiang, J.; Han, J.; Huang, Y., A Dual-Insertion Type Sodium-Ion Full Cell Based on High-Quality Ternary-Metal Prussian Blue Analogs. *Adv. Energy Mater.* **2018**, *8* (11), 1702856.
49. Do, M. P.; Fischer, P. J.; Nagasubramanian, A.; Geder, J.; Kühn, F. E.; Srinivasan, M., Investigation of the Electrochemical and Thermal Stability of an Ionic Liquid Based $\text{Na}_{0.6}\text{Co}_{0.1}\text{Mn}_{0.9}\text{O}_2/\text{Na}_{2.55}\text{V}_6\text{O}_{16}$ Sodium-Ion Full-Cell. *J. Electrochem. Soc.* **2019**, *166* (6), A944-A952.

Chapter 7

7 Nanoscale Surface Modification of High-Voltage Layered Sodium Cathode via Atomic Layer Deposition of Aluminum Phosphate with Enhanced Cycle Performance

Rechargeable sodium-ion batteries (SIBs) have been considered as promising candidate devices for large-scale energy storage application due to the low cost and rich natural sources of Na. Developing high-voltage cathodes is strategically pivotal to achieve a high-energy-density SIBs. P2-type layered $\text{Na}_{2/3}\text{Ni}_{1/3}\text{Mn}_{2/3}\text{O}_2$ is considered a promising cathode owing to its high theoretical capacity and operating voltage. However, it suffers from severe phase transition and unstable cathode-electrolyte interface at high voltage. Herein, we report an electrochemically stable nanoscale surface coating of AlPO_4 on the $\text{Na}_{2/3}\text{Ni}_{1/3}\text{Mn}_{2/3}\text{O}_2$ with controllable thickness via atomic layer deposition (ALD). By alleviating the severe structure change and protecting the active materials from attack by the acidic environment, the AlPO_4 coated $\text{Na}_{2/3}\text{Ni}_{1/3}\text{Mn}_{2/3}\text{O}_2$ electrodes show an enhanced cycling performance and rate capability. The electronic structure of the system was examined using X-ray Absorption Near-Edge Structure (XANES). The findings in this study underscore the significance of thickness controllable nanoscale coating layers and pave the way for the development of high-voltage sodium cathode materials.

7.1 Introduction

Lithium-ion batteries (LIBs) are currently dominating the portable electronics market due to their high specific capacity, good power density, and long cycle life.¹⁻⁴ However, the increasing demand for large-scale electrical energy storage (EES) applications such as electric vehicles (EVs) and renewable power stations would bring great pressure on the limited lithium resources, thereby causing a great surge of lithium price. Thus, new energy storage systems with reasonable price are in desperate need and attracting a lot of research interests.⁵⁻⁶ Sodium-ion batteries (SIBs) are recently attracting much attention and considered as an ideal alternative to LIBs for large-scale EES because of the rich natural resources and wide global distribution of sodium as well as similar charge storage mechanism to LIBs.⁸ Since the cathode materials are the bottleneck component affecting the whole energy density, cost, and cycle life in a full cell, seeking of suitable cathode materials is of crucial importance for the development of SIBs.¹⁰

Within the past decade, many efforts have been devoted to developing high-performance sodium cathode materials, such as layered metal oxides,¹¹⁻¹² pyrophosphate,¹³⁻¹⁴ olivine phosphates,¹⁵ fluorophosphates¹⁶, and fluorosulfates.¹⁷ Among the various cathode materials, sodium-based layered metal oxides (Na_xMO_2 , M= one or more transition metals) show great advantages including high operating voltage, high theoretical capacity, and facile preparation. In particular, P2-type $\text{Na}_{2/3}\text{Ni}_{1/3}\text{Mn}_{2/3}\text{O}_2$ has been extensively investigated due to its high theoretical capacity of 173 mAh g^{-1} and high operating voltage with a flat plateau above 4 V originated from the high redox potential of $\text{Ni}^{2+}/\text{Ni}^{4+}$ couple. Despite possessing such merits, some major problems remain to be resolved during charge/discharge process: 1) A P2-O2 phase transition stemming from an oxygen framework shift will take place during the cycling process when charged to a high voltage of above 4.2 V, leading to a severe capacity decay. Meanwhile, an inevitable volume shrinkage of around 23% associated with the phase transition will cause the isolation of active materials from conducting materials, thus resulting in a fast capacity fading. 2) The carbonate-based electrolyte tends to decompose when charged to the high voltage, generating detrimental contaminants, such as HF. The acid thus produced can attack the active materials, leading to an inevitable capacity degradation at high cut-off voltage.¹⁸⁻¹⁹

Accordingly, numerous studies have focused on suppressing the irreversible phase transition by partially substituting active metal elements with electrochemical inactive elements (Mg, Zn, Al, Ti, etc.), which have been proved to be an effective way to stabilize the crystal structure, thus enhancing the capacity retention.²⁰⁻²⁸ Although these doping attempts are promising, the electrochemical performance is still not satisfactory as doping inactive ions will inevitably lose some capacity. Recently, surface modification has been demonstrated to be a promising approach to improve the electrochemical performances of sodium layered oxides. For example, our group first reported atomic layer deposition (ALD) of Al_2O_3 on the layered P2-type $\text{Na}_{2/3}(\text{Mn}_{0.54}\text{Ni}_{0.13}\text{Co}_{0.13})\text{O}_2$ (MNC) cathodes, the MNC electrode coated with 2 ALD cycles of Al_2O_3 exhibits an enhanced electrochemical stability as the metal oxide coating layer provides structural stability against mechanical stresses generated during the charge/discharge process.²⁹ Later on, Zhou et al. introduced an Al_2O_3 coating layer on the P2- $\text{Na}_{2/3}\text{Ni}_{1/3}\text{Mn}_{2/3}\text{O}_2$ cathode to stabilize the electrode at high voltage via a wet-chemistry method, and the coated electrode displayed a high initial discharge capacity of 160 mAh g^{-1} with enhanced cycle retention of 73.2% after 300 cycles.³⁰ Alvarado et al.³¹ also demonstrated the ALD coating of Al_2O_3 on P2- $\text{Na}_{2/3}\text{Ni}_{1/3}\text{Mn}_{2/3}\text{O}_2$ cathode. X-ray photoelectron (XPS) results revealed that the coated electrodes contained polymeric species such as poly (ethylene oxide), which is beneficial for forming a more flexible cathode-electrolyte interface (CEI) that can mitigate the exfoliation of $\text{Na}_{2/3}\text{Ni}_{1/3}\text{Mn}_{2/3}\text{O}_2$ particles. Although previous studies demonstrate that Al_2O_3 coating can enhance the cyclic performance, a dense insulator Al_2O_3 layer would result in a decreased rate performance. Additionally, Al_2O_3 is intrinsically unstable to an acid environment. Thus, we still face great challenges with seeking a promising and electrochemically stable coating material.

Herein, we report a novel nanoscaled surface coating of alumina phosphate (AlPO_4) on P2- $\text{Na}_{2/3}\text{Ni}_{1/3}\text{Mn}_{2/3}\text{O}_2$ with well-controlled coating thickness via atomic layer deposition. Soft X-ray absorption near-edge spectroscopy (XANES), which probes the local chemical change of the element of interest, suggests that the surface coating layer has effectively protected the surface Ni from being oxidized. The effect of ALD coating thickness on the electrochemical performance including cycling performance and rate capabilities was investigated. The results clearly demonstrate the positive impact of the ultrathin AlPO_4 coating layer on the electrochemical performance of P2- $\text{Na}_{2/3}\text{Ni}_{1/3}\text{Mn}_{2/3}\text{O}_2$.

7.2 Experimental Section

7.2.1 Preparation of P2-Na_{2/3}Ni_{1/3}Mn_{2/3}O₂

The P2-Na_{2/3}Ni_{1/3}Mn_{2/3}O₂ powders were synthesized by a simple solid-state reaction method. Typically, a stoichiometric mixture of Na₂CO₃ (99%, Sigma-Aldrich), NiO (99%, Sigma-Aldrich), and Mn₂O₃ (99%, Sigma-Aldrich) was ball-milled for 5 h in ethanol. An excess amount of 5% Na₂CO₃ was added to compensate for the sodium loss at high temperature. The mixture was dried at 80°C for 10 h. The obtained powders were then pressed into pellets, afterward, the pellets were heated at 900°C for 12 h. The heated pellets were cooled to room temperature and then transferred to an argon-filled glovebox until use.

7.2.2 Atomic layer deposition of AlPO₄ on P2-Na_{2/3}Ni_{1/3}Mn_{2/3}O₂

AlPO₄ was deposited on the P2-Na_{2/3}Ni_{1/3}Mn_{2/3}O₂ powders at 250°C in a Savannah 100 ALD system (Ultratech/Cambridge Nanotech, USA) using trimethylaluminum (TMA, (CH₃)₃Al, 98% STREM Chemicals), trimethyl phosphate (TMPO, (CH₃)₃PO₄, 97% STREM Chemicals), and distilled water (H₂O) as precursors. AlPO₄ was deposited in an exposure model by the sequence of TMA pulse (0.5 s) - exposure (1s) - purge (10 s) – H₂O pulse (1s) – exposure (1s) – purge (15 s) – TMPO pulse (2s) – exposure (1s) – purge (10 s)- H₂O pulse (1s)- exposure (1s)-purge (10s). Nitrogen gas (99.999 %) was used as a carrier gas at a flow rate of 20 sccm. AlPO₄ layers were directly deposited on the P2-Na_{2/3}Ni_{1/3}Mn_{2/3}O₂ powders by repeating the above ALD cycles. In this work, 2, 5, 10, and 20 ALD cycles were selected to control the coating thickness, each of the sample was denoted as NMO-nAP, where n means the ALD cycle number and AP means AlPO₄.

7.2.3 Materials characterization

X-ray diffraction (XRD, Bruker D8 Advance, Cu-K α source) was utilized to investigate the phase purity of the pristine and ALD AlPO₄ coated P2- Na_{2/3}Ni_{1/3}Mn_{2/3}O₂ samples. The morphologies of the samples were characterized by a Hitachi S-4800 field emission scanning electron microscopy (FESEM) and a transmission electron microscopy (TEM, FEI Quanta FRG 200 F, operating at 200 kV). The soft X-ray absorption spectroscopy (XAS) measurements of Ni L_{3,2} edges, Mn L_{3,2} edges, and O K edge were conducted at the Spherical Grating Monochromator (SGM) beamline with a photon energy of 250 – 2000 eV at Canadian Light Source (CLS).

7.2.4 Electrochemical performance measurements

The electrodes were prepared by mixing active material, acetylene black (AB) and poly(vinylidene fluoride) (PVDF) in a ratio of 80:10:10 in N-methyl-pyrrolidone (NMP). The slurry was then pasted on Al foils and dried at 80°C under vacuum for overnight. Subsequently, the dried electrode was punched and assembled into a CR-2032 coin cell in an argon-filled glovebox. Sodium metal was used as the counter electrode. 0.5 M NaPF₆ dissolved into propylene carbonate (PC, 2% FEC) was used as the electrolyte. Glass fiber (GF) was used as the separator. Cyclic voltammetry (CV) and electrochemical impedance spectroscopic (EIS) measurements were performed on a Bio-Logic multichannel potentiostat 3/Z (VMP3). The cells were tested on a Land system between a voltage range of 2.0-4.3 V vs. Na⁺/Na at room temperature.

7.3 Results and Discussions

7.3.1 Morphology and Structure Characterization

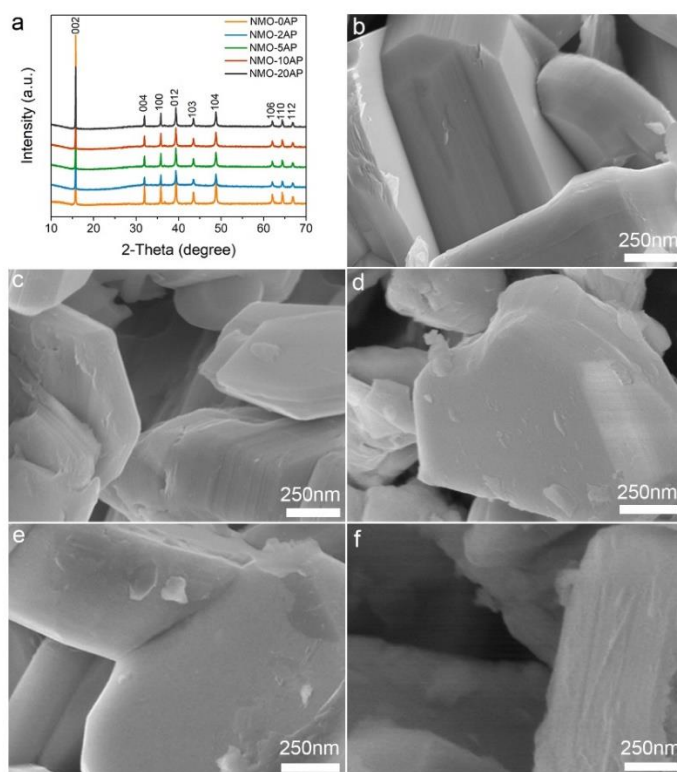


Figure 7.1 a) XRD patterns of pristine NMO and AlPO₄-coated NMO samples; Typical SEM images of b) bare NMO, c) NMO-2AP, d) NMO-5AP, e) NMO-10AP, and f) NMO-20AP.

The crystal structures of pristine NMO and AlPO_4 coated NMO samples (denoted as NMO-nAP, where n means the ALD cycle numbers and AP means AlPO_4) are determined by X-ray diffraction (XRD). As presented in **Figure 7.1a**, the pristine NMO displays characteristic peaks which could be well indexed to a hexagonal layered structure with a space group of $P6_3/mmc$. The XRD patterns of NMO-nAP samples also show the same characteristic peaks, suggesting that the surface ALD AlPO_4 coating did not affect the structure of the pristine NMO. And no peaks associated with AlPO_4 were observed in the crystal structure after AlPO_4 coating due to the ultrathin and amorphous nature of the coating layers.³²⁻³³

The morphologies of pristine NMO and AlPO_4 coated NMO samples were first characterized by scanning electron microscopy (SEM). **Figure S7.1** clearly shows that the pristine NMO prepared from traditional solid-state-reaction (SSR) method is composed of uniform plate-like micro-sized particles, and the particles size is around 2-3 μm . The magnified image of the pristine NMO particles in **Figure 7.1b** presents a laminated structure with very smooth surfaces and well-defined edges. In contrast, the particles with ALD AlPO_4 coating layers display a gradually rougher surface associated with the coating layer increasing as clearly shown in **Figure 7.1c-1f**. Especially after 20 cycles of ALD AlPO_4 coating, the surface of the particles is so rough that some pleats even occur. **Figure S7.2** shows the energy-dispersive X-ray spectroscopy (EDX) mapping images of bare NMO particles, which suggests the homogeneous distributions of Ni, Mn, and Na within the whole particles. The presence of Al and P elements on the surface of the NMO-2AP, NMO-5AP, and NMO-10AP particles was also confirmed by SEM EDX mappings as presented in **Figure S7.3-S7.5**.

Transmission electron microscopy (TEM) was further conducted on NMO-20AP sample to confirm the coating layer. The low-resolution TEM (**Figure 7.2a**) shows a plate-like morphology with a thin layer coated on the surface. The high-resolution TEM (HRTEM) in **Figure 7.2c** clearly reveals that the thickness of the coating layer is approximate to 4 nm and the coating layer exhibits amorphous nature, which is in accordance with the XRD results. **Figure 7.2d-2i** present the EDX elemental mappings for the orange rectangle region in Figure 2a. It can be observed that Al and P are uniformly distributed on the surface of the NMO particles.

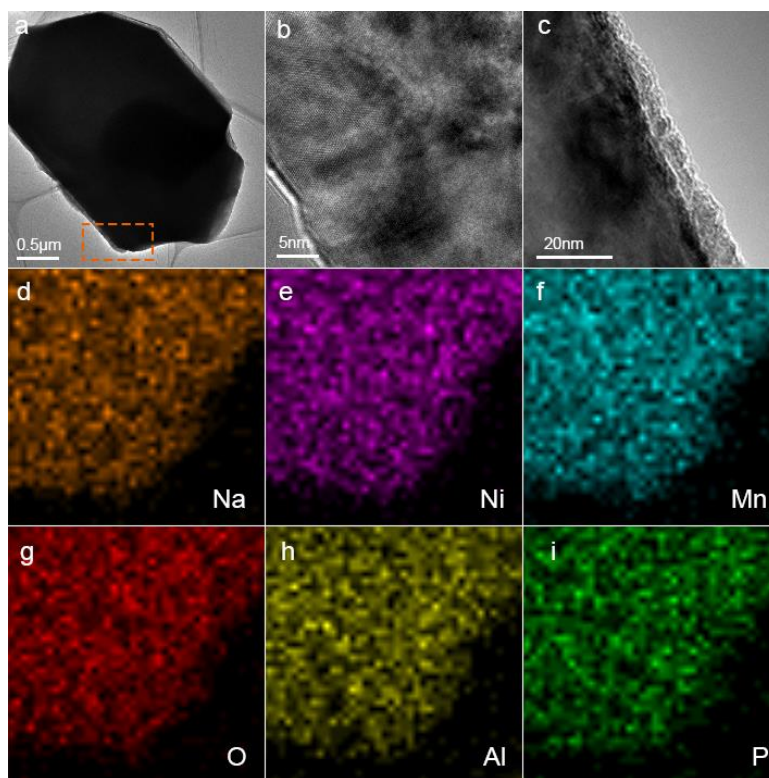


Figure 7.2 a) Low-resolution TEM image, b) and c) HRTM images; (d-i) elemental mapping of Na, Ni, Mn, O, Al, and P of the NMO-20AP, respectively.

To investigate whether the thin surface coating layer affects the valence states and electronic structures of Ni and Mn in the pristine NMO, soft X-ray absorption spectroscopy (XAS) was used to obtain the XANES on the Mn $L_{3,2}$ -edges and Ni $L_{3,2}$ -edges for bare NMO and NMO-10AP samples (**Figure 7.3a and 7.3b**) in total electron yield (TEY) mode, which has a surface probing depth of a few nm. Metal $L_{3,2}$ -edges usually reveal the electronic transition from $M 2p_{3/2}$ and $2p_{1/2}$ to an unoccupied 3d states, and the peaks corresponding to $L_{3,2}$ edges are very sensitive to oxidation state, spin state, local symmetry (e.g. tetrahedral vs octahedral) and bond covalence. Both Mn L-edge and Ni L-edge spectra show a negligible difference before and after surface coating, indicating that the ALD thin coating layer did not alter the surface oxidation state of Ni and Mn in the NMO nor its local structure. Compared with the standard MnO_2 and NiO XANES features, it can be revealed that the valence state of Mn and Ni in both samples are primarily Mn^{4+} and Ni^{2+} , respectively³⁴

The O K-edge can be divided into two regions. Pre-edge peaks below 535 eV are ascribed to electronic transition from O 1s state to O 2p-TM 3d hybridized state of e_g and t_{2g} character. The broad peaks above 535 eV correspond to transition to O 2p-TM 4sp hybridized state. The O K-edge spectra of bare NMO and NMO-10AP samples are both collected in TEY and fluorescence yield (FY) modes, the latter is sensitive to the bulk while TEY is sensitive to the surface with contributions from both the AlPO₄ coating and the electrode materials. As shown in **Figure 7.3c**, the O K-edge of two samples in FY mode display similar features, suggesting that the coating did not affect the bulk electronic structures of NMO. **Figure 7.3d** shows the O K-edge in TEY mode, the pre-edge peak of NMO-10AP at around 530 eV shows a reduced intensity compared with that of the bare NMO, which indicates that surface coating layer can avoid the oxidation of surface Ni as the intensity decrease of this pre-edge peak means fewer holes in the O 2p-TM 3d hybridized orbitals, suggesting a lower valence state of the surface metals.³⁵ It should be noted that AlPO₄ exhibits no absorption features at 530 eV of its O K-edge XANES but a broad absorption at ~ 540 eV which contributes to the background in the XANES of the coated samples in this energy region.

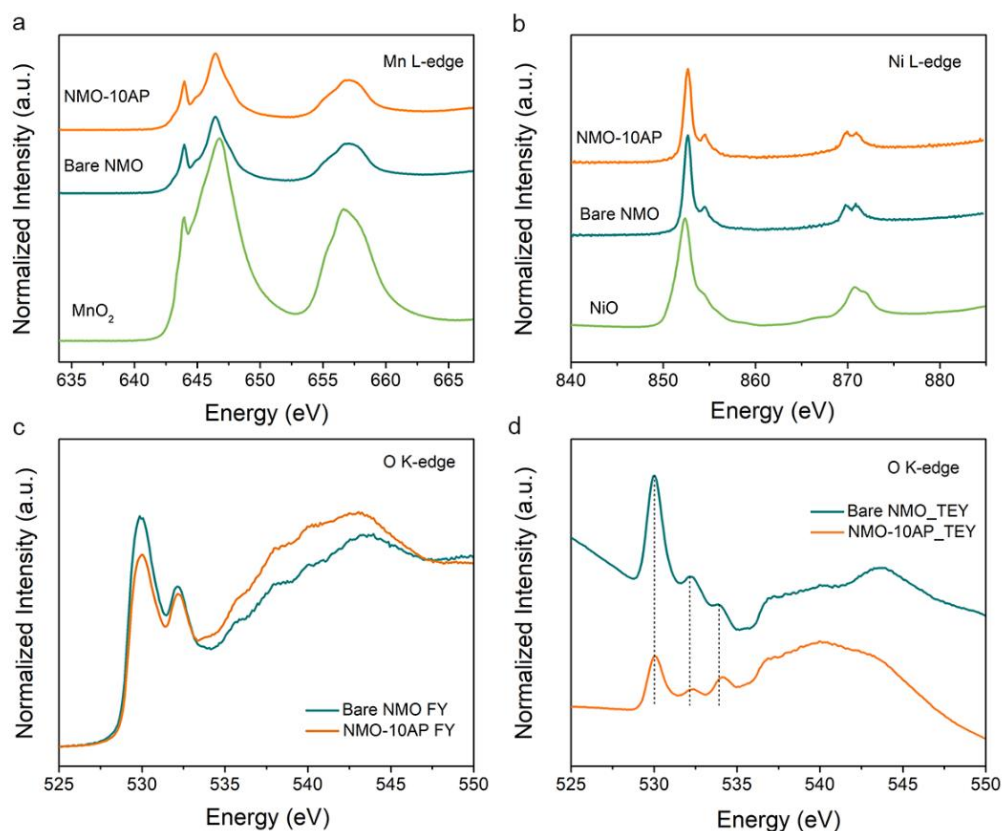


Figure 7.3 a) XAS spectra of Mn L_{3,2}-edges and Ni L_{3,2} edges of bare NMO, NMO-10AP, and standard MnO₂; b) XAS spectra of Ni L_{3,2}-edges of NMO, NMO-10AP, and standard NiO collected in TEY mode; c) and d) O K-edges of bare NMO and NMO-10AP collected in FY and TEY modes, respectively.

7.3.2 Electrochemical Characterization

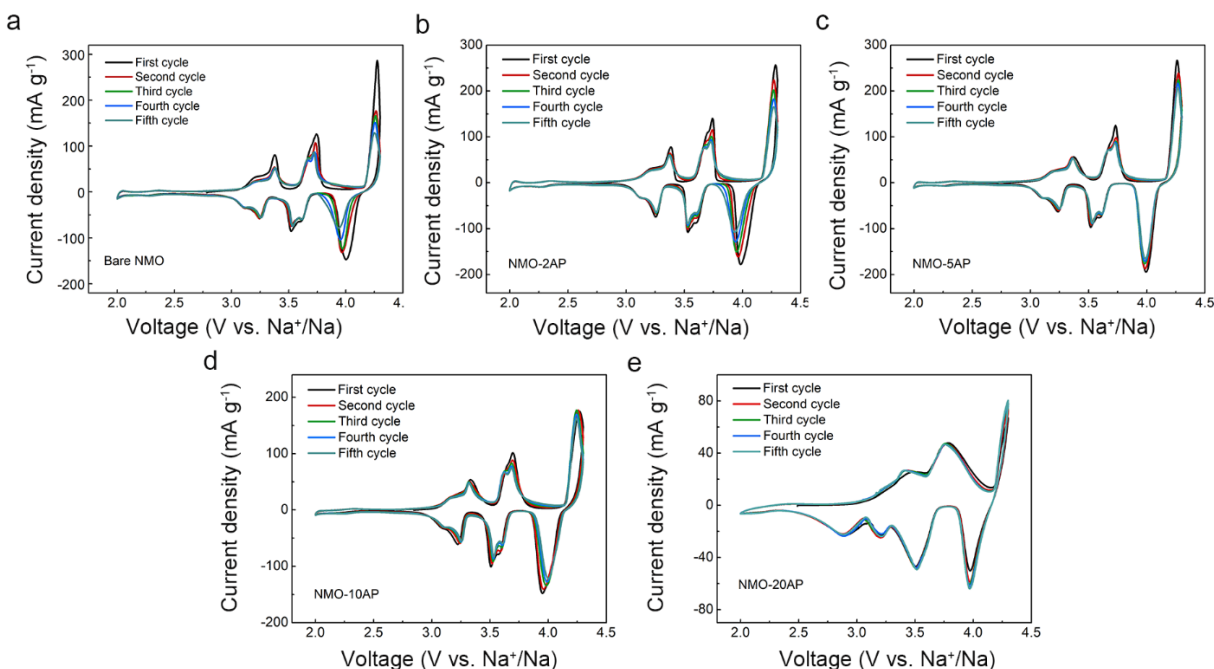


Figure 7.4 Cyclic voltammetry of a) bare NMO, b) NMO-2AP, c) NMO-5AP, d) NMO-10AP, and (e) NMO-20AP.

To study the electrochemical behaviors of bare NMO and NMO coated with various ALD cycles of AlPO₄, cyclic voltammetry (CV) measurements were first conducted at a scanning rate of 0.1 mV s⁻¹ within a voltage range of 2.0 – 4.3 V. As shown in **Figure 7.4**, three main pairs of redox peaks can be observed in the CV curves for all the samples, corresponding to the charge/discharge plateaus of the voltage profiles. The reversible oxidation/reduction peaks at around 3.37/3.25 V and 3.75/3.52 V are attributed to the redox reactions of Ni²⁺/Ni³⁺ and Ni³⁺/Ni⁴⁺, respectively.³⁶ A higher redox peak appeared at around 4.0/4.22 V can be ascribed to the phase transition from P2 to O2, which will cause the layered structures gliding and thus lead to a decreased cycle stability.³⁷

It should be noted that the redox peaks below 4.0V for all the samples can be well overlapped in the first five cycles, indicating that the redox reactions at lower voltage show good reversibility and does not alter the layer structure. Interestingly, the surface coating layer has an obvious effect on the higher redox peaks, it is clearly observed that the redox peaks at high voltage undergo enhanced reversibility with increasing coating thickness. Particularly, the electrode with 20 ALD cycles of AlPO_4 displays a higher reversible redox reaction at high voltage, indicating improved structural stability during the charge/discharge process.

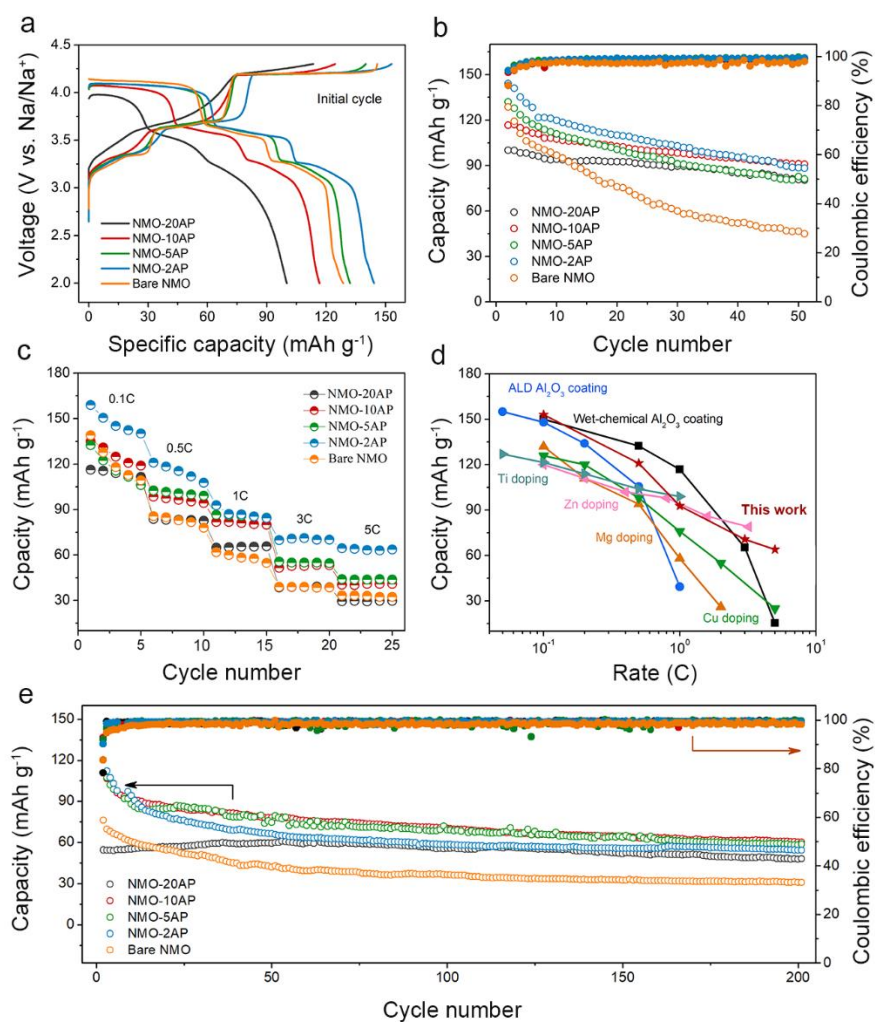


Figure 7.5 Electrochemical performance comparison of a) the initial galvanostatic charge/discharge profiles of bare NMO and various AlPO_4 -coated NMO samples within the voltage range of 2.0-4.3V at 0.5 C; b) cyclic performance of bare NMO and AlPO_4 -coated NMO samples at 0.5 C; c) rate capabilities of bare NMO and AlPO_4 -coated NMO samples

at various current densities; d) A comparison of the rate performance between this work and the work previously reported in the literature; e) The long-term cyclic performance of bare NMO and AlPO₄-coated NMO samples over 200 cycles at a rate of 2C.

The sodium storage performance of bare NMO and AlPO₄ coated NMO samples were evaluated in coin cells with Na metal as the counter electrode. The initial charge/discharge voltage profiles of bare NMO and various ALD-coated NMO electrodes measured at 0.5C are displayed in **Figure 7.5a**. All of the electrodes show three obvious slopes and voltage plateaus during the charge/discharge process, which are consistent with the CV results. As indicated in **Figure 7.5a**, an initial discharge capacity of approximately 128 mAh g⁻¹ was obtained from the bare NMO electrode within the voltage range of 2.0-4.3V, whereas the NMO-2AP electrode exhibited an enhanced initial discharge capacity of 144.2 mAh g⁻¹, which suggests that the ultrathin coating layer might facilitate the Na diffusion. However, the initial discharge capacities of the NMO-5AP, NMO-10AP, and NMO-20AP electrodes are 140, 119, and 95 mAh g⁻¹, respectively, which presents a linearly decrease with the coating thickness increasing. This phenomenon can be ascribed to the thicker inactive AlPO₄ layer restricting the Na ions diffusion from the electrolyte into the bulk active material, which inevitably reduces the activity of active species in the electrochemical reaction.^{19, 38}As a consequence, the 20 cycles of ALD-coated NMO electrode delivered a greatly reduced initial capacity and coulombic efficiency.

To further investigate the coating effects on cycling stability, the cycling performance of various NMP-nAP electrodes was examined at 0.5C over 50 cycles. It is displayed in **Figure 7.5b** that the bare NMO electrode suffered from a dramatic capacity fading with only 48% capacity retention after 50 cycles. This rapidly capacity decay resulted from the severe structural changes during the charge/discharge process, which is consistent with previous reports.³⁷In contrast, the ALD-coated electrodes show improved capacity retention compared to the uncoated electrode. It should be noted that the capacity retention of the coated electrodes demonstrates a linearly increases with the increasing coating thickness. Among all the coated electrodes, the electrode with 10 cycles of ALD coating shows the best discharge capacity of around 94 mAh g⁻¹ at the 50th cycle with capacity retention of 78%. It is worth to note that the 20 cycles of ALD-coated electrode displayed superior cyclic stability with 80% capacity remaining at 50th cycle although it presented a lower initial

discharge capacity. The improved cyclic stability of the coated electrodes might be attributed to the existing of the stable coating layer, which could suppress the electrolyte oxidation under high voltage and mitigate the exfoliation of NMO particles.³⁹⁻⁴¹

Furthermore, the rate capabilities of the bare NMO electrode and ALD AlPO₄ coated electrodes were compared at various current densities as displayed in **Figure 7.5c** and **Figure S7.6**. It can be observed that the bare NMO, NMO-2AP, NMO-5AP, and NMO-10AP electrodes all undergo a fast capacity decay in the first five cycles at 0.1C, which is caused by the irreversible structural change. However, the NMO-20AP electrode revealed a relatively stable cyclic performance, indicating that 20 cycles of coating layer could effectively mitigate the structural change. Comparing the overall rate- performance results, it can be found that the NMO-2AP electrode exhibits a higher capacity than those of the bare NMO and other coated NMO electrodes, suggesting an enhanced ion transport. High capacity of approximately 70 mAh g⁻¹ was obtained for 2 cycles of the ALD-coated electrode at a high rate of 5C. However, the 20 cycles of coated electrode presented a greatly reduced rate capability, which might be a result of the high Na ion resistance of the thick insulating coating layer. **Figure 7.5d** compares the rate capabilities of this work with previously reported data in the literature. It clearly reveals that doping inactive elements greatly reduce the capacity of the NMO electrodes, on the contrary, surface coated NMO electrodes could maintain a higher capacity. Moreover, compared with Al₂O₃ coating reported in the literature, ALD AlPO₄ coated NMO electrode in this work displays superior capacity, especially at a high C-rate.

The long-term cyclic performance at a high current density is essential for practical application of the energy storage devices. Thus, the long-term cycle stability of various NMO-nAP electrodes was tested at a high rate of 2C over 200 cycles. As shown in **Figure 7.5e** and **Figure S7.7**, the 2 cycles of ALD-coated NMO exhibits the highest initial discharge capacity of 121.2 mAh g⁻¹ among all the electrodes. In contrast, the bare NMO electrode only delivers an initial discharge capacity of 76.2 mAh g⁻¹, with only 40.3% of the initial capacity remained after 200 cycles. Notably, all the coated electrodes exhibit enhanced cycle stability as shown in **Figure S7.8**. It is worth noting that the NMO-10AP electrode delivers a high capacity of 60 mAh g⁻¹ at the 200th cycle, which is almost twice that of the bare NMO.

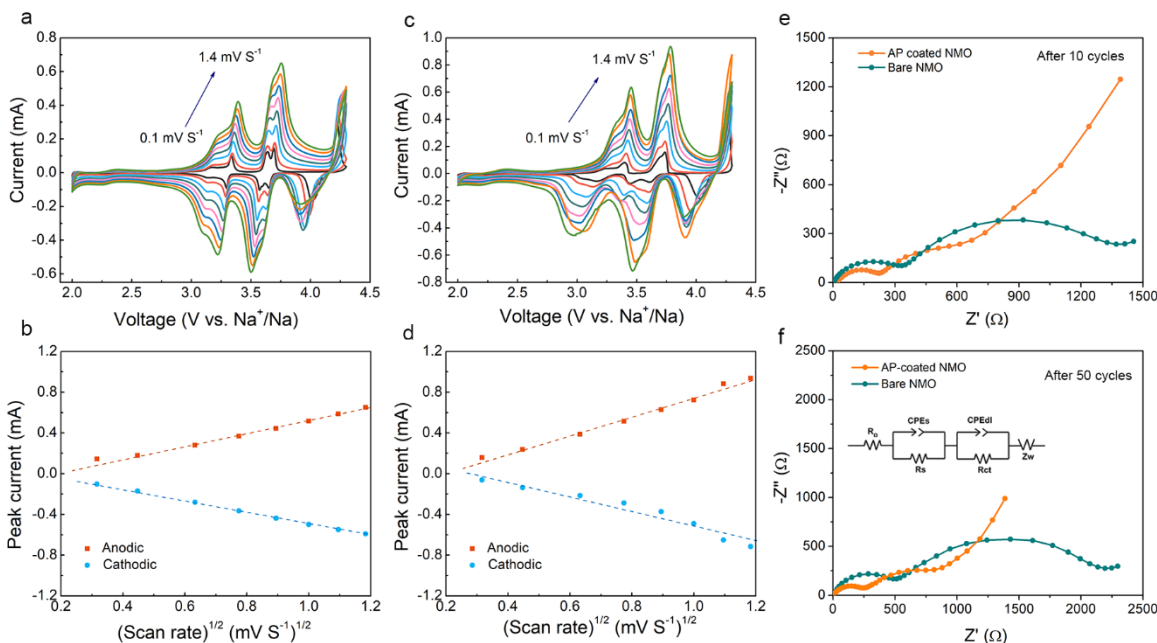


Figure 7.6 Cyclic voltammogram curves of (a) NMO-2AP and (c) bare NMO electrodes at various scanning rates (0.1, 0.2, 0.4, 0.6, 0.8, 1.0, 1.2, and 1.4 mVs^{-1}); (b) and (d) are the corresponding linear relationship between the peak current and the square root of the scan rates; (e) and (f) are EIS curves after 10 cycles and 50 cycles.

To better understand the high-rate capabilities of AlPO_4 -coated electrodes. CV measurements with varied scan rates were investigated to study the kinetic behavior of the bare and coated NMO. **Figure 7.6a** and **7.6c** are the CV profiles of the bare and NMO-2AP electrodes, respectively. **Figure 7.6b** and **7.6d** show the corresponding linear relationship between the peak current and the square root of the scan rates. The Na diffusion coefficients (D_{Na}) values can be calculated according to the Randles-Sevick equation⁴²⁻⁴³:

$$I_p = 2.69 \times 10^5 n^{3/2} A D^{1/2} v^{1/2} C_0 \quad (1)$$

Where I_p is the peak current of anodic or cathodic peaks, n is the number of electrons per formula during the insertion, A is the geometric area of the electrode, D is the Na diffusion coefficient, v is the scan rate and C_0 is the concentration of Na^+ in the electrode. The average D_{Na} values of bare NMO and NMO-2AP samples are $1.97 \times 10^{-11} \text{cm}^2 \text{s}^{-1}$ and $3.86 \times 10^{-11} \text{cm}^2 \text{s}^{-1}$ during the charging process, respectively. The improved D_{Na} value of the 2 cycles of ALD-coated electrode should be one of the reasons for the enhanced rate capacities and cycling performance.

In order to study the effect of the AlPO_4 coating layer on the formation of solid electrolyte interface (SEI), electrochemical impedance spectra (EIS) measurements were conducted on bare NMO and coated NMO electrodes after different cycling at 0.5C. The Nyquist plots and a fitted equivalent circuit are shown in **Figure 7.6e and 7.6f**. In particular, the semicircle at high frequency stands for the Na^+ migration resistance (R_s) through the surface layer, which reflects the resistance of SEI. The semicircle at medium frequency can be assigned to the charge transfer resistance (R_{ct}) at the cathode-electrolyte interface. The inclined line at low frequency (Warburg impedance Z_w) is related to the Na^+ diffusion into the bulk of the electrode materials. The values of the R_s for each sample after different cycles are listed in **Table S7.1**, it can be seen that bare NMO exhibits a larger R_s value of 336.1Ω after 10 cycles, whereas the AlPO_4 coated NMO shows a decreased R_s value of 218.5Ω , suggesting a smaller SEI impedance (Figure 6e). This also indicates that the AlPO_4 coating could suppress the electrolyte decomposition, which is mainly because that the AlPO_4 layer could protect the active materials from direct contact with the electrolyte. Moreover, the R_s of the bare NMO electrode increased to 485.9Ω after 50 cycles, whereas the increase of R_s impedance was negligible for AlPO_4 coated NMO electrode. The impedance comparison demonstrates that the AlPO_4 coating layer is effective for stabilization of the cathode-electrolyte interface, leading to a thinner SEI on the electrode compared to the bare NMO electrode. These results reveal that the nanoscale surface coating could effectively improve the electrochemical performance of the pristine electrode.

7.3.3 Post-cycling Characterization

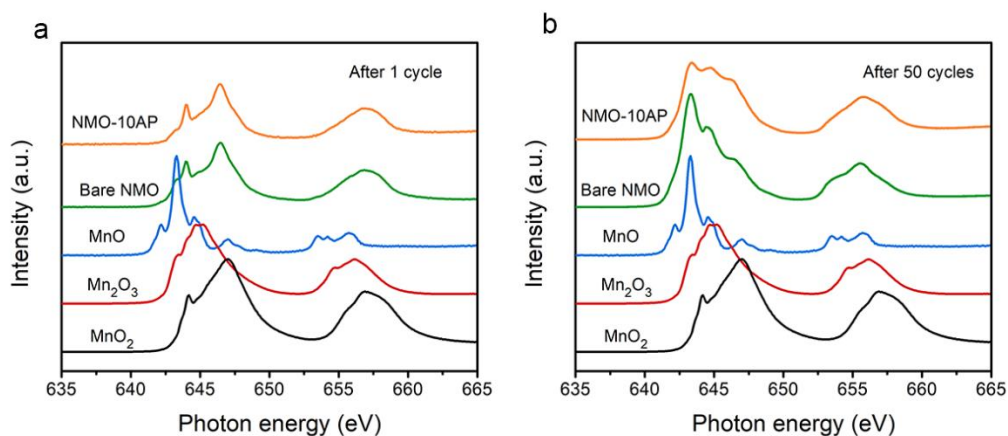


Figure 7.7 XANES Mn L_{3,2}-edges of bare NMO and NMO-10 AP electrodes after (a) 1 cycle and (b) 50 cycles compared with standard MnO, MnO₂, and Mn₂O₃.

To further study the effect of the coating layer on the cathode, XANES was collected on the Mn L_{3,2}-edges of the electrodes after different cycles. **Figure 7.7a** shows the Mn L_{3,2}-edges of the bare NMO and NMO-10AP electrodes after 1 cycle, it can be found that both the bare NMO and NMO-10AP electrodes present predominantly Mn⁴⁺ features which match well with standard MnO₂. This suggests that the valence state of Mn does not change after a few cycles, which can maintain the structure of the cathode. However, after 50 cycles, the Mn in both electrodes was partially reduced to Mn²⁺ (**Figure 7.7b**). Interestingly, the NMO-10AP electrode displays a much lower intensity ratio of Mn²⁺/Mn⁴⁺ than the bare NMO electrode, indicating the less reduction of Mn on the coated NMO surface by the electrolyte. This reduction hampering of Mn can be attributed to the protective role of AlPO₄ against the electrolyte oxidation. In other words, the right amount of AlPO₄ coating layer can suppress the dissolution of Mn²⁺ into the electrolyte, thus improving the structural stability of the cathode material.

7.4 Conclusions

In summary, we have demonstrated herein for the first time the novel ALD coating of AlPO₄ layer on the P2-NMO layered cathode materials with a controllable thickness. We have systematically studied the effect of the coating thickness on the cyclic performance and rate capability of the NMO cathode material. The results show that the AlPO₄-coated NMO electrodes exhibit superior cyclic stability and enhanced rate capabilities. The findings in this study underscore the significance of thickness controllable nanoscale coating layers and provide a new insight for designing high voltage SIBs cathodes for future applications.

Acknowledgements

The work was supported by Natural Science Foundation of China (NSFC) (Grant U1432249), the National Key R&D Program of China (Grant 2017YFA0205002), and the Priority Academic Program Development (PAPD) of Jiangsu Higher Education Institutions. This is also a project supported by Jiangsu Key Laboratory for Carbon-Based Functional Materials and Devices and the Collaborative Innovation Center of Suzhou Nano Science & Technology. This work was also

supported by the Natural Science and Engineering Research Council of Canada (NSERC), the Canada Research Chair Program (CRC), the Canada Foundation for Innovation (CFI), and the University of Western Ontario (UWO). Synchrotron measurements were conducted at the Canadian Light Source (CLS), which is supported by National Research Council of Canada (NRC), Canada Foundation for Innovation (CFI), Canadian Institute of Health Research (CIHR), NSERC and the University of Saskatchewan, Jiwei Wang acknowledges the support of a travel grant by CLS.

7.5 References

1. Bruce, P. G.; Scrosati, B.; Tarascon, J. M., Nanomaterials for rechargeable lithium batteries. *Angew. Chem. Int. Ed.* **2008**, *47* (16), 2930-46.
2. Tarascon, J. M.; Armand, M., Issues and challenges facing rechargeable lithium batteries. *Nature* **2001**, *414*, 359.
3. Gao, X.; Wang, J.; Zhang, D.; Nie, K.; Ma, Y.; Zhong, J.; Sun, X., Hollow NiFe₂O₄ Nanospheres on Carbon Nanorods as A Highly Efficient Anode Material for Lithium-Ion Batteries. *J. Mater. Chem. A* **2017**, *5*, 5007-5012.
4. Gao, X.; Wang, J.; Zhang, D.; Adair, K.; Feng, K.; Sun, N.; Zheng, H.; Shao, H.; Zhong, J.; Ma, Y.; Sun, X.; Sun, X., Carbon coated bimetallic sulfide nanodots/carbon nanorod heterostructure enabling long-life lithium-ion batteries. *J. Mater. Chem. A* **2017**, *5* (48), 25625-25631.
5. Hwang, J.-Y.; Myung, S.-T.; Sun, Y.-K., Sodium-ion batteries: present and future. *Chem. Soc. Rev.* **2017**, *46* (12), 3529-3614.
6. Sung-Wook, K.; Dong-Hwa, S.; Xiaohua, M.; Gerbrand, C.; Kisuk, K., Electrode Materials for Rechargeable Sodium-Ion Batteries: Potential Alternatives to Current Lithium-Ion Batteries. *Adv. Energy Mater.* **2012**, *2* (7), 710-721.

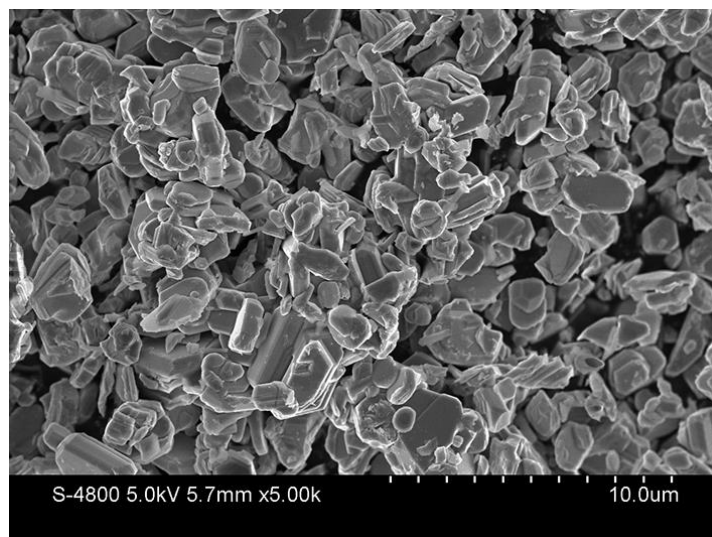
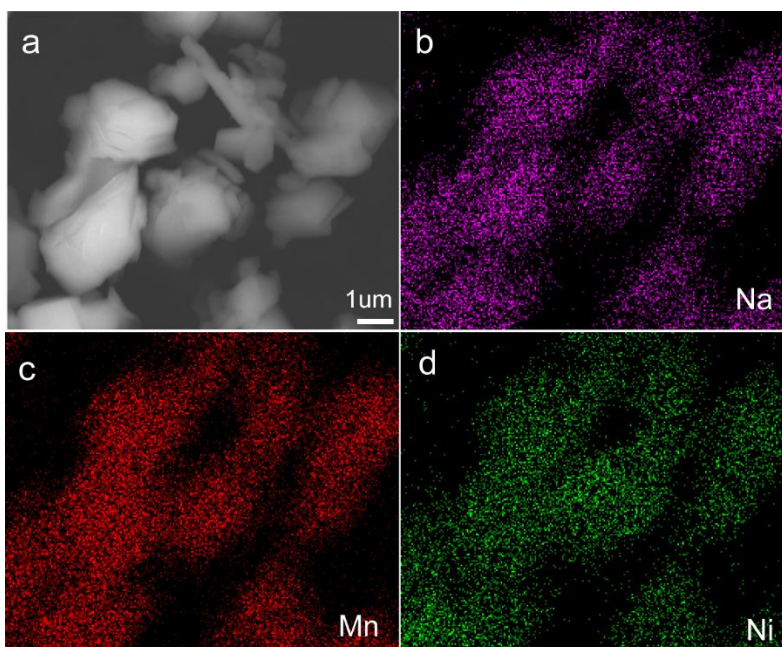
7. D., S. M.; Donghan, K.; Eungje, L.; S., J. C., Sodium-Ion Batteries. *Adv. Funct. Mater.* **2013**, *23* (8), 947-958.
8. Pan, H.; Hu, Y.-S.; Chen, L., Room-temperature stationary sodium-ion batteries for large-scale electric energy storage. *Energy Environ. Sci.* **2013**, *6* (8), 2338-2360.
9. Shinichi, K.; Wataru, M.; Toru, I.; Naoaki, Y.; Tomoaki, O.; Tetsuri, N.; Atsushi, O.; Kazuma, G.; Kazuya, F., Electrochemical Na Insertion and Solid Electrolyte Interphase for Hard-Carbon Electrodes and Application to Na-Ion Batteries. *Adv. Funct. Mater.* **2011**, *21* (20), 3859-3867.
10. Xiang, X.; Zhang, K.; Chen, J., Recent Advances and Prospects of Cathode Materials for Sodium-Ion Batteries. *Adv. Mater.* **2015**, *27* (36), 5343-5364.
11. Han, M. H.; Gonzalo, E.; Singh, G.; Rojo, T., A comprehensive review of sodium layered oxides: powerful cathodes for Na-ion batteries. *Energy Environ. Sci.* **2015**, *8* (1), 81-102.
12. Ortiz Vitoriano, N.; Drewett, N.; Gonzalo, E.; Rojo, T., High Performance Manganese-based Layered Oxide Cathodes: Overcoming the Challenges of Sodium Ion Batteries. *Energy Environ. Sci.* **2017**.
13. Ni, Q.; Bai, Y.; Wu, F.; Wu, C., Polyanion-Type Electrode Materials for Sodium-Ion Batteries. *Adv. Sci.* **2017**, *4* (3), 1600275-n/a.
14. Tamaru, M.; Chung, S. C.; Shimizu, D.; Nishimura, S.-i.; Yamada, A., Pyrophosphate Chemistry toward Safe Rechargeable Batteries. *Chem. Mater.* **2013**, *25* (12), 2538-2543.
15. Casas-Cabanas, M.; Roddatis, V. V.; Saurel, D.; Kubiak, P.; Carretero-González, J.; Palomares, V.; Serras, P.; Rojo, T., Crystal chemistry of Na insertion/deinsertion in FePO₄-NaFePO₄. *J. Mater. Chem.* **2012**, *22* (34), 17421-17423.

16. Tripathi, R.; Wood, S. M.; Islam, M. S.; Nazar, L. F., Na-ion mobility in layered $\text{Na}_2\text{FePO}_4\text{F}$ and olivine $\text{Na}[\text{Fe,Mn}]\text{PO}_4$. *Energy Environ. Sci.* **2013**, 6 (8), 2257-2264.
17. Barpanda, P.; Oyama, G.; Nishimura, S.-i.; Chung, S.-C.; Yamada, A., A 3.8-V earth-abundant sodium battery electrode. *Nat. Commun.* **2014**, 5, 4358.
18. Li, X.; Liu, J.; Banis, M. N.; Lushington, A.; Li, R.; Cai, M.; Sun, X., Atomic layer deposition of solid-state electrolyte coated cathode materials with superior high-voltage cycling behavior for lithium ion battery application. *Energy Environ. Sci.* **2014**, 7 (2), 768-778.
19. Xiao, B.; Liu, J.; Sun, Q.; Wang, B.; Banis, M. N.; Zhao, D.; Wang, Z.; Li, R.; Cui, X.; Sham, T. K.; Sun, X., Unravelling the Role of Electrochemically Active FePO_4 Coating by Atomic Layer Deposition for Increased High-Voltage Stability of $\text{LiNi}_{0.5}\text{Mn}_{1.5}\text{O}_4$ Cathode Material. *Adv. Sci.* **2015**, 2 (5), 1500022.
20. Wang, P. F.; You, Y.; Yin, Y. X.; Wang, Y. S.; Wan, L. J.; Gu, L.; Guo, Y. G., Suppressing the P2-O2 Phase Transition of $\text{Na}_{0.67}\text{Mn}_{0.67}\text{Ni}_{0.33}\text{O}_2$ by Magnesium Substitution for Improved Sodium-Ion Batteries. *Angew. Chem. Int. Ed. Engl.* **2016**, 55 (26), 7445-9.
21. Singh, G.; Tapia-Ruiz, N.; Lopez del Amo, J. M.; Maitra, U.; Somerville, J. W.; Armstrong, A. R.; Martinez de Ilarduya, J.; Rojo, T.; Bruce, P. G., High Voltage Mg-Doped $\text{Na}_{0.67}\text{Ni}_{0.3-x}\text{Mg}_x\text{Mn}_{0.7}\text{O}_2$ ($x = 0.05, 0.1$) Na-Ion Cathodes with Enhanced Stability and Rate Capability. *Chem. Mater.* **2016**, 28 (14), 5087-5094.
22. Hemalatha, K.; Jayakumar, M.; Bera, P.; Prakash, A. S., Improved electrochemical performance of $\text{Na}_{0.67}\text{MnO}_2$ through Ni and Mg substitution. *J. Mater. Chem. A* **2015**, 3 (42), 20908-20912.

23. Wu, X.; Guo, J.; Wang, D.; Zhong, G.; McDonald, M. J.; Yang, Y., P2-type $\text{Na}_{0.66}\text{Ni}_{0.33-x}\text{Zn}_x\text{Mn}_{0.67}\text{O}_2$ as new high-voltage cathode materials for sodium-ion batteries. *J. Power Sources* **2015**, *281*, 18-26.
24. Hasa, I.; Passerini, S.; Hassoun, J., Toward high energy density cathode materials for sodium-ion batteries: investigating the beneficial effect of aluminum doping on the P2-type structure. *J. Mater. Chem. A* **2017**, *5* (9), 4467-4477.
25. Pang, W.-L.; Zhang, X.-H.; Guo, J.-Z.; Li, J.-Y.; Yan, X.; Hou, B.-H.; Guan, H.-Y.; Wu, X.-L., P2-type $\text{Na}_{2/3}\text{Mn}_{1-x}\text{Al}_x\text{O}_2$ cathode material for sodium-ion batteries: Al-doped enhanced electrochemical properties and studies on the electrode kinetics. *J. Power Sources* **2017**, *356*, 80-88.
26. Pengfei Wang, H. Y., Xinyu Liu, Yuguo Guo, Na^+ /vacancy disordering promises high-rate Na-ion batteries. **2018**, *4* (3), eaar6018.
27. Yoshida, H.; Yabuuchi, N.; Kubota, K.; Ikeuchi, I.; Garsuch, A.; Schulz-Dobrick, M.; Komaba, S., P2-type $\text{Na}_{(2/3)}\text{Ni}_{(1/3)}\text{Mn}_{(2/3-x)}\text{Ti}_{(x)}\text{O}_2$ as a new positive electrode for higher energy Na-ion batteries. *Chem. Commun.* **2014**, *50* (28), 3677-80.
28. Shanmugam, R.; Lai, W., Study of Transport Properties and Interfacial Kinetics of $\text{Na}_{2/3}[\text{Ni}_{1/3}\text{Mn}_x\text{Ti}_{2/3-x}]\text{O}_2$ ($x = 0, 1/3$) as Electrodes for Na-Ion Batteries. *J. Electrochem. Soc.* **2014**, *162* (1), A8-A14.
29. Kaliyappan, K.; Liu, J.; Lushington, A.; Li, R.; Sun, X., Highly Stable $\text{Na}_{2/3}(\text{Mn}_{0.54}\text{Ni}_{0.13}\text{Co}_{0.13})\text{O}_2$ Cathode Modified by Atomic Layer Deposition for Sodium-Ion Batteries. *ChemSusChem* **2015**, *8* (15), 2537-2543.

30. Liu, Y.; Fang, X.; Zhang, A.; Shen, C.; Liu, Q.; Enaya, H. A.; Zhou, C., Layered P2-Na_{2/3}[Ni_{1/3}Mn_{2/3}]O₂ as high-voltage cathode for sodium-ion batteries: The capacity decay mechanism and Al₂O₃ surface modification. *Nano Energy* **2016**, *27*, 27-34.
31. Alvarado, J.; Ma, C.; Wang, S.; Nguyen, K.; Kodur, M.; Meng, Y. S., Improvement of the Cathode Electrolyte Interphase on P2-Na_{2/3}Ni_{1/3}Mn_{2/3}O₂ by Atomic Layer Deposition. *ACS Appl. Mater. Interfaces* **2017**, *9* (31), 26518-26530.
32. Deng, S.; Xiao, B.; Wang, B.; Li, X.; Kaliyappan, K.; Zhao, Y.; Lushington, A.; Li, R.; Sham, T.-K.; Wang, H.; Sun, X., New insight into atomic-scale engineering of electrode surface for long-life and safe high voltage lithium ion cathodes. *Nano Energy* **2017**, *38*, 19-27.
33. Xiao, B.; Wang, B.; Liu, J.; Kaliyappan, K.; Sun, Q.; Liu, Y.; Dadheech, G.; Balogh, M. P.; Yang, L.; Sham, T.-K.; Li, R.; Cai, M.; Sun, X., Highly stable Li_{1.2}Mn_{0.54}Co_{0.13}Ni_{0.13}O₂ enabled by novel atomic layer deposited AlPO₄ coating. *Nano Energy* **2017**, *34*, 120-130.
34. Fang, X.; Lin, F.; Nordlund, D.; Mecklenburg, M.; Ge, M.; Rong, J.; Zhang, A.; Shen, C.; Liu, Y.; Cao, Y.; Doeff, M. M.; Zhou, C., Atomic Insights into the Enhanced Surface Stability in High Voltage Cathode Materials by Ultrathin Coating. *Adv. Funct. Mater.* **2017**, *27* (7), 1602873.
35. Ma, C.; Alvarado, J.; Xu, J.; Clément, R. J.; Kodur, M.; Tong, W.; Grey, C. P.; Meng, Y. S., Exploring Oxygen Activity in the High Energy P2-Type Na_{0.78}Ni_{0.23}Mn_{0.69}O₂ Cathode Material for Na-Ion Batteries. *J. AM. Chem. Soc.* **2017**.
36. Lee, D. H.; Xu, J.; Meng, Y. S., An advanced cathode for Na-ion batteries with high rate and excellent structural stability. *Phys. Chem. Chem. Phys.* **2013**, *15* (9), 3304-3312.
37. Lu, Z.; Dahn, J. R., In Situ X-Ray Diffraction Study of P2-Na_{2/3}Ni_{1/3}Mn_{2/3}O₂. *J. Electrochem. Soc.* **2001**, *148* (11), A1225.

38. Wu, F.; Zhang, X.; Zhao, T.; Li, L.; Xie, M.; Chen, R., Multifunctional AlPO₄ Coating for Improving Electrochemical Properties of Low-Cost Li[Li_{0.2}Fe_{0.1}Ni_{0.15}Mn_{0.55}]O₂ Cathode Materials for Lithium-Ion Batteries. *ACS Appl. Mater. Interfaces* **2015**, 7 (6), 3773-3781.
39. Jo, C.-H.; Jo, J.-H.; Yashiro, H.; Kim, S.-J.; Sun, Y.-K.; Myung, S.-T., Bioinspired Surface Layer for the Cathode Material of High-Energy-Density Sodium-Ion Batteries. *Adv. Energy Mater.* **2018**, 8 (13), 1702942.
40. Jo, J. H.; Choi, J. U.; Konarov, A.; Yashiro, H.; Yuan, S.; Shi, L.; Sun, Y.-K.; Myung, S.-T., Sodium-Ion Batteries: Building Effective Layered Cathode Materials with Long-Term Cycling by Modifying the Surface via Sodium Phosphate. *Adv. Funct. Mater.* **2018**, 28 (14), 1705968.
41. Kaliyappan, K.; Liu, J.; Xiao, B.; Lushington, A.; Li, R.; Sham, T.-K.; Sun, X., Enhanced Performance of P2-Na_{0.66}(Mn_{0.54}Co_{0.13}Ni_{0.13})O₂ Cathode for Sodium-Ion Batteries by Ultrathin Metal Oxide Coatings via Atomic Layer Deposition. *Adv. Funct. Mater.* **2017**, 27 (37), 1701870.
42. Das, S. R.; Majumder, S. B.; Katiyar, R. S., Kinetic analysis of the Li⁺ ion intercalation behavior of solution derived nano-crystalline lithium manganate thin films. *J. Power Sources* **2005**, 139 (1), 261-268.
43. Yue, J.-L.; Zhou, Y.-N.; Yu, X.; Bak, S.-M.; Yang, X.-Q.; Fu, Z.-W., O3-type layered transition metal oxide Na(NiCoFeTi)_{1/4}O₂ as a high rate and long cycle life cathode material for sodium ion batteries. *J. Mater. Chem. A* **2015**, 3 (46), 23261-23267.

Supporting Information**Figure S7.1 SEM image of the pristine P2- Na_{2/3}Ni_{1/3}Mn_{2/3}O₂****Figure S7.2 SEM image of pristine NMO and corresponding EDX mapping of Na, Ni, and Mn**

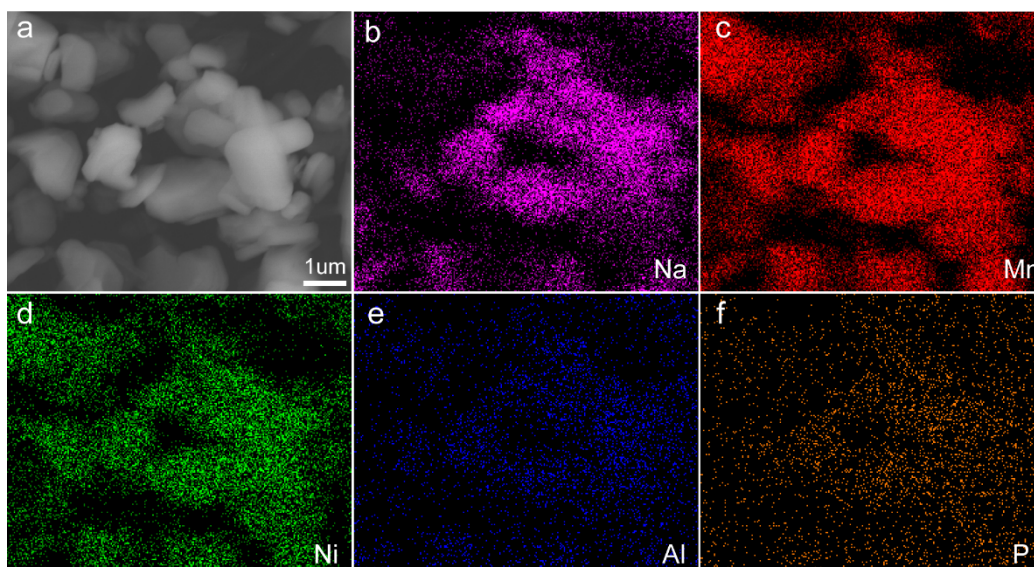


Figure S7.3 SEM image of NMO-2AP and corresponding EDX elemental mapping of Na, O, Ni, Mn, Al, and P.

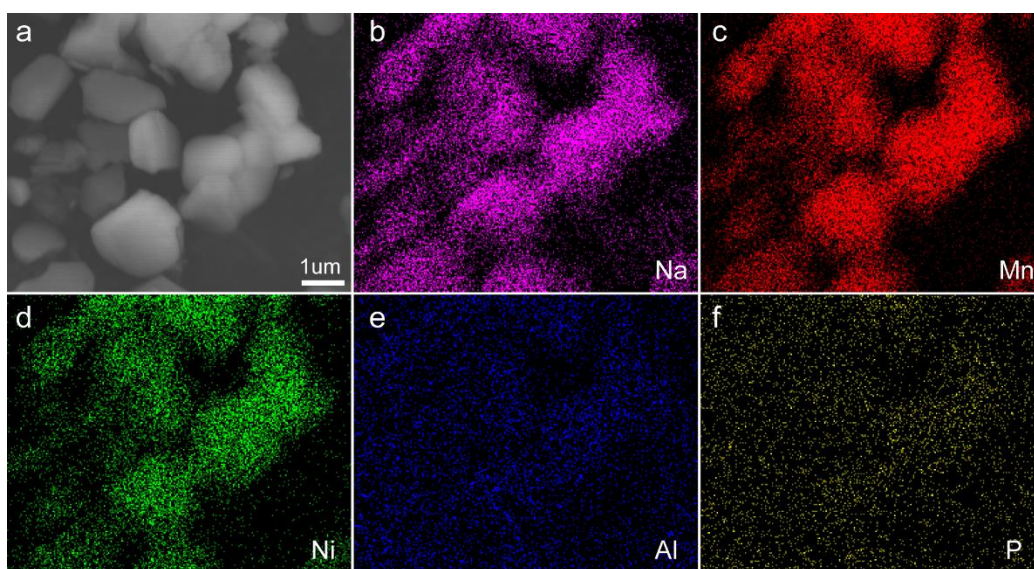


Figure S7.4 SEM image of NMO-5AP and corresponding EDX elemental mapping of Na, Mn, Ni, Al, and P

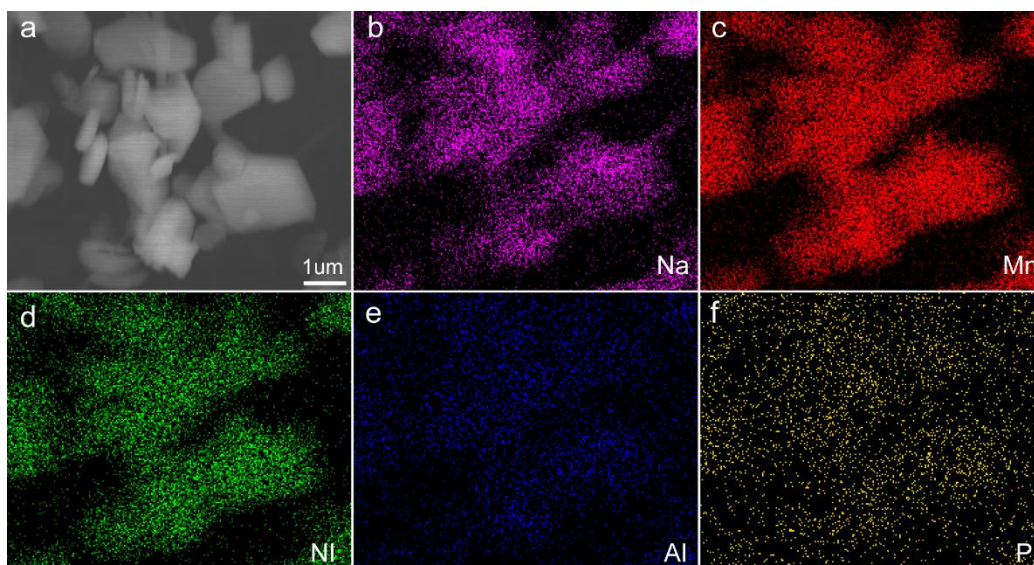


Figure S7.5 SEM image of NMO-10AP and corresponding EDX elemental mapping of Na, Mn, Ni, Al, and P.

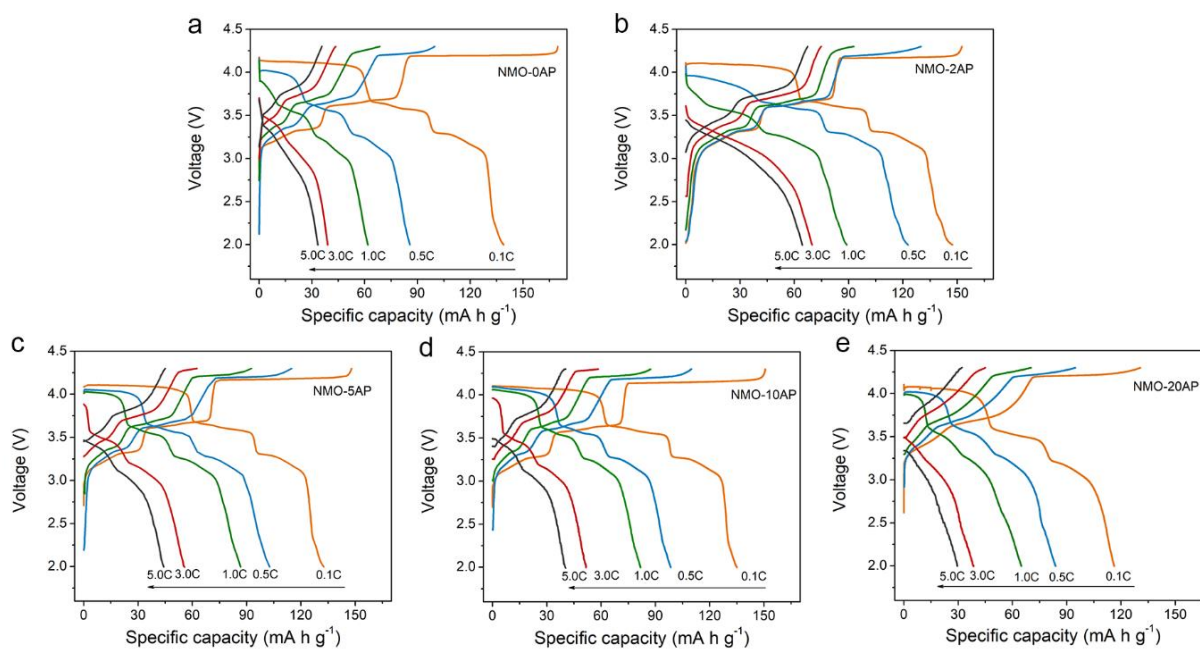


Figure S7.6 Charge/discharge curves of bare NMO and NMO-nAP electrodes at different current densities.

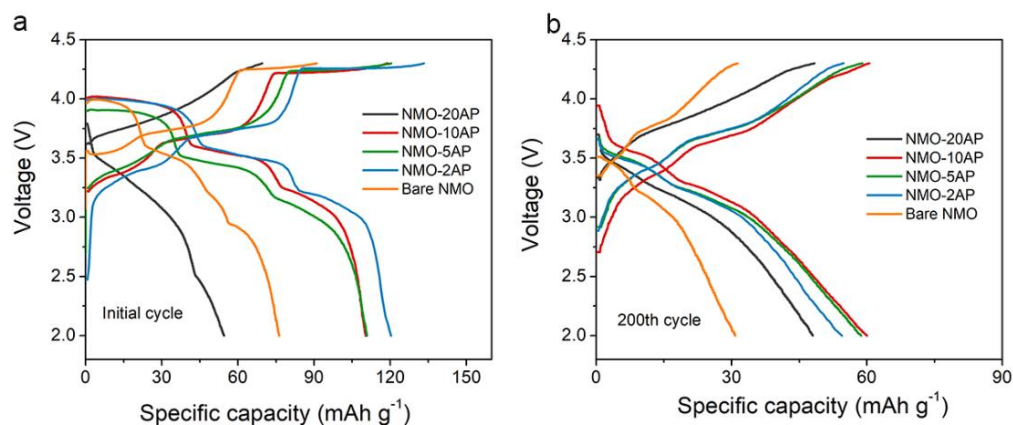


Figure S7.7 a) Initial cycle charge/discharge curves; b) 200th cycle charge/discharge curves of the bare NMO and NMO-nAP electrodes.

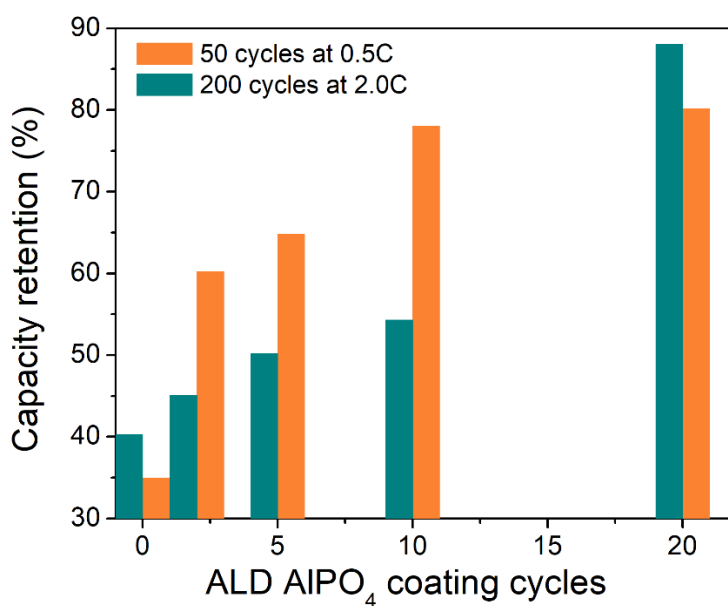


Figure S7.8 Capacity retention comparisons between bare NMO and AP coated NMO electrodes over 50 cycles at 0.5C and 200 cycles at 2.0C.

Table S7.1. Rs value of bare NMO and AP coated NMO electrodes after 10 cycles and 50 cycles.

Electrode	Rs (Ω) after 10 cycles	Rs (Ω) after 50 cycles
Bare NMO	336.1	485.9
AP coated NMO	218.5	257.6

Chapter 8

8 Summary and Future Work

8.1 Conclusions

Rechargeable batteries have attracted significant attention due to their high energy density and power density as well as pollution-free operation. However, traditional manufacturing methods are hard to fabricate thick electrodes with fast electron/ion transport due to the planar structure limitations. Moreover, electrodes and electrolytes fabricated by traditional techniques have limited form factors and mechanical flexibility. Extrusion-type 3D printing techniques thus have been applied to design various 3D architectures for achieving high-performance Li/Na batteries.

In chapter 3, 3D patterned self-supported thick LFP electrodes for high areal energy and power density LIBs were realized by an optimized extrusion-type 3D printing technique. The resulting unique 3D structured electrodes were constructed by continuous layer-by-layer filaments composed of interconnected porous polymer frameworks and continuous conducting carbon networks, thereby greatly improving ion and electron transport. The well-designed 3D microstructures were demonstrated to increase the surface area and maintain a short ion transport distance even within a thick electrode, facilitating the electrolyte penetration into the active materials as well as ion/electron diffusion. Due to these structural merits, the 3D-patterned electrodes exhibited superior electrochemical performance over conventional thick flat electrodes in terms of specific capacity and cycling stability. Moreover, an ultrathick LFP electrode of 1500 μm 3D electrodes with 8 printed layers was fabricated and presented a high areal capacity of approximately 7.5 mA h cm^{-2} and energy density of 69.41 J cm^{-2} at a power density of 2.99 mW cm^{-2} , demonstrating comparable values with reported high-performance LFP cathodes fabricated by both 3D printing and other methods in literature. This work thus provides a facile, low cost, and easily scaled way to fabricate high areal loading/thick electrode to achieve high areal energy density with high power density, which holds great promise for future practical application of high energy density lithium-ion batteries.

In chapter 4, a novel facile 3D printing approach was developed to rapidly construct patterned Si electrodes with vertically aligned and multi-scaled porous structures to achieve high areal capacity

LIBs. Compared to the conventional flat 2D Si electrodes, the 3D-printed Si electrodes possessed vertically aligned mass/ionic transport pathways and macro/micro-scaled porosities, which helped facilitate the electron/ion transport within the whole electrodes and effectively helped mitigate the large volume expansion during cycling by providing extra negative space. From the structural advantages, the 3D-printed Si was able to exhibit a superior areal capacity of around 3 mAh cm^{-2} (corresponding to a specific capacity of 1450 mAh g^{-1}) after 60 cycles. Moreover, the 3D-printed Si delivered excellent performance merits under different areal mass loadings. Even under a high mass loading of 3.81 mg cm^{-2} , the 3D-printed Si displayed an extremely high areal capacity of $10.31 \text{ mAh cm}^{-2}$ ($2706.04 \text{ mAh g}^{-1}$). This work demonstrated a facile 3D printing approach to design unique architecture for realizing a high-performance Si anode. These techniques hence open a promising avenue for developing other advanced energy systems in the future.

In chapter 5, We have developed a low-cost aqueous-based printable ink for fabricating uniform LAGP thin films via an advanced extrusion-type 3D printing approach. Compared with the conventional pressed thick LAGP pellets, the printed thin LAGP can not only reduce the total weight of a cell but also shorten the Li^+ transport distance, which could increase the energy density and power density of a solid battery. Benefiting from these merits, a $\text{LiFePO}_4(\text{LFP})/\text{Li}$ solid battery with the printed LAGP thin film as the electrolyte delivers a superior specific capacity of around 130 mAh g^{-1} even at a high rate of 5C, which is much higher than that of the battery with a thick LAGP pellet (1mm) fabricated by conventional cold-sintering technique. This method offers the flexibility of fabricating thin solid-state electrolytes with controllable thickness in a low-cost and efficient way. In addition, various patterned LAGP architectures are easily fabricated, broadening the diversity of solid batteries with various size and shapes. This work thus would shed light on fabricating desirable solid-state electrolytes for next-generation high-energy-density solid-state batteries.

In chapter 6, an extrusion-type 3D printing approach was first developed to construct a high-performance SMB which was assembled by a printed $\text{Na}@r\text{GO}/\text{CNT}$ anode and a printed NCNFM cathode. The 3D-printed $\text{Na}@r\text{GO}/\text{CNT}$ anode possesses multiple porosities, which could provide abundant active reaction sites and enable fast Na^+ transport. Moreover, the resultant 3D structured $\text{Na}@r\text{GO}/\text{CNT}$ can effectively suppress the Na dendrite growth by decreasing the local current

density and releasing the huge volume change of Na during cycling. As a result, the printed Na@rGO/CNT composite can deliver extremely stable performance over 2000 h (~1000 cycles) at a current density of 1 mA cm^{-2} . Even with a high capacity of 3 mAh cm^{-2} , the Na@rGO/CNT composite can still exhibit a long cycle life of 300 h at a current density of 3 mA cm^{-2} , which is almost three times higher than that of the bare Na foil. On the other hand, the 3D-printed microstructured NNCFM cathode composed of interconnected CNTs and porous polymer framework can enable fast electron and ion transport as well as facilitated electrolyte penetration within the whole electrode. This work thus offers a promising approach to construct high-performance Na-metal batteries, which can also be extended to develop next-generation high energy density Na-S and Na-O₂ batteries.

In order to further increase the energy density of a SIB, chapter 7 demonstrated the developing of high-voltage layered P2-Na_{2/3}Ni_{1/3}Mn_{2/3}O₂ (NMO) cathodes. We further apply an electrochemically stable nanoscale surface coating of AlPO₄ on the NMO cathode with controllable thickness via atomic layer deposition (ALD). The effect of coating thickness on the electrochemical performances was systematically studied. The results show that ALD AlPO₄-coated NMO electrodes exhibit superior cycling stability and enhanced rate capabilities. The electronic structure of the system was examined using X-ray Absorption Near-Edge Structure (XANES). The XANES results revealed that the AlPO₄ coating layer could suppress the reduction of Mn upon cycling, which could help improve the structural stability of the cathode.

8.2 Future Work

This thesis has successfully developed various printable inks and designed unique 3D microstructures via an advanced extrusion-type 3D printing technique for energy storage applications. 3D printing has shown great advantages in fabricating Li/Na battery electrodes and solid-state electrolytes. Future research can be directed to the developing of novel battery component inks and new battery forms.

This thesis first presents the fabrication of 3D-patterned self-supported thick LiFePO₄ via an extrusion-type 3D printing approach. The designed unique 3D architectures could improve the electron/ion transport within the electrode as discussed in chapter 3. However, it is known that

LiFePO₄ has a low working plateau of around 3.4 V and a relatively low theoretical capacity of 170 mAh g⁻¹, resulting in a limited energy density. Therefore, promising cathodes with high capacity and high voltage plateau, such as LiCoO₂, LiNi_{0.8}Mn_{0.1}Co_{0.1}O₂, and LiNi_{0.5}Mn_{1.5}O₄, can be adopted for developing high-energy-density LIBs.

Chapter 4 describes the employing 3D printing approach for designing patterned Si anodes with vertically aligned and multi-scaled porous structures in order to achieve high-areal capacity LIBs. Although high areal capacity can be obtained, the long-term cycling performance still needs to be further improved. In this case, further work can be focused on developing 3D-patterned graphene/Si electrodes by using the extrusion-type 3D printing method, since graphene could greatly enhance the conductivity of the electrode while the designed 3D structures can effectively mitigate the huge volume expansion of Si during cycling processes. Moreover, the combination of 3D-printed Si anodes with printed high-capacity and high voltage cathodes should be investigated to realize a printed high-performance full battery.

In chapter 5, we demonstrate the fabrication of LAGP solid electrolytes via the 3D printing method. The printed solid electrolyte has a thickness of around 100 μm, which can significantly shorten the Li⁺ transport path when applied in a solid battery. In the future, complex 3D structured solid electrolytes can be developed to construct 3D solid-state batteries. For instance, a dense-porous solid-state electrolyte framework can be fabricated by the 3D printing approach. In this unique structure, the porous part can be acted as a host for cathode materials, while the thin dense layer can separate the cathode and the anode. This dense-porous structure can considerably increase the loading of cathode materials, thus improving the energy density of a solid battery.

In chapter 6, we fabricate self-supported 3D structured Na@rGO/CNT composite anodes and O₃-NaCu_{1/9}Ni_{2/9}Fe_{3/9}Mn_{3/9}O₂ (denoted as NCNFM) cathodes using the layer-by-layer extrusion-type 3D printing approach for high-energy-density SMBs. The resultant 3D structured Na composite can effectively suppress the Na dendrite growth by decreasing the local current density and releasing the volume change during the sodiation/desodiation process. In the future, we can develop high capacity cathodes, such as sulfur cathodes and air-based cathodes, for realizing all-printed Na-S and Na-O₂ batteries.

To further increase the energy density of a sodium-ion battery, we developed high-voltage layered P2- $\text{Na}_{2/3}\text{Ni}_{1/3}\text{Mn}_{2/3}\text{O}_2$ (NMO) cathodes in chapter 7. By applying ALD AlPO_4 coating layer on the NMO particles, the reduction of Mn was suppressed upon cycling, which could improve the structural stability of the cathode. Future work can be focused on 3D printing of high-voltage sodium layered cathodes and combining them with ALD techniques for achieving long-term high-areal capacity sodium cathodes.

Appendices

Appendix: PERMISSION FROM AMERICAN SOCIETY OF CHEMISTRY



RightsLink®

Home

Create Account

Help



Title: Toward High Areal Energy and Power Density Electrode for Li-Ion Batteries via Optimized 3D Printing Approach

Author: Jiwei Wang, Qian Sun, Xuejie Gao, et al

Publication: Applied Materials

Publisher: American Chemical Society

Date: Nov 1, 2018

Copyright © 2018, American Chemical Society

LOGIN

If you're a **copyright.com user**, you can login to RightsLink using your copyright.com credentials. Already a **RightsLink user** or want to [learn more?](#)

PERMISSION/LICENSE IS GRANTED FOR YOUR ORDER AT NO CHARGE

This type of permission/license, instead of the standard Terms & Conditions, is sent to you because no fee is being charged for your order. Please note the following:

- Permission is granted for your request in both print and electronic formats, and translations.
- If figures and/or tables were requested, they may be adapted or used in part.
- Please print this page for your records and send a copy of it to your publisher/graduate school.
- Appropriate credit for the requested material should be given as follows: "Reprinted (adapted) with permission from (COMPLETE REFERENCE CITATION). Copyright (YEAR) American Chemical Society." Insert appropriate information in place of the capitalized words.
- One-time permission is granted only for the use specified in your request. No additional uses are granted (such as derivative works or other editions). For any other uses, please submit a new request.

BACK

CLOSE WINDOW

Copyright © 2019 [Copyright Clearance Center, Inc.](#) All Rights Reserved. [Privacy statement.](#) [Terms and Conditions.](#) Comments? We would like to hear from you. E-mail us at customercare@copyright.com

Curriculum Vitae

Name: Jiwei Wang

Post-secondary The University of Western Ontario

Education and London, Ontario, Canada

Degrees: 2015-present Ph. D. Candidate

Soochow University

Suzhou, Jiangsu, China

2012-2015 M.S.

East China University of Science and Technology

Shanghai, China

2008-2012, B. Eng

Related Work Teaching Assistant in Chemistry

Experience The University of Western Ontario

2016-2019

Publications:

1. **J. Wang**, Q. Sun, X. Gao, C. Wang, W. Li, F. Benjamin. M. Zheng, T. Sham*, and X. Sun*. Toward High Areal Energy and Power Density Electrode for Li-Ion Batteries via Optimizing 3D Printing Approach. ACS Appl. Mater. Interfaces, **2018**, 10, 39794-39801.

2. **J. Wang**, T. Sham, and X. Sun. 3D Printing of Vertically Aligned and Patternable Silicon Anodes for High Areal Capacity Li-Ion Batteries. **(To be submitted)**

3. **J. Wang**, and X. Sun. 3D Printing of Shape-Versatile and Thin Solid Electrolyte for High-Performance Solid-State Li-Metal Batteries. **(To be Submitted)**

4. **J. Wang**, and X. Sun. 3D Printing of High-performance Sodium Metal Batteries. (**To be Submitted**)
5. **J. Wang**, T. Sham, and X. Sun. Nanoscale Surface Modification of High-Voltage Layered Sodium Cathode via Atomic Layer Deposition of Aluminum Phosphate with Enhanced Cycle Performance. (**To be Submitted**)
6. Y. Sun, Y. Zhao, **J. Wang**, J. Liang, C. Wang, Q. Sun, X. Lin, K. Adair, T. Sham, and X. Sun*. A Novel Organic “Polyurea” Thin Film for Ultralong-Life Lithium-Metal Anodes via Molecular-Layer Deposition. *Adv. Mater.*, **2019**, 31, 1806541.
7. X. Gao, Q. Sun, X. Yang, J. Liang, A. Koo, **J. Wang**, F. Benjamin, T. Sham, and X. Sun. Toward A Remarkable Li-S Battery via 3D Printing. *Nano Energy*, **2019**, 56, 595-603.
8. Y. Zhao, J. Liang, Q. Sun, L. Goncharova, **J. Wang**, C. Wang, K. Adair, X. Li, F. Zhao, Y. Sun, R. Li, and X. Sun. In Situ Formation of Highly Controllable and Stable Na_3PS_4 as A Protective Layer for Na Metal Anode. *J. Mater. Chem. A*, **2019**, 7, 4119-4125.
9. C. Wang, K. Adair, J. Liang, X. Li, Y. Sun, X. Li, **J. Wang**, Q. Sun, F. Zhao, X. Lin, R. Li, H. Huang, and X. Sun. Solid-State Plastic Crystal Electrolytes: Effective Protection Interlayers for Sulfide-based All-Solid-State Lithium Metal Batteries. *Adv. Funct. Mater.*, **2019**, 1900392.
10. X. Gao, X. Yang, M. Li, Q. Sun, J. Liang, J. Luo, **J. Wang**, W. Li, J. Liang, Y. Liu, S. Wang, Y. Hu, T. Sham, X. Sun. Cobalt-doped SnS_2 with Dual Active Centers of Synergistic Absorption-Catalysis Effect for High-S Loading Li-S Batteries. *Adv. Funct. Mater.*, **2019**, 1806724.
11. X. Gao, X. Yang, Q. Sun, J. Luo, J. Liang, W. Li, J. Wang, S. Wang, M. Li, R. Li, T. Sham, and X. Sun. Converting a Thick Electrode into Vertically Aligned “Thin Electrodes” by 3D-Printing for Designing Thickness Independent Li-S Cathode. *Energy Storage Mater.*, **2019**

Conference Presentations:

J. Wang, T. K. Sham, and X. Sun et al. (Oral) Nanoscale Surface Modification of High-Voltage Layered Sodium Cathode via Atomic Layer Deposition of AlPO_4 with Enhanced Cycle Performance. The 102nd Canadian Chemistry Conference and Exhibition (CCCE 2019), 2019, Quebec, Canada